THÈSE présentée par :

Redouane BOUCHAALA

Soutenue le : **18 Septembre 2017**

Pour obtenir le grade de : **Docteur de l'université de Strasbourg**

Discipline/ Spécialité: Nanophysique-Biophysique

Nanoparticules organiques fluorescentes à base de lipides : intégrité et relargage de principes actifs in vitro et in vivo

THÈSE dirigée par :

  M. KLYMCHENKO Andrey   Directeur de recherche CNRS, Université de Strasbourg

  M. DJABI Smail   Professeur, Université de Sétif 1-Algerie

RAPPORTEURS :

  Mme. TEXIER Isabelle   Directeur de recherche CEA, Grenoble

  M. GUERIOUNE Mohamed   Professeur, Université Badji Mokhtar -Annaba -Algérie

AUTRES MEMBRES DU JURY :

  M. ZUBER Guy   Directeur de recherche CNRS, Université de Strasbourg

  M. BOUAMAMA Larbi   Professeur, Université de Sétif 1-Algerie

Acknowledgements

This thesis work is an important part in my life, a real adventure that will leave many memories. My strongest gratitude goes to my supervisor Dr. Andrey Klymchenko, the man who taught me everything that I know in scientific research. I appreciate his continuous support during my PhD, motivation, advises, patience, immense source of knowledge and inspiration. Thanks for his guidance during my research and thesis writing, thanks for being a boss and a friend. We say that in life there are encounters that mark you forever, Andrey was one of them, with his unique personality, interesting discussions, passion, generosity, great knowledge, positive attitude and laughters. I could not imagine a better supervisor than him.

This PhD would never be possible without some helpful people. I would thank Pr. Yves Mély for welcoming me in his laboratory, Pr. Djabi Smail my co-supervisor for his continuous support, guidance and help, Pr. Abdelkrim Beniaiche without whom this adventure would not be made.

I'd like to thank the jury members Dr. Isabelle Texier, Pr. Mohamed Guerioune, Pr. El Arbi Bouamama and Dr. Guy Zuber for accepting our request to evaluate this work.

Many thanks to our numerous collaborators, namely Dr. Nicolas Anton, Pr. Thierry Vandamme, Dr. Jacky G Goetz, Luc Mercier, Dr. Olivier Lefebre. It was a pleasure to work together on different projects and to learn a lot from them.

I'm thankful to Dr. Youri Arntz, Dr. Julien Godet, Dr. Nicolas Humbert, Dr. Halina Anton, Dr. Jurga Valanciunaite, Dr. Andreas Reisch for discussions. Dr. Ludovic Richert, Dr. Frederic Pryzbilla and Pr. Pascal Didier for their help with the microscope. Moreover, I'd like to thank Ingrid Barthel and Romain Vauchelles for their assistance, and especially Marlyse Wernert for her availability, help and smile. To Dr. Guy Duportail for his help with French papers, his kindness and for providing me newspaper.

I thank all my colleagues from Laboratory of Biophotonics and pharmacology for the friendly atmosphere in the lab, useful discussions and happy moments. Specially Rajhans, Bogdan, Marianna, Lesia, Katya, Sasha, Oleksii, Evgen, Hassan, Waseem, Tanveer, Doriane, Iryna,

1

Contents

List of Abbreviations

CMC	Exceeds critical micelle concentration
Cy	Cyanine dyes
DLS	Dynamic light scattering
DOPC	1,2-Dioleoyl-sn-glycero-3-phosphocholine
DOX	Doxorubicin
EPR	Enhanced permeation and retention
FCS	Fluorescence correlation spectroscopy
FRET	Förster resonance energy transfer
FLIM	Fluorescence lifetime imaging microscopy
FBS	Foetal bovine serum
F888	49-Dioctylamino-3-octyloxyflavone
HLB	Hydrophilic-lipophilic balance
IVM	Intravital microscopy
ICG	Indocyanine Green dyes
MSNs	Mesoporous Nanoparticles
MCT	Medium-chain triglycerides
MRI	Magnetic resonance imaging
NR668	Lipophilic Nile red
NIR	Near-infrared
NR	Nile red dyes
NPs	Nanoparticles
NLC	Nanostructured Lipid Carriers
NCs	Nanocarriers
OCT	Optical coherence tomography
PEG	Poly(ethylene glycol)
PTT	Photothermal therapy
PAT	Photoacoustic tomography
PLGA	Poly (D, L-lactide-co-glycolide)
PTX	Paclitaxel
PDT	Photodynamic therapy
PIT	Phase inversion temperature
PBS	Phosphate-buffered saline
PK	Pharmacokinetics
QY	Quantum yield
QDs	Quantum Dots
ROS	Reactive oxygen species
SLN	Solid Lipid Nanocarriers
TIRF	Total internal reflection fluorescence microscopy
TPB	Tetraphenyl borate
UCNPs	Upconversion Nanoparticles

Aim of PhD thesis

Nowadays, nanocarriers present an attractive field for researchers and pharmaceutical industry, on account of their possible application as a drug delivery system in biomedical applications. They have the ability to improve the pharmacokinetics, solubility and toxicity profile of certain drugs, and potentially augmenting their therapeutic index. However, disappointing results in recent clinical trials have compelled some to question nanocarriers potential as drug delivery and create debate about delivery problems. The poor delivery may be the result of stability, design, pharmacokinetics or bioavailability, or simply due to intrinsic biological variability. Nanocarriers complexity requires in-depth in vitro and in vivo quantitative evaluation of their behavior, with a focus on encapsulation, stability, blood interactions and release properties.

The aim of my PhD project is the development of fluorescence based techniques for characterization of lipid nanocarriers integrity and the release of active molecules in vitro and in vivo.

Using a specially designed dyes as models of drugs, the following points have been addressed:

- ➢ The integrity of the lipid nanocarriers and the release followed by Förster resonance energy transfer (FRET) technique in vitro and in vivo.
- ➢ The integrity of the lipid nanocarriers and the release followed by fluorescence correlation spectroscopy (FCS).
- ➢ Encapsulation of organic nanocarriers and the release characterized by chemical bleaching.
- ➢ Photo-triggered controlled release of active molecules from lipid nanocarriers in vitro and in vivo.

Adopting and developing these techniques, could help overcoming the challenges and the difficulties in obtaining rapid, quantitative characterization of nanocarriers stability and cargo release directly in biological media and living organisms.

PART 1

Bibliographical overview

Chapter 1: Fluorescence

During the past 20 years there has been a remarkable growth in the use of fluorescence in many disciplines, especially in biology and imaging. This use is going more and more at the level of single-molecule detection and in vivo imaging, because fluorescence is a highly sensitive *in situ* technique. This chapter first introduces the basic concepts of fluorescence, its main characteristics and describes some essential phenomena that were used in this thesis, such as fluorescence correlation spectroscopy and energy transfer.

1- Principles of fluorescence

Fluorescence is a part of a more general phenomenon called photoluminescence, which correspond to the emission of light from an electronically excited state of a given molecule. Depending on the nature of exited state either a singlet or a triplet state, photoluminescence includes fluorescence and phosphorescence. A singlet or a triplet state indicates the decay of the excited energy level and depends on the spin orientation of two paired electrons, singlet is formed if the spins are not parallel, and consequently, if the spins are parallel, a triplet is formed. The fluorescence phenomena occur if the emission takes place from the singlet excited state that has been populated after light absorption. The emission rates of fluorescence are typically 10^8 s^{-1}, so that a typical fluorescence lifetime is around a nanosecond. When the emission occurs from the triplet excited state, the phenomenon is described as phosphorescence; transitions to the ground state are forbidden and the emission rates are slow ($>10^{-3}$ s^{-1}), so that phosphorescence lifetimes are typically on the time scale of milliseconds.

The fluorescence process is usually described by the Jablonski diagram [1] (Figure 1.1). For any molecules, different electronic states exist (S_0, S_1, S_2 and T_1), each electronic states are subdivided into vibrational and rotational energy levels. Fluorescence includes several events; first, the molecule is excited by absorption of an exciting photon (represented by the energy $h\nu_1$) leading to a transition to a higher electronic energy state S_2, then rapidly relax to the lowest excited state S1 by dissipating a part of its energy in the surrounding environment, this phenomenon is usually called internal conversion and occurs within 10^{-12} s.
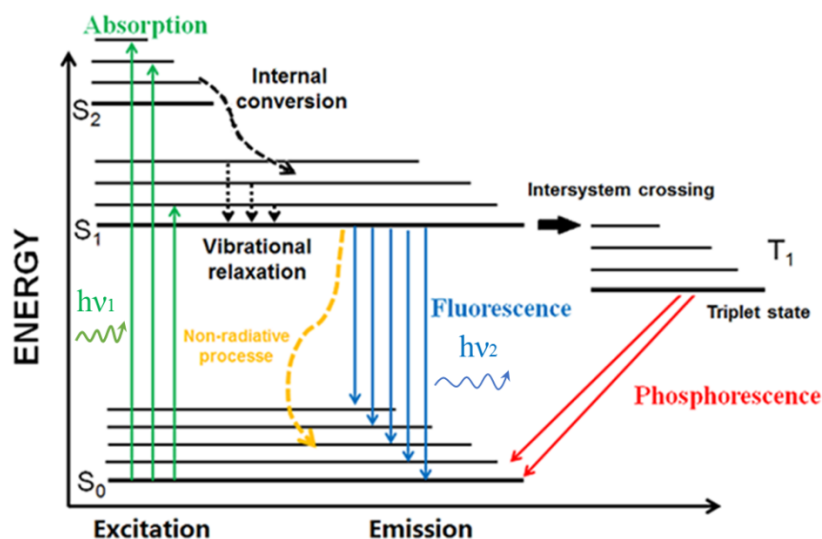
Figure 1.1. Jablonski diagram illustrating the transition between electronic states and major phenomena resulting from this transition. Adopted from ref [2].

From the excited state S_1, the molecules will reach the ground state S_0 via different competitive processes. Molecules relax ($S_1 \rightarrow S_0$) directly by emitting another photon ($h\nu_2$) and it is known as fluorescence, or can undergo a spin conversion ($S_1 \rightarrow T_1$) called intersystem crossing. As transition T1 to the singlet ground state is forbidden (but it can be observed because of spin – orbit coupling), the rate constants for triplet emission are several orders of magnitude smaller than those for fluorescence. Emission from T1 is termed phosphorescence, and is generally shifted to longer wavelengths (lower energy) relative to the fluorescence. Other important non-radiative process is Forster Resonance Energy Transfer, where a molecule in S_1 state (donor) gives the energy to another molecule (acceptor). This phenomenon will be described in the chapter 3. Molecules which are able to show electronic transitions resulting in fluorescence are known as fluorophores or fluorescent dyes. A fluorophore can be excited either by one photon or multiphoton excitation (two-photon generally), the latest one is more and more used in bio-imaging because it provides higher resolution of focal volume and deep tissue imaging through the optical windows of living tissue (700- 1400 nm).

2- Characteristics of fluorescence

2.1- Emission and excitation spectra / absorbance

Emission spectrum is the most common measured fluorescence parameter. Basically, it is the intensity of the emitted light recorded as a function of wavelength at a fixed excitation. This spectrum allows us to deduce interesting behaviours of the system under investigation,

regarding the shift in emission maximum or / and the variation of emission intensity. Some biological and chemical assays are based on the variation in these parameters. Generally, the same fluorescence emission spectrum is observed independently of the excitation wavelength, this is known as Kasha's rule [3]. Excess energy is rapidly dissipated upon excitation into higher electronic and vibrational levels, leaving the fluorophore in the lowest vibrational level of S1. This relaxation occurs in about 10^{-12} s and because of it, emission spectra are mostly independent of the excitation wavelength.

By contrast, excitation spectrum is obtained by fixing the emission wavelength and the fluorescence intensity variation is recorded as the exciting wavelength is changed. Typically, the excitation spectrum covers a large wavelength range, which usually corresponds to the fluorophore absorption spectrum, unless the existence of some species in the ground state in different forms (aggregates, complexes, tautomeric forms, etc.), the excitation and absorption spectra are no longer super-imposable. The measurements of emission and excitation spectra should take into account the characteristics of the detector.

The ability of a molecule to absorb light at particular wavelengths can be considered in the context of the Beer–Lambert law, which is a mathematical equation expressing how matter is absorbing light $C = \dfrac{A}{\varepsilon \times L}$. This law illustrates that the light emerging from molecules is regulated by three phenomena: (i) the concentration (C) of the molecules, (ii) the optical path length (L) that the light must travel through the sample, (iii) the photon probability to be absorbed by the sample (the extinction coefficient ε of the substance). One of the absorption spectroscopy applications is the determination (A) of the concentration of molecules in solution, by the knowledge of the extinction coefficient.

2.2- Stokes Shift and Solvatochromism

The Stokes shift is the gap between the two maxima of absorption and emission spectra (expressed in wavenumbers). This parameter gives information on the exited states and it is due to the rapid relaxation to the lowest vibrational level of S_1. Moreover, fluorophores further relax to the higher vibrational levels of S_0, resulting in extra loss of excitation energy. In addition to these effects, fluorophores can display additional Stokes shifts due to complex formation, solvent effects, and/or energy transfer, charge transfer, proton transfer and other excited-state reactions.

Solvent polarity can affect strongly the fluorescence of a particular fluorophore possessing high change in the dipole moment on electronic excitation. This solvent effect becomes stronger with the increase in the solvent polarity, leading to a shift of the emission to lower energies. This shifting is called fluorescence solvatochromism.

2.3- Quantum yield and fluorescence brightness, Fluorescence lifetime

Fluorescence quantum yield and fluorescence lifetime are among the most important characteristics of a fluorophore. The quantum yield QY of a fluorophore is the number of emitted photons relative to the number of absorbed photons, according to the following equation:

$$QY = \frac{k_f}{k_f + k_{nr}} \tag{1.1}$$

Where the two rate constants k_f and k_{nr} are, respectively, the radiative rate constant, and the non-radiative rate constant. These two cover all possible competing deactivation pathways, such as intersystem crossing, internal conversion or other intra- and intermolecular quenching mechanisms. Practically, the simplest method to determine the quantum yield is the measurement of fluorescence efficiency relative to that of a standard fluorophore with known QY value. For that, absorption and emission spectra for our sample and the reference, are measured at the same excitation wavelength with the same condition. the QY is calculated as:

$$QY = QY_{ref} \frac{\eta^2}{\eta_{ref}^2} \frac{I}{A} \frac{A_{ref}}{I_{ref}} \tag{1.2}$$

Where QY_{ref} is the quantum yield of our reference fluorophore, η is the solvent refractive index, I is the integrated fluorescence intensity and A is the absorbance at excitation wavelength. In this setup experiment to avoid inner filter effect and to assure intensity linearity response, the absorbance A should be kept ≤ 0.1. On the other hand, the brightness of a given fluorophore is determined by the molar extinction coefficient and quantum yield, both of which are specific for each fluorophore : $B = QY \times \varepsilon$.

The fluorescence lifetime τ_f is defined by the average time that given molecules stay at the excited state before emitting a photon:

$$\tau_f = \frac{1}{k_f + k_{nr}} \tag{1.3}$$

Two popular methods for the determination of fluorescence lifetime exist, time-correlated single-photon counting TCSPC (time domain) and the phase modulation method (frequency domain). Based on lifetime a very popular and powerful microscopy technique emerged: the fluorescence lifetime imaging microscopy (FLIM) [3].

2.4- Quenching

The decrease in the fluorescence intensity by different processes is called quenching. As example, we can cite the collisional quenching upon contact with some other molecule (the quencher) in solution when the excited-state fluorophore is deactivated, the molecules are not chemically altered in the process. Different molecules can act as collisional quenchers, such as halogen anions, amines, oxygen and electron-deficient molecules like acrylamide [4]. The mechanism of quenching varies with the fluorophore-quencher pair. Other type of process leading to quenching is where the fluorophore can form non-fluorescent complexes with quenchers. This process called static quenching, occurs in the ground state without any diffusion. Quenching can also occur by a non-molecular mechanism, such as attenuation of the incident light by the fluorophore itself or other absorbing species. Also we can cite auto-quenching where many fluorophores show different spectroscopic properties in concentrated solutions: fluorescence often becomes quenched while increasing the concentration of dyes. This phenomenon is termed "aggregation-caused quenching".

2.5- Anisotropy

Measurements of anisotropy are based on the photoselective excitation of fluorophores by polarized light (Figure 2.1). Dyes absorb preferentially photons whose electric vectors are aligned parallel to the dye transition moment. This transition has a defined orientation with respect to the molecular axis. In isotropic solution the fluorophores are randomly oriented, any molecules whose transition dipole moments are oriented parallel to the electric field vector E will be excited preferentially [1]. As a result, this selective excitation drives to partially oriented fluorophores population and in partially polarized fluorescence emission. Emission also occurs with the light polarized along a fixed axis in the fluorophore. The relative angle between these moments determines the maximum measured anisotropy (r_0). The fluorescence anisotropy (r) and polarization (P) are defined by:

$$r = \frac{I_\parallel - I_\perp}{I_\parallel + 2I_\perp} \tag{1.4}$$

$$p = \frac{I_{\parallel} - I_{\perp}}{I_{\parallel} + I_{\perp}} \tag{1.5}$$

where $I_{\parallel}$ and $I_{\perp}$ are the fluorescence intensities of the vertically and horizontally polarized emission, when the sample is excited with vertically polarized light. Anisotropy and polarization are both expressions for the same phenomenon.
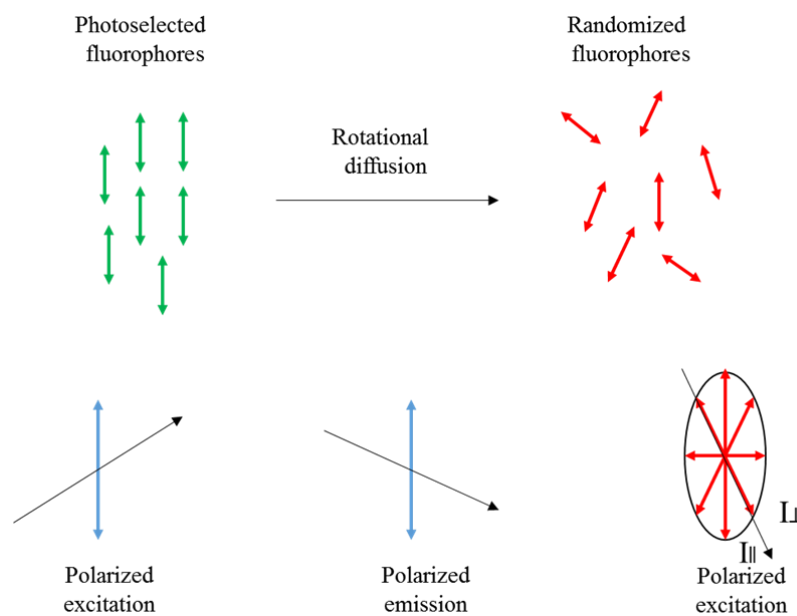
Figure 1.2. Effect of polarized excitation and rotational diffusion on the polarization or anisotropy of the emission. Adopted from ref [1].

The measured anisotropy can be decreased to lower values than the maximum theoretical values by several phenomena. One of them is rotational diffusion, which occurs during the excited state lifetime and displaces the emission dipole of the fluorophore. Measurement of this parameter provides information about the relative angular displacement of the dyes between the times of emission and absorption. In liquid solution most fluorophores rotate in 50 to 100 ps. Thus, during excited-state lifetime the molecules can rotate many times, polarized emission orientation is randomized. For this reason, fluorophores in non-viscous solution have anisotropies close to zero. Transfer of excitation between fluorophores also results in decreased anisotropies. Measurements of anisotropy of fluorophore dispersed in nanoparticles can inform us about the environment around this fluorophore (liquid or solid).

Anisotropy is commonly used in the biochemical fluorescence sensing applications [5]. It provides information's on the size and the rigidity by giving response in the change of rotational mobility for fluorescent reporter in various molecular environments. For example, if the free

fluorescent molecule has a small size, it rotates rapidly and exhibits a low value of anisotropy. On target binding the size of this rotating unit increases producing a sharp rise in anisotropy. When the molecules are in solid environment, the rotation is very low, which also results in high values of fluorescence anisotropy.

3- Fluorescent Probe

Fluorescent probes are very important tools in biological research. The choice of the appropriate probe depends on the application. We can distinguish:

i)   Natural fluorophores such: tryptophan, fluorescent proteins, plant pigments.

ii)   Synthetic dyes.

iii)   Fluorescent nanoparticles.

3.1- Natural fluorophores

Known as "intrinsic fluorophores" they present conjugated double bonds. Most proteins exhibit absorption and emission in the ultraviolet (UV) region due to aromatic amino acids. Other natural fluorophores in tissue include the reduced form of nicotinamide adenine dinucleotide (NADH) and flavin adenine dinucleotide (FAD), porphyrines, etc. Fluorescent proteins, such as green fluorescent protein, are special family of proteins, containing a special fluorophore formed from several amino acids [6]. These proteins are used as tags to label a protein of interest inside live cells.

3.2- Synthetic dyes

Organic fluorophores became an indispensable tool for fluorescent imaging and sensing. They are used for labelling biomolecules or fluorescence sensing [7,8]. Typically, they contain several combined aromatic rings and are characterized by a strong absorption and emission bands in visible range extending to near-IR of the electromagnetic spectrum, due to presence of delocalized π-electrons forming discrete energy states. Their size is commonly less than 1 nm and their quantum yields can vary from zero to nearly 100 %. The small size allows their incorporation into biological structures such as double-stranded DNA and bio-membranes with minimal perturbation [9].

Organic dyes offer tremendous possibilities in applications due to immense variations of their structures and diversity of their spectroscopic properties.
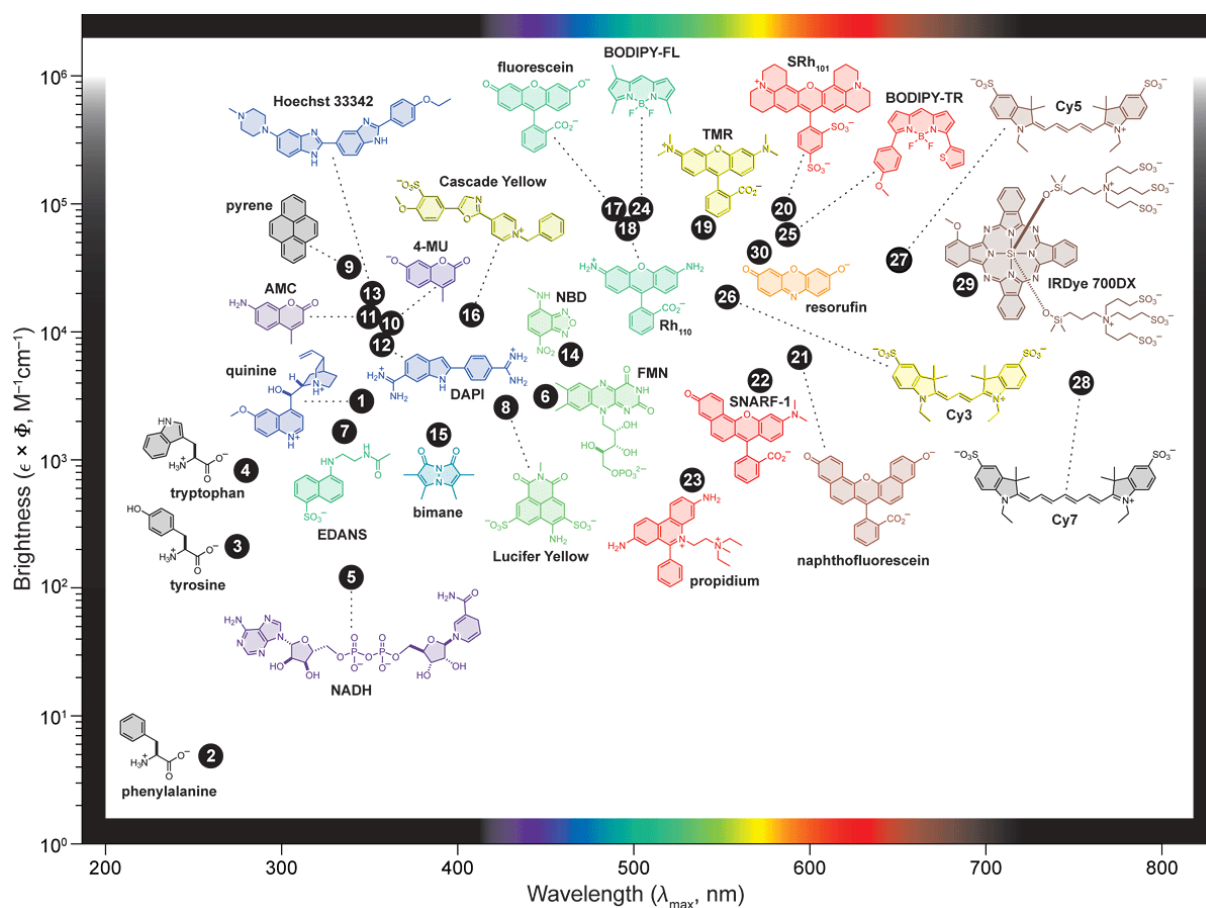
Figure 1.3. Fluorophore brightness versus the wavelength of maximum absorption (λ_{max}) for different classes of fluorophores. The colors of depicted structure illustrate their wavelengths of emission (λ_{em}). Adopted from ref [10].

With regard to applications, fluorescent dyes could be classified into two categories: non-responsive (labels) and responsive (sensors/probes).

For the "label" activity the dyes must show highest brightness and contrast, also optimal protection against various quenching and bleaching effects or perturbations by the interactions with the medium [11]. There are several classes of dyes that conform to optimal labels criteria like derivatives of fluorescein and rhodamine [12], BODIPY [13] and cyanine dyes [14]. These dyes families having rigid skeleton, exhibit minimal vibrations-related energy losses. Their electronic density is delocalized symmetrically over the whole structure, which provides high QY and low spectral sensitivity to the environment. As example of this kind of dyes we present below the cyanine dyes which were used in one of our studies.

Cyanine dyes are composed of a polymethine chain between two amino/imino groups, which can be illustrated by the simple representation (i.e., $R_2N-(CH=CH)_n - CH=N^+R_2$), where n is a small number that defines the electronic conjugation length, and the nitrogens being a part of

the conjugated chain usually form part of a heterocyclic system [15]. This family of dyes is widely used in ultrasensitive imaging and spectroscopy, especially for biological applications. By variation of the polymethine chain length, the absorption can be tuned from the visible and near-infrared region. This family of dyes is characterized by high extinction coefficients (1.2 and $2.5 \times 10^5 M^{-1}$ cm^{-1}) and moderate to high quantum yields between 0.04 and 0.4 as well as good photostability, with a lifetime in the ranging from 0.2 to 2.0 ns.
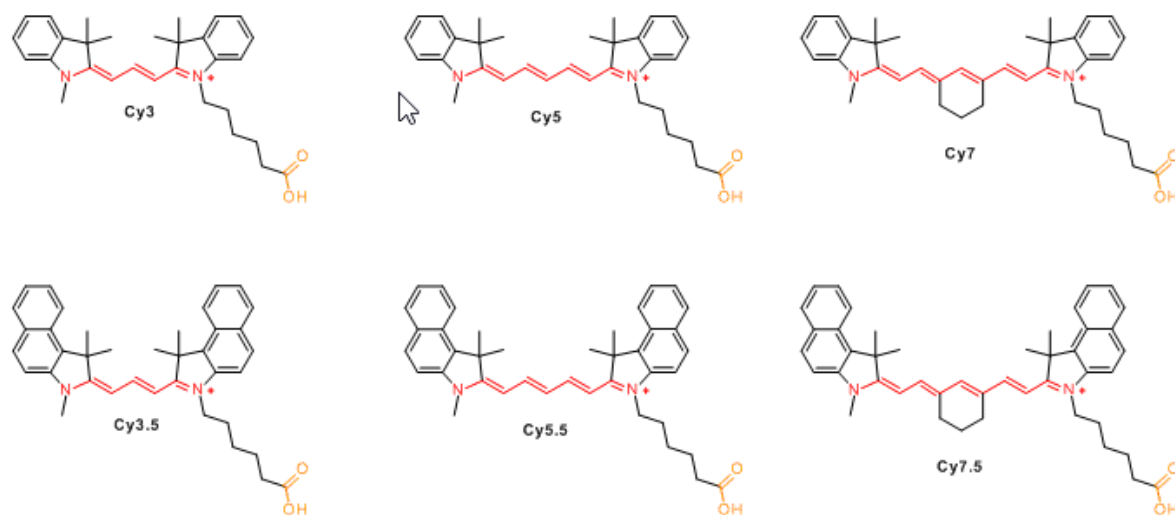
Figure 1.4. Examples of different cyanine dyes. Adopted from ref [16].

Alternatively, for the "sensors" activity, dyes must show high brightness to reach the highest dynamic range of response in terms of variations of lifetime, intensity or of the wavelength of emission. To achieve that, some photophysical mechanisms of response need to be exploited, like ESIPT (excited-state intramolecular proton transfer) [17], ICT (intramolecular charge transfer), FRET (Forster resonant energy transfer) [18], quenching, isomerization, formation of exciplexes, etc. Based on organic dyes family as hydroxychromone derivatives [19], Pyrene and Nile red [9], probes for sensing biomolecular interaction and monitoring biophysical properties of biomembranes were developed [20]. Other types of molecular probes were also developed for sensing pH, temperature, oxygen, metal ions in living systems [21]. Here, a particular attention will be paid to Nile red [20,22].

Nile red is a solvatochromic dye that shows a poor solubility in water, but in solvent it demonstrates strong fluorescence, with intensity maxima as indicators of the fluorophore environment properties. Nile red shows interesting spectroscopical properties, such as large stokes shift, good quantum yields (up to 50%) and extinction coefficient (45,000 M^{-1} cm^{-1})

which is suitable for intracellular imaging. With increase in solvent polarity, its emission maximum shifts to the red and the QY decreases.
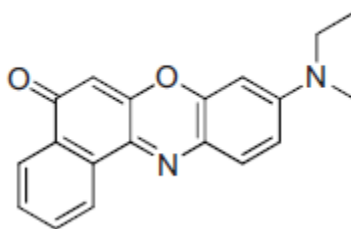
Figure 1.5. Nile red Fluorophore

3.3- Fluorescent nanoparticles

Fluorescent nanoparticles have attracted a lot of attention as a new class of probes for bioimaging [23]. They demonstrate unique electronic structures and optical properties, unusual chemical and physical characteristics. As example we can cite: quantum dots and clusters, upconversion nanoparticles, carbon dots, fluorescent organic dye nanoparticles, dye-doped silica nanoparticles, dye-loaded polymer or lipid nanoparticles. More description of these systems will be developed further in this manuscript.

4- General requirements for fluorescent probes

For high-quality imaging and sensing in biology, fluorescent probes should fit some criteria [24,25]:

- High quantum yield (QY); it means that some photochemical processes such as bleaching or radical formation will be reduced leading to higher fluorescence intensity.
- High extinction coefficient (ε); in this case higher brightness will be achieved, driving to the use of low excitation intensity. The latest one could be useful in imaging for living tissue without damage or imaging of very low quantity of fluorophores [26].
- Optimal excitation wavelength (λ_{ex}); to avoid autofluorescence, the excitation wavelengths longer than 400-460 nm are preferable. For deeper penetration in tissue imaging, NIR sources of excitation are optimal [27].
- Optimal emission wavelength (λ_{em}); it should be selected with the account of wavelength dependence of the detector sensitivity and sample transparency.
- Large Stokes shift; for reducing light-scattering effects, a strong separation between absorption and emission bands is needed. Also for more efficient collection of emitted

light using broad-band filters or larger monochromator slits. Moreover, it can reduce homo-FRET (excitation energy transfer between the same dye molecules).

- Optimal fluorescence lifetime τ; depending on the application it can be selected long or short by choosing the dye and its environment, because the lifetime depends on the temperature and the dye immediate environment [28].

- High photostability; higher dye chemical reactivity in the excited states leads to the degradation of the fluorophore (photobleaching). This photobleaching is due to some photochemical reaction that often involves molecular oxygen and is coupled with the production of singlet oxygen. In sensing applications, photostability is not a big problem because it does not require exposure to intensive light. But in single molecular studies and super-resolution microscopy, where the dye molecules are subjected to high light intensities, photostability is an important issue. Regarding this, in many of these experiments oxygen scavenging systems are used for improving the dye photostability [29].

- Solubility and environmental stability. The physical and chemical properties of the dyes (polarity, charge distribution, reactivity to form covalent bonds, ability to participate in π–π stacking, hydrogen bonding and other noncovalent interactions) determine its distribution in a heterogeneous system, moreover, the dye has to be chemically stable and less sensitive to external factor like pH or temperature if this sensitivity is not wanted.

5- Near-IR Dyes

Fluorescence-based imaging techniques offer high temporal and spatial resolution compared to ultrasound imaging, CT, MRI, PET [30,31]. For in vitro applications, super-resolution microscopy offers optical resolution well below 100 nm and fast image acquisition on the millisecond timescale allowing real-time imaging for many cellular processes [30].

For in vivo experiments, fluorescent techniques are limited by the scattering and strong attenuation of visible light (400 nm–650 nm) by biological matter (collagens, hemoglobin, lipid membranes, etc.), in addition of strong auto-fluorescence throughout the visible spectrum [32,33], rendering deep tissue imaging practically impossible in this spectral region. To overcome these problems, attention has shifted to the two so-called near-infrared biological windows from 650 nm to 950 nm (NIR1) and 1000 nm to 1350 nm (NIR2) [34,35]. In this spectral regions, light can penetrate much deeper into biological samples with minimum

absorbance and auto-fluorescence with reduced scattering, affording high signal-to-background ratio SBR (Figure 1.6). Rendering fluorescence-based imaging a viable alternative with a high spatial and temporal resolution allowing precise quantifications.
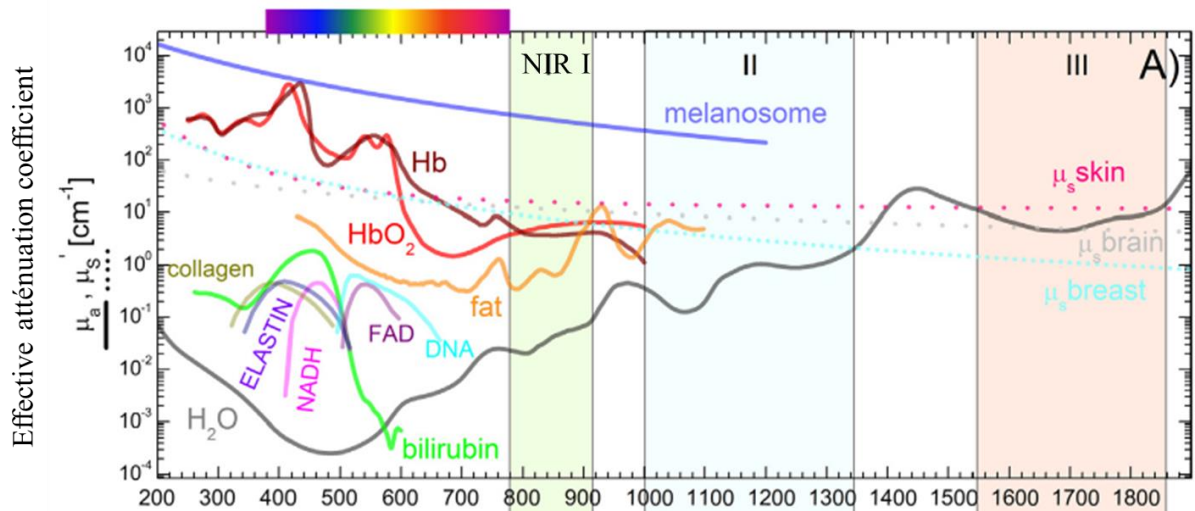
Figure 1.6. Near-infrared optical windows in biological tissues. The effective attenuation coefficient as a function of wavelength show that absorption and scattering from oxygenated blood, deoxygenated blood, skin and fatty tissue is lowest in the NIR I and NIR II spectral region. Adopted from ref [36].

Last decade with advances in imaging instrument allowed efficient detection of long-wavelength NIR photon. However, few fluorophores with sufficient fluorescence quantum yields in the NIR region were developed, especially in aqueous surroundings. One should mention cyanines 5.5, 7 and 7.5, some squaraine dyes [37], methylene blue (MB) and the FDA approved Indocyanine green (ICG) [38]. In addition to dyes, we can also cite quantum dots, carbon nanotubes, UCNPs, and gold nanorods.

These recently developed NIR emitters have emerged in biomedical imaging from contrast-enhanced imaging and molecular imaging of specific biomarkers, both for preclinical animal studies and clinical diagnostics and interventions.

Chapter 2: Nanocarriers

Nanotechnology emerged as new field involving manipulation of the matter at nanometer scale, which outcomes in a novel class of materials with innovative properties for a wide range of applications. Nanoparticles are a part of these new materials, with a size between 1–100 nm. Their use in diverse areas has been vastly explored in recent years, particularly in the biomedical field. Nanoparticles were used in diverse range of applications, such as biosensors, drug delivery, molecular imaging, and novel theranostic systems. In this chapter, we will introduce different kind of nanoparticles and their applications, with stress on lipid nanocarriers, their definition, methods of synthesis and characterisation. Additionally, their use in research as fluorescent nanocarriers are summarized.

1- Terminology clarification

Before beginning this chapter, some term definitions should be clarified. The first one is between nanoparticles (NPs) and nanocarriers (NCs). The term nanoparticle is the most general term for nanosystems with the size under 100 nm, with more than 600,000 times used in published article titles according to Web of Science database. By contrast, nanocarriers was used 8,000 times. Also NPs are used as term in all kind of application starting from manufacturing and materials, environment, energy and electronics, food applications, finishing by biomedical applications as sensor, drug delivery and imaging agent. NCs is used like a sub-class of nanoparticles, as a transport module for another substance (Protein, DNA, RNA, Drug and Contrast agent); it is more related to the use in biomedical field. Most of research on nanocarriers is being applied to their potential use in nanomedicine and drug delivery, especially in chemotherapy. Term nanocarriers generally refers to organic nanoparticles, composed of lipids or polymers. Among lipid nanocarriers one should mention liposomes, nanoemulsions, solid lipid nanoparticles, lipid nanocapsules and nanostructed lipid carriers.

Sometimes different terms are used for relatively similar lipid materials. According to Benoit and co-workers, nanoparticles containing oil core and shell composed of PEGylated phospholipids are called nanocapsules [39,40]. On the other hand, Muller et al as well as McClements et al used term nanoemulsion for different lipid based nanocarriers.

To simplify the situation in the terminology, I will call all these systems lipid nanocarriers. Moreover, all lipid systems containing liquid core will be termed nanoemulsions.

2- Nanoparticles in biomedical applications :

2.1- Inorganics nanoparticles

2.1.1- Quantum Dots (QDs)

QDs have semiconductor nanocrystal core, generally from the group II–VI or group III–V elements in periodic table (CdS, CdSe, CdTe, ZnS, PbS), coated by a shell to modify their physicochemical properties and promote solubility (Figure 2.1). With size ranging from 2 to 30 nm, they possess unique luminescent properties such a high photostability, high quantum yields and absorption coefficient. Their photoluminescence emission band can easily be tuned from the UV to the IR regions by varying the particle size or composition [41].

QDs particular characteristics make them attractive for the biomedical field such as imaging, diagnosis and therapeutic applications [42]. Thus, QDs were used for multicolor imaging and single-cell molecular profiling [3], also for simultaneous multi-species tracking in live cells [44]. In addition, QDs were proved promising for multiplexing, as example, for *in situ* molecular profiling of breast cancer biomarkers [45,46]. Recently, to overcome the poor transmission of visible light through biological tissues, NIR emitting QDs were proposed. The examples of their applications include in vivo imaging of tumor markers, such as EGFR [47,48]. Moreover, QDs operating in the second near-infrared region (1100 – 1400 nm) emerged as probes for deep-tissue dynamic imaging of the circulatory system [49], including lymphatic drainage, vascular networks, and angiogenesis [50]. In these cases, exceptional image resolution was achieved, because of deeper penetration of light in this region. Additionally, the use of QDs in targeted delivery have increased with the possibility to graft on their surface chemically reactive ligands as well as active biomolecules, such as proteins and nucleic acids.

Despite the research of different groups to use QD nanoparticles as a drug delivery nanocarriers [51], the application of QDs nanocarriers for drugs present a lot of challenges, such as limited encapsulation capacity, presence of toxic elements and incomplete excretion pathway [52,53].
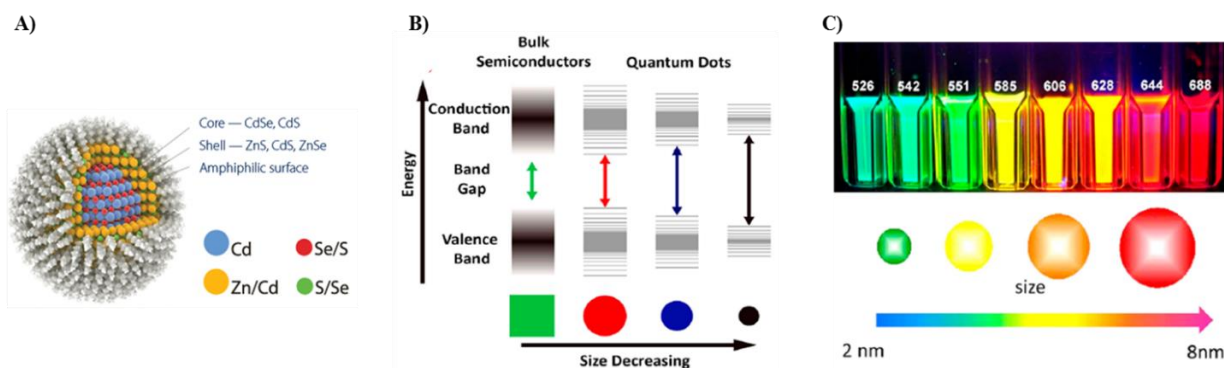
Figure 2.1. Schematic representation of QD and its energy levels. A) Schematic structure of QDs. Image adopted from physicsworld.com. B) Energy splitting diagrams for QDs due to the quantum confinement effect: semiconductor band gap increases with decrease in size of the nanocrystal. C) Example of QDs with a size-dependent luminescence. Adopted from ref [54].

2.1.2- Upconversion Nanoparticles (UCNPs)

UCNPs have emerged as a new class of theranostic agents [55]. In general, it consists of the host matrix such as $NaYF_4$ or CaF_2 doped with the rare earth ion like Yb^{3+}, Tm^{3+}, Er^{3+}, or Ho^{3+} in which electronic transitions occur (Figure 2.2). UCNPs exhibit unique optical properties; they absorb NIR light and emit shorter wavelength UV/visible photons [56]. In addition to these properties, which allow elimination of background signal and deeper tissue penetration of light, UCNPs are highly photostable [57], without blinking and have narrow emission bands, controlled shapes and sizes. These make them promising candidates for biomedical applications such as imaging, photodynamic therapy (PDT) and drug delivery.

In photodynamic therapy application, a photosensitizer is in proximity with UCNPs. At NIR light illumination, UCNPs emit visible light allowing FRET to the photosensitizer and the production of ROS (reactive oxygen species), which affect cell viability. The photosensitizer can be loaded either by chemical linkage to the carbon chains at the surface of UCNPs [58], or physically loaded in nanoparticles. As example, two photosensitizers MC540 and ZnPc were loaded into UCNPs mesoporous silica shell, where the emission of the upconversion nanoparticles matched with the absorbance of these two photosensitizers. These photosensitizers activation at single 980-nm wavelength enhanced the therapeutic efficacy of PDT in mice xenograft melanoma tumor [59].

In the same way, UCNPs were tested for drug delivery systems using a photorelease mechanism. Doxorubicin anti-cancer drug was loaded into mesoporous silica-coated UCNPs,

modified by azobenzene molecules [60]. By irradiation with NIR laser light the trans–cis photo-isomerization of the azobenzene molecules lead to the release of the drug in biological samples. Alternatively, photo-cleavable moieties were implemented for release of siRNA [61], and dyes molecules from UCNPs [62].

UCNPs can also be suitable material for bio-imaging due to their NIR excitation and can provide high image resolution. In multiplexed in vivo imaging research, UCNPc were used for lymph node mapping and in vivo tumor cell tracking, where PEGylated particles with three emission colors were synthesized by varying the molar ratio between Yb and Er. The resulting image exhibited higher in vivo detection and sensitivity compared to quantum dots [63].

In spite of UCNPs different advantages, it remains to overcome some major limitations, like low quantum yield, need of strong laser powers, low solubility and biocompatibility.
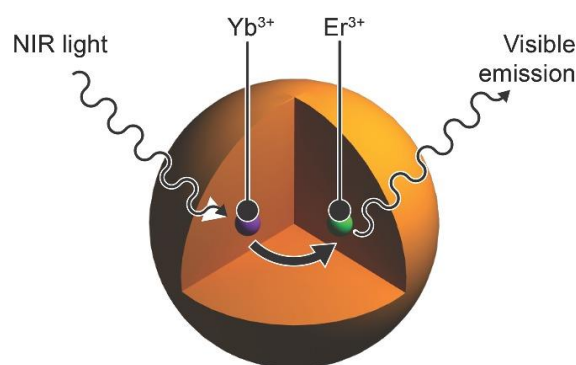
Figure 2.2. Schematic representation of a core/shell upconversion nanoparticle showing absorption of NIR light at 980 nm upconverted to visible light. Adopted from ref [64].

2.1.3- Carbon Nanotubes

Carbon nanotubes are tubular hydrophobic networks of carbon atoms prepared by rolling up of graphene, with unique structural, electronic, optical and mechanical properties. They are divided into single-walled carbon nanotubes (SWNTs) and multiwalled nanotubes (MWNTs) [65] (Figure 2.3).

SWNTs present remarkable optical properties, as NIR region absorbance, high photothermal effect, in addition of large endocytosis. Hence, they present a large interest of the scientific community and have been considered for biomedical imaging [66], drug delivery [67], photothermal therapy [68], as well as PDT. Carbon nanotubes are insoluble in most aqueous media, creating toxicity problems. Various surfactants and polymers were used to overcome

their poor solubility, however, their toxicity remains a controversial issue. Specifically, the problem of delayed clearance in the lungs was reported by some researchers [69,70].
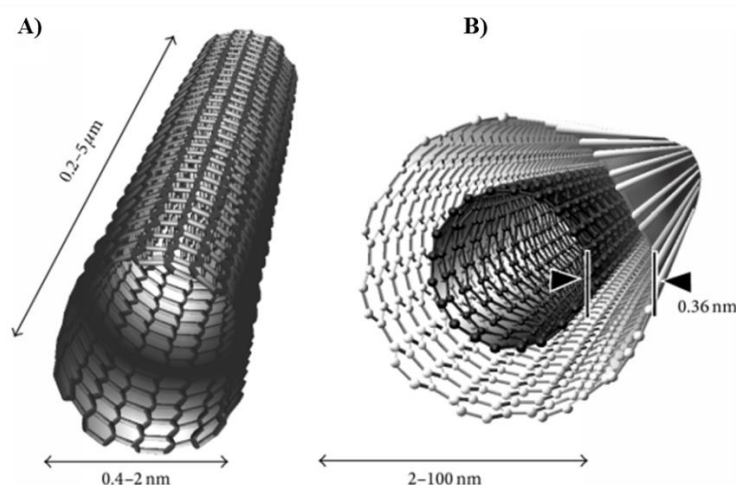
Figure 2.3. Schematic representation of carbon nanotubes showing typical dimensions of length, width. A) Single-walled carbon nanotube (SWCNT). B) Multiwalled carbon nanotube (MWCNT). Adopted from ref [71].

2.1.4- Gold Nanoparticles

Gold nanoparticles (AuNPs) have recently been widely used in many therapeutic and diagnostic procedures in the biomedical field [72], mainly due to their unique structural and optical characteristics.

AuNPs are particles composed of an Au core and a surface coating. They can be colloidal or clustered and can be synthetized through different methods [73]. The most used is the chemical reduction method, namely reduction of a gold salt solution with reducing agent such as borohydrides or citrate generating Au (0). Then, they are stabilised to avoid agglomeration by stabilizing/capping agents such as citrate or alkane thiols. The synthetic versatility of AuNPs facilitates manipulation of particle size, shape and surface like shown in Figure 2.4, offering unique chemical and optical properties.

AuNPs absorption depends on size and shape. Sphere nanoparticles absorb well in the visible region, whereas gold nanorods and nanoshells show strong light absorption in the NIR region. Under external light excitation collective oscillation of electrons occurs on their surface. This phenomenon is called plasmon resonance (LSPR), and is dependent on the size and shape of AuNPs [74]. With size increasing, the surface plasmon absorption shifts to red or NIR region.

With shape changing from sphere to rode, both longitudinal and transverse oscillation of electrons can be induced.
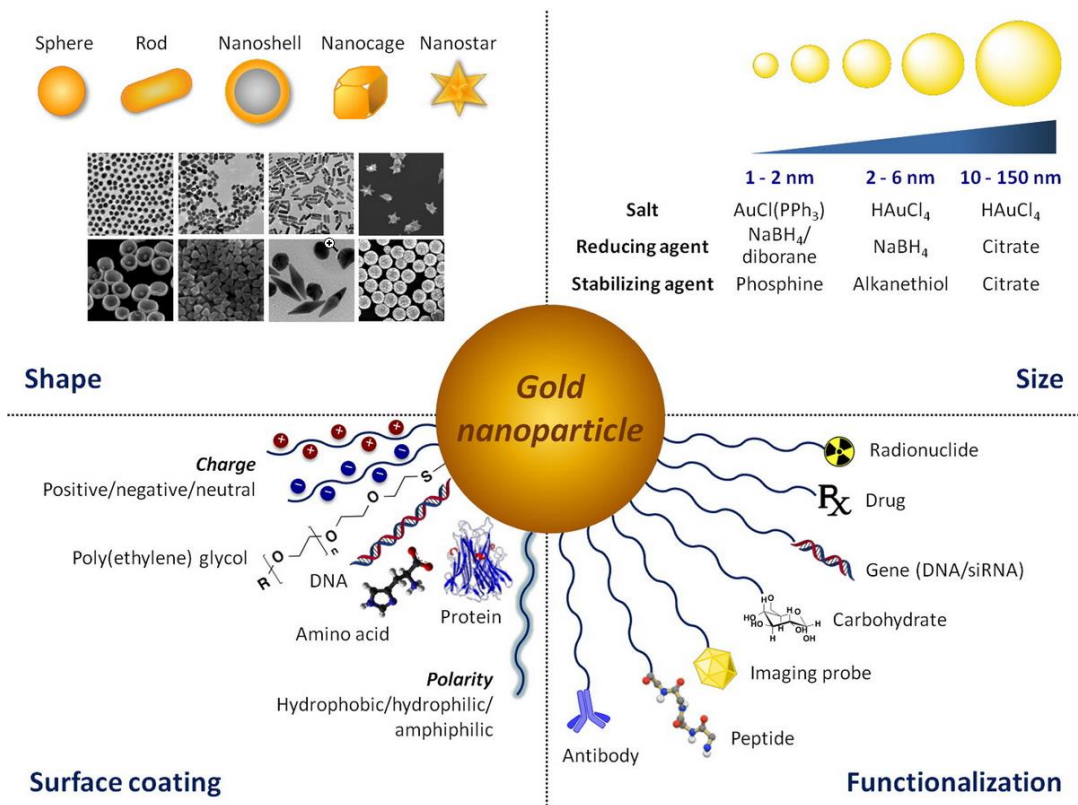
Figure 2.4. Versatility of AuNPs offer a unique platform for tailoring particle size, shape, surface coating and functionalization. Adopted from ref [75].

Due to LSPR proprieties and NIR absorption, gold nanoparticles are applied in different imaging techniques like optical coherence tomography (OCT) imaging [76], photoacoustic tomography (PAT), as well as fluorescence imaging. In early study, Chulhong Kim et al explored gold nanocages conjugated with melanocyte stimulating hormone, as a contrast agent for quantitative molecular PAT of melanomas in vivo, achieving contrast 300% higher than the control [77]. Moreover, gold nanoparticles have a high electron density, leading to efficient absorption of X-rays, which brings them in the area of X-ray-based imaging as contrast agent for computed tomography (CT) [78].

AuNPs efficiently absorb light and convert it to heat; therefore they can be used for ablation of tumor cells in photothermal therapy [79,80], and thermoresponsive controlled drug release. In drug delivery application, AuNPs are associated with organic nanocarriers such polymers or liposomes to deliver the cargo drugs or peptide upon external laser irradiation. As example, liposomes and gold nanoparticles were used to construct a cluster "bomb" structure for and

multi-order Paclitaxel release for liver tumor treatment upon laser illumination of the gold nanoparticles [81]. In addition to all these multiple applications of AuNPs, they are largely used as a sensor for in vitro detection of biomolecules [82].

2.1.5- Mesoporous Silica Nanoparticles (MSNs)

Mesoporous silica nanoparticles (MSNs) are class of silica nanoparticles with periodic mesoporous of hexagonal, cubic or lamellar structures in the range of 2 to 50 nm [83]. Diverse mesoporous silica nanoparticles were developed using different synthetic methods, such a modified Stöber method, dissolving reconstruction and self-assembly, soft and hard templating [84].

MSNs have been widely applied in biomedical research, especially as delivery nanocarriers for different drugs, dyes and active molecules. This interest is due to the intrinsic propriety of mesoporous nanoparticles, including pore size and volume, favourable chemical properties allowing surface modifications (Figure 2.5).

Even though their inorganic nature, the mesoporous MSNs are promising solution for responsive drug release under triggers. As an example, Huang et, al developed 50 nm nanoparticles with bio-cleavable disulfide bonds (-S-S-) directly incorporated, which break within tumor microenvironment [85]. As a result, high chemotherapeutic outcome was achieved in vitro and in vivo.
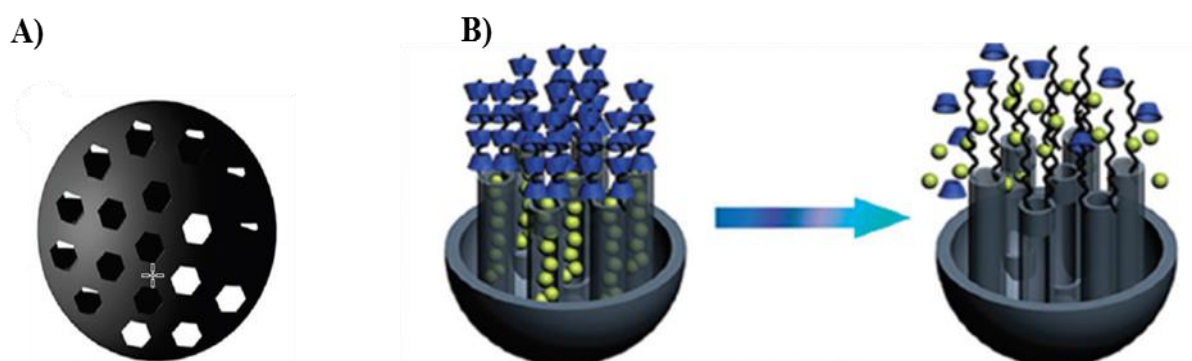
Figure 2.5. Representation of mesoporous nanoparticles system. A) Structural illustration of MSNs. B) responsive release switches on MSNs. Adopted from ref [86].

2.2- Organics Nanocarriers

2.2.1-Dendrimers

Dendrimers are a family of three-dimensional, nanoscale hyperbranched polymers, characterized by a symmetrical branched architecture and ultra-small size (typically <5 nm) with high monodispersity (Figure 2.6). They can be functionalized and conjugated with drugs or dyes, and their synthesis is based on the principles of robust high-yield chemistry. Nowadays, they are conjugated either with drug [87], or dyes for using as molecular probes [88]. Fluorescent dendrimers have relatively low quantum yield when used as fluorescent contrast agent because of dye self-quenching and their brightness is controlled by their size. However, these organic nanoparticles are costly to fabricate, and majority of them are toxic producing cell membrane damage [89].
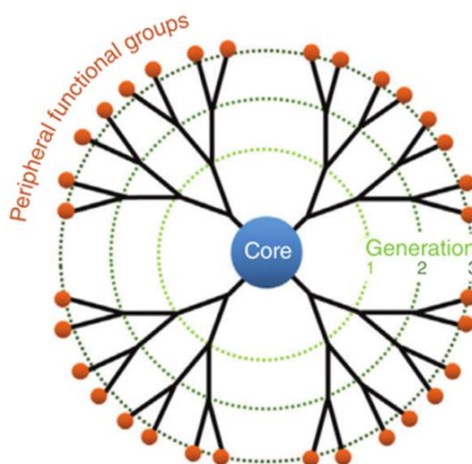
Figure 2.6. Architectural components of dendrimers. Adopted from ref [90].

2.2.2- Micelles

Micelles are amphiphilic macromolecules that self-assemble into core−shell structured nanocarriers, in which the hydrophilic parts are in contact with surrounding solvent and hydrophobic parts are in the center; their diameter is between 5 and 100 nm (Figure 2.7). They can be classified according to their amphiphilic core: polymeric or lipid micelles.

Lipid micelle are prepared with water soluble surfactant bearing hydrophobic chain linked to a polar head group. The latter can be small charged group or hydrophilic polymer, such as Polyethylene Glycol (PEG) [91], Cremophor ELP being an important example [92]. Polymeric micelles are made from block copolymers composed of hydrophobic and hydrophilic blocks

[93]. Due to their lower CMC (critical micelle concentration), polymeric micelles display better stability against dilution compared to lipid one, allowing retention of active molecule for a longer period of time in blood pool [94].
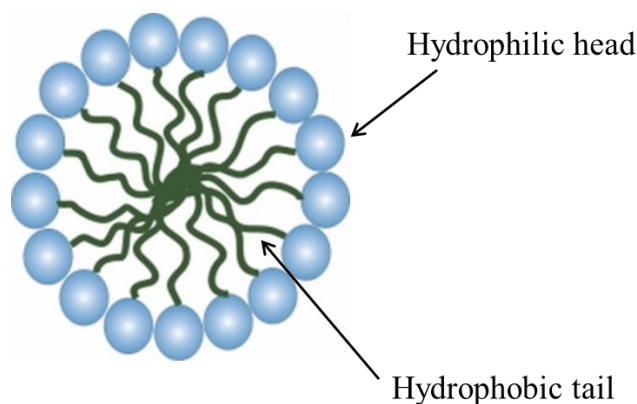
Figure 2.7. Figure illustrating micelle architecture.

Micelles are used as drug delivery systems to carry hydrophobic drugs entrapped in or covalently bound to the hydrophobic core leading to dramatic improvement in their aqueous solubility. As example, the solubility of anticancer drug paclitaxel (PTX) was increased 5,000 fold when it was formulated in poly(d,l-lactide)-MePEG diblock copolymer [95], and this formulation is currently in clinical trials. Other common utilization of micelles is in stimuli-responsive delivery mode, where drug can be released either by internal stimulus such as pH [96], enzymatic reactions [97], reactive oxygen species (ROS) [98], and temperature. Alternatively, external signal such as ultrasound, heat and light, can be used, where these last stimuli are widely associated with photothermal and photodynamic therapy (PDT) issues. In a recent study, Gao et al reported that photosensitizer (Ce6)-loaded micelles integrating cyanine dye have huge potential as theranostic tool for tumor localization via NIR / photoacoustic imaging modalities with superior cancer effect via subsequent combining photothermal therapy (PTT)/photodynamic therapy (PDT) [99].

For other applications, several micellar forms of contrast agent have been established for different imaging modes like magnetic resonance imaging (MRI) and X-ray computed tomography (CT). Recently, bimodal fluorescent/photoacoustic imaging agent, based on NIR Squaraine dye encapsulated into Pluoronic F-127 micelles was proposed, exhibiting high photostability and low cytotoxicity in biological conditions, with good contrast in animal experiment using fluorescence imaging and photoacoustic tomography modalities [100].

Recently, Shulov et al presented an interesting concept of new shell-cross-linked fluorescent micelles, with PEGylated cyanine 3 and 5 bis-azides forming a covalently attached shell on the surface of micelles of amphiphilic calixarene bearing four alkyne groups. The final micelles displayed small size of 7 nm, good quantum yield and stability in biological media. They were 2-fold brighter than quantum dots (QD-585) under microscopy, which make them suitable new platform for developing bright protein-sized responsive nanoparticles for bioimaging [101].

2.2.3- Polymeric Nanocarriers

Polymeric nanoparticles NPs are colloid systems with an average size of 10-300 nm prepared from natural or synthetic polymers. Recently, they have gathered a lot of interest in nanomedicine as drug or protein nanocarriers, also in imaging as fluorescent nanoparticles. Within in vivo applications, they have the capacity to protect their active content, with long circulation time and controlled release. In addition, they offer great versatility in modifying their size, chemical composition, morphology, biodegradability and surface functionality [102].

Nowadays, the most used polymers for nanoparticles include poly (lactic acid) (PLA), poly (glutamic acid) (PGA) and poly (D, L-lactide-co-glycolide) (PLGA), due to their biocompatibility and biodegradability properties [103]. Beside, poly (methyl methacrylate) (PMMA), poly(caprolactone) (PCL), N-(2-hydroxypropyl)-methacrylate copolymers (HPMA), poly (ortho ester) (POE) and Chitosan are aslo widely used [104].

Various methods for preparation of polymer NPs were proposed. One of them is direct polymerization of monomers (Fig 2.8). In different types of emulsions, such as (conventional) emulsion [105], mini-emulsion[106], and micro-emulsion [107]. The type of emulsion depends on the surfactant concentration (> cmc in emulsion, < cmc in mini-emulsion, >> cmc in micro-emulsion) and the method of homogenization (shear in emulsion, high shear, ultrasound in mini-emulsion and low shear in micro-emulsion) [108].
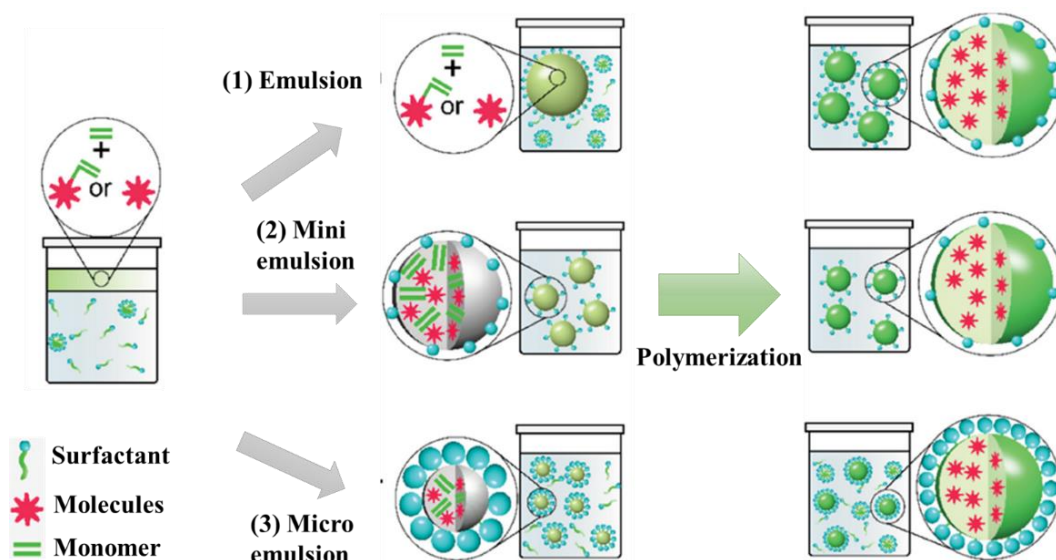
Figure 2.8. Preparation of polymer NPs though polymerization of a monomer. Adopted and modified from ref [108].

The other strategies for polymeric NPs synthesis is based on preformed polymers, following three main approaches: emulsification solvent evaporation, nanoprecipitation, and self-assembly (Figure 2.9). In emulsification solvent evaporation method, the polymer is dissolved in water-immiscible solvent and dispersed in an aqueous phase containing stabilizer. Then nanoparticles are generated under sonication or high-speed homogenization, followed by evaporation of the solvent. NPs of size 100-200 nm could be obtained [109].

Nanoprecipitation (also called solvent displacement technique) is based on the addition of polymer, dissolved in a solvent, to aqueous phase [110]. Formation of NPs occurs due to rapid diffusion of the solvent into the aqueous phase (and vice versa) and polymer supersaturation. Concentration of polymer, amount of organic and aqueous phase and mixing procedure influence the size. NPs from <10 nm up to hundreds nm could be obtained. Currently, nanoprecipitation method is probably the most used method to obtain fluorescent polymer NPs and therapeutic polymeric nanocarriers. Reisch et al based on this technique obtained very small fluorescent polymeric nanoparticles with size nearly 15 nm using different charged polymer [111]. In other study, Zhu et al used it as single self-assembly step to generate polymeric nanoparticles with simultaneous installation of targeting proteins on the exterior and loading of therapeutic proteins in the interior [112].

Finally, the self-assembly method is used for some amphiphilic polymer, who can self-assembly into NPs in form of micelles under thermodynamic conditions. In this case, a solution of

polymer dissolved in organic solvent is mixed with an aqueous phase, then the aggregation of the hydrophobic part of polymer takes place when the concentration exceeds critical micelle concentration (CMC) [113]. In fact, this approach lead to polymeric micelles, which were already mentioned above.
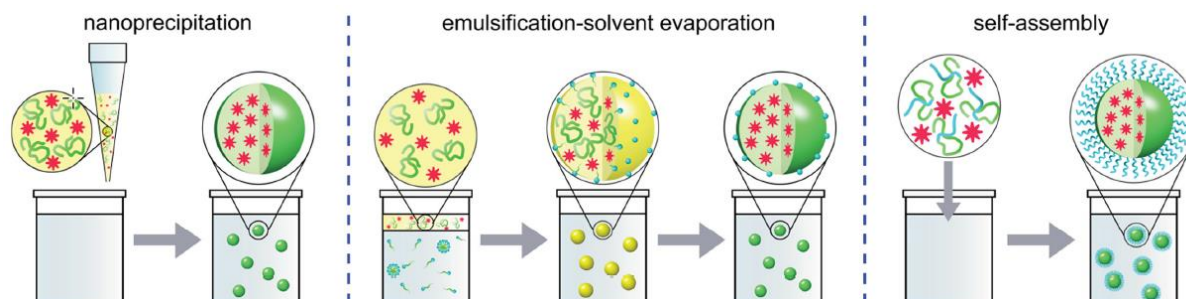
Figure 2.9. Techniques used for the preparation of polymeric NPs from preformed polymers. Hydrophobic polymer segments are shown in green, hydrophilic ones in blue, organic solvent in yellow. Adopted and from ref [108].

Polymeric nanoparticles serve as excellent drug or protein therapeutic carriers; the release can be tailored via controlled polymer biodegradation or appropriate stimulus effect. One of the most successful translation from bench to clinical trial was based on work led by Farokhzad and co-workers. They developed docetaxel encapsulated in to PLGA-b-PEG polymeric nanoparticles and surface functionalized with RNA aptamers, that target prostate cancer cells over-expressing the prostate-specific membrane antigen (PSMA) receptor, with up to 77-fold increase in binding compared to non-targeted controls [114]. Therefore, administration of this aptamer-NPs containing docetaxel was highly effective at tumor size reduction, showing almost complete tumor reduction and 100% survival.

Next, this concept was taken by BIND Therapeutics to clinical development translation with the most optimal hit; BIND-014- as the first targeted and controlled release polymeric NPs, for cancer chemotherapy. However, until now in clinical trial, polymeric nanocarriers failed to demonstrate higher activity against tumors from their parent drug. Highlighting the need for better patient selection [115,116], and better understanding of the release mechanism undergoing with these nanoparticles in vitro and in vivo [117]. Moreover, the engineering of polymeric nanocarriers that can avoid the immune system with prolonged circulation is needed. Among the lines of reflection to this problem, researchers turned to nature by designing a biomimetic nanoparticles. In one report, the group of Zhang report that PLGA nanoparticles

coated with the membrane of blood platelets can hide from the body's immune responses, and possess higher binding properties that allow them to target desired cells and tissues [118].

In other approaches, polymeric nanoparticles are used for fluorescence bioimaging and sensing in order to achieve extreme brightness and contrast using biodegradable materials. For that purpose, dyes with high concentration are encapsulated inside the nanoparticles. However, because of dyes aromatic flat structure, this encapsulation induces quenching caused by aggregation of these fluorophores in tight confinement, besides the excitation energy transfer phenomena. These processes affect the fluorescence quantum yield and reduce the brightness of dye-loaded polymer NPs. Recently, an original approach was employed by Klymchenko group, where they encapsulated inside PLGA NPs, an association of bulky hydrophobic counterions (tetrakis (pentafluorophenyl) borate) with ionic dyes (Rhodamine C18) in the form of salts, achieving small nanoparticles of 40 nm diameter and high dyes loading up to 5 wt% with minimized quenching [119]. These PLGA fluorescent nanoparticles express a QY of 23% being ≈6-fold brighter than QDs-605. What is more, these NPs showed reversible and nearly complete ON/OFF switching (blinking), opening the way for further application of dye-doped NPs for super-resolution imaging by direct stochastic optical reconstruction microscopy (dSTORM) [120]. Also, this systems was applied successfully to cyanine dyes leading to bare coded fluorescent nanoparticles for single cells tracking experiment [121].

2.2.4- Lipid Nanocarriers

Over the past decade, there have been major advances in the development of nanocarriers as delivery systems for drugs, peptides, proteins and contrast agents. Among them, lipid-based nanocarriers have great potential to solubilize, protect, encapsulate and deliver lipophilic bioactive components to desired target, achieving bioavailability and avoiding side-effects.

These nanocarriers are made from biocompatible lipids, such as phospholipids, fatty acids, cholesterol and triglycerides, in addition of surfactants and aqueous phase. Numerous advantages of the lipid matrix make the lipid-based nanocarriers potentially ideal drug delivery systems. Due to bio-compatibility and bio-degradability characteristics, these systems are prone to be less toxic as compared to other delivery systems, such as polymeric nanoparticles.

Before discussing nanoemulsions, which was the main subject of my research work, it is useful to begin with a brief overview of the other major lipid nanocarriers, focusing on their advantages and limitations.

2.2.4.1- Liposomes

First described in the 1960s by Bangham [122], liposomes are spherical vesicles formed from lipid bilayer shells enclosing aqueous interior compartments. PEGylated or not PEGylated, they can encapsulate hydrophilic agents inside the central aqueous compartment and entrap hydrophobic agents within the lipid bilayer. Liposomes are prepared mainly with lipid and/or phospholipid molecules, dissolved in an organic solvent (chloroform generally), followed by an evaporation step, rehydration of the film in an aqueous solvent, and finally processing with different techniques such as [123]:

- Extrusion: with high pressure extruder, liposomes are structurally modified to large unilamellar vesicles (LUV) or nanoliposomes, depending on the pore-size of the filters employed [124].
- Sonication: which is the most widely applied method because of its simplicity [125]. It can be realized by bath or probe sonication. However, this method presents some disadvantages, like low internal volume/encapsulation efficiency and metal pollution by the probe.
- Microfluidization: employing a microfluidizer without using solvent, based on divided pressure stream into passing each part across a tiny aperture and leading the flows to each other inside the chamber of microfluidizer [126]. This method has been applied in pharmaceutical field to produce liposomes due to the large volume production capacity, with adjustable average size and high capture efficiency.
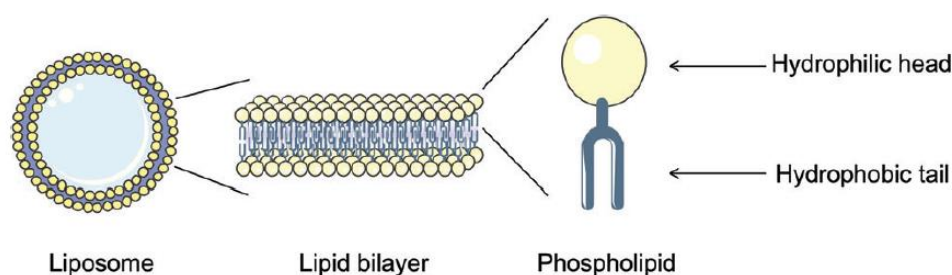
Figure 2.10. Schematic diagram of a liposome. Adopted from ref [127].

Liposome technology used as nanocarriers is extensively developed, a number of liposome-based drug formulations are available for human use and many products are under different clinical trials [128]. Doxil® was the first successful liposome-based product, introduced in US market in 1995, for the treatment of patient with ovarian cancer. Barenholz and co-workers were behind the development of this approach [129]. It consists of a Doxorubicin-loaded

PEGylated liposomal bilayer with a size of 80–90 nm, comprising hydrogenated soy phosphatidylcholine (HSPC), cholesterol (CHOL) and methyl-distearoyl phospho-ethanolamine PEG 2000 (DSPE–PEG) sodium salt. Despite its large use in the cancer therapy due to its long circulation time, good pharmacokinetics and pharmacodynamics, the Doxil® does not improve therapy efficiency comparing to normal doxorubicin, but offers better life for the patient and less side effects like hair loss and reduced cardiotoxicity. Subsequently, other formulations based on liposomes came to market, including Myocet®, Depocyt®, and Onivyde® [130].

Supplementary, huge effort is made in order to confer stimuli-responsive properties to liposomes for delivery of active molecules (drug, siRNA, protein, etc.), with different chemical and physical activation methods (pH, enzyme, redox, and light) [131]. Light triggered release from liposomes is one of the most popular method, where a photosensitizer, NIR dyes or gold nanoparticles are encapsulated inside the liposome and activated by photons to initiate the release process. Recently, Kohane group developed, based on this technique, an ultrasensitive phototriggered local anesthesia in superficial or deep tissues, where gold nanorods were attached to low temperature sensitive liposomes (LTSL), encapsulating tetrodotoxin and dexmedetomidine. Near-infrared light (808 nm) engender heat gold nanorods leading to rapid release of the anesthesia agent. They demonstrate that for in vivo situation, only 1-2 min irradiation at ≤ 272 mW/ cm^2 is needed to produce repeatable and adjustable on-demand infiltration anesthesia or sciatic nerve blockade with minimal toxicity. This effect is correlated with the power and the time of irradiation [132].

Furthermore, dyes can be also associated with liposome for photothermal and photodynamic therapy, photosensitizer dyes are encapsulated inside in order to generate singlet oxygen [133]. Also NIR dyes are used, due their deep penetration to generate the photothermal effect [134]. These last years, Indocyanine Green (ICG) was a subject of multiple studies for photothermic and photodynamic therapy [135]. Yoon et al engineered liposomal Indocyanine Green (ICG) for photothermal purpose. The photothermal effect of different lipid compositions and ICG ratio was evaluated. They showed that optimized formulation has greater anticancer effects in a mouse tumor model compared with other liposomal formulations and the free form of ICG. Then it was served to visualize the metastatic lymph node around the primary tumor under fluorescence imaging guidance, and ablate the lymph node with the enhanced photothermal effect, indicating the potential for selective treatment of metastatic lymph node [136].

2.2.4.2- Solid Lipid Nanocarriers (SLNs)

Solid lipid nanocarriers were introduced at the beginning of the 1990s by Müller research group [137,138], in order to develop an alternative carrier system to liposomes, emulsions and polymeric nanoparticles. SLN are composed of lipid being solid at physiological temperatures such as mono-, di- and triglycerides, fatty acids, waxes and steroids, stabilized by surfactants [139]. Having a highly-ordered crystalline structure, they are very stable. This type of nanoparticles designed with the idea that the usage of solid lipids instead of liquid oils may provide prolonged drug release, as the bioactive substance has much lower diffusion rate and it can be controlled by controlling the physical state of the lipid matrix of SLN [140]. The average diameter of SLNs is from 100 to 1000 nm. Solid lipid nanocarriers appear to be promising drug delivery systems, especially for oral administration . The SLN formulations are generated by both high- and low-energy methods [141].

Three models for the location of the drug within the SLN were described [142] (Figure 2.10):
- The homogeneous matrix model.
- The drug enriched shell model.
- The drug-enriched core model.

◆ Drug model

| Drug homogenized matrix model | Drug enriched shell model | Drug enriched core model |
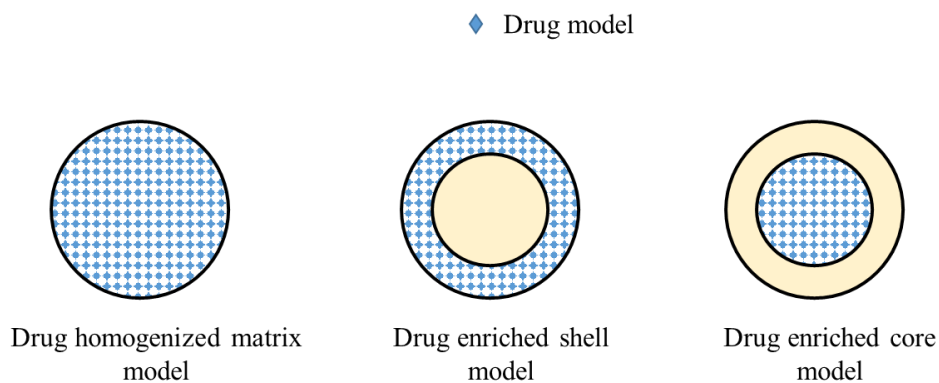
Figure 2.11. Models for drug incorporation into SLNs.

Among these models, the difference is mainly due to the chemical nature of the active ingredient, lipid and surfactant, as well as the process parameters [143]. For the matrix model, there is a homogeneous dispersion of the drug in the lipid matrix. It occurs when the nanocarriers are produced by cold homogenization technique without the use of a drug solubilizing- surfactant, or when lipophilic drugs are incorporated using hot homogenization technique into SLNs. In the drug-enriched shell model, the lipid core is surrounded by lipid corona, due to the lipid precipitation mechanism that occurs at cooling stage when the

recrystallization temperature of the lipid is reached [144]. This model is suitable for dermatological application.

The drug-enriched core model happens when the crystallization mechanism is opposite to the previous model. The drug is melted close to its saturation solubility, the cooling decreases the solubility and leads to drug crystallization before to the lipid.

Solid lipid nanocarriers were extensively applied for drug delivery [145]. The loading efficiency is affected by several factors: the drug solubility, the miscibility of the melted drug with lipid environment, the physical and chemical structure of the solid matrix, and the polymorphism state of the material [146]. Recently, a proof of concept was realized showing that SLNs were able to cross the blood-brain barrier. The surface was covalently modified with an Apolipoprotein E-derived peptide exploiting the warm microemulsion process. Different administration routes were used, with a result that a pulmonary administration is related to high confinement in the brain of mice compared to intravenous and intraperitoneal routes, without causing any inflammation reaction [147]. In the same way, Gondomi et al used PEGylated SLNs modified with two axo-glial-glycoprotein antigens, anti-Contactin-2 or anti-Neurofascin, considered as the main target of autoimmune reaction in multiple sclerosis. This formulation demonstrated a higher uptake up to 8 times with the surface-modified SLNs in the brain tissue [148]. Moreover, SLNs were also used for oral [149,150], ocular [151], dermal administration routes as well as for gene therapy application [152,153] .

However, the important drawback of SLNs is their low drug loading capacity and drug expulsion (burst release) after polymorphic transition during storage; with the increase in crystal perfection, less space remains to accommodate drug molecules. In addition, the formation of drug-enriched shell leads to burst release (Figure.2.12) [154]. To overcome this problem, a second generation of SLN was developed, which is named nanostructured lipid carriers (NLCs).
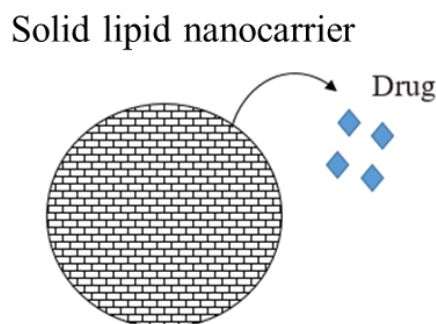
Figure 2.12. Expulsion of the drug during the polymorphic transition.

2.2.4.3- Nanostructured Lipid Carriers (NLCs)

Nanostructured lipid nanocarriers, are the second generation of solid lipid nanocarriers. They achieve higher loading capacity by mixing solid and liquid lipid [155]. With less-ordered crystalline structure, the drugs should be better encapsulated inside the lipid core and, therefore, their release during storage is minimized.

Three types of NLC have been described (Figure.2.13):
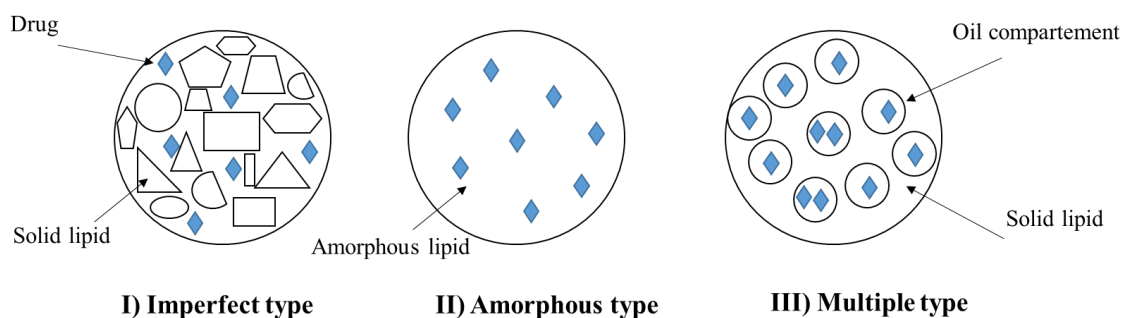
Figure 2.13. Different types of NLC: I-the imperfect type; II-the amorphous type; III-multiple type. Adopted from ref [155].

1) **The imperfect type**: it consists of small amounts of liquid lipids (oils) mixed with large amount of solid lipids. This incompatibility leads to imperfections in the matrix structure offering space for a drug in the core allowing higher loading.

2) **The amorphous type**: The nanocarriers are solid but in an amorphous state. Crystallization upon cooling is avoided by the addition of significant amount of liquid lipids with a special structure such as Miglyol ® 812 or isopropylmyristate [156]. Therefore, the consequent drug expulsion during storage is prevented.

3) **The multiple types**: also known as multiple Oil in Fat in Water (O/F/W) nanocarriers. An excess amount of liquid oil is mixed with the solid lipid. Above the solubility, a phase separation occurs with the formation of oily nano-vesicles within the solid lipid matrix. Thus, the drug is dissolved in the oil and is protected by the surrounding solid lipids.

The most used lipids and surfactants for preparation of active material-loaded NLC are [157]:

- Liquid lipids: squalene, Corn oil, α-tocopherol/vitamin E, Oleic acid, Medium chain triglycerides (MCT)/caprylic- and capric-triglycerides, Soybean oil.
- Solid lipids: Stearic acid, Carnauba wax, Glyceryl monostearate, Cetyl palmitate, Glyceryl palmitostearate, Propylene glycol monostearate.

- Emulsifier: Tween 80/20, Poloxamer 188, Lecithin, Sodium dodecyl sulfate (SDS).

Selection of an appropriate lipid mixture is crucial for NLC successful production with suitable chemical and physical characteristics [158]. Indeed, liquid and solid must be spatially incompatible together as much as possible, which means that oil should not participate in the solid crystalline matrix and the solid lipid should not be dissolved in the liquid one. Moreover, they need to be stable against oxidation and lipolysis. NLCs production techniques are similar to that of solid lipid nanocarriers, as hot/cold homogenization, solvent emulsification–evaporation, solvent diffusion and phase inversion techniques.

NLC are particularly suitable for encapsulating and delivering lipophilic bioactive molecules and other lipophilic compounds such as flavors, antimicrobials and drugs into aqueous-based foods [158,159]. Further, NLCs are very popular for dermal applications. As example, the skin penetration of the antioxidant coenzyme Q10 (CoQ10) is raised with the encapsulation in ultra-small NLCs [160].

The possibility of using NLC as delivery system has been explored for many compounds in pharmaceutical area. It has been shown that nanostructured lipid carriers, grafted with the antigen ovalbumin (OVA) and injected into mice immunized with OVA, produced much higher antibody titers for all tested formulations (different size and surface charge) as compared to that immunized OVA or OVA formulated in Complete Freund Adjuvant (CFA, positive control) [161]. The NLCs with size 80 nm anionic lipid particles were the most efficient antigen carrier for eliciting higher humoral immune response, as well as cellular immune response. These results open new way for application of these kind of nanocarriers in nanomedicine.

In addition, NLCs are used as fluorescent contrast agent, Isabelle Texier group focused for long years to develop this specific application. In 2009 they encapsulated Cyanine dyes into lipid nanocarriers containing soybean oil and wax (Suppocire®) as a core, stabilized by surfactant Myrj™ 53 (polyethylene glycol 50 stearate) and phospholipid lecithin. It was shown that it is very fluorescent and able to accumulate passively in various subcutaneous tumors in mice [162]. Later, they called it Lipidots® with a range of dyes associated covering all visible spectra (DiO, DiI, DiD, DiR, and Indocyanine Green (ICG)) [163]. This newly developed contrast agents compete by their optical properties with commercial QDs (QTracker®705). They enable lymph nodes multichannel in vivo imaging in mice using doses lower than 2 pmols of particles. Moreover, Lipidots® have very low toxicity, which make this tool for in vivo fluorescence imaging for tumor Diagnosis and Lymph Node Resection applications [164].

Recently, based the same approach they developed new dye-loaded lipid nanoparticles for long-term and sensitive in vivo near-infrared fluorescence imaging, named LipImage™ 815 [165]. This tool was applied into two clinical studies. The first one was the evaluation of LipImage™ 815 application for intraoperative fluorescence imaging (IOFI) in the surgical excision of malignant masses in dogs, with good result showing that this new fluorescent agent allows for good discrimination between tumoral and healthy tissues during the surgery [166]. Secondly, a phase-0/phase-I study of LipImage™ 815 for near-infrared fluorescence imaging in healthy dogs was finished, with conclusion that the optimal dosage of 2.0 μg/kg allowed the achievement of a fluorescence signal suitable for surgery guidance application without any acute side effects [167].

2.2.4.4- Lipid Nanocapsules

Defined as a core-shell structure composed of a liquid oily core and an amorphous surfactant shell, they were introduced by Heurtault et al, and formulated by phase inversion temperature (PIT) method plus the temperature cycling treatment [168,169]. Composed of medium-chain triglycerides oily phase (Labrafac® WL 1349), they are surrounded by a surfactant shell made of lecithin and hydrophilic nonionic surfactant, PEGylated surfactants (Kolliphor®HS15). The aqueous phase consists of MilliQ® water and NaCl. Lecithin was introduced in the formulation, and has been shown to increase the nanocapsule stability [170,171]. An other surfactant Lipoid® S75-3 is also added to increase stability. The particles obtained have a storage stability of more than 18 months. Nevertheless, the structure of these lipid nanocapsules is quite similar to the nanoemulsions. Just the lecithin is added more, and the PIT method is used.

The group of Jean-Pierre Benoit is the specialist for using and developing these lipid nanocapsules in vitro and in vivo, with a large spectrum of applications. Indeed, they have shown that lipid nanocapsules are very interesting for oral administration for different drugs [172], such as paclitaxel and milifostine [173,174]. Also lipid nanocapsules demonstrated in vitro stability in simulated gastrointestinal media [175]. Recently, their last in vitro study shows that nanocapsules cross the intestinal epithelium model (Caco-2 cell model) in intact form, opening a way for their oral administration [176].

2.2.4.5- Lipid Nanoemulsions

a) Introduction:

Lipid nanoemulsions or what we call liquid lipid nanocarriers, are emulsions with droplet size under 100 nm. Typically, it is a mixture of two immiscible phases, oil and water in addition of an emulsifier (generally surfactant). The emulsifier decreases the interfacial tension and helps to obtain small sized droplets which are more stable against creaming and sedimentation.

Based on composition of oil and water portions, nanoemulsions can be:
- Oil in water (O/W), where oil droplets are dispersed in continuous aqueous phase.
- Water in oil (W/O), where water droplets are dispersed in continuous oil phase.
- Multiple nanoemulsions (W/O/W).

In this manuscript, all our definitions and applications are about the most known and used nanoemulsions, which are oil in water (O/W) type (Figure 2.14).
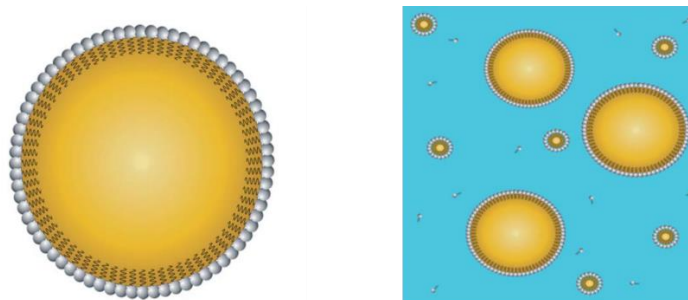
Figure 2.14. Schematic diagram of nanoemulsions fabricated from oil, water and surfactant. Adopted from ref [177].

Nanoemulsions can be prepared into different dosage forms, like cream, liquids [178], spray [179], aerosols, gels [180], and can be administrated by different routes as oral [181], intravenous, pulmonary and ocular [182,183]. The characteristics, concentration of ingredients and preparation conditions [184], play crucial role in the formation and final characteristics of the nanoemulsions. They affect:

- *Droplet characteristics*: concentration, size, distribution, physical state.
- *Interfacial characteristics*: thickness, electrical charge, polarity, rheology and permeability.
- *Phase characteristics*: density, viscosity, refractive index, interfacial tensions.

b) Components

The lipid (oil):

Generally, nanoemulsions contain 5-80% oil in order to solubilize the active molecules, it can be formulated using triglycerides [labeled as long chain triglycerides (LCT), medium-chain triglycerides (MCT) or short chain tri glycerides (SCT) depending on their chain lengths], mineral oils, marine oil, flavor oils, or essential oils [185,186]. D-α-Tocopherol (vitamin E) family has been extensively used as a carrier in nanoemulsions [187,188]. Oleic acid and ethyl oleate have been also used. The physicochemical characteristics of the oil, such as refractive index, density, viscosity and interfacial tension, impact the stability and formation of nanoemulsions. As example, it has been reported that the lower interfacial tension and viscosity, the smaller are the nano-droplets [189].

Emulsifier (surfactant):

Surfactants are amphiphilic molecules that have both hydrophilic and lipophilic parts in their molecular structure. They stabilize nanoemulsions by reducing interfacial tension, and prevent aggregation. The HLB (hydrophilic-lipophilic balance), which is the ratio of hydrophilic to lipophilic groups on a molecule, can be a good index for emulsifier relative affinity to the water and oil phases. With HLB ≥10, emulsifier has a higher affinity for water (hydrophilic), and with HLB ≤10 has a higher relative affinity for oil (lipophilic) [190].

The frequently used surfactants in nanoemulsions are Cremophor EL (Polyoxyl-35 castor oil) [191], Tween 20, 40, 60 and 80 (Polyoxyethlene sorbitan monolaurate) [192], lecithin (phosphatidylcholine) derived from egg yolk or soybean [193], poloxamer family [194] and sodium dodecyl sulfate [195], amphiphilic proteins like casein and polysaccharides [196]. Solutol HS-15 (polyoxyethylene-660-hydroxystearate) is also regularly used [197]. The surfactant selection does not just affect size and stability, but determines also the toxicity, pharmacokinetics and pharmacodynamics of a nanoemulsions.

Aqueous Phase:

The aqueous phase composition plays an important role in nanoemulsion physicochemical properties. A variety of water-soluble constituents, including minerals, acids, bases, flavors, preservatives, vitamins, sugars, proteins, and polysaccharides, can be added to the aqueous

phase to change its properties [198]. pH and viscosity of the aqueous phase may impact the stability of the nanoemulsions.

c) Formulation methods

Different formulation methods were proposed for the preparation of nanoemulsions, classified into two categories: high-energy emulsification methods and low-energy emulsification methods.

High-energy emulsification methods

It consists of applying high disruptive forces with mechanical devices capable of causing the breakup of oil droplets and dispersing them into the water phase. Such disruptive forces are achieved via ultrasonicators, microfluidizers or high pressure homogenizers which are industrially scalable. Their versatility is in the fact that any oil can be subjected to nanoemulsification. The disadvantages are in the cost of the instrument and generation of high operational temperatures, and the size cannot be reduced under 50 nm.

- *Microfluidizer*

The starting material pass several times through a chamber, consisting of microchannel under influence of a high pressure displacement pump (500–50,000 psi), resulting in very small droplet as shown in Figure 2.15. The microfluidizer uses hydraulic shear, intense turbulence, impact and cavitation, to effect size reduction. This technique requires cooling due to the impaction energy generated by collision of droplets.
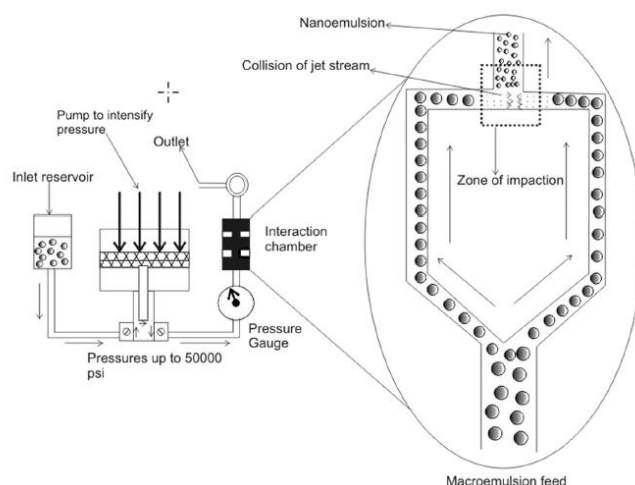
Figure 2.15. Setup and functioning of a microfluidizer for nanoemulsion formulation. Adopted from ref [199].

▪ *Piston gap homogenizer*

A coarse emulsion is pumped through a narrow gap (≤10 μm), between rapidly moving rotor and fixed stator. Grinding force, high shear and stress generated between the rotor and stator, cause the size reduction as shown in Figure 2.16. Fixing dissipation gap can give the required size.
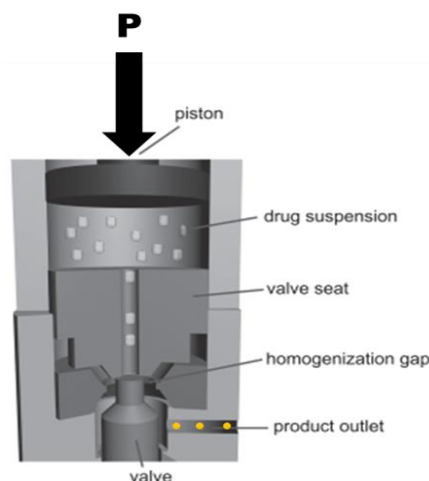
Figure 2.16. Basic principle of high pressure homogenization using a piston gap homogenizer. Adopted from ref [200].

▪ *Ultrasonication:*

It consists of applying a strong ultrasonic energy with a high-frequency wave, in a small volume to agitate particles in a sample. This action produces cavitation bubbles which continue to grow until they implode, then create a jet stream of surrounding liquid, pressurizing dispersed droplets and reducing their size. Increasing sonication time and input power decrease droplet size [201].

Typical sonicators consist of a piezoelectric probe which generates intense disruptive force at its tip as shown in Figure 2.17. These probes are available in a variety of dimensions which affect their functionality. Ultrasonication requires less energy expenditure compared to other high energy methods. On another side, the drawback of this technique is contamination induced by probe degradation. This can be avoided in scale up manufactory, by using special column capable of producing ultra-sonic waves.
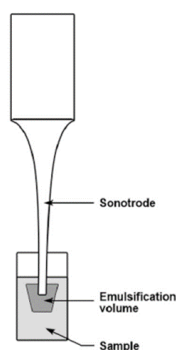
Figure 2.17. Schematic illustration of ultrasonication method for emulsification.

Low-energy emulsification methods

Nanoemulsions can be prepared by low-energy emulsification methods, using the energy stored in the system to produce ultra-fine droplets. Based on diverting the intrinsic physicochemical properties of the surfactants, co-surfactants and excipients composing the formulation, it includes spontaneous emulsification or phase inversion method. Low energy methods are sometimes limited by oil type and emulsifiers that can be used. However, they are simple, solvent free, cost effective, producing small size droplets.

- *Phase inversion temperature (PIT) method:*

PIT exploits the change in aqueous/oil solubility of surfactants in response to temperature fluctuation as shown in Figure 2.18. It involves via an intermediary bicontinuous phase ordered conversion of a W/O to O/W emulsion or vice versa. Emulsion of oil, water and surfactant is heated at defined temperature (PIT) and then rapidly cooled. The change in temperature from low to high leads to opening and reversal of interfacial structure causing phase inversion. Then cooling leads to closed structure, trapping oil for nanoemulsion generation. Surfactant and the oil should be well mixed [202].

The influence of the formulation (electrolyte concentration, temperature, etc.) and composition parameters (ratio surfactant/oil), has been largely reported on the potentialities to formulate nanometric-scaled emulsion droplets [203].
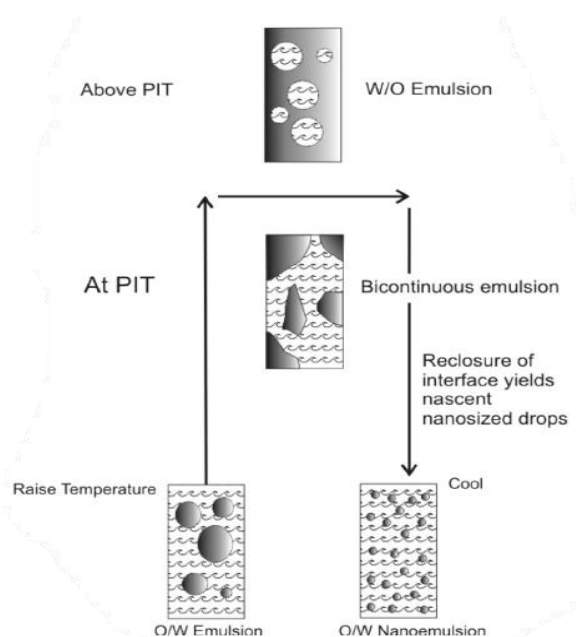
Figure 2.18. Schematic representation of phase inversion temperature method for nanoemulsification. Adopted from ref [199].

- *Spontaneous emulsification:*

Spontaneous emulsification may occur when immiscible liquids in non-equilibrium conditions are in contact and gently homogenized. In short time, a kinetically stable nanoemulsions is formed [204]. This phenomenon is triggered by gradients of chemical potential between the phases, which under certain conditions lead to negative values of free energy of emulsification. Different explanations were formulated to understand this phenomena, but it still remains not completely elucidated. A simple mechanism was proposed by Anton et al. The spontaneous emulsification was attributed to the penetration of the water phase into oily phase, resulting in the break-up of this phase [205].

As shown in Figure 2.19, when the lipophilic mixture of oil and surfactant, homogenized under temperature and stirring (Figure 2.19.A), is in contact with water (Figure 2.19.B), the aqueous phase penetrate the oil, solubilizing the surfactant molecules (Figure 2.19.C). Surfactant molecules stabilize the newly formed droplet while nanoemulsions are generated (Figure 2.19.D), with size between 20 and 200 nm depending on the ratio oil/surfactant, with excellent monodispersity (0.1-0.2). Not all surfactant and oil are adapted to this method, however some optimal conditions can be found, like the complete solubility of the surfactant in the oily phase, which can be improved by raising the temperature. A good choice of specific physiochemical characteristics of ingredients is needed.
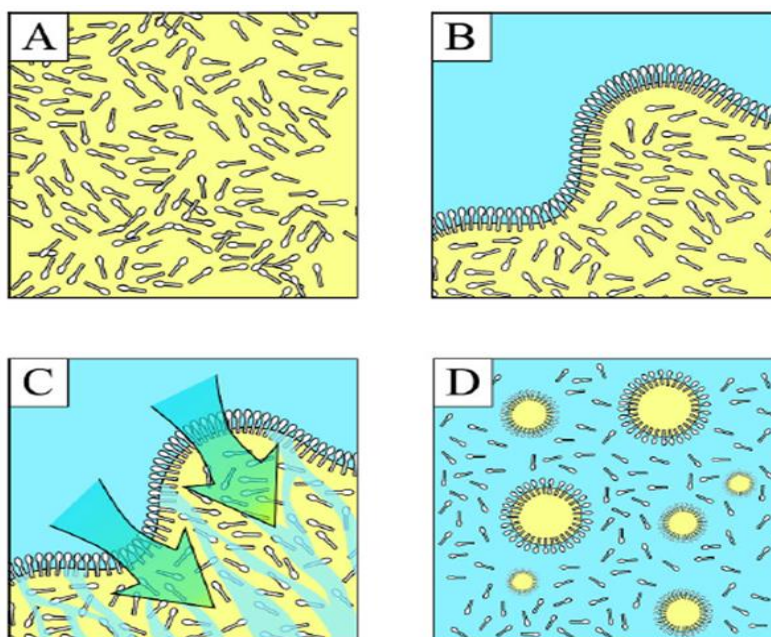
Figure 2.19. Illustration of mechanism driving spontaneous emulsification. Adopted from ref [206].

d) Nanoemulsion stability

With an appropriate selection of system components, composition and preparation method, nanoemulsions, non-equilibrium systems, are wide kinetically stable system for months, compared to emulsions (micrometer-size droplets) due to their small droplets size, stability against dilution or even against temperature changes. Figure 2.20 summarizes the different destabilization mechanism of nanoemulsions, namely flocculation, coalescence, Ostwald ripening and creaming/ sedimentation.
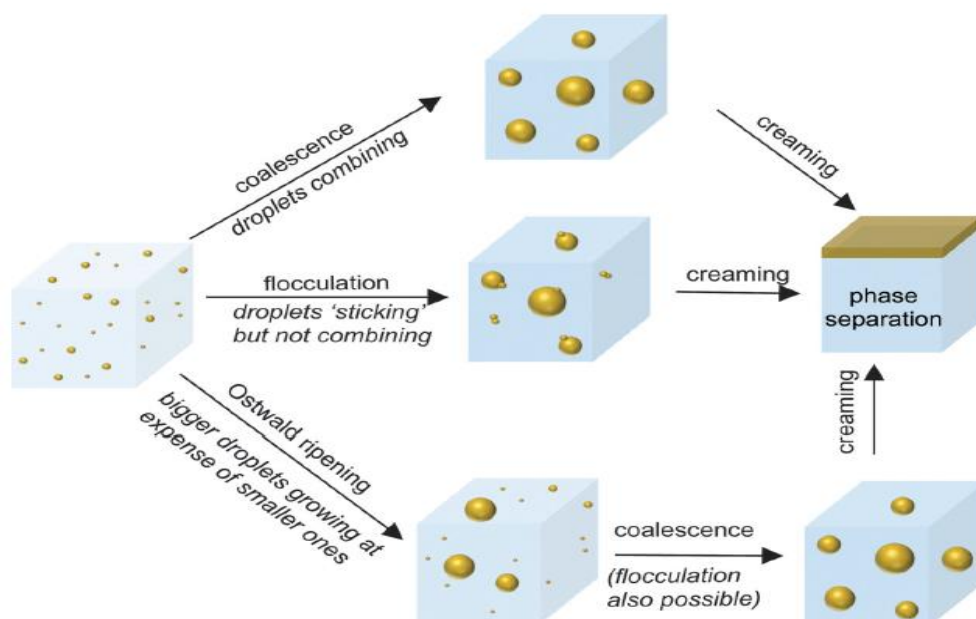
Figure 2.20. Illustration of different nanoemulsions destabilization mechanisms. Adopted from ref [207].

It is hard to distinguish between coalescence and flocculation in emulsion. In coalescence, droplets merge one with each other and become larger. During flocculation, because of attractive interactions, the droplets come closer to each other (stick but not combine) and move as a single entity, this mechanism is irreversible. The DLVO theory explains that it is due to the low potential interaction for the droplet–droplet [208].

However, nanoemulsions are stable against sedimentation or creaming due to their small droplet size. Also, the absorbed layer of emulsifier on the droplet surface generates electrostatic and steric interactions, which increase the repulsive maximum, thus stabilizing nanoemulsions against flocculation and coalescence [209].

Ostwald ripening is the main breakdown stability process of nanoemulsions [210]. It occurs because of the solute chemical potential within droplets of different sizes, as a consequence of Laplace pressure. The dispersed phase chemical potential is higher in smaller droplets than in larger ones, contributing to driving force for mass transfer from the smaller to the larger droplets. Thus the smaller droplets become smaller and the larger droplets grow. One critical factor affecting Ostwald ripening rate is the solubility of the dispersed phase in the continuous phase. The Ostwald ripening rate follow this equation [211]:

$$d^3 = d_0^3 + \frac{64\sigma c_\infty v^3 D}{9RT} \, t \qquad (2.1)$$

Where d_0^3 is the initial average diameter number, σ is the interfacial tension, c_∞ is the solubility of the dispersed phase in the continuous phase, v is the molar volume of the dispersed phase, D is the diffusivity of the dispersed phase in the continuous phase, R is the ideal gas constant and T is the temperature of the system. Using derivative, the Ostwald ripening rate ω_0 has the value $\frac{64\sigma c_\infty v^3 D}{27RT}$. ω_0 decreases with addition of an insoluble emulsifier to the continuous phase [212]. However, this is not very effective on the long term because it increases the flocculation/coalescence rate due to reduction in steric repulsion between droplets.

Nanoemulsions stability is controlled by various factors:

- *Ionic strength*: Delmas et al, showed that increase in the ionic strength of the continuous phase decreases the repulsive forces. As a result, the emulsions have a much higher probability of flocculating/coalescing [212].

- *Polydispersity*: higher is the polydispersity, higher is the Ostwald ripening rate, due to high difference in chemical potential between droplets.

- *Solubility*: it makes easier for dispersed phase molecules to travel through the continuous phase.

- *Additive products*: destabilizes the rates by changing the properties, like interfacial tension, droplet elasticity, and interaction potential between droplets.

- *Emulsifier concentration*: increasing this parameter causes the increase in destabilization rate, argued by the enhanced diffusion of oil due to micelle formation and lowering of Gibbs elasticity [213]. This is not always true because the inter-droplet interactions are different for different systems.

- *Temperature:* some studies showed that increase in the temperature, increases the ripening rate, due to change in dispersed phase solubility and diffusivity

The stability of nanoemulsions is not easy to monitor because of all previous cited parameters, affecting their stability. For that reason and with the idea to apply these nanoemulsions as eventual drug nanocarriers, the development of different tests for in vivo and in vitro stability and release monitoring, is an urgent topic to investigate.

e) Application of nanoemulsions in biomedical field

With their unique proprieties such as small size, stability, transparent appearance, tunable rheology, encapsulation capacity, biodegradation and bioavaibility, nanoemulsions are attractive candidates for application in food [214], cosmetics [215], pharmaceutical and

biomedical industries [199]. Here, we will focus just on biomedical applications as drug delivery systems and imaging agents.

As drug delivery systems, nanoemulsions encapsulating active molecules can be administrated with various modes in human body, such as topical, ocular, intravenous, intranasal, and oral routes. Nanoemulsions were largely exploited as a drug delivery carrier for multitude of cancers [216,217]. To overcome the multidrug resistance (MDR), nanoemulsions encapsulating hydrophobic and hydrophilic drugs, paclitaxel (PTX) and 5-fluoroucacil (5-FU), were used, functionalized by vitamin E (VE) and tocopherol poly (ethylene glycol) succinate (TPGS). This combined therapy led to dramatic inhibition of tumor growth, especially in the PTX-resistant KB-8-5 tumors, where Taxol had little therapeutic effect. Combined therapy allows simultaneous interruption of diverse biochemical pathways, resulting in increased therapeutic response and low toxicity [218]. In other studies, Coleman and coworkers used folate and gadolinium targeting paclitaxel nanoemulsions to overcome multidrug resistance in ovarian cancer. In vitro cytotoxicity showed a 270-fold drop in IC50 in SKOV3TR cells as compared to docetaxel alone, and efficient accumulation in tumor-bearing mice [219]. In addition, cationic nanoemulsions encapsulated TNFα siRNA where used via intranasal brain delivery [220,221], in order to prevent chronic neurodegenerative disorders and neuro-inflammation [222]. Several formulations using nanoemulsions as drug nanocarriers are in clinical trial pipeline [223–225].

Other important application of nanoemulsions is biomedical imaging. Attia et al used iodinated nanoemulsions as X-ray contrast agent, which allowed evaluation in situ of their pharmacokinetics and biodistribution [226]. They compared three different iodinated oils formulated with PEGylated surfactantq. As shown in Figure.2.20, the iodinated nanoemulsions displayed high contrast enhancement in blood with similar half-life around 6 h, but very different accumulation sites. While iodinated monoglycerides exhibited low accumulation in liver and spleen, high accumulation in spleen was observed for iodinated castor oil and in liver for vitamin E.
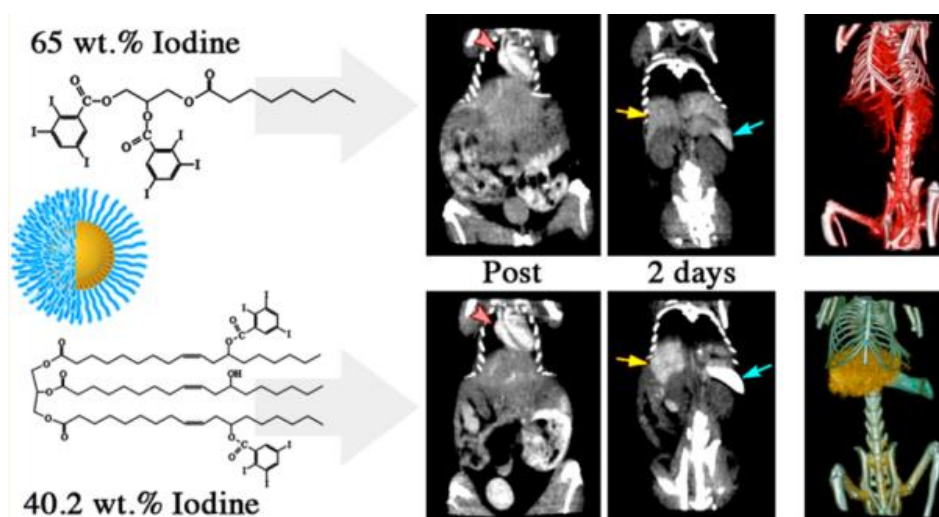
Figure 2.21. Illustration of iodinated nanoemulsion as a contrast agent. Adopted from ref [226].

Recently, so-called "high intensity focused ultrasound-responsive perfluorocarbon nanoemulsions" have emerged as a new class of smart multifunctional vehicles which exhibit high ultrasound imaging contrast and can release their payload in a controlled manner [227,228]. Perfluorocarbons are fluorinated liquids which include perfluoropentane, perfluorohexane perfluorodecalin, perfluorooctyl bromide, etc. Fluorine-19 isotope in these fluorinated carbons enables quantitative fluorine-19 magnetic resonance imaging [229]. When they are stimulated with ultrasound these volatile compounds vaporize, transforming the nanoemulsions system into high-contrast microbubbles for delivery, therapy and imaging [230,231].

In one similar study, nanoemulsions were used as blinking nanometer-size contrast agents, to develop a new class of laser-activated nano-droplets (LANDs) for super-resolution ultrasound imaging as shown in Figure.2.22. This LANDs can be repeatedly optically triggered to blink between vaporization state and native liquid droplet. The resulting spatially stationary and temporally transient microbubbles provide high ultrasound contrast. After processing algorithm, this new system provides high resolution molecular imaging deep in the tissue in vivo, almost an order of magnitude better than conventional ultrasound imaging [232].
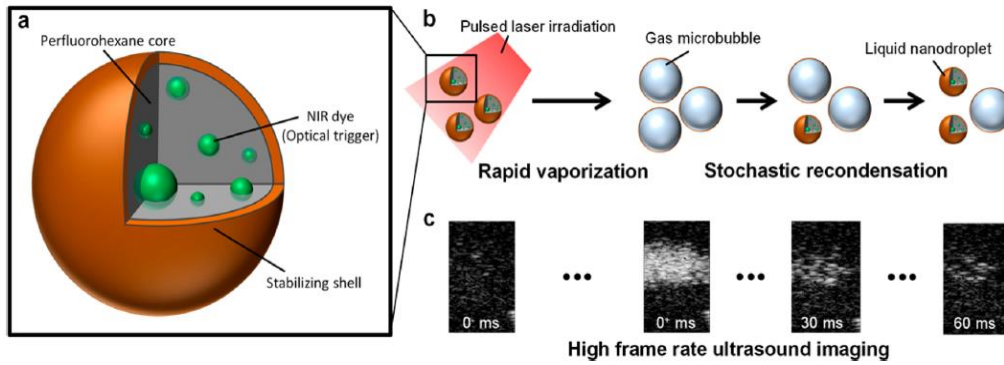
Figure 2.22. schematic representation of laser-activated nano- droplets (LANDs) for super-resolution ultrasound imaging. Adopted from ref [232].

Nanoemulsions were also investigated as fluorescence imaging tool, Mulder and coworkers used it as a multifunctional platform for imaging guided therapy, where fluorescence is the second function beside the MRI, providing near-infrared fluorescence imaging with Cy7 dye [233]. Klymchenko and coworkers designed new bright nanoemulsions droplets based on Nile Red derivative (NR668) without any leakage and showed that they can be useful and efficient optical contrast agents for in vitro and in vivo applications [234]. Later the same group achieved 8 wt.% of dye loading into nanoemulsions, using modified cyanine dye (DiI) with counterion tetraphenylborate. The latter drastically improves solubility of the dye in oil and prevents formation of non-fluorescent aggregates. This new ultra-bright nanoemulsions contrast agent containing >10,000 cyanine molecules, are >100-fold brighter than quantum dots, allowing for the first time single-particle tracking in the blood flow of live zebrafish embryo as shown in Figure 2.23, revealing both the slow and fast phases of the cardiac cycle with minimal cytotoxicity [235]. These results provided a solid background for my PhD project.
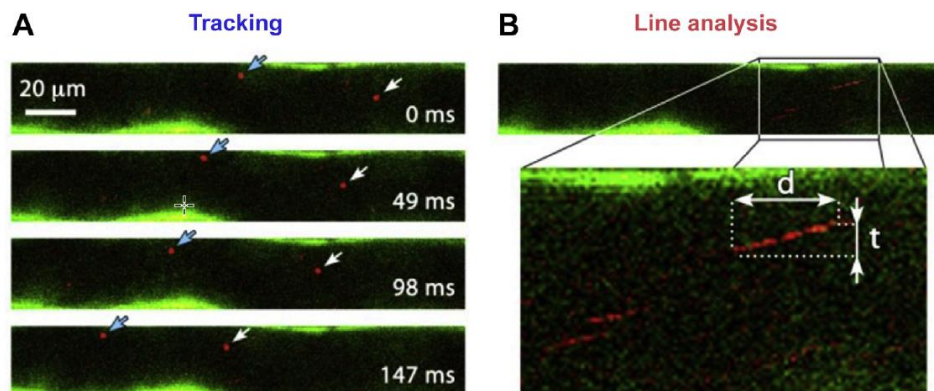
Figure 2.23. Single-particle tracking of DiI-TPB nano-droplets in zebrafish vessels. (A) During the diastole single particles were followed in consecutive frames. (B) During the systole, the velocity was calculated from the shape of the line, which is a result of the movement of the particles during the line scanning. Adopted from ref [235].

Chapter 3: Optical instrumental techniques for nanocarriers characterization

Nanocarriers have been an attractive field of research, due to their ability to improve the pharmacokinetics, stability and toxicity profile of certain drugs, potentially augmenting their therapeutic index. Moreover, disappointing results in recent clinical trials have compelled some to question nanomedicine's potential and create debate about delivery problems [236–239]. The poor delivery may be the result of stability, design, pharmacokinetics or bioavailability, or simply due to intrinsic biological variability.

Nanocarrier complexity requires in-depth in vitro and in vivo quantitative evaluation of nanoparticle behavior, with a focus on stability and interactions with blood components, especially for controlled release platforms.

In addition, the cancer drug delivery process consists of five critical steps, known as CAPIR cascade: circulation in blood, accumulation and penetration into the tumor, cellular internalization, and drug release. Thus, the global efficiency of a nanomedicine is determined by its efficiency in each step [240]. Hence, optimal nanomedicine (nanocarriers for drug delivery) should have 2R2SP properties, where (2R) is "drug retention vs release ", (2S) "surface stealthy vs sticky" and (P) "tumor penetration" [241].

- ➢ 2R is the required property in terms of loading, and stability from burst release during transport in blood compartments and tumor tissues, while having an efficient release of the active molecule at the target.
- ➢ 2S indicates the properties needed in terms of nanocarrier surface, on demand stealthy or sticky.
- ➢ P is the ability to penetrate in tumor tissues and to reach remote tumor cells from blood vessels.

If the nanocarriers possess the 2R2SP properties, they will be able to pass the CAPIR cascade successfully at right time and place, reaching high therapeutic efficiency.

In this scenario, there is an urgent need for the development and improvement of characterization techniques to monitor and follow the mentioned indicators in vitro and in vivo.

In this respect, optical techniques and instruments represent promising, simple and non-invasive approach to address this problem of nanocarrier evaluation.

The use of optical instrumentation has the advantage of tissue accessibility (for NIR region), the multitude of photophysical and photochemical processes at the molecular level (e.g., fluorescence, luminescence, multiphoton absorption, and second-harmonic generation), as well as detection sensitivity and resolution.

In the following pages we will provide a general overview of the principle fluorescence optical techniques, which were used in the last years to characterize and follow nanocarriers in vitro and in vivo at moderate costs even for very long-term experimental designs.

1- Fluorescence correlation spectroscopy (FCS)

1.1- Theoretical view

Fluorescence correlation spectroscopy is a method allowing temporal and spatial analysis of low concentration biomolecules. While most of the fluorescence techniques are interested in the intensity of the fluorescence signal, the FCS is based on the analysis of the temporal fluctuations of the fluorescence intensity measured in a small volume (focal volume). While generally these fluctuations are considered as measuring noise, the FCS technique exploits these to gain information of the system dynamics. The treatment of the fluctuations by autocorrelation function allows the measurement of the self-similarity of repeated measurements with time. Among the information that can be drawn from this technique, we can cite the local concentration of fluorescent biomolecules, their diffusion constant, the brightness of these molecules. All the phenomena affecting fluctuation of the fluorescent signal can in theory be apprehended by FCS. Fluctuations within the focal volume may arise from the changes in fluorescence characteristics due to reaction kinetics or conformational changes. They also can be from the diffusion of molecules in and out this volume. In addition, photophysical rate constants can change the fluctuations. This technique is non-invasive and highly sensitive.

1.1.1- Autocorrelation: principle and modelling of data

<div align="center">(A)   (B)   (C)</div>
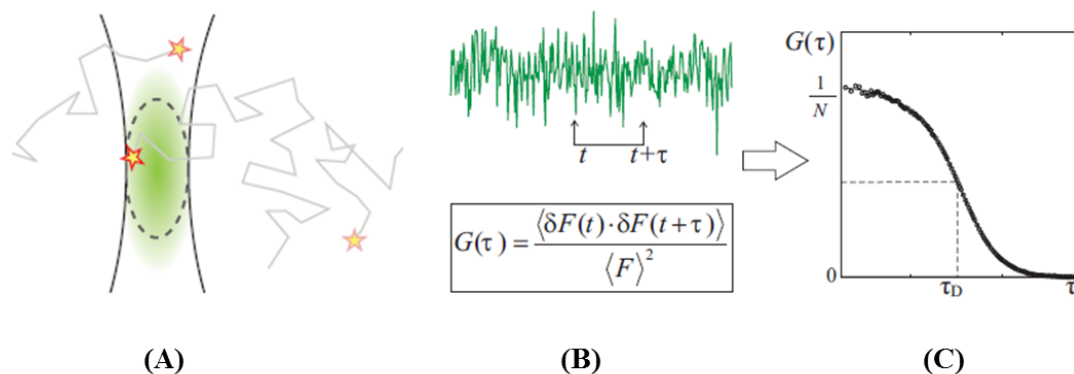
Figure 3.1. Schematic illustrating the principle of FCS **A)** Excitation beam focused in a liquid. **B)** Probe diffusing through the detection volume give rise to a fluctuating intensity trace from which the auto-correlation curve, can be calculated .**C)** Parameters of interest are obtained by fitting a mathematical model, the correlation function to the experimental correlation curve.

The main origin of the fluctuation is the Brownian motion of the particles entering and exiting from the excitation volume. The number of particles present in the focal volume at time (t) follows the Poisson law. The root of the variation in the average number of molecules within the focal volume can be given by [88]:

$$\frac{\sqrt{\langle(\delta N^2)\rangle}}{\langle N\rangle} = \frac{1}{\sqrt{\langle N\rangle}} \tag{3.1}$$

This implies that the relative fluctuations become more important when the concentration of tag species decreases (limited nevertheless by the fact that the fluorescence signal must be greater than the residual noise). In practice, the number of molecules within the focal volume can range from 0.1 to 1000, which implies for a focal volume of 0.3fl, a concentrations ranging from sub-nanomolar to micromolar. These ranges of concentrations are largely compatible with the "physiological" concentrations that can be observed within cells.

Autocorrelation curve is formulated as:

$$G(\tau) = \frac{1}{N}\left(1 + \frac{\tau}{\tau_d}\right)^{-1}\left(1 + \frac{1}{S^2}\frac{\tau}{\tau_d}\right)^{-0.5} \tag{3.2}$$

Where τd is the diffusion (correlation) time, N is the mean number of fluorescent species within the two-photon excitation volume, and S is the ratio between the axial and lateral radii of the excitation volume

1.1.2- Instrumentation
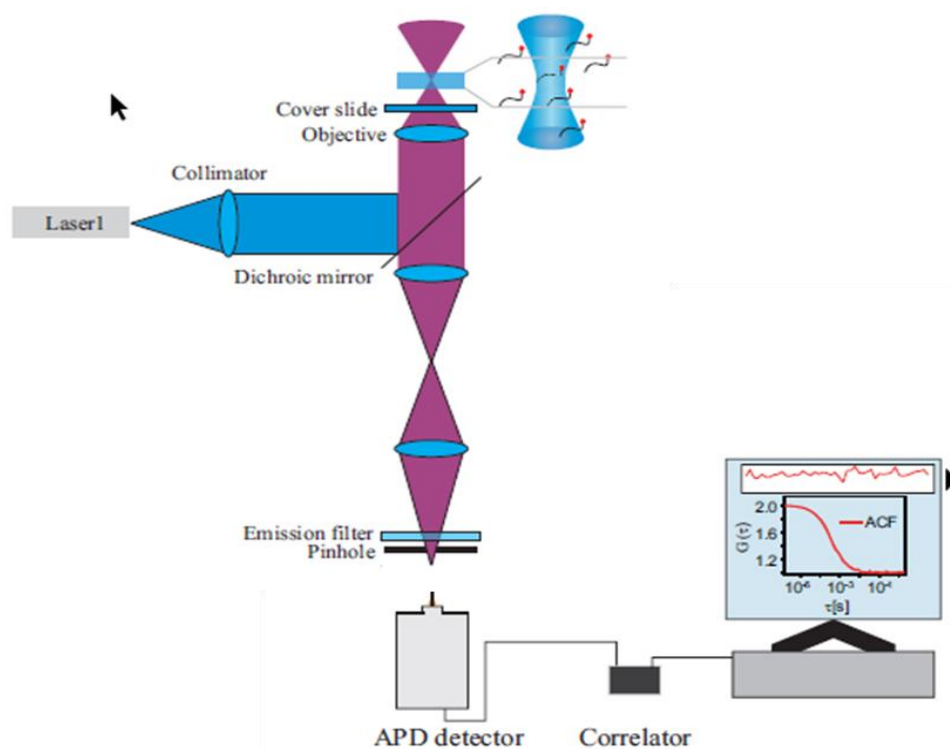
Figure 3.2. Scheme of a confocal set up for Fluorescence Correlation Spectroscopy. Adopted from ref [242].

Typically, a confocal FCS setup is used as shown in Figure 3.2. an aqueous solution containing emissive species is placed on the wells plate. The collimated laser beam is reflected by a dichroic mirror into an objective with a high numerical aperture (NA), to create a diffraction-limited spot. The emitted fluorescence light is collected by the same objective. Transmitted through the dichroic mirror, and focused onto a pinhole which eliminates all light emitted from outside the focal volume. The signal is detected by an avalanche photo diode in single-photon-counting mode, then correlated to generate the FCS curve.

The autocorrelation curve has some properties that are important to notice:

- When a fluorescent molecule is in the centre of the focal volume, the fluorescence signal will be highly correlated with time, because of higher probability to detect a large

number of photons consecutively. With molecule diffusion out of detection volume, this correlation decreases continuously, until the correlation is totally lost indicating that the molecule has diffused away completely.

- The correlation decay with time will be proportional to the diffusion rate of the molecule.

- The autocorrelation curve depends on the concentration of emissive species. At low concentration of the species, the intensity fluctuation will be larger. Indeed, molecule entering or leaving the focal will cause important signal variations. In contrast, at a high concentration, this variation of signal will be smaller. There is a direct connection between the amplitude of the autocorrelation curve and the inverse concentration of the fluorescing molecules. For that reason, FCS can measure the concentration of fluorescing molecules [244].

- For various time scales, the properties of the fluorescent molecules can determine the temporal behaviour of the autocorrelation function as it is shown in Figure 3.3. A phenomena called photon anti-bunching can be observed at nanosecond scale [245]. The fact that after a single fluorescent molecule excitation, the dyes cannot emit more than one photon per excitation cycle, which reduces the chance to observe two consecutive photons from one and the same molecule at very short correlation times. The antibunching effect is used for several measurements like oligomerization and quenching kinetics [246]. For longer times, other processes come into play. On a picosecond to nanosecond time scale we have molecular rotation diffusion dynamics if excitation and/or detection are performed with polarization filters. On a microsecond time scale, G(t) is dominated by fast intramolecular structural dynamics and photophysical processes like triplet state. Moreover, at millisecond to the second level scale the autocorrelation curve presents its typical decay due to the diffusion of the molecules out of the detection region [247].

- In addition to normal Fluorescence correlation spectroscopy (FCS) we can find other single molecule technique based on FCS like Fluorescence cross-correlation Spectroscopy (FCCS) and Fluorescence lifetime FCS, etc. [248].

Practically, fluorescence correlation spectroscopy (FCS) is used in research, for the study of multitude processes like molecular interactions, chemical kinetics and other single molecules parameters. Also this technique emerges as a new tool to characterize

nanoparticles, especially their size, brightness, binding, and to evaluate stability in fluorescent nanoparticles.
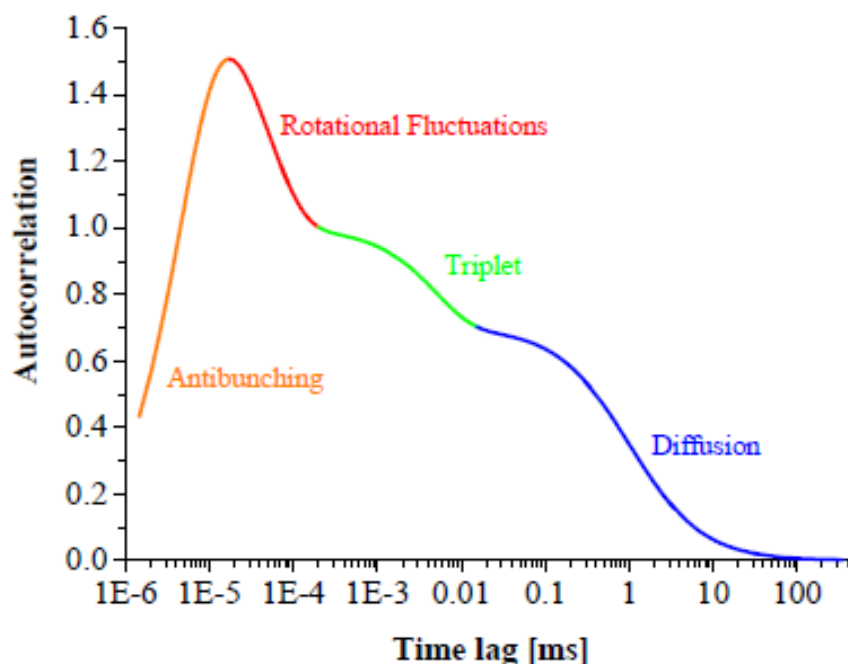
Figure 3.3. Timescales of various processes monitored by autocorrelation analysis. Adopted from ref [243].

1.2- Application of FCS for nanoparticles characterizations

This single molecule technique is used until now in vitro to determine the nanocarrier size, stability, release and interaction with surrounded media. Klymchenko et al, could measure the size, brightness, concentration and the ratio dyes / droplet for lipid nanoemulsion carriers encapsulating Nile Red dyes (NR) and lipophilic Nile red (NR668). Moreover, based on ability of FCS to measure the variation in emissive species number, they could monitor the dye release into serum medium [249]. In another example, Kristensen at al demonstrated the ability of FCS technique to quantify the release of dyes from large vesicles, outlining the mathematical framework required and the appropriate methodology for successful quantification. Moreover, they applied the previous methodology to investigate the release of an antimicrobial peptide (Mastoparan X), showing that Mastoparan X forms transient transmembrane pores in unilamellar lipid vesicles, resulting in size-dependent leakage of molecules [250].

Based on the correlation time, FCS is a powerful tool to measure the size of nanocarriers as good as DLS (Dynamic light scattering) technique [251]. According to FCS, polymeric nanocarriers stability and interaction with proteins were tested. It was shown that 15 nm

PMMA-SO$_3$H nanocarriers precipitate in phosphate buffer saline, showing that these nanocarriers are not stable under physiological salt concentrations. On the other hand, their hydrodynamic diameter doubled in presence of 10% fetal bovine serum (FBS), indicating strong protein adsorption at the particle surface. By contrast, the addition of the nonionic surfactant Tween 80 and the amphiphilic block copolymer Pluronic F-127 to the nanocarriers increased significantly their stability in presence of salts and prevented protein adsorption [111].

Andresen group used FCS in order to understand the liposome protein corona binding affinities and dynamics of common types of blood plasma proteins. They used FCS as shown in Figure 3.4 to investigate the binding of labeled Alexa Fluor 488 human serum albumin (HSA) to standard types of PEGylated fluid-phase liposomes (consisting of DOPC and DOPE-PEG2k), and PEGylated gel-phase liposomes (consisting of DSPC and DSPE-PEG2k) with various PEG chain surface densities [252].
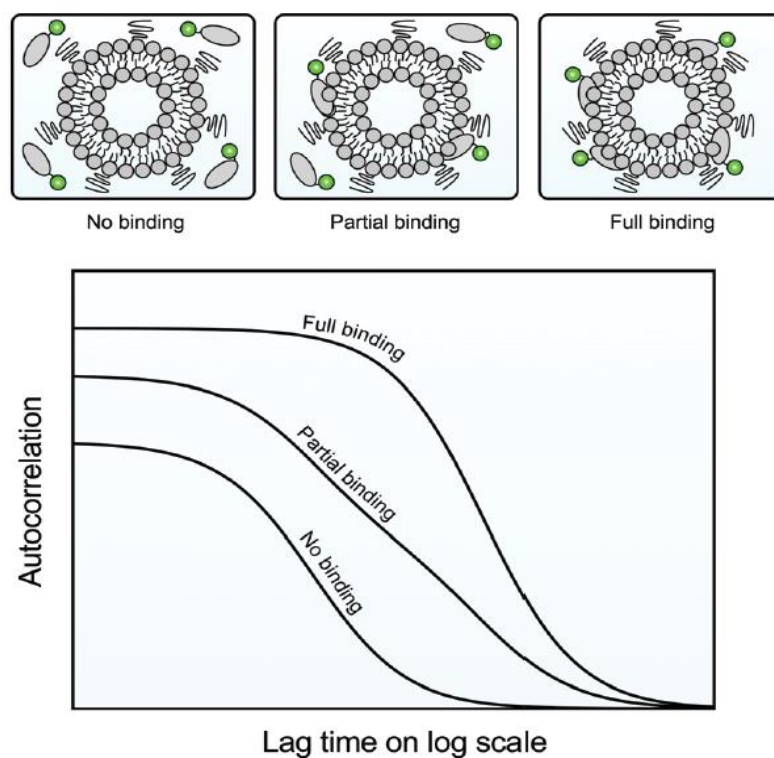
Figure 3.4. Schematic illustration of how FCS can be used for studying binding of fluorescently labeled proteins to liposomes. Adopted from ref [252].

No binding of HSA to the DOPC-based PEGylated liposomes was detected. By contrast, it was found that HSA could bind tightly to the DSPC-based PEGylated liposomes (typical dissociation time longer than 24 h), although only a low number of HSA molecules were bound

(on the order of ~2–5 on average per liposome) under conditions at which the liposomes were at least partially saturated with HSA. The same approaches were applied to lipid coated quantum dots by another group [253]. This FCS-based methodology could be applied in systematic studies on the interactions of blood plasma proteins with nanocarriers, potentially providing a basis for formulating a model of the protein corona on different nanocarriers circulating in the bloodstream.

Other molecular behaviors of nanocarriers were followed by FCS due to the very high sensitivity of the technique, like the hydrophobic collapse of pH responsive hairy nanoparticles at the individual particle level [254]. As a model system, 20 nm fluorescent nanoparticles with polystyrene core and poly (N, Ndiethylaminoethyl methacrylate) (PDEA) shell were used. It was shown (Figure 3.5) that when the pH is increased, PDEA chains grafted to a small polystyrene core collapse similarly to freely diffusing PDEA chains. In this process, the concentration plays an important role. At high and moderately low concentrations, the pH-induced collapse leads to aggregation and thus lowers of the nanoparticle mobility. At very low concentrations, however, the hydrophobic collapse is associated with decrease of nanoparticle size and increase in their mobility.
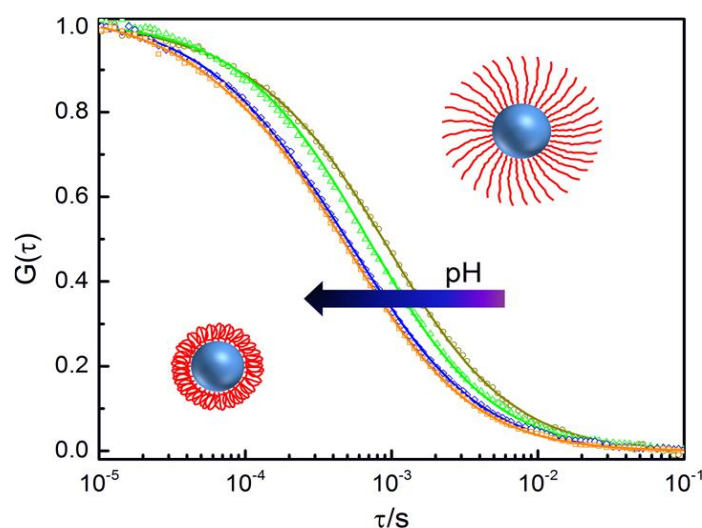
Figure 3.5. Hydrophobic collapse of pH responsive hairy nanoparticles at the individual particle level monitor by FCS technique. Adopted from ref [254].

Recently, ex vivo diffusion dynamics of PEGylated liposomes in the intact vitreous of porcine eye was elucidated by FCS. This parameter is an important aspect of the efficacy of intravitreal administered nanomedicines for the treatment of posterior segment eye diseases [255]. The coefficients in the intact vitreous (D_{Vit}) were determined in function of the zeta potential of polyethylene glycol functionalization, and compared with previous studies where non-

PEGylated cationic nanocarriers have no diffusion, while neutral and anionic have shown diffusion. It was shown that high cationic charge of nanocarriers is associated with significant cytotoxicity due to cell membrane disruption. On the other hand, it was demonstrated that PEGylated cationic liposomes can diffuse through the vitreous and can reach the vitreoretinal region.

2- Förster resonance energy transfer (FRET)

2.1- Theoretical view

FRET has become a popular tool in biological and chemical investigations, Förster described and modeled the phenomenon during the 1940s [256]. FRET is a photo-physical process by which energy is transferred in non-radiative manner, from a fluorophore in its excited electronic state (the donor D) to another fluorophore (the acceptor A) through intermolecular long-range dipole–dipole interactions. This phenomenon is possible only if the emission spectrum of the donor overlaps with the absorption spectrum of the acceptor. Additionally, donor and acceptor should be located at separation distances within ~1–10 nm from each other. For this high sensitivity to distance, FRET technique is considered as a "molecular ruler". Practically, when the transfer of energy occurs, the intensity of the donor emission decreases, while that of the acceptor increases (if the latter is emissive).
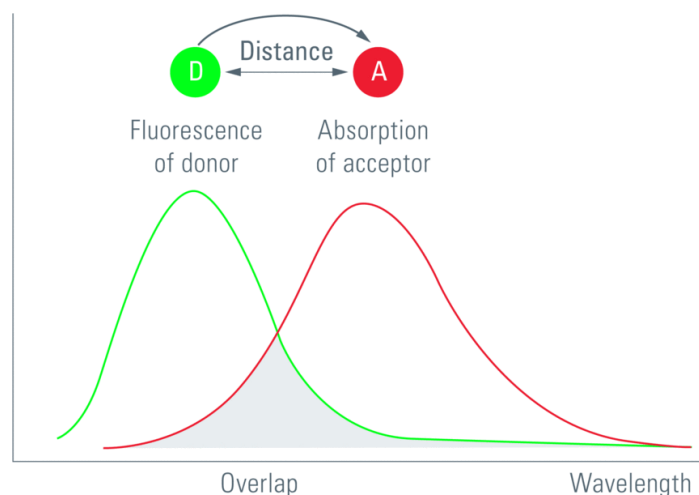
Figure 3.6. Spectral overlap between emission of donor and absorption of acceptor. Adopted from ref [257].

2.1.1- Mathematical formalism of FRET

The FRET is determined by the following key parameters [4,258].

a)-Förster distance:

It represents the distance at which resonance energy transfer is 50% efficient. The rate of transfer from a donor to an acceptor, $k_{FRET}(r)$, is given by :

$$k_{FRET}(r) = \left(\frac{R_0}{r}\right)^6 \frac{1}{\tau_D} \tag{3.3}$$

where r is the distance between the D and A , τ_D is the decay time of the donor in the absence of acceptor (lifetime of D in absence of energy transfer), R_0 is the Förster radius; the transfer efficiency is 50% when the donor – acceptor distance is equal to the Förster critical radius (Figure 3.7).

R_0 generally between 1-10 nm, can be determined from spectroscopic data:

$$R_0^6 = \frac{9(\ln 10)k^2 \Phi_D^0}{128\pi^5 N_A n^4} J \tag{3.4}$$

where k^2 is the orientation factor, Φ_D^0 is the fluorescence quantum yield of the donor in the absence of transfer, n is the refractive index of the medium, J is the spectral integral and can be written both in wavenumber and in wavelength scales:

$$J = \int F_\lambda(\lambda)\varepsilon(\lambda)\lambda^4 d\lambda \tag{3.5}$$

where F_λ is the normalized emission spectrum of the excited donor, and ε is the absorption coefficient of the acceptor.
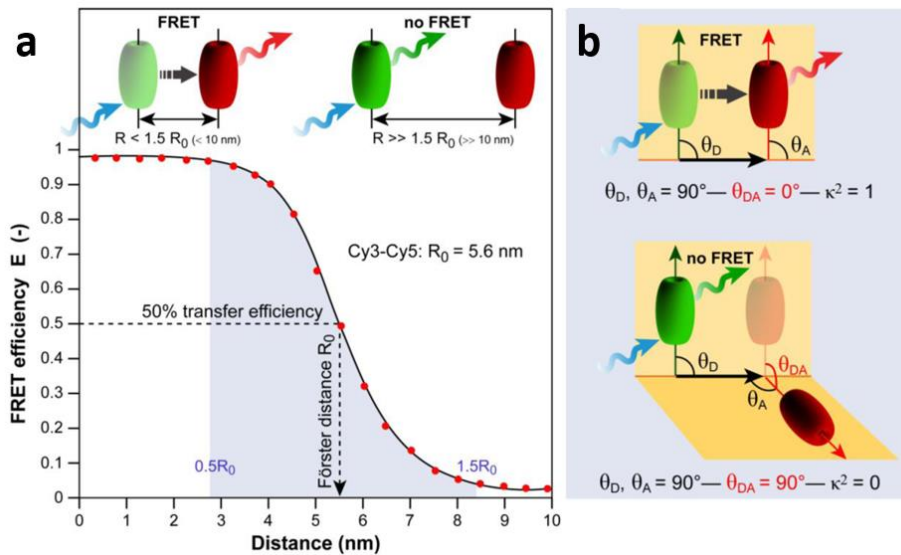
Figure 3.7. Schematic representation of FRET as a photo-physical process. FRET efficiency depends on the distance **a)** and orientation **b)** of D (green ellipse) and A (red ellipse). Adopted from ref [259].

b)-FRET Efficiency:

It is defined as the fraction of excited molecules that undergo energy transfer from the donor to the acceptor and can be expressed in terms of the rate constants of the processes involved:

$$E_{FRET} = \frac{k_{FRET}}{k_{FRET} \times k_{f,donor}} \tag{3.6}$$

Where E_{FRET} is the FRET efficiency, k_{FRET} the rate of energy transfer and $k_{f,donor}$ is the radiative decay rate of donor . Also the efficiency can be expressed as a function of the ratio r / R $_0$:

$$E_{FRET} = \frac{1}{1 + (r/R_0)^6} \tag{3.7}$$

The FRET efficiency can be measured experimentally either by spectroscopic method or life time data, in different number of ways. The most famous ones are [260,261]:

Measurements based on Donor emission

$$E_{FRET} = 1 - \frac{I_D^A}{I_D} \tag{3.8}$$

where I_D and I_D^A are the emission intensities of donor (D) in the absence and presence of acceptor (A), respectively. If the experimental conditions for "D" and "DA" FRET measurements are similar, this is usually a good approximation leading to adequate results.

Measurements based on Donor lifetime

$$E_{FRET} = 1 - \frac{\tau_D^A}{\tau_D} \tag{3.9}$$

where τ_D and τ_D^A are the decay times in absence and in presence of A, respectively. Since lifetime is independent of D concentration, this method induces less to errors. But when the donor has more than one lifetime, no simple, universal expression for the FRET efficiency exists, since this will depend on the origin of the different lifetimes measured.

Measurements based on A emission

Donor emission is not an evidence of FRET, because the donor can be quenched. The only sure evidence of energy transfer from D to A is to measure the intensity of A after excitation of D, If A is fluorescent molecule, the FRET efficiency can be determined by quantification of the A intensity.

$$E_{FRET} = \frac{I_A^D A_A^A - I_A^A A_A^D}{I_A^A A_D^D} \tag{3.10}$$

where I_A^D is the A intensity following D excitation, I_A^A is the A intensity following A excitation, A_A^A is the A absorbance at the A excitation wavelength, and A_A^D and A_D^D are the A and D absorbance, respectively, at the D excitation wavelength.

Measurements using D/A intensity ratio (ratiometric FRET)

The ratiometric method is the easiest way to characterize the FRET efficiency, using the ratio between the D and A emission intensity. The "relative" FRET efficiency is given as:

$$E_{FRET} = \frac{I_A}{I_D + I_A} \tag{3.11}$$

where I_A and I_D are the total A and D fluorescence intensities, respectively, both following D excitation. If the D and A spectra overlap, the mixed D + A spectrum must be decomposed into isolated D and A component spectrum.

2.1.2- Distinction in energy transfer process

Energy transfer from donor (D) to an acceptor (A) occurs in a variety of situations, for that a distinction should be made between hetero-transfer and homo-transfer, between radiative and non-radiative transfer [262].

When the two dyes are chemically different, the energy transfer from an excited molecule D * (donor) to A (acceptor) according to D * + A→D+ A* is named hetero-transfer. If the donor and acceptor are identical, we have homo-transfer: D *+ D→D+D*. It can be detected in rigid and highly viscous environments by the loss of fluorescence anisotropy. If this process can repeat itself because the excitation migrates over several molecules, it is called excitation transport. The overlap integral J is the parameter that often determines the choice of donor and acceptor for particular needs.

In radiative transfer, a photon emitted by a molecule D is absorbed by a molecule A (or D). It is observed when the average distance between them is larger than the wavelength, it depends on the overlap of spectra and dyes concentration. Non-radiative transfer occurs at distances less than the wavelength without emission of photons.

2.1.3- FRET applications:

FRET is widely applied in physical and life science because it allows following many processes and reactions in vitro and in vivo. The basic information being sought is whether or not two molecules are close to each other and if that distance changes as a result of some process. Here listed some examples of applications: [263–265]

- Ligand–receptor interactions and conformational changes;
- Proteins: In vivo protein–protein interactions, protein folding kinetics, enzyme activity assays;
- Membrane organization;
- Nucleic acid structures and sequences, interaction with drugs, DNA triple helix, automated DNA sequencing;
- Nucleic acid–protein interactions;
- Immunoassays and Biosensors;
- Pathogen detection and disease investigation;
- Nanoparticles integrity and stability.

2.2- Application of FRET for nanoparticles characterizations

Förster Resonance Energy Transfer (FRET) is becoming a valuable tool for analyzing diverse aspects of interactions among biological molecules in their natural environments [266]. The singularity of FRET has been its capacity to convert near-field bimolecular interactions into far field signals that explain some functions and behaviors of biological systems. In the last years, due to the exquisite sensitivity of FRET to monitor changes in the donor acceptor distance, it has been used as a technique for the nanocarrier characterization, specifically their stability and drug release ability in vitro and in vivo.

Mulder group was the first to introduce it in the nanocarrier field, when they studied the *in vitro* lipoprotein-lipoprotein (natural nanocarriers) interaction, exchange dynamics, and the influence of Apo lipoproteins on these processes. A lipoprotein-based nanoparticle that consisted of a quantum dot (QD) core and Cy5.5 labeled lipid coating was prepared. The QD/Cy5.5 ratios enabled to follow high density lipoprotein (HDL)-cell interactions and exploited FRET to visualize HDL association with live macrophage cells [267]. Later, as shown in Figure 3.8, using QDs and Cy7 dyes, they demonstrated the dissociation of self-assembled lipid shell of QDs in a mouse model upon intravenous administration [268].
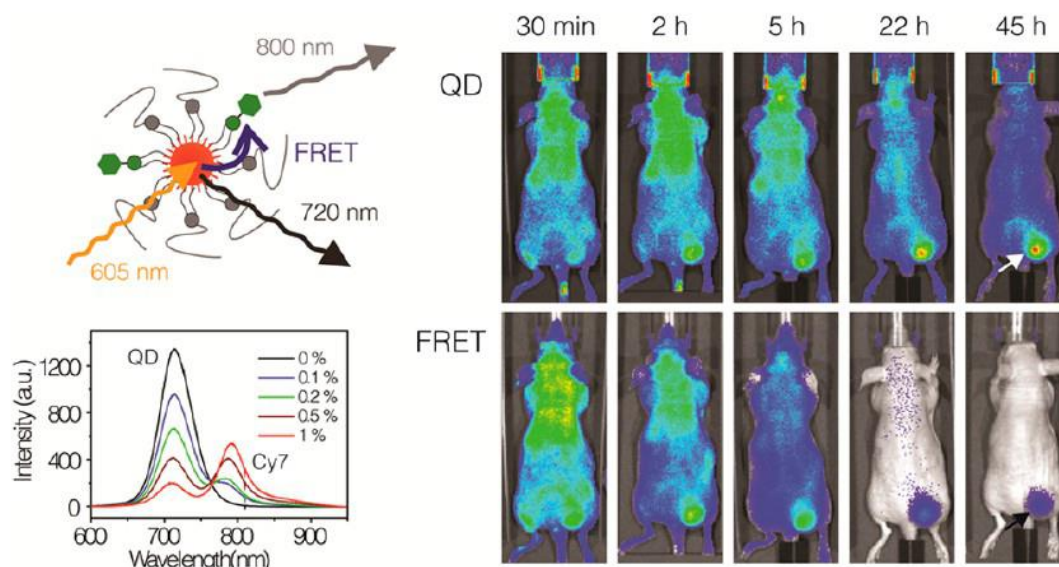
Figure 3.8. FRET based method for monitoring the dissociation of QD710-Cy7-PEG in xenograft tumor mouse model. Adopted from ref [268].

Using Cy7, which is one of the most efficient near infrared dyes, and low concentration of QDs, qualitative imaging was done based on FRET technique, while the quantitative FRET imaging was done only by intravital microscopy.

In lipid nanocarriers, FRET technique was firstly adopted by Texier and coworkers to study the fate of Lipidots® contrast agents in vitro. In this case, nanostructured lipid nanocarriers were loaded with different cyanine FRET pairs (DiO/DiI and DiI/DiD). The fate was monitored by confocal microscopy using Lipidots® (DiI/DiD) incubated with HEKβ3 cells [269]. Then FRET approach was extended to characterize LNE (lipid nanoemulsion) and LNC in vitro and in vivo. As shown in Figure 3.9, the dissociation of the nanocarriers was associated with the release of its components into the medium, which should resulted in the loss of the FRET signal [270]. However, DiI/DiD couple is not optimal for in vivo whole animal imaging because it does not operate in the NIR region.
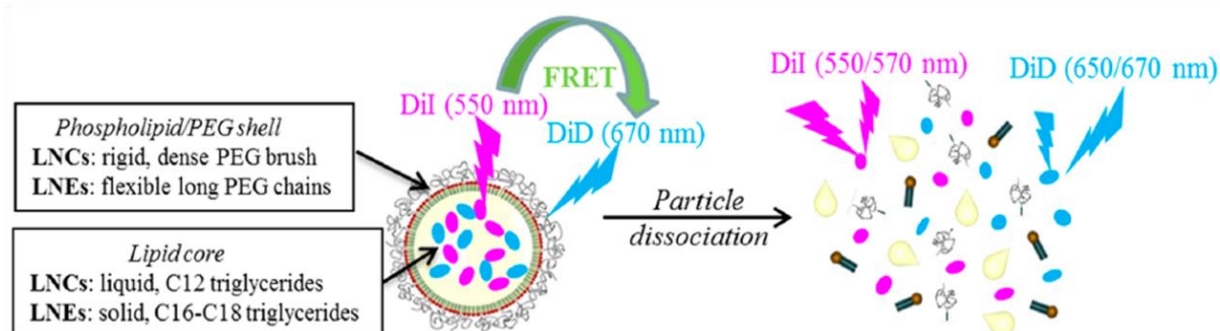
Figure 3.9. Illustration monitoring the dissociation of lipid nanocarriers by FRET. Adopted from ref [270].

This point was addressed by the same group in their more recent work, where they were able to exploit FRET imaging directly in healthy mice and organs to compare the behavior of different lipid nanocarriers formulations. Regarding the biodistribution, stealth lipid nanocarriers, developed based on LNC containing PEGylated phospholipids, displayed extended blood circulation lifetime over conventional LNCs. The former showed good stability over several hours after intravenous injection, and accumulation in the intestine, ovaries and skin [271]. Nevertheless, the FRET efficiency of DiD/FP730-C18 pair was not very high because of the low solubility of the two dyes (DiD at 1.2 mmol/$L_{Labrafac}$ and FP730-C18 at 3 mmol/$L_{Labrafac}$), so that the dynamic range changes in the donor/acceptor ratio were limited. This issue was addressed during my PhD work (see below), where we drastically improved loading of NIR dyes into nanocarriers and thus achieved strong FRET based response to changes in the nanocarriers integrity [272].

We should also mention recent studies by Roger et al. Using DiI/DiD FRET pair, it was shown that lipid nanocapsules maintained full integrity after crossing a human intestinal epithelium model (Caco2 cell monolayer), via transcytosis [176]. Furthermore, near-infrared cyanine 5.5 and 7.5 dyes conjugated to squalene were used to study gemcitabine-squalene nanocarriers SQGem, in order to monitor their stability in rat blood. While NPs were stable in water up to 24 h, the rapid drop of the FRET signal in the rat blood clearly indicated a fast disassembly of the NPs in this medium, resulting in the release of individual SQGem molecules able to insert into lipoproteins, probably as a result of similarities between the squalene moiety and cholesterol [273].

FRET technique was also implemented for real-time monitoring of the in vivo stability of polymeric micelles [274] and porphysomes [275], affording the capabilities to rapidly and efficiently evaluate a library of synthetically derived systems as new nanocarrier platforms. Additionally, some reports mentioned the ability of FRET for intracellular monitoring/imaging of the release of doxorubicin. Chen et al studied the release from pH-responsive doxorubicin (DOX)-loaded NPs, made of N-palmitoyl chitosan bearing a Cy5 moiety (Cy5eNPCS), as an anticancer delivery device [276]. Cy5eNPCS has the ability to self-associate allowing the close proximity between the donor (DOX) and the acceptor (Cy5) required for FRET. They found that DOX fluorescence in the cytosol was first seen when NPCS NPs were present in the slightly acidic early endosomes. Following NPCS NPs trafficking into a more acidic organelle (late endosomes/lysosomes), a more evident release of DOX into the cytosol was observed; the

released DOX was then gradually accumulated in the cell nuclei, leading to a significant cytotoxicity.

Recently, an important paper was published by Zhao et al, where they used in vivo FRET imaging to systematically investigate how drug–carrier compatibility affects drug release in a tumor mouse model [277]. Firstly, they created a range of poorly water-soluble model drugs with different physicochemical properties as shown Figure 3.10-(a). These model drugs consisted of a near-infrared fluorescent (NIRF) dye, Cy7, with varying tail components X (X = carboxylic acid (CA), C12, OLA and PLGA2k). Hydrophobicity and miscibility were considered as two independent parameters, e.g. a drug with good miscibility may not necessarily have a high hydrophobicity.
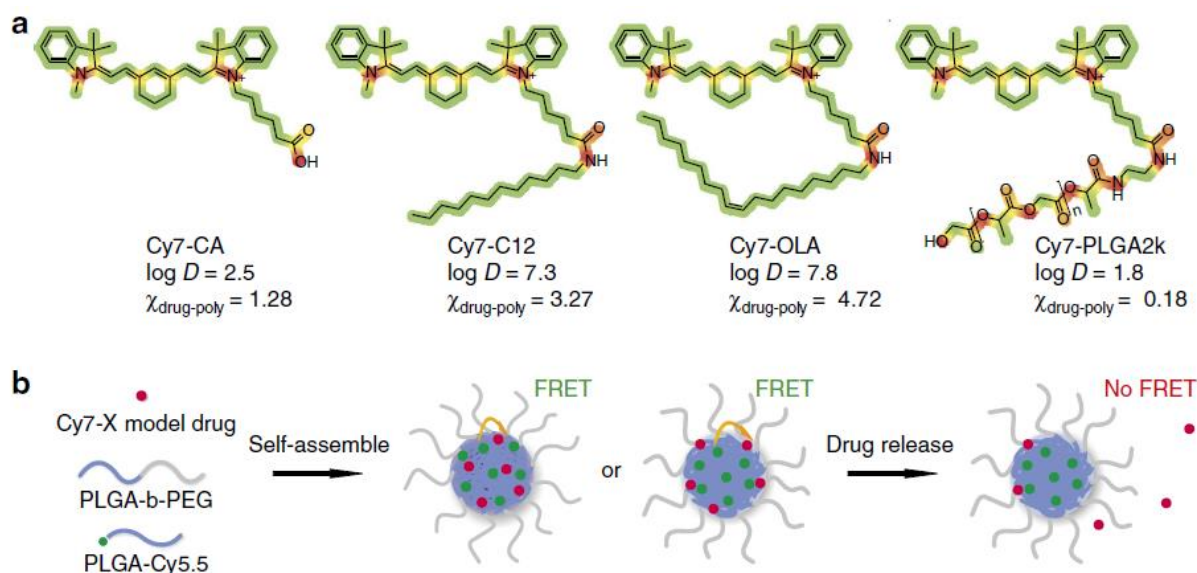
Figure 3.10. Cy7-X model drugs release in serum from Cy5.5-NP: Cy7-X FRET nanoparticles. (a) Chemical structures of Cy7-X (b) Schematic showing Cy5.5-NP: Cy7-X FRET nanoparticle. Where log D and $w_{drug-poly}$ are consecutively the hydrophobicity and miscibility. Adopted from ref [277].

The nanocarriers were synthesized through self-assembly of the block-copolymer PLGA–block-poly (ethylene glycol) (PLGA–PEG). Cy5.5 conjugated to the polymer served as a FRET donor in the core of NPs, while Cy7-X was the acceptor. Based on linear relation between the average Cy7-X loading per particle and measured FRET/Cy5.5 intensity ratio (FRET ratio), the amount of Cy7-X in the particle were estimated in situ through direct emission spectra measurements.

It was found that the different Cy7-Xs released more quickly at increased FBS concentrations and at higher temperatures. The release rates also depended on the Cy7-X's hydrophobicity and miscibility, following the order: CA>C12>OLA>PLGA2k. Thus, Cy7-X migrated from the original carrier particles to different serum components, with distributions varying among the albumin and globulin portion, high-density lipoproteins and low-density lipoproteins. In human serum, the drug release dynamics depended on serum protein composition and concentration, which implies that the stability of nanoparticle drug assembly needs to be carefully considered when translating nanomedicine to the clinic.

NIR FRET imaging also showed differential drug release in tumors at similar order as in the circulation (PLGA2k>OLA>CA), albeit at a slower rate [277]. Furthermore, biodistribution studies of nanocarriers 24 h after administration indicated that, while all the Cy5.5-NP carrier displayed very similar distribution patterns in major organs and tumors, the distribution of the different Cy7-Xs greatly varied. In the tumor, Cy7-OLA's and Cy7-PLGA2k's tissue concentrations were significantly higher than Cy7-CA's. This implies that the 'stickier' the drug is to the particle, the higher the tumor uptake will be. Finally, on the basis of these findings, general guidelines for more efficient drug delivery were proposed and applied to doxorubicin, which increased the delivery efficiency and improved antitumor efficacy.

Another new application of FRET system, is the possibility to follow in a real-time the nanocarrier formation. Sanchez-Gaytan et al presented a new technology that integrated a microfluidics-based nanoparticle synthesis method and FRET microscopy imaging to visualize nanoparticle self-assembly in real time (Figure 3.11). It was successfully applied to different nanocarriers systems, such as nanoemulsions, drug-loaded block-copolymer micelles, and nanocrystal-core reconstituted high-density lipoproteins [278].
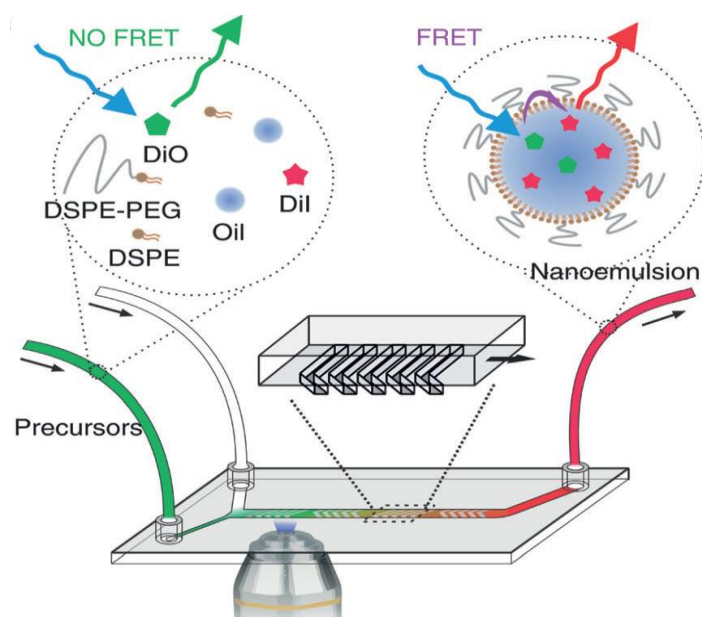
Figure 3.11. Real-time nanoemulsions formation monitoring using a fluorescence microscope on a microfluidics device. Adopted from ref [278].

3- Fluorescence-lifetime imaging microscopy FLIM

As FLIM is highly useful for quantitative fluorescence measurements, it was applied to study drug release from nanocarriers. Using FLIM in 2D cell monolayers (Figure 3.12), Basuki et al were the first to demonstrate the potential use of FLIM and phasor plot representation, to monitor the in situ release of DOX from nanoparticles via the intracellular degradation of pH responsive bonds (imine), distinguishing conjugated and native (free) DOX in live cells. Iron oxide nanoparticles with grafted polymer shells, attached to doxorubicin (DOX) via imine bonds, providing a controlled release mechanism for DOX in acidic environments [279].
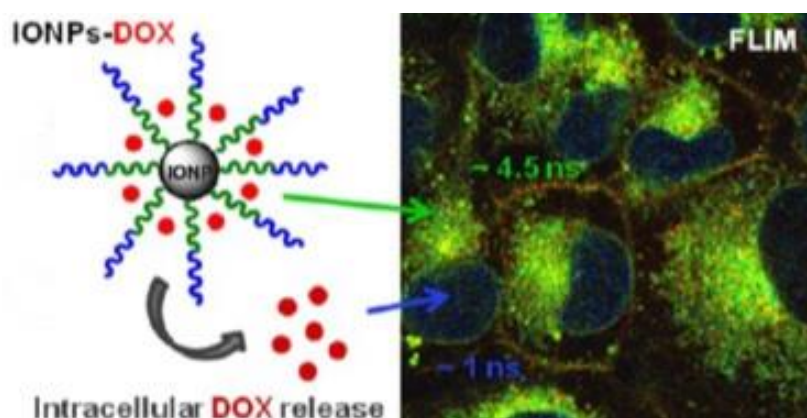
Figure 3.12. In vitro monitoring of Doxorubicin released from nanoparticles via FLIM imaging technique. Adopted from ref [279].

The nanoparticles were shown to be readily up taken by H1299 cell lines, and intracellular release of DOX was proven using in vitro FLIM measurements. Using the fluorescence lifetime difference exhibited by native DOX (~1 ns) compared to conjugated DOX (~4.6 ns), the intracellular release of conjugated DOX was in situ monitored and estimated using phasor plot representation, showing a clear increase of native DOX with time. The results obtained from FLIM were corroborated using confocal microscopy, clearly showing DOX accumulation in the nuclei.

Furthermore, in light trigger release experiments with a photothermal heating of PLGA nanocarriers, FLIM was applied to measure the temperature inside polymeric nanocarriers with high spatial resolution. It was found that exposure to laser light resonant with the vibrational absorption of water (980 nm) in the NIR region can induce release of payloads encapsulated in particles made from inherently non-light-sensitive polymers such as poly (lactic-co-glycolic acid) (PLGA). Water molecules absorb optical energy through vibrational transitions and the excitation energy is rapidly converted into heat. FLIM was used to extract intra-particle temperatures by comparing fluorescein lifetime to a standard curve generated by direct heating of the dye. The dye inside irradiated hydrogels showed a systematic decrease in the fluorescein lifetime with increasing irradiation at 980 nm. This thermometric methodology allowed temperature measurements inside nanocarriers [280].

We should mentioned also some recent developments in application of FLIM to improve characterization of nanocarriers, their interactions and penetration studying into skin [281]. In particular, FLIM allows for the discrimination of target molecules, e.g. fluorescently tagged nanocarriers, against the auto-fluorescent tissue background and, due to the environmental sensitivity of the fluorescence lifetime, also offers insights into the local environment of the nanoparticle and its interactions with other biomolecules. As example, the penetration of silver nanoparticles (Ag NPs) into porcine skin ex vivo, association of FLIM and two-photon tomography revealed that Ag NPs signal declined dramatically from the surface to 4 µm in depth and then became much weaker and completely disappeared at a depth of 12 to 14 µm. This results confirmed the maximum penetration depth of Ag NPs at ~14 µm [282]. In in vitro experiment, Alnasif et al studied the skin penetration of Nile Red loaded dendritic core–multishell (CMS) nanocarriers. FLIM proved a stable dye-nanocarriers complex and revealed peculiarities of nanocarriers–skin interactions [283].

4- Intravital microscopy IVM

Intravital microscopy enables combined measurement of pharmacodynamics and pharmacokinetics (PD / PK) at the single-cell level, and has facilitated answering main questions regarding the biological mechanisms of in vivo nanocarriers behavior.

In its simplest form in mice, IVM is implemented on the ear thin skin, which can be taped flat to the microscope stage. This approach is fast, reliable, and permits easy valuation of PK and extravasation in healthy model tissue. The mouse ear has the same melanocyte distribution compared to humans and therefore serves as a site for implantation of intradermal xenograft melanoma, ensuing imaging studies [284]. For deeper tissue imaging, generally more invasive surgical approaches are required by window chambers or intraoperative/endoscopic orthotropic imaging (Figure 3.13).

- *The windows chambers:* to allow longitudinal imaging for long time surgically implanted window chambers are usually used in IVM [285]. The skinfold chamber as shown in (Figure 3.13 B) is the easiest one for making stable and clear images. This window is made of a metal bracket sutured to a folding to the skin, generally on the mouse back, with a glass cover slip substituted over a surgically removed section of skin, and is classically used for imaging subcutaneous tumor models, lymph nodes, and mammary fat pad tumors when placed over the fat pad. We can cite also mammary imaging windows and abdominal imaging windows [286].

- *Orthotropic imaging and immobilization:* It is performed in the absence of surgically implanted windows at a wide range of anatomical sites (Fig 3.13 A). This imaging ideally occurs with a scarified animal and orthotropic sites can be surgically externalized, manipulated and imaged. This can be useful for abdominal organs [287] or superficial tissue structures [288]. When performing IVM surgeries, we need to take attention to movement, damaged vasculature, thermal regulation and desiccation. Moreover, IVM can be made by endomicroscopy (Fig 3.13 C).

- *Image processing and analysis:* Compared to in vitro microscopy, IVM data are complex firstly in terms of artifacts linked to motion, tissue auto-fluorescence and scattering, secondly due to complex biology of different cell types and structures working dynamically in three dimensions. For analyzing and interpreting data, computational methods have been developed [289], which involve automated or semi-

automated processing [290], as well as corresponding correction techniques and plugin software's [291,292].

Recent IVM advances benefited enormously from computational tools for (i) tracking single-cell movement with time; (ii) mapping vessel structures and 3D cellular distributions; (iii) image phenotypes-based classification of cell and vessel populations; and (iv) simulating the combined pharmacokinetics and pharmacodynamics of drugs moving from vessels to individual cells.
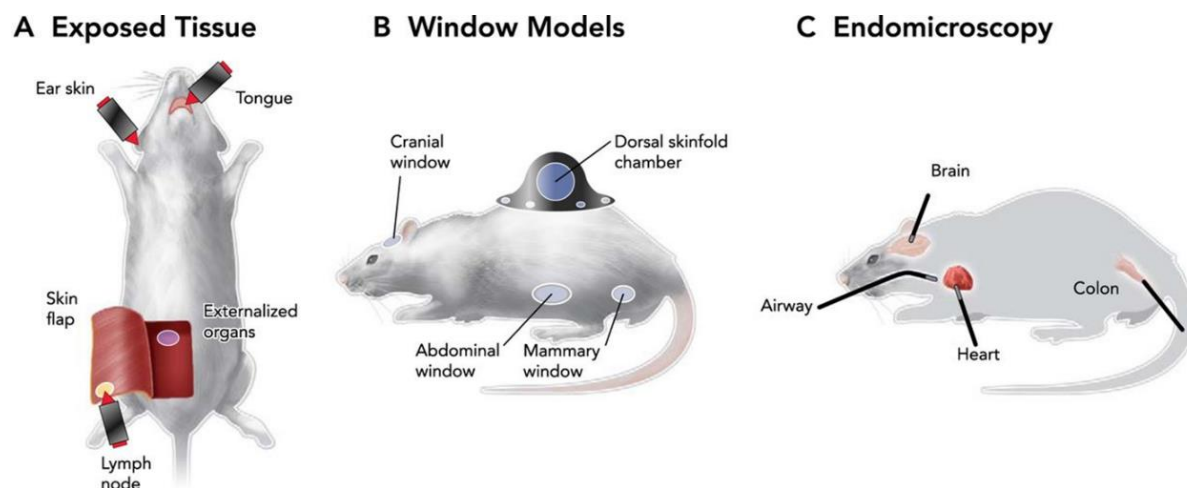
Figure 3.13. Three strategies for intravital imaging have been proposed to overcome limited penetration of light into tissue: through intact or surgically exposed tissue (A), by implanting an optically transparent window (B), or by inserting miniature endoscopic probes (C).Adopted from ref [293].

In nanomedicine, IVM can address the following critical questions [294]:

- The physiological and mechanistic barriers for therapeutic nanocarriers (NCs) accumulation in target cells.
- What determines cellular patterns of NCs uptake and distribution?
- Does drug loaded NCs reach their target (cancer cells) or do they accumulate in host cells (and if yes in which types)?
- If targeting moieties help in terms of NP distribution and effectiveness.
- Can NP targeting and efficacy be optimized by other strategies?
- Correlation between local drug concentrations and antitumor effects.
- Are there bystander effects that explain the local anticancer effects of some nanotherapeutics?
- The biological mechanisms that govern NP clearance and toxicity.

For evaluating changes in vascular structure and neovascularization at drug target sites with nanocarriers, IVM became a standard tool. As example, IVM was used to evaluate the positive and negative effect of the nanocarriers encapsulating the anti-vascular endothelial growth factor receptor (α-VEGFR) (Figure 3.14). It was found that α-VEGFR allows superior NCs perfusion by normalizing vascular structure. It restricts tumor penetration by reducing vessel permeability. Taking benefice from tumor vasculature remodeling, nanocarriers of 20-40 nm size had also lesser degree of diffusional hindrance, resulting in a more homogeneous distribution within the tumor, improving the NCs delivery [295].
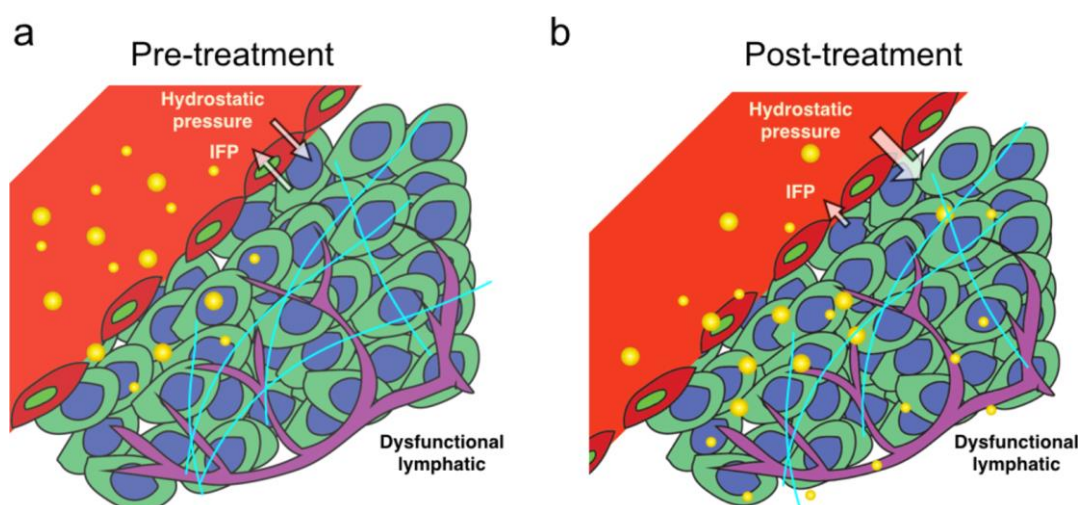
Figure 3.14. Proposed mechanism of improved nanoparticle delivery into tumors after vessel remodeling .Adopted from ref [295].

Other IVM studies by Kataoka group supported this conclusion, showing that efficiency of polymeric micelles depended on size, with better diffusion of smaller particles (≤50 nm) into poorly permeable tumors such as often found with pancreatic cancer. Furthermore, increasing the permeability of hypovascular tumors using TGF-β signaling inhibitor improved the accumulation and distribution of the larger 70 nm micelles, offering a way to enhance the efficacy of larger nanomedicines [296]. By contrast, correlation in macroscopic tumor uptake between NPs of contrasting size (~20 nm vs. ~100 nm) and coating (dextran vs. PEG) can still be strong [297]. Moreover, it was shown (Figure 3.15) that permeability of tumor blood vessels includes a dynamic phenomenon characterized by vascular bursts followed by brief vigorous outward flow of fluid (named 'eruptions') into the tumor interstitial space [298]. These can explain the enhanced extravasation of nanoparticles from the tumor blood vessels, allowing even large particles to access tumor interstitial space. This finding supported the strategy of

using enhanced permeability and retention (EPR) effect for drug delivery and then to release small molecule therapeutics to travel throughout the tumor tissue.
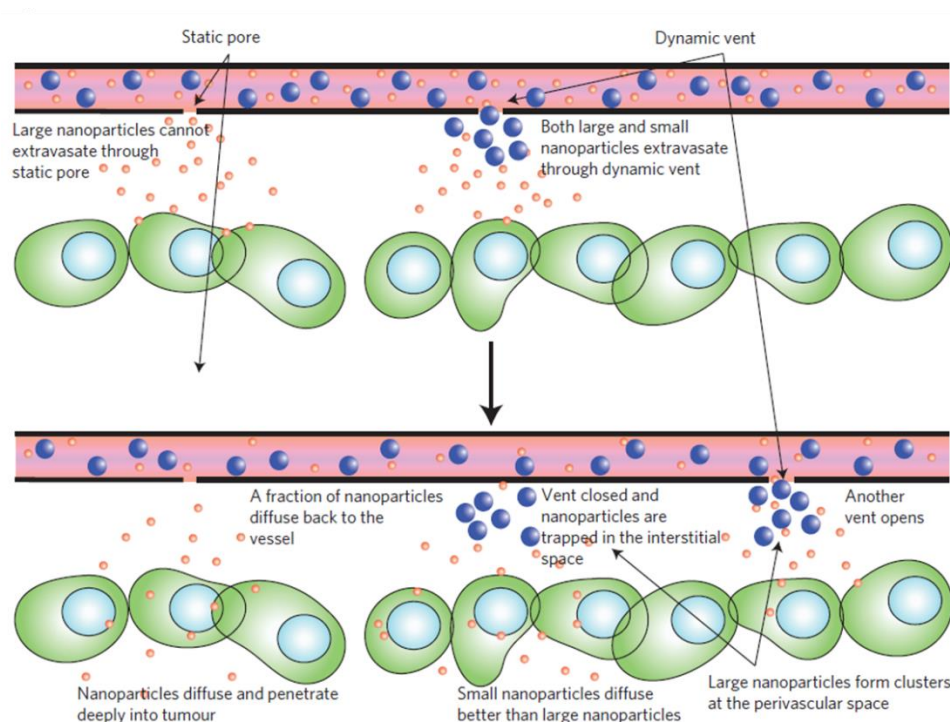
Figure 3.15. Scheme showing the implications of dynamic vents for drug delivery. Adopted from ref [298].

Furthermore, Smith et al indicated using real-time intravital microscopic imaging that nanocarriers shapes and geometries have an effect on extravasation across three different murine tumor models [299]. Likewise, the effect of PEG density on accumulation kinetics at (sub)-cellular resolution in tumors was studied by IVM for ligand-functionalized nanoemulsions. Counterintuitively, yet reliable with the PEG density conformation models in vitro and in vivo, the highest specificity and targeting efficiency was observed at a low PEG surface density [300].

Recently, real time IVM started to be used for the evaluation of NCs degradation and payload liberation. Hagen and coworkers showed that only 0.4% of the doxorubicin added as liposomal formulation entered the nucleus, with slow translocation and apparent accumulation in cytoplasm [301], unlike free doxorubicin which was 26%. In vivo intravital microscopy revealed the sequestering of liposomal doxorubicin in the lysosomal compartment causing limited delivery to the nucleus. This trap makes the bioavailable concentration of Doxil-

delivered doxorubicin significantly lower and therefore ineffective as compared to free doxorubicin in killing tumor cells.

For pharmacokinetics analysis IVM has been used to demonstrate that liposomal daunorubicin showed longer plasma half-life compared to its non-encapsulated counterpart [302]. Also the same conclusion was made for polymeric encapsulation of a cisplatin-related prodrug and free cisplatin. In this case, the initial burst-phase of payload immediately after injection was followed by more gradual release profiles, which can be attributed to changing stability and thermodynamics when NCs are diluted [303]. IVM in addition provided information on the NCs aggregation and coagulation processes, especially as they occur in microvasculature, as was reported for cationic siRNA-loaded hydrogel NCs [304].

Intravital microscopy can be used also with FRET for investigation of drug release dynamics in the vasculature, revealing that drug–carrier compatibility, including their hydrophobicity and miscibility, strongly affects in vivo stability and release rate in the circulation [277].

5- Dynamic light scattering DLS

DLS (dynamic light scattering) – also known as photon correlation spectroscopy, is the most commonly used non-invasive technique for measuring the hydrodynamic size of nanocarriers. It requires minimal sample preparation and no pre-experimental calibration [305]. it's based on measuring Brownian motion of NCs in suspension.
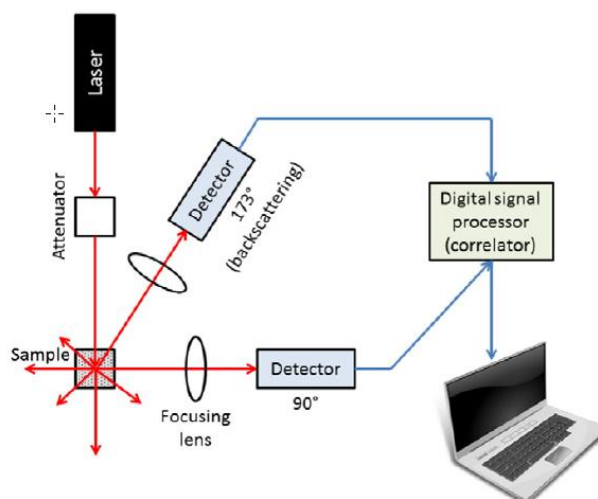
Figure 3.16. Schematic showing the instrumentation of DLS.

Brownian motion could be measured by analyzing the rate of scattered light fluctuation. The scattered light from the nanocarriers is proportional to 6th power of their radius , Rayleigh theory (elastic scattering) is applicable for small molecules and particles whose diameters are less than 1/10th of the laser wavelength and it is isotopic and not angle dependent [306]. However, when particles become larger than $\lambda/10$, the scattering changes from being isotropic to a distortion in the forward scattering direction, where Mie scattering (inelastic scattering) theory is applied [307].

The size could be obtained from the correlation function. To obtain mean size (Z-average diameter) and the particles distribution (Polydipersity index PDI), a single exponent fitting is applied. Multiple-exponential fit gives us the intensity size distribution. Mie theory is used by default to convert the intensity size distributions into volume and number for all sizes of particles.

6- Other different techniques

Presently, researchers around the word are engineering and developing more and more innovative optical techniques and approaches for nanocarrier characterization. This manuscript will be not enough to cite and describe them all. Thus, we will give a short overview in the flowing paragraph of some other techniques.

Single molecule TIRF microscopy is one of the most powerful tools for nanocarrier investigation either for tracking or photophysics evaluation [308]. Boreham et al used it in order to answer to a challenging question of distribution of active molecules inside nanocarriers [309]. For that, lipophilic fluorescent drug mimetic, ATTO-Oxa12 was encapsulated inside lipid nanostructed carriers (NLC). Then they were immobilized on the cover glass and imaged under super resolution microscopy, to analyse the step length distributions (SLD) and the resulting time resolved mean square displacements (MSD). "Visit maps", highlighting the places visited by the fluorophores, were generated for visualizing affinity based interactions to resolve the underlying structures with sub-diffraction resolution. Results revealed that inside NLC of 160 nm, the dyes ATTO-Oxa12 is distributed in the oily component in spherical shape of 70 nm and 120–130 nm diameter, both smaller than the NLC size (+160 nm). Moreover, two-color stochastic optical reconstruction microscopy (STORM) can be also used, for sizing and positioning of nanoparticles inside cells and probing their interaction with the cellular machineries at nanoscale resolution [121].

Multimodal optical imaging has been used to establish the mechanism of the long-circulating nanocarriers for atherosclerotic plaque targeting in a rabbit animal. Cy7-labeled liposomal nanoparticles (Cy7-LN) were allowed to circulate for different time (0.5, 6, and 24 h), and animals were subsequently sacrificed. In addition, Evans Blue (EB) was intravenously injected, which bind to albumin and stains sites with enhanced endothelial permeability in atherosclerosis. The abdominal aortas were imaged with NIRF imaging, revealing that nanocarriers targeting in atherosclerosis is reliant on vascular permeability. Moreover, using a fluorescence fiberscope, it was shown that nanocarriers can enter the plaque from the luminal side due to a dysfunctional endothelium or from micro-vessels present in the adventitia that originate from the vasa vasorum. This accumulation at inflammatory sites can be explained by the fact that nanocarriers are taken up by mononuclear cells in the circulation or in the spleen and, consequently, migrate to sites of enhanced permeability such as brain ischemia and myocardial infarction [310].

Another technique developed recently for assessing nanocarrier distribution in biological tissues in 3D, is the Laser-Induced Breakdown Spectroscopy (LIBS) [311].
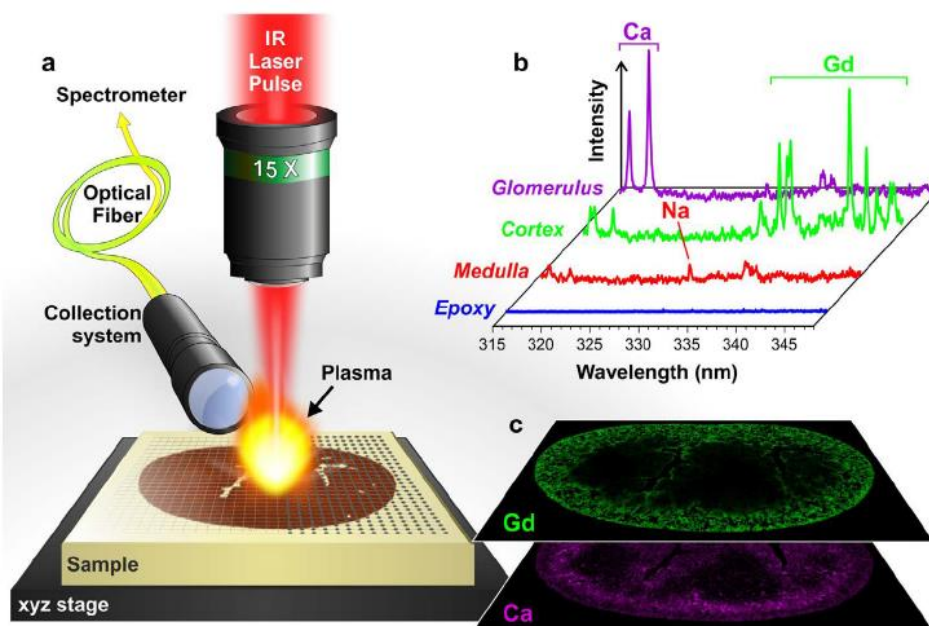
Figure 3.17. General protocol for LIBS imaging. (a) Schematic view of the LIBS instrument (b) Example of single-shot emission spectra covering the 315–345 nm spectral range recorded in different regions of the mouse kidney with the characteristic emission lines of calcium (Ca), sodium (Na), and Gd. (c) Example of relative abundance images of Gd (green) and Ca (violet) represented in a false color scale. Adopted from ref [311].

LIBS technique (Figure 3.17) is based on laser-induced plasma generation by focusing laser pulses on the surface of the sample of interest. The technique permits a specific optical response to be produced from the constituting elements, resulting from the electronic relaxation of atoms and ions excited by the high plasma temperature. Then, using an optical spectrometer, elemental maps can be obtained in a pixel-by-pixel manner by scanning the sample surface over the region of interest.

This methodological proof-of-concept study was conducted in the context of the renal clearance of 5 nm Gd-based nanoparticles in nude mice. Applying LIBS to biological imaging allows imaging chemical elements at the organ scale with ppm-scale sensitivity and a pixel size of up to $10 \times 10 \, \mu \, m^2$. Moreover, LBPS is a fast method (100 times faster than other 3D techniques) and compatible with standard optical microscopy. Likewise, Chan group developed 3D optical mapping of nanoparticle distribution in intact tissues [312,313].

PART II

Results and discussions

1- Integrity of lipid nanocarriers in bloodstream and tumor quantified by near-infrared ratiometric FRET imaging in living mice (Publication-1)

Lipid nanocarriers (NCs) emerged as promising candidates for drug delivery and cancer targeting because of their low toxicity, biodegradability and capacity to encapsulate a drug or a contrasting agent [314]. However, because of poor understanding of their in vivo fate and integrity, their translation from laboratory to biomedical applications is limited.

We hypothesed in this work that Förster Resonance Energy Transfer (FRET) technique could be exploited for real time investigation of their stability in vivo, due to the extreme sensitivity of FRET to donor acceptor distance. Consequently; encapsulating together donor and acceptor inside a nanocarrier should guarantee high FRET efficiency when the nanoparticle is intact. Then, the loss of the FRET signals would indicate disintegration of the nanocarriers associated with the release of its components into the medium (Figure 1).

Figure 1. Concept of FRET NCs that can report on their integrity by change in their emission color. Chemical structures of oil LabrafacWL (medium chain triglyceride) and Cremophor ELP (PEGylated surfactant) as well as lipophilic cyanine 5.5 and 7.5 dyes (Cy5.5LP and Cy7.5LP) with their bulky hydrophobic counterions are shown.

Using our recently developed approach of hydrophobic counterion (TPB) [235], we encapsulated inside a lipid nanocarrier of 100 nm size two lipophilic NIR cyanine dyes: Cy 5.5/TPB as a FRET donor and Cy 7.5/TPB as an acceptor [272].

Then, our FRET based concept for nanoccarriers integrity was validated in vitro by spectrophotometry to verify the response of our FRET NCs to their disintegration. Likewise, we assessed the stability of these FRET NCs by incubating them in serum (100%), a model of a biological medium in vivo. The results showed a good stability of our NCs making them suitable for whole-animal NIR imaging through intravenous injection.

Next, they were retro-orbitally injected into healthy and tumor bearing mice. Using two-color whole animal NIR imaging, we could quantify the content of the nanocarriers and their integrity directly in blood circulation, liver and tumor xenografts of living mice. This methodology revealed that the particles remained stable in the blood circulation for at least 6h. They accumulated in tumor rapidly in nearly intact form (77% after 2h) through permeability and retention effect (EPR), and then disintegrated with half-life of 4.4 h (Figure 2). In conclusion, we developed a FRET approach that allows direct visualization and quantification of nanocarriers integrity in vivo.

A) Integrity of NCs over time for liver and tail vein, directly healthy mice

Blood : integrity ~ 93 % after 6 h.
Liver : half-life ~ 8.2 h.
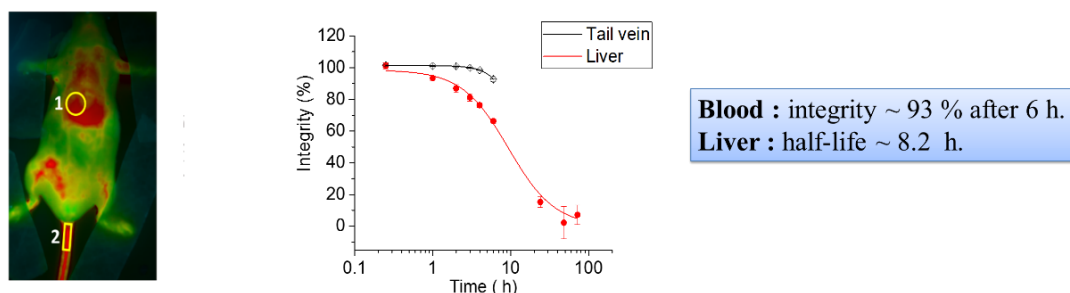
B) Integrity of NCs over time for tumor and tail vein, directly mice bearing tumor

Blood : integrity ~ 71 % after 6 h.
Tumor : half-life ~ 4.4 h.

Figure 2. Quantitative analyses of the integrity of lipid NCs in: A) healthy mice and B) mice bearing tumor. Integrity was estimated based on calibration of our in vivo imaging setup [272].

This work was published in *Journal of Controlled Release;* the article is enclosed below

Integrity of lipid nanocarriers in bloodstream and tumor quantified by near-infrared ratiometric FRET imaging in living mice

Redouane Bouchaala [a,b,1], Luc Mercier [c,1], Bohdan Andreiuk [a,d], Yves Mély [a], Thierry Vandamme [e], Nicolas Anton [e,*], Jacky G. Goetz [c,*], Andrey S. Klymchenko [a,*]

[a] Laboratoire de Biophotonique et Pharmacologie, UMR CNRS 7213, University of Strasbourg, 74 route du Rhin, 67401 Illkirch Cedex, France
[b] Laboratory of Photonic Systems and Nonlinear Optics, Institute of Optics and Fine Mechanics, University of Setif 1, 19000, Algeria
[c] MN3T, Inserm U1109, LabEx Medalis, Fédération de Médecine Translationnelle de Strasbourg (FMTS), University of Strasbourg, F-67200, France
[d] Organic Chemistry Department, Chemistry Faculty, Taras Shevchenko National University of Kyiv, 01601 Kyiv, Ukraine
[e] CNRS UMR 7199, Laboratoire de Conception et Application de Molécules Bioactives, University of Strasbourg, 74 route du Rhin, 67401 Illkirch Cedex, France

ARTICLE INFO

ABSTRACT

Lipid nanocarriers are considered as promising candidates for drug delivery and cancer targeting because of their low toxicity, biodegradability and capacity to encapsulate drugs and/or contrasting agents. However, their biomedical applications are currently limited because of a poor understanding of their integrity in vivo. To address this problem, we report on fluorescent nano-emulsion droplets of 100 nm size encapsulating lipophilic near-infrared cyanine 5.5 and 7.5 dyes with a help of bulky hydrophobic counterion tetraphenylborate. Excellent brightness and efficient Förster Resonance Energy Transfer (FRET) inside lipid NCs enabled for the first time quantitative fluorescence ratiometric imaging of NCs integrity directly in the blood circulation, liver and tumor xenografts of living mice using a whole-animal imaging set-up. This unique methodology revealed that the integrity of our FRET NCs in the blood circulation of healthy mice is preserved at 93% at 6 h of post-administration, while it drops to 66% in the liver (half-life is 8.2 h). Moreover, these NCs show fast and efficient accumulation in tumors, where they enter in nearly intact form (77% integrity at 2 h) before losing their integrity to 40% at 6 h (half-life is 4.4 h). Thus, we propose a simple and robust methodology based on ratiometric FRET imaging in vivo to evaluate quantitatively nanocarrier integrity in small animals. We also demonstrate that nano-emulsion droplets are remarkably stable nano-objects that remain nearly intact in the blood circulation and release their content mainly after entering tumors.

1. Introduction

Nanoscale vehicles (nanocarriers, NCs) become indispensable tools for in vivo imaging [1–3], drug delivery [4,5] and image-guided surgery [6,7]. One key requirement that any NC has to meet is to maintain its integrity until it reaches the target, for example a tumor [8,9]. This would ensure robust delivery of active molecules and/or provide the best signal to noise ratio when NCs are used as contrasting agents. However, suitable methods for assessing nanocarrier stability and the cargo leakage (such as dialysis, size exclusion chromatography, FCS, etc) are sparse and mostly operate in vitro [10]. Therefore, while providing

useful information, these model experiments cannot resolve fundamental issues such as the passage of NCs through the bloodstream, which includes shear forces, opsonization and uptake, and other undesirable interactions with off-target cells [11–13]. Moreover, in the context of tumor targeting, it is of utmost importance to assess whether NCs are capable of maintaining their load upon extravasation from the systemic circulation into the tumor (Fig. 1). Additionally, a reliable method for assessing their integrity can inform on the time scale of release of NCs' content upon tumor targeting through EPR (enhanced permeation and retention) effect [14,15]. Therefore, it is essential to monitor the integrity of the nanocarriers in vivo, preferably in real time. Current methods to study the integrity of the nanocarriers in vivo are very limited. In addition to radiolabelling assays [16], the highly promising approach is fluorescence imaging in the near-infrared (NIR) region, which now ranges from classical 2D imaging of small animals up to fluorescence-mediated tomography that enables quantitative 3D imaging

* Corresponding authors.
  E-mail addresses: nanton@unistra.fr (N. Anton), jacky.goetz@inserm.fr (J.G. Goetz), andrey.klymchenko@unistra.fr (A.S. Klymchenko).
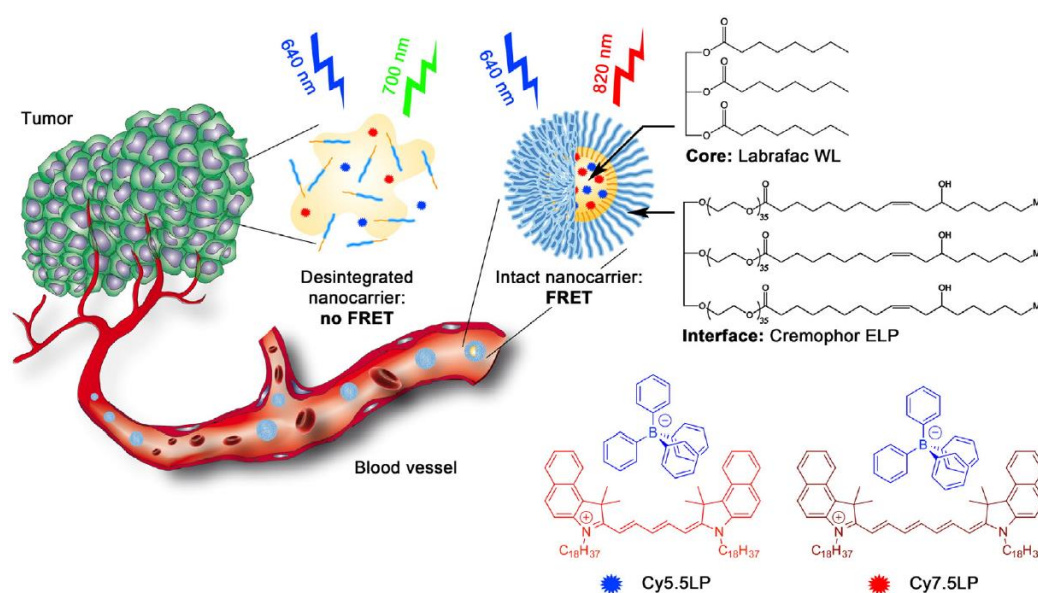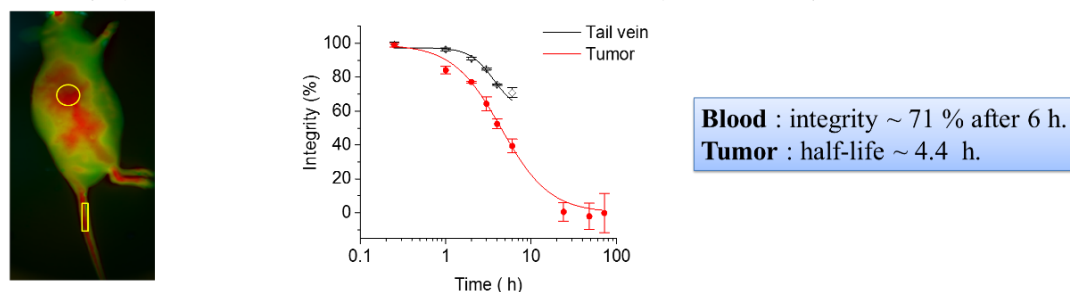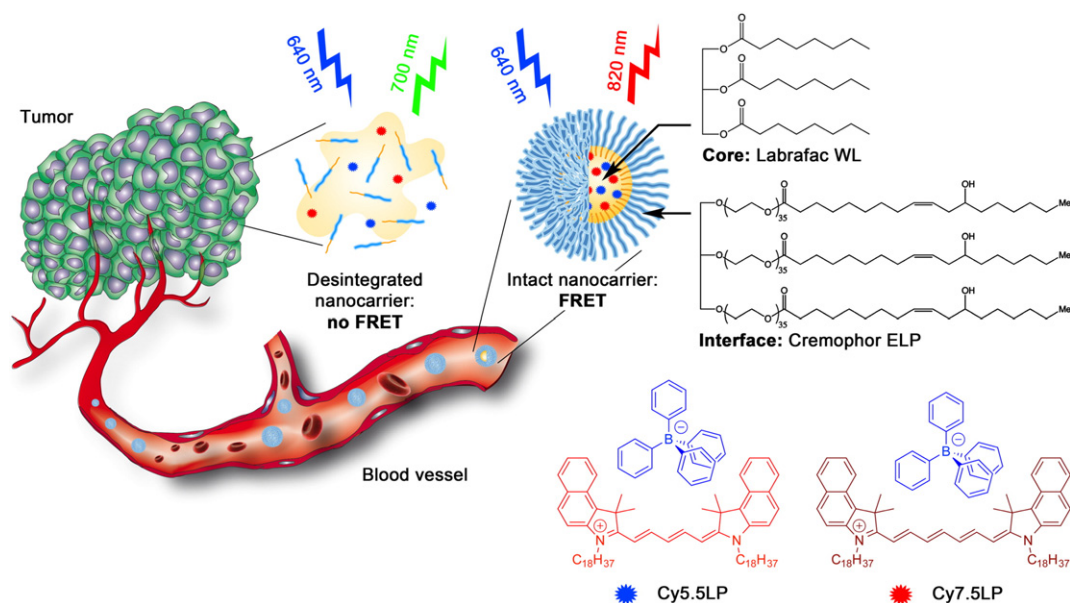[1] These authors contributed equally to this work.

Fig. 1. Concept of FRET NCs that can report on their integrity by change in their emission color. Chemical structures of oil Labrafac WL (medium chain triglyceride) and Cremophor ELP (PEGylated surfactant) as well as lipophilic cyanine 5.5 and 7.5 dyes (Cy5.5LP and Cy7.5LP) with their bulky hydrophobic counterions are shown.

[17–20]. Importantly, optical imaging modality provides access to Förster Resonance Energy Transfer (FRET), which acts as a molecular ruler between the donor and acceptor dyes and has been extensively used to characterize properties of bio-/nano-materials and their response to biological environments [13,21–23]. It is particularly suitable to study the integrity of a nanocarrier, because of exquisite sensitivity of FRET to changes in the donor acceptor distance. Thus, encapsulation of both donor and acceptor inside a nanocarrier should ensure high FRET efficiency, while the loss of the nanocarrier integrity associated with the release of its components into the medium should result in the loss of the FRET signal. Moreover, when FRET occurs between two fluorescent dyes, dual emission of NCs can be obtained, which opens possibilities for quantitative ratiometric measurements using fluorescence detection in two distinct optical windows. It is only very recently that FRET imaging has been used for monitoring in vivo the integrity of NCs. It has been successfully applied to monitor biodistribution and integrity of polymer micelles [24], hybrid organic-inorganic nanoparticles [9] and nanoemulsion droplets [25]. However, these studies only showed global FRET signal from the mice or a tumor, without imaging directly the particle integrity in the blood circulation, where these nanocarriers are actually injected. For this purpose, only indirect ex vivo measurements and intravital microscopy, which requires complex dedicated setup, were realized to date [9,26,27]. Moreover, the studies were limited to qualitative evaluation and no quantification of nanocarrier integrity directly in living mice was reported to date. Quantitative in vivo fluorescence imaging of NCs integrity can be achieved only after some key limitations of existing fluorescent NCs are addressed. The first limitation is the insufficient fluorescence signal from NCs that is contaminated by the background from animal tissue. This could be overcome by high dye loading into NCs with minimal self-quenching of the encapsulated dyes and injecting large quantities of NCs into mice without toxic effects. Moreover, the loaded dyes should operate in the NIR region (>700 nm), where the absorption, light-scattering and auto-fluorescence of the tissue are minimal [28–30]. Second, intensity of the FRET signal was usually analyzed, making the assessment of nanocarrier integrity only qualitative. Quantification requires internal control, which can be realized by ratiometric FRET imaging, obtained by division of two images (e.g. acceptor/donor). In contrast to intensity, the measured ratio values are absolute, being independent of concentration of emissive species and light source intensity [31,32].

However, only one rare example used ratio imaging in application to analyze FRET of nanocarriers in vivo [33]. The problem is that in majority of examples FRET donor emits below near-infrared (NIR) window (<700 nm), so that its signal is strongly attenuated by tissue absorption and contaminated by light scattering and auto-fluorescence. Therefore, quantitative and reliable ratiometric in vivo imaging requires both donor and acceptor species to emit in the near-infrared (NIR) region above 700 nm.

Among the existing nanocarriers for drugs and contrasting agents in the biomedical research, lipid nano-emulsion emerged recently as a promising alternative [34–36]. Although nano-emulsions were mainly used for the last >20 years as template for nanoparticle preparation [37], only in the last years they attracted attention as nano-carriers in pharmacy and cosmetics application [38,39]. Nano-emulsifications enable preparation of lipid nanocarriers of well-defined size from FDA approved materials using direct approaches that do not use organic solvents [40]. This feature is particularly attractive for high quality fluorescence imaging as it enables injecting maximal amount of nanocarriers with minimal harm to an animal [34,35]. However, as nano-emulsions are essentially liquid objects, two major problems need to be addressed before they can be broadly used in drug delivery and/or as contrasting agents. First, efficient encapsulation of material and active compounds, without fast leakage, needs to be achieved. Second, in vivo stability is required to ensure proper delivery. Both issues are actively debated over the last years [25,41–43]. Recently, we introduced an original concept to improve the loading of cyanine dyes into the oil droplet, which is based on the use of hydrophobic counterions [44]. Cyanine dyes usually bear inorganic counterions such as perchlorate or iodide that are responsible for poor solubility of these dyes in oils. By replacing these ions with tetraphenyl borate (TPB), we were able to improve solubility >40-fold and create 90 nm lipid droplets bearing exceptional number of cyanine dyes (~12,000 per droplet, 8 wt% dye loading) that remained efficiently fluorescent [44]. The extreme brightness of these NCs enabled pioneer single particle tracking in vivo in a zebrafish embryo model. However, this unique counterion approach has never been applied to NIR cyanine dyes, required for in vivo imaging, and it has never been used to generate FRET inside nanocarriers, needed to assess the NCs integrity.

In the present work, we synthesized lipophilic cyanine 5.5 and 7.5 dyes bearing long alkyl chains and TPB counterion (Cy5.5LP and

Cy7.5LP, respectively, Fig. 1) and encapsulated them inside lipid nanocarriers at concentrations required for highly efficient FRET, *i.e.* 1% in oil. These dyes ideally fit the NIR spectral region for *in vivo* imaging, where, notably, our cyanine 7.5 is an apolar analogue of indocyanine green commonly used for *in vivo* imaging [45,46]. The obtained ultrabright FRET NCs were successfully injected and monitored in healthy and tumor-bearing mice. We were able, for the first time, to visualize and quantitatively assess lipid nanocarrier integrity directly in the bloodstream, liver and tumor of living mice. We showed that lipid NCs remain nearly intact in the blood circulation, and they can enter the tumor with minimal loss of their integrity followed by the release their content with a half-life of 4.4 $\pm$ 0.3 h. Thus, we provide a robust imaging methodology to follow the evolution of lipid NCs *in vivo*, showing their remarkable stability *in vivo* and capacity to deliver their content into the target cancer tissues.

2. Materials and methods

2.1. Materials

All chemicals and solvents for synthesis were from Sigma Aldrich. Cremophor ELP® (Kolliphor ELP®) was provided by BASF (Ludwigshafen, Germany), Labrafac WL® (medium chain triglycerides) by Gattefossé (Saint-Priest, France). Ultrapure water was obtained using a MilliQ® filtration system (Millipore, Saint-Quentin-en-Yvelines, France). Fetal bovine serum (FBS) was acquired from Lonza (Verviers, Belgium) and Gibco-Invitrogen (Grand Island, USA).

2.2. Synthesis of Cy5.5LP and Cy7.5LP

2.2.1. 1,1,2-trimethyl-3-octadecyl-1H-benzo[e]indol-3-ium iodide (1)

250 mL round-bottom flask equipped with magnetic stirring bar was charged with 1,1,2-trimethylbenz[e]indole (1 eq., 6.88 g, 32.9 mmol) and 1-iodooctadecane (2 eq., 25 g, 65.7 mmol), 100 mL of 2-butanone was added subsequently. Reaction mixture was refluxed for 24 h, then cooled down to r.t. Reaction mixture was cooled down to r.t., diethyl ether was added and formed solid part was filtered off and washed with 100 mL of diethyl ether. Obtained crystals of crude product were redissolved in DCM and precipitated back while by adding diethyl ether, afterwards filtered and washed with diethyl ether. Product was obtained as slightly green crystals in 76% yield (14.73 g).

^{1}H NMR (400 MHz, CDCl$_3$) δ 8.10 (d, J = 8.7 Hz, 1H), 8.08 (dd, J = 8.0, 1.1 Hz, 1H), 8.04 (dd, J = 8.2, 1.3 Hz, 1H), 7.76 (d, J = 8.9 Hz, 1H), 7.72 (ddd, J = 8.3, 6.9, 1.4 Hz, 1H), 7.65 (ddd, J = 8.1, 6.9, 1.2 Hz, 1H), 4.78 (t, J = 7.7 Hz, 2H), 3.19 (s, 3H), 1.97 (p, J = 7.8 Hz, 2H), 1.87 (s, 6H), 1.52–1.41 (m, 2H), 1.40–1.30 (m, 2H), 1.28–1.19 (m, 26H), 0.85 (t, J = 7.0 Hz, 3H).

^{13}C NMR (100 MHz, CDCl$_3$) δ 195.25, 138.34, 137.29, 133.82, 131.56, 130.17, 128.77, 127.97, 127.74, 122.96, 112.59, 56.04, 50.56, 32.00, 29.77, 29.76, 29.73, 29.70, 29.65, 29.55, 29.43, 29.41, 29.24, 28.26, 26.92, 22.85, 22.76, 17.03, 14.18.

HRMS (m/z): [M]$^+$ calcd for C$_{33}$H$_{52}$N 462.40943; found 462.40854.

2.2.2. Dioctadecylcyanine 5.5 chloride (2)

1,1,2-trimethyl-3-octadecyl-1H-benzo[e]indol-3-ium iodide (1) (1 eq., 2 g, 3.39 mmol) was placed in 50 mL round-bottom flask. 10 mL of dry pyridine was added *via* syringe. Then, 1,1,3,3-tetramethoxypropane (1.5 eq., 0.835 g, 0.838 mL, 5.09 mmol) was quickly added dropwise to the boiling solution of indoleninium salt using syringe. Reaction mixture was stirred under reflux for 3 h. After cooling down to room temperature solvent was removed under reduced pressure. To the obtained residue 50 mL of dichloromethane were added. Obtained solution was washed three times with 1 N HCl, then with brine and water. The crude product was purified by flash column chromatography on silica gel using ethyl acetate/dichloromethane

(9:1) mixture as eluent. Cyanine was obtained as dark blue-greenish viscous oil in 76% yield (2.8 g).

^{1}H NMR (400 MHz, CDCl$_3$) δ 8.55 (t, J = 13.0 Hz, 2H), 8.20 (d, J = 8.5 Hz, 2H), 7.90 (d, J = 8.6 Hz, 4H), 7.64–7.54 (m, 2H), 7.44 (t, J = 7.5 Hz, 2H), 7.32 (d, J = 8.8 Hz, 2H), 6.74 (t, J = 12.4 Hz, 1H), 6.24 (d, J = 13.7 Hz, 2H), 4.14 (t, J = 7.5 Hz, 4H), 2.12 (s, 12H), 1.83 (p, J = 7.6 Hz, 4H), 1.46 (p, J = 7.6, 7.0 Hz, 4H), 1.40–1.33 (m, 4H), 1.30–1.18 (m, 52H), 0.85 (t, J = 6.7 Hz, 6H).

^{13}C NMR (100 MHz, CDCl$_3$) δ 174.60, 153.33, 139.40, 134.46, 131.81, 130.44, 129.94, 128.32, 127.83, 125.11, 122.65, 110.44, 103.10, 51.53, 44.64, 32.00, 29.79, 29.77, 29.74, 29.70, 29.66, 29.55, 29.48, 29.44, 27.93, 27.80, 27.08, 22.77, 14.21.

HRMS (m/z): [M]$^+$ calcd for C$_{69}$H$_{103}$N$_2$ 959.81158; found 959.8098.

2.2.3. Dioctadecylcyanine 7.5 chloride (3)

1,1,2-trimethyl-3-octadecyl-1H-benzo[e]indol-3-ium iodide (1) (2.2 eq., 1029 mg, 1.75 mmol) and glutaconaldehydedianil hydrochloride (1 eq., 226 mg, 0.794 mmol) were mixed in 10 mL of pyridine, afterwards Ac$_2$O (13.4 eq., 1087 mg, 1 mL, 10.6 mmol) was added and the reaction mixture was heated to 60 °C while stirring and left for 3 h. After reaction was finished, solvents were evaporated at vacuum, and the crude product was dissolved in DCM, washed with 0.1 N HCl (3 times), brine and water. DCM layer was dried over Na$_2$SO$_4$, the solvent was evaporated and the product was purified by column chromatography on silica (gradient DCM/MeOH 99/1–95/5). Product was obtained as a green solid (926 mg, 0.906 mmol, 52%).

^{1}H NMR (400 MHz, CDCl$_3$): δ 8.16 (d, J = 8 Hz, 2H), 8.06 (t, J = 12 Hz, 2H), 7.97 (bs, 1H), 7.92 (d, J = 8 Hz, 4H), 7.61 (t, J = 7 Hz, 2H), 7.46 (t, J = 7 Hz, 2H), 7.35 (d, J = 9 Hz, 2H), 6.67 (t, J = 12 Hz, 2H), 6.25 (d, J = 12 Hz, 2H), 4.14 (bs, 4H), 2.04 (s, 12H), 1.87 (m, J = 7 Hz, 4H), 1.49 (m, J = 7 Hz, 4H), 1.39 (m, J = 7 Hz, 4H), 1.26 (bs, 52H), 0.88 (t, J = 7 Hz, 6H).

^{13}C NMR (100 MHz, CDCl$_3$): δ 173.07, 157.04, 151.02, 139.74, 133.98, 131.83, 130.59, 130.09, 128.41, 127.87, 126.27, 125.06, 122.47, 110.56, 103.39, 51.155, 44.76, 32.06, 29.842, 29.807, 29.76, 29.72, 29.60, 29.53, 29.50, 27.86, 27.14, 22.82, 14.26.

HRMS (m/z): [M]$^+$ calcd. For C$_{71}$H$_{105}$N$_2^+$ 985.8272; found 985.8290.

2.2.4. Dioctadecylcyanine 5.5 tetraphenylborate (Cy5.5LP)

Dioctadecylcyanine 5.5 chloride (1 eq., 100 mg, 0.1 mmol) was dissolved in 5 mL of DCM, sodium tetraphenylborate (3 eq., 103 mg, 0.301 mmol) was added and the dispersion was sonicated for 5 min. TLC control has shown full conversion. Afterwards, the mixture was purified on a silica column, eluent DCM/MeOH 95/5 (product goes almost with front). Dioctadecylcyanine 5.5 tetraphenylborate (109.2 mg, 0.085 mmol, 85%) was obtained as blue-green viscous oil and used without further characterisation.

2.2.5. Dioctadecylcyanine 7.5 tetraphenylborate (Cy7.5LP)

Dioctadecylcyanine 7.5 chloride (1 eq., 200 mg, 0.18 mmol) was dissolved in 5 mL of DCM, sodium tetraphenylborate (3 eq., 184 mg, 0.539 mmol) was added and the dispersion was sonicated for 5 min. TLC control has shown full conversion. Afterwards, the mixture was purified on a silica column, eluent DCM/MeOH 95/5 (product goes almost with front). Dioctadecylcyanine 7.5 tetraphenylborate (218 mg, 0.167 mmol, 93%) was obtained as green viscous oil and used without further characterisation.

2.3. Formulation and characterisation of lipid nanocarriers

Dye loaded nanoemulsions were produced by spontaneous nanoemulsification. Briefly, the dyes (Cy5.5LP and Cy7.5LP) were firstly dissolved in Labrafac WL® (56 mg) at concentrations ranging from 0.1 to 1% by weight. Then, Cremophor ELP® (also called Kolliphor ELP®) was added (44 mg), and the mixture was homogenized under magnetic stirring at 37 °C for 10 min up to complete homogenisation. Finally,

nanoemulsions were generated with the addition of ultrapure (Milli-Q) water (230 mg). Size distributions were determined by dynamic light scattering using a Zetasizer Nano series DTS 1060 (Malvern Instruments S.A).

2.4. Fluorescence spectroscopy

Absorption and fluorescence spectra were recorded on a Cary 4 spectrophotometer (Varian) and a Fluoromax 4 (Jobin Yvon, Horiba) spectrofluorometer, respectively. Fluorescence emission spectra were performed at room temperature with 670 and 760 nm excitation wavelengths for Cy5.5LP and Cy7.5LP loaded nanocarrier, respectively. The emission spectra were corrected from for the wavelength-dependent response of the detector. All fluorescence measurements were done using solutions with absorbance ≤0.1 at the wavelength of excitation. The relative fluorescence quantum yield was measured using DiD dye in methanol (QY = 33%) as reference using excitation at 630 nm [47].

2.5. FRET-based stability test

The stability of lipid nanocarriers was estimated using Forster resonance Energy transfer (FRET) between two encapsulated dyes, 1% of Cy5.5LP (with respect to Labrafac WL®) as energy donor and 1% of Cy7.5LP as energy acceptor were used. The NCs were diluted 10,000 times from the original formulation and incubated in water and 100% of fetal bovine serum (FBS). High dilution was needed to avoid saturation of serum by lipids of NCs. The donor in the nanocarriers was excited at 670 nm. The semi-quantitative parameter of FRET efficiency was calculated according to the following equation E = A/(A + D) [48], where A and D are the maximum of fluorescence intensity of the acceptor and donor, respectively.

2.6. Cytotoxicity studies

In 96-well plates, HeLa cells were seeded at a concentration of 1×10^4 cells per well in 200 μL of the DMEM growth medium and then incubated overnight at 37 °C in humidified atmosphere containing 5% CO_2. Next, we add the lipid Nanocarriers (1% Cy5.5LP–Cy7.5LP), by substituting the culture medium for a similar one containing variable dilutions of the Nanocarriers. After incubation for 24 h, the medium was removed. Then, the wells were filled with cell culture medium containing MTT, incubated for 4 h at 37 °C, and the formazan crystals formed were dissolved by adding 100 μL of DMSO and shaked for 10 min. We measure the absorbance at 570 nm with a microplate reader (Xenius, Safas). Experiments were carried out in triplicate, and expressed as a percentage of viable cells compared to the control group.

2.7. Subcutaneous tumor grafting and administration of FRET nanocarriers

Adult (10 months) immuno-deficient mice (NMRI-Foxn1nu/Fox1nu, Janvier labs, 1) were anesthetized via gas anesthesia (isoflurane) system prior to tumor cell grafting. Anesthetized mice were injected subcutaneously (in the flank) with 100 μL of a solution made of 50% PBS and 50% Matrigel containing 1.10^6 of D2A1 (murine mammary carcinoma) cells [49]. Tumors were grown over a period of 20 days before administrating lipid nanocarriers. The mouse studies were performed according to the Guide for Care and Use of Laboratory Animals (E67-6-482-21) and the European Directive with approval of the regional ethical committee (CREMEAS for Comité Régional d'Ethique en Matière d'Expérimentation Animale de Strasbourg, AL/73/80/02/13). Mice received food and water ad libitum; they were checked daily and tumor growth never exceeded 20 days, leading to low-size tumors with no impact on the animal's health. All efforts were made to minimize suffering and euthanasia was performed using CO2. General health status was monitored regularly by

independent observers. Sacrifice of the animal was effectuated when reaching limit ethical endpoints. Before administration of the nanocarriers solution, mice were anesthetized by intraperitoneal injection of a mixture of ketamine (100 mg/kg) and xylazine (10 mg/kg). The nanocarriers were administrated by retro-orbital injection (100 μL) as previously performed for other purposes [50].

2.8. In vivo whole animal FRET imaging

Whole- and live-animal imaging of the FRET signal in healthy and tumor-bearing mice was performed by using a luminograph (NightOwl, Berthold Technologies). Anesthetized mice (isoflurane) were placed repeatedly in the luminograph, and positioned either on the flank or the back. Mice were imaged using a halogen lamp, (75 W, 340–750 nm) and emission of the two dyes was collected separately using separate filters sets (630/700 nm for Cy5.5LP, and 630/820 nm for Cy7.5LP). The experiments with healthy and tumor bearing mice were repeated three times.

2.9. Calibration of the ratiometric response of NCs to disintegration

To calibrate the ratiometric response of NCs to disintegration in our in vivo imaging setup, we model the disintegration NCs by mixing intact FRET NCs with NCs containing separately donor and acceptor at low concentration, with the preservation of the same concentration of dyes: 100% integrity corresponds to FRET NCs (1% of Cy5.5LP and 1% of Cy7.5LP) diluted in PBS 1000-fold from the original formulation, while 0% integrity corresponds to a mixture of NCs containing separately donor (0.1% of Cy5.5LP) and acceptor (0.1% Cy7.5LP), both diluted at 100-fold in PBS. Intermediate mixtures were made, where the level of integrity (%) is defined as the fraction of Cy5.5LP/Cy7.5LP dyes in the FRET NCs with respect to the total amount of these dyes. They were placed into 96-well plate and imaged using the NightOwl setup. The measurements were done in triplicate. The obtained values of the A/(A + D) ratio were plotted vs % of integrity and the data were fit with an exponential function (1):

$$y = a + be^{cx} \tag{1}$$

where $a = 0.14572$; $b = 0.1254$; $c = 0.01748$, y is A/(A + D) and x is FRET pair concentration (wt%).

As another model of the complete disintegration of NCs, solution FRET NCs diluted 1000-fold in dioxane was placed into 1 mL Eppendorf® tube and imaged by the NightOwl setup.

2.10. Image analysis of the FRET signal in the living mice

The ratiometric images were built using a homemade plugin (developed by Romain Vauchelles) under ImageJ that divides the image of the 840 nm channel by that of the 700 nm channel. For each pixel, a pseudocolor scale is used for coding the ratio, while the intensity is defined by the integral intensity recorded for both channels at the corresponding pixel. Image analysis was performed by using the ImageJ software [51]. The tail vein, liver and tumor were manually delimitated and the mean intensity of the delimitated region was determined for each respective time point and channel for three healthy and three tumor-bearing mice. For both donor and acceptor channels, the signal was corrected for the background using the mice before injection (in the corresponding region of interest). Then the corrected values of A/(A + D) were converted into the FRET pair concentration using Eq. (1). The obtained values of FRET pair concentration were then plotted vs time and fitted using a logistic function (2):

$$y = a_2 + \frac{(a_1 - a_2)}{\left(1 + \left(\frac{x}{x_0}\right)\right)^p} \tag{2}$$

where y is the FRET pair concentration (wt%); x is time; other parameters were calculated during the fitting procedure. This fit was further used to calculate the integrity half-life.

2.11. Statistical analysis

Student's t-test was used to evaluate the statistical significance between two sample groups. The differences between the results were considered to be significant when the p-values were <0.05.

3. Results and discussion

Nanoemulsions were selected as NCs for several reasons. First, they are very efficient at encapsulating materials. Second, nanoemulsions can be easily formulated by spontaneous emulsification with non-toxic compounds compatible with the parenteral administration route, so that they can be intravenously injected at high concentrations into mice with minimal harm [34,35]. The latter is particularly attractive to achieve superior contrast for imaging nanocarriers directly in the blood circulation. Cyanines 5.5 and 7.5 dyes were selected for encapsulation, because they are an excellent FRET couple with ideal spectral properties for *in vivo* whole-animal imaging. Indeed, cyanine 5.5 derivatives are among the most commonly used NIR imaging agents with convenient excitation 650–700 nm and emission in NIR region (>700 nm). Moreover, cyanine 7.5 absorption spectrum overlaps perfectly with the emission spectrum of cyanine 5.5 (Fig. S2), while its emission in NIR region at 840 nm is perfectly separated from the emission of cyanine 5.5, making this couple perfectly tailored for ratiometric FRET imaging. To achieve both strong brightness and highly efficient FRET inside NCs, cyanines 5.5 and 7.5 should be encapsulated at very high concentrations up to 1 wt% in oil, as we earlier showed for other FRET pair [41]. Therefore, their hydrophobic analogues, dioctadecylcyanines 5.5 (**2**) and 7.5 (**3**), were synthesized bearing long alkyl chains to ensure their high lipophilicity. Nevertheless, their solubility in labrafac oil (medium chain triglycerides) was only 0.15 and 0.05 wt%, for **2** and **3**, respectively. Therefore, we replaced their inorganic counterion (chloride) with bulky hydrophobic tetraphenylborate, which, according to our earlier study, improved drastically the solubility of the cyanine 3 dye DiI [44]. The obtained new salts, Cy5.5LP and Cy7.5LP (Fig. 1), showed much higher solubility in labrafac, 7 and 4 wt%, respectively. Then, nano-emulsions (lipid NCs) were generated by the spontaneous emulsification of dye-loaded oil and non-ionic surfactant (Cremophor® ELP), giving rise to fluorescent PEGylated droplets sizing around 90–100 nm (Table S1). To generate FRET NCs, we prepared NCs encapsulating increasing amount of Cy5.5LP and Cy7.5LP. As expected, the emission spectra recorded after

excitation of the energy donor showed strong dependence on the concentration of the FRET pair (Fig. 2A). Thus, at 0.1% of dyes, the emission spectrum was very close to that of Cy5.5LP alone, while at higher concentrations, a long wavelength emission, corresponding to the FRET acceptor, appeared and became dominant at ≥0.5% of the dyes. It should be noted that the emission maximum of Cy7.5LP shifted gradually to the red with increase in the dye content (Fig. 2A). Similar concentration-dependent red shifts were previously observed for Cy3 dye in lipid droplets [44]; they could be related to some aggregation of the dyes, homo-FRET, as well as to small changes in the oil core properties at higher dye concentrations. Remarkably, the total (donor + acceptor) fluorescence quantum yield (QY) of NCs encapsulating FRET pair at 1% loading of each dye was 11%. Although this value was lower than the QY of NCs with 1% of Cy5.5LP alone (27%), it remained relatively high to ensure high brightness to these NCs, important for *in vivo* imaging. For comparison, QY of NIR dye indocyanine green measured in phosphate-buffered saline (PBS) is 2.4% [52]. Here, we achieved much higher QY already for the FRET system. Moreover, because NCs minimize potential interactions of loaded dyes with tissues *in vivo*, they allow the use of higher dye concentrations, which is essential for achieving optimal imaging contrast for NIR imaging.

Then, to verify the response of our FRET NCs to their disintegration, we forced this process by adding excess of water miscible organic solvent dioxane, which should destroy NCs by solubilizing its components. As a result, a strong emission of Cy5.5LP dye was observed, while the emission of Cy7.5LP was fully hampered (Fig. 2B). This result confirmed that integrity of NCs, where Cy5.5LP and Cy7.5LP are in very close proximity within the NCs, can be assessed based on FRET signal. We next assessed the stability of these FRET NCs by incubating them in serum (100%), used as model of a biological medium *in vivo*. As a semi-quantitative parameter of FRET efficiency, we used the band intensity ratio of acceptor to the sum of acceptor and donor, A/(A + D), so-called proximity ratio [48,53]. This ratio showed only a mild decrease over 24 h of incubation in serum (Fig. 2C) and nearly no change in water, demonstrating the relative stability of our FRET NCs. Therefore, we concluded that these new FRET NCs, owing to good stability and relative ease in monitoring their integrity, should be perfectly suited for whole-animal NIR imaging through intravenous injection.

Before testing the integrity of our NCs *in vivo*, we evaluated cytotoxic effects of NCs by performing a cell viability assay *in vitro* on tumor cells. In the dilution range between 10,000 and 500, blank and dye-loaded FRET NCs did not show any significant cytotoxicity (Fig. S3). NCs were however cytotoxic when used at a 200-fold (and below) dilution. Importantly, the presence of both dyes (Cy5.5LP and Cy7.5LP) in the NCs had no added cytotoxic effect. It should be noted that the dilution factor that we further used in our mice experiments corresponded to ~1000-
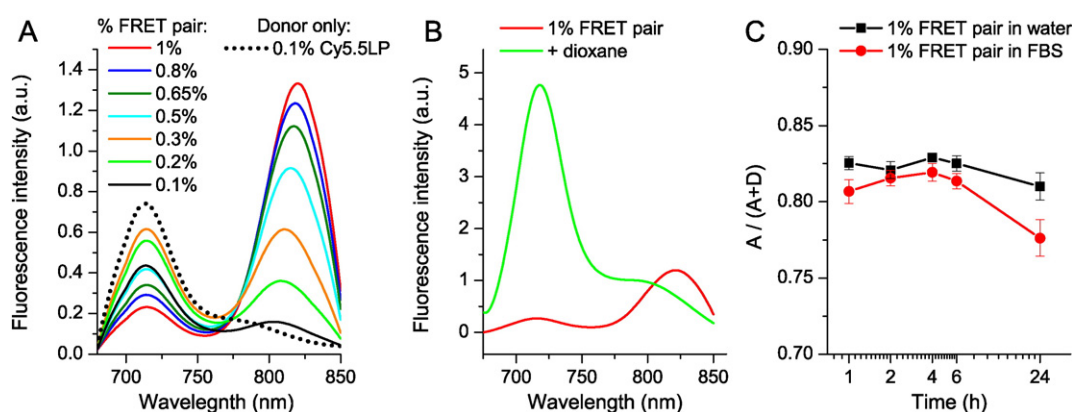
Fig. 2. FRET in the lipid NCs. (A) Fluorescence spectra of dye-loaded NCs as a function of weight % of FRET pair (corresponds to % of each dye). The spectra were recorded for the same 1000-fold dilution of NCs in water. (B) Disintegration of NCs by dioxane: fluorescence spectra of NCs encapsulating 1% of Cy5.5LP and 1% of Cy7.5LP diluted 1000-fold in water or in dioxane. (C) Stability of FRET NCs in serum: FRET signal, expressed as A/(A + D) ratio, for different incubation times in 100% serum or water at 37 °C. To avoid saturation of serum by lipids of NCs, 10,000-fold dilution from original formulation was used. Excitation wavelength was systematically 670 nm.

fold, which is well in the low cytotoxicity range according to the present data.

We then performed whole-animal *in vivo* NIR imaging of anesthetized and immobilized nude mice (Fig. S4) upon parenteral venous administration (retro-orbital) of the FRET NCs suspension, diluted to 50-fold in PBS (the dye concentration in the injected solution was 0.16 mM). We used 630 nm illumination in order to excite Cy5.5LP dye. Emission was collected at two wavelengths: at 700 nm to observe emission of the FRET donor Cy5.5LP, and at 820 nm to observe emission of the FRET acceptor Cy7.5LP (Fig. 3). In order to evaluate directly FRET changes independently of concentration, we also generated ratio images where emission of the acceptor was divided by the emission of the donor (A/D, Fig. 3). Before injection, only low fluorescence was observed for 700 nm channel and negligible signal at 820 nm (Fig. 3A). Right after injection (15 min), the emission of Cy7.5LP corresponding to FRET increased significantly, while emission intensities collected in the Cy5.5LP channel remained very close to auto-fluorescence levels observed before injection (Fig. 3B). This strong FRET fluorescence suggested that the integrity of our FRET NCs was well preserved *in vivo* 15 min after their parenteral injection. Even more importantly, we obtained high imaging contrast in the FRET channel, where blood circulation could be distinguished, notably in the tail and in the back legs vasculature (see arrows 1 and 2 in Fig. 3B). Strikingly, efficient FRET (high A/D ratio in red) highlighted strongly vascularized organs,
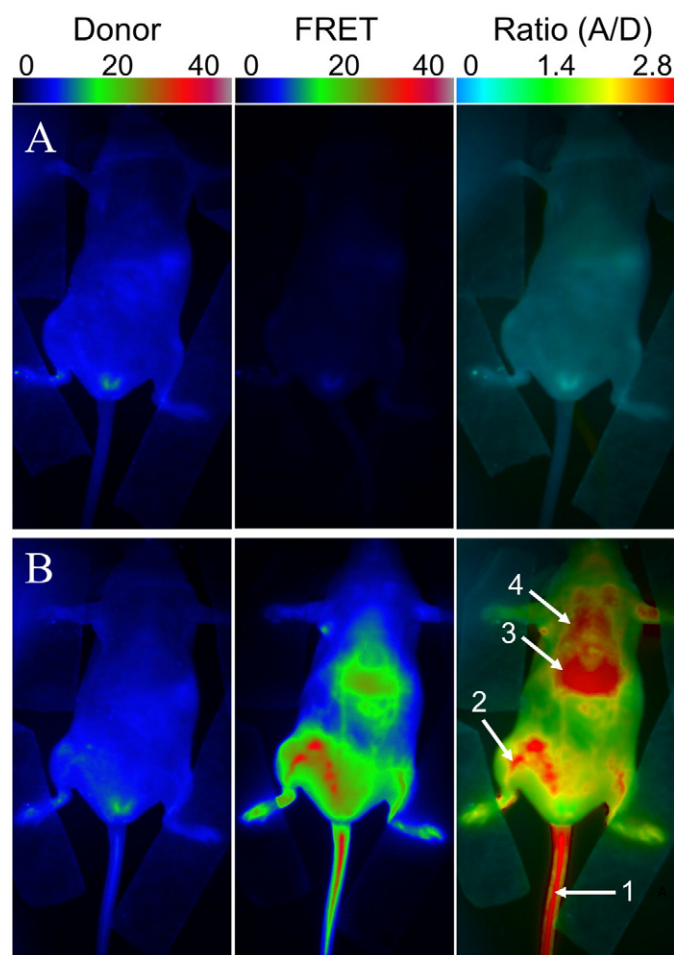
Fig. 3. FRET imaging of healthy nude mice before (A) and after (B) injection of NIR-FRET lipid NCs (1% of Cy5.5LP and Cy7.5LP each). Left panels present intensity images of the Cy5.5LP channel (700 nm), middle panels present images of Cy7.5LP channel (820 nm), while the right panels present ratiometric images (acceptor/donor). The excitation wavelength was 630 nm. Numbers of arrows show vasculature of tail (1) and back leg (2) as well as liver (3) and lungs (4).

particularly liver. Other organs sitting above the liver, such as the lungs and potentially thyroid glands, were also resolved with our FRET NCs. Thus, the use of ratiometric imaging of whole living mice with our FRET NCs provided remarkably high resolution, where both the blood circulation and several important organs were easily revealed.

Further time-course imaging experiment revealed that fluorescence intensities of our NIR dyes and the associated ratio underwent dramatic evolution. The fluorescence intensity gradually increased in the Cy5.5LP channel, and became significant after 6 h, reaching maximal values only after 24 h. On the contrary, overall FRET intensity gradually decreased, so that after 24 h it was much lower than that at Cy5.5LP channel (Fig. 4). The ratio (A/D) imaging confirmed the continuous decay of the FRET signal as the initial red pseudo-color changed to green, and reached the lowest levels (blue) 24 h post-injection (Fig. 4 and S5). Remarkably, this color switch corresponded to ~30-fold decrease in the A/D ratio within 24 h, indicating profound changes of FRET in our NCs as well as high sensitivity and dynamic range of the ratio imaging. This experiment reveals, using FRET imaging, the time-course of disintegration of our NCs. When the control NCs, containing only Cy5.5LP were injected, the emission at the donor (Cy5.5LP) channel was much higher than that at the acceptor one, whatever the post-injection time (Fig. 4 and S7). The obtained ratio images gave very similar blue pseudo-coloring all over the mice body for different post-injection times (Fig. S7), in agreement with total absence of FRET in the control NCs. They matched well with the images obtained at 24 h post-injection of the FRET NCs, where the FRET signal was lost (Fig. 4). Interestingly, we obtained high-quality contrast in the Cy5.5LP channel 15 min after injection of our control donor dye-loaded NCs, and could easily discern both the vasculature network as well as highly-vascularized organs such as the liver. However, in contrast to the ratio imaging with FRET NCs, fewer details were observed (*i.e.* no lungs and less blood vessels). The time-lapse experiment showed a gradual decay of the fluorescence intensity from the tail vasculature (tail vein) with complete disappearance of the signal after 24 h (Fig. 4 and S8).

To provide connection between observed pseudo-color and the integrity of our NCs, we performed a calibration of our imaging set-up with diluted solutions of NCs containing mixtures modeling different integrity levels. As our dyes did not show significant leakage in serum even within 24 h, we consider that disintegration of NCs observed *in vivo* results in the destruction of the droplets themselves. The latter would lead to the dilution of the liberated dyes in the surrounding tissue especially in their lipid structures (lipid membranes and droplets), producing the loss of FRET. In this case, to model fully disintegrated NCs, we mixed NCs containing separately donor and acceptor dyes at low concentration (0.1%). The final concentration of each dye in this model mixture was identical to that in our FRET NCs, but in this case donor and acceptors dyes were isolated from each other and diluted in the oil of NCs. This system should mimic disintegrated NCs, where liberated donors/acceptor dyes are highly diluted in lipid environments of the tissue. We also prepared mixtures of FRET NCs and NCs containing separated FRET partners, where % of integrity was defined as the fraction of the dyes in the intact FRET NCs with respect to total amount of dyes in the mixture. Decrease in the integrity level produced drastic variation of the two-band emission of NCs with rapid increase in the donor emission and less pronounced decrease in the acceptor emission (Fig. 5B). These changes were expected as the fraction of non-FRET NCs increased. Then, using our *in vivo* imaging setup, we observed that a decrease in the NCs integrity correlated with a rapid increase in the donor channel, with only minor decrease in the acceptor one (Fig. 5C), in line with the spectroscopic data. Ratiometric images of the intact FRET NCs appeared in red, which reliably matched the blood circulation of healthy mice at 15 min after injection (Fig. 4). Subsequently, the decrease in the NCs integrity level produced gradual change of the pseudo-color to yellow, green and then to blue, reflecting the drop of the A/D ratio (Fig. 5C). Remarkably, changes in the pseudo-color of our calibrating solution followed the same trend as those in the ratiometric images
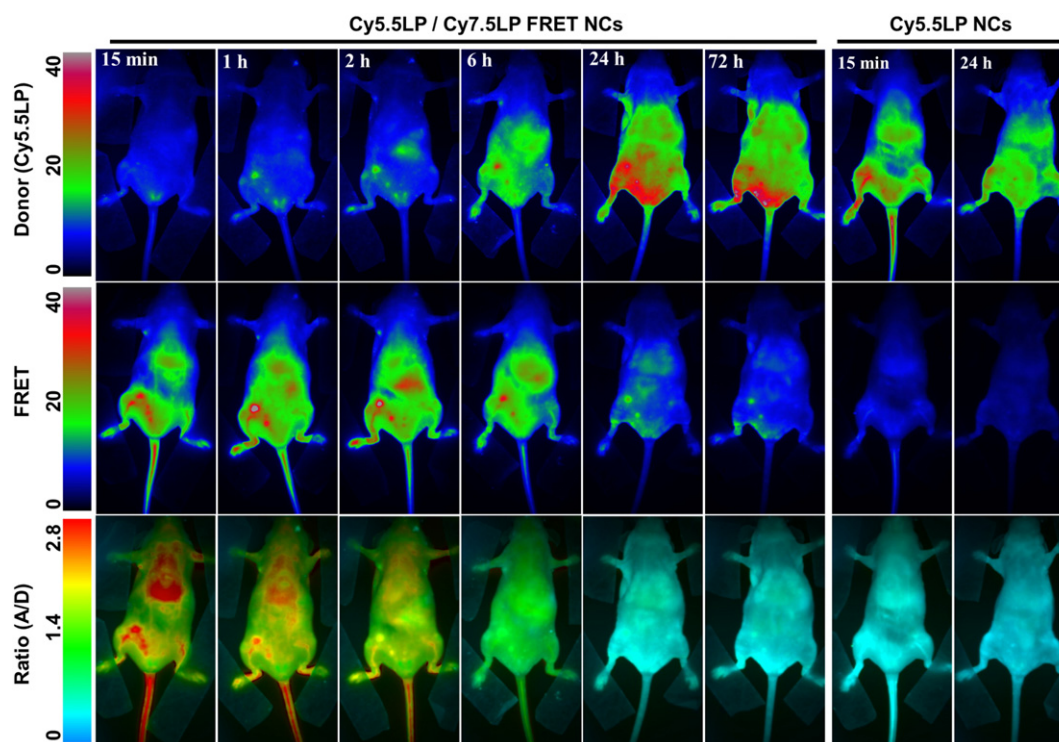
Fig. 4. FRET imaging of healthy nude mice at different times after injection with NIR-FRET lipid NCs (1% of Cy5.5LP and Cy7.5LP each) and control NCs containing only Cy5.5LP dye (1%). Upper panels present intensity images of the Cy5.5LP channel (700 nm), middle panels present images of Cy7.5LP channel (820 nm), while the lower panels present ratiometric images (acceptor/donor). The excitation wavelength was 630 nm. Experiment was repeated on three mice, the set of data for the other two mice (15 min post-injection) is reported in the Supplementary information section (Fig. S6).

of mice in the course of 24 h. The same color switch to blue was observed once the NCs were diluted in dioxane (Fig. 5C), which was an additional model of NCs disintegration. Based on the calibration results, the ratio images obtained in living mice could directly be correlated to NCs integrity *in vivo*. To realize quantitative analysis of the changes in the NCs integrity, we first corrected the data from the background signal in liver and tail vein for both 700 and 820 nm channels, and used them to obtain the $A/(A + D)$ ratio, which is used here as a semi-quantitative measure of the overall FRET efficiency in our samples. This ratio remained stable for 2–3 h post-injection in the tail vein (Fig. 6B), indicating remarkable stability of NCs in the blood circulation. In sharp contrast, this ratio showed significant drop in the liver, indicating significant loss of FRET and thus NCs integrity on the time scale of 2–3 h. Although we cannot provide absolute values of FRET efficiency simply based on the $A/(A + D)$ ratio [48,53,54], we could directly correlate this ratio with the integrity level of NCs (Fig. 5D) using calibration images in Fig. 5C, recorded by the same imaging setup with identical emission filters. The obtained plot of $A/(A + D)$ ratio *vs* integrity level of NCs was fitted using a non-linear equation and then used as our calibration curve. Consequently, this allowed us to estimate integrity of our NCs over time for liver and tail vein, directly in living mice (Fig. 6C). This analysis revealed dramatic difference in the stability of NCs in blood circulation and liver. At 6 h of post-administration, the integrity of NCs in the liver decreased to 66 ± 2%, whereas in blood circulation NCs remained practically intact with integrity level reaching 93 ± 2% (Fig. 6C) ($p < 0.0003$, n = 3). The integrity half-life of NCs was 8.2 ± 0.4 h in the liver of healthy mice. Unfortunately, this parameter could not be assessed for the blood circulation since NCs were cleared from the blood on the shorter time scale. Indeed, our experiments with NCs containing only donor dye (Cy5.5LP) (Fig. S7) confirmed that the circulation half-time was 3 ± 1 h (Fig. S8). Therefore, after 6 h, most of NCs were cleared from the blood circulation, so the detected signal in the tail region was produced mainly by surrounding tissues. Thus, the lipid NCs remain stable until their clearance from the blood. On the

other hand, our data suggest that liver can disintegrate lipid NCs on the time scale of hours.

Next, because NCs bear great potential in tumor targeting, we administrated our FRET NCs to tumor-bearing animals, where murine tumor cells (D2A1) were subcutaneously xenografted in the flank of nude mice 20 days before NCs injection (see photo of one tumor bearing mice in Fig. S4). Thus, assuming that EPR would lead to accumulation of NCs in tumors, the basic question we asked was whether the NCs enter tumor in their intact or disintegrated form. Upon administration of NCs, we observed a significant targeting of the microenvironment of the tumor by our NCs, which led to fluorescence around tumor in the FRET channel and almost negligible fluorescence in the Cy5.5LP channel (Fig. 7A and Fig. S9). This fluorescence signal corresponded to high A/D ratio (observed in red), indicating efficient FRET, similar to that in the tail vessel. Thus, the fluorescence observed in the peri-tumoral region can be assigned to the tumor-associated vasculature, which contains high concentration of intact FRET NCs. Already at 1 h post-injection, the tumor region displayed very strong FRET signal, even though signal collected in the Cy5.5LP channel remained very low (Fig. 7A). In this case, the absolute intensity of the donor channel was only 5.7 ± 1.3 (arbitrary units, a. u.), whereas for control NCs with only donor Cy5.5LP, the intensity in the tumor region at 1 h injection was 26 ± 2 (a. u.). This much lower intensity of the donor channel suggested the efficient FRET-based quenching of the donor inside the FRET NCs accumulated in the tumor. Ratio image at 1 h showed mainly yellow-red color in the tumor region, which indicated that after accumulation in the tumor the FRET remained very high despite a small decrease. These observations suggested that (*i*) the lipid NCs underwent a specific, rapid and efficient accumulation into the xenografted tumor, through the tumor-associated vasculature, and (*ii*) they remain, to a large extent, intact for at least 1 h within tumor region. Intensity of the FRET signal in tumor reached maximum values 2 h post-injection and then remained stable over the time-course of the experiment. In contrast, the fluorescence intensity in the donor channel increased slowly over the first
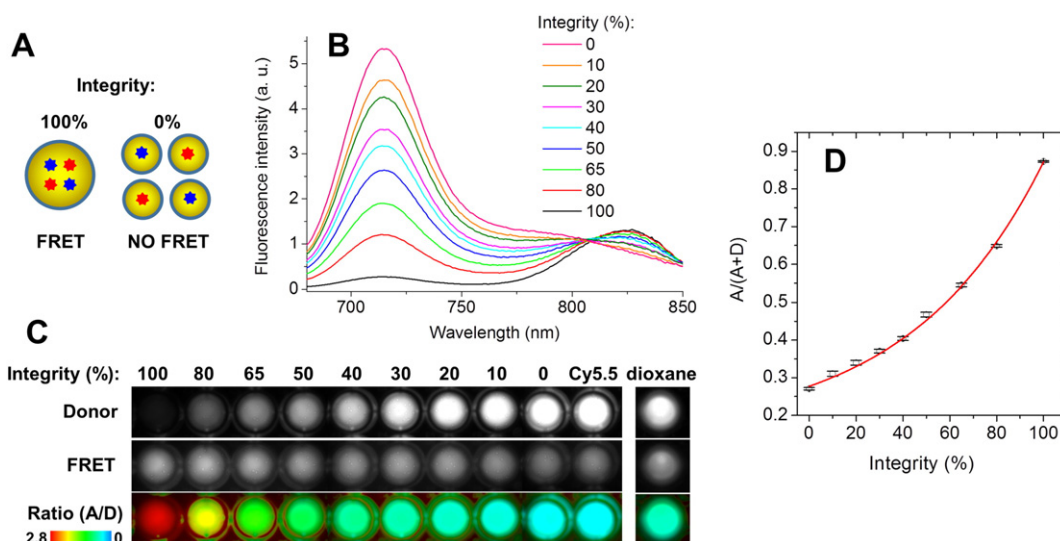
Fig. 5. Calibration of ratiometric *in vivo* images using mixtures of intact FRET NCs with NCs containing separately donor and acceptor at low concentration. The mixing is done to preserve the same concentration of dyes: 100% integrity corresponds to FRET NCs (1% of Cy5.5LP and 1% of Cy7.5LP) diluted in PBS 1000-fold from the original formulation, while 0% integrity corresponds to a mixture of NCs containing separately donor (0.1% of Cy5.5LP) and acceptor (0.1% Cy7.5LP), both diluted at 100-fold in PBS. The latter mixture models the disintegrated NCs, where donor and acceptor separate and get diluted in the tissue (A). (B) Fluorescence spectra of the obtained solutions. (C) Fluorescence images of these mixtures acquired with the *in vivo* imaging set-up: donor (Cy5.5LP) channel (upper panels), acceptor (Cy7.5LP) FRET channel (middle panels), and the acceptor/donor ratio images (lower panels). NCs containing only donor dye (Cy5.5LP) and FRET NCs diluted 1000-fold in dioxane (second model of the complete disintegration) are also shown. (D) Calibration curve of A/(A + D) ratio *vs* the level of integrity of NCs obtained based on data in (C) panel. The error bars represent the standard error of the mean ($n = 3$).

6 h post-injection, but drastically increased 24 h post-injection. The ratiometric imaging showed that relative intensity of the FRET acceptor decreased continuously with time, reaching the lowest values after 24 h of incubation. Experiments with control NCs containing only donor dye Cy5.5LP confirmed rapid accumulation of NCs into the tumor region already at 1 h post-injection (Fig. 7A). The acceptor channel remained dim in the tumor region, in line with expected absence of FRET. The intensity in the donor channel continued to gradually increase over time, reaching saturation after 24 h, whereas in the acceptor channel the intensity remained poor (Fig. S11). Imaging of mice organs (Fig. S12) dissected from animals at 24 h post-administration revealed that fluorescence of tumor was slightly brighter than that of liver (by 30%, $p = 0.02$, n = 4). By contrast, fluorescence of other studied organs (spleen, lungs, heart and kidneys) was many-fold lower ($p \leq 0.0002$, n = 4), suggesting that both tumors and liver are the main targets for accumulation of our NCs, in line with the whole animal *in vivo* imaging data.

After accounting for the background fluorescence, we quantified the FRET proximity ratio in tumor-bearing mice by analyzing the A/(A + D) ratio (Fig. 7B) and then converted it to the NCs integrity level for different post-administration times (Fig. 7C). Importantly, after 2 h, when the signal of NCs from the tumor region was already very strong (Fig. 7A), the integrity of NCs was still at $77 \pm 1\%$ (Fig. 7C), indicating that they

could enter the tumor with minimal loss of integrity. Nevertheless, the loss of integrity was faster than in the blood circulation. Indeed, in tail vein after 6 h NCs integrity was at $71 \pm 3\%$, whereas for tumor it dropped already to $40 \pm 4\%$ (Fig. 7C) ($p < 0.003$, n = 3). The integrity half-life for our NCs in tumor was 4.4 ± 0.3 h, which was even faster than in the liver of healthy mice (8.2 ± 0.4 h, $p < 0.001$, n = 3). We provide the first evidence for the kinetics of disintegration of lipid NCs in tumor bearing mice *in vivo* and show that the lipid NCs preserve their content in the blood circulation, then they can enter tumors with minimal loss of integrity and finally after accumulation in the tumors they disintegrate on the time scale of hours. One should also note that disintegration of NCs inside blood circulation of tumor bearing mice was considerably faster than in healthy mice, which can be seen from the integrity levels at 6 h of post-administration ($71 \pm 3\%$ vs $93 \pm 2\%$, $p < 0.003$, n = 3). On the other hand, the clearance from blood circulation, measured using control NCs bearing only Cy5.5LP (Fig. S11) in tumor-bearing mice was similar to that in healthy mice (Fig. S8).

In conclusion, we propose here an original approach to obtain near-infrared lipid nanocarriers with efficient FRET and excellent brightness. It is based on hydrophobic counterions that increase many-fold the solubility of cyanines dyes in oil and thereby enable their high loading inside NCs, required for FRET. We provide here clear demonstration that these new NCs allow reliable imaging and monitoring NCs' integrity *in*
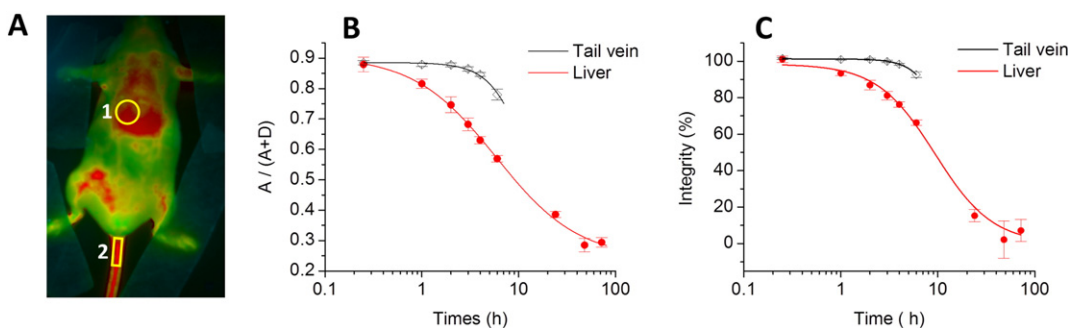
Fig. 6. Quantitative analysis of NCs integrity in living mice. (A) Ratio image of healthy mice showing the regions of interest: liver (1) and tail vein (2). (B, C) Analysis of the A/(A + D) ratio (B) and integrity (C) of NCs in different regions of healthy mice as a function of post-administration time. Ratio analysis in the tail vein was done until 6 h, because after that the signal was too low. Three mice were analyzed, the error bars represent the standard error of the mean (n = 3).
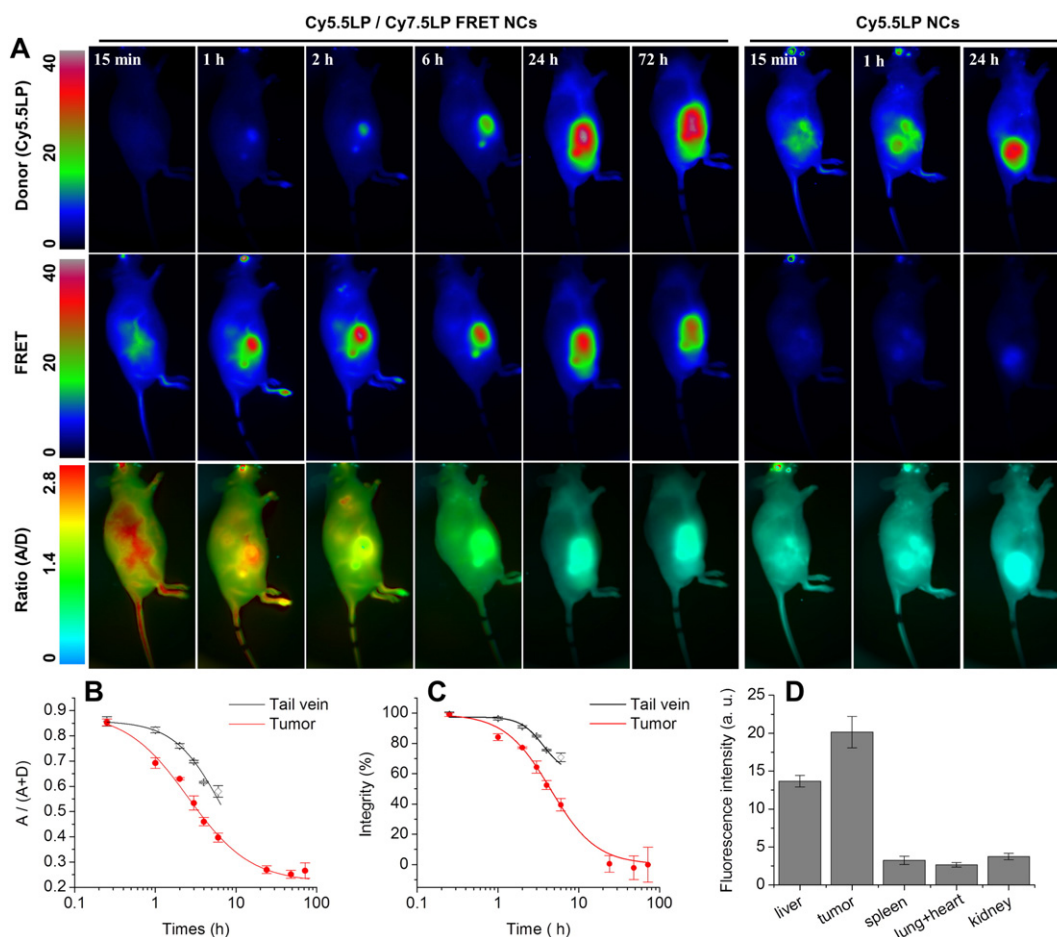
Fig. 7. (A) FRET imaging of tumor-bearing nude mice at different times after injected with NIR-FRET lipid NCs (1% of Cy5.5LP and Cy7.5LP each) or control NCs with donor dye only (1% of Cy5.5LP dye). Upper panels present intensity images of the Cy5.5LP channel (700 nm), middle panels present images of Cy7.5LP channel (820 nm), while the lower panels present ratiometric images (acceptor/donor). The excitation wavelength was 630 nm. Experiment was repeated on three mice, the set of data for the other two mice is reported in the Supplementary information section (Fig. S10). (B, C) Analysis of the A/(A + D) ratio (B) and integrity (C) of NCs in different regions of tumor-bearing mice as a function of post-administration time. Three mice were analyzed, the error bars represent the standard error of the mean (n = 3). (D) Fluorescence intensity of organs dissected from animals at 24 h post-administration with NCs containing 1% of Cy5.5LP dye. The error bars corresponds to standard error of the mean (n = 4). Images of organs are presented in Fig. S12.

vivo. Notably, we provide here whole-animal imaging with apparently higher resolution compared to existing FRET systems for *in vivo* imaging [9,24,25]. Importantly, we were able to accurately resolve the follow-up of NCs integrity directly in the blood circulation of living mice, which was possible before only by using dedicated intravital microscopy [9, 27]. The high-quality of the obtained images is probably due to relatively high fluorescence quantum yield, dye-loading and injection dose, as well as optimal NIR spectral excitation and emission windows of our FRET NCs. Moreover, by dividing two emission channels, we generated high quality ratiometric images capable of resolving some features of the vascular system and tissues that are usually not assessable by live whole-animal fluorescence imaging. The intensity ratio is the absolute parameter, which is almost independent on the concentration of the imaging agent and excitation light intensity [31,32,55,56]. Therefore, the ratio signal provides quantitative information about the changes in the emission spectra of the probe in the imaged system. In our case, due to calibration of the spectral response of the FRET NCs directly under the *in vivo* imaging setup, we achieved a reliable read-out of the integrity of our NCs by ratiometric analysis, which would not be possible using absolute intensity measurements. It should be noted that in addition to calibration of the imaging system, this method requires subtraction of the background, which is relatively high in small animal fluorescence imaging. One important point that is difficult to take into account is the difference in the penetration depth for 700- and 820-nm light [30], which may affect the precision of the quantitative analysis.

The described methodology enabled, for the first time, to quantify by *in vivo* fluorescence imaging the integrity of NCs in different regions of healthy and tumor-bearing mice. It revealed that injected NCs remain nearly intact after 6 h in the blood circulation of healthy mice, whereas their integrity significantly dropped to 66 ± 2% in the liver of healthy mice, and up to 40 ± 4% in tumors. Nevertheless, lipid NCs appeared remarkably stable as they could enter tumors rapidly with minimal loss of integrity, showing for instance 77 ± 1% of the integrity at 2 h of post-injection. Thus, NCs can preserve their content in the blood circulation, enter tumors in nearly intact form and then release this content on the time scale of hours. This data shows the strong potential of NCs as efficient carriers of drugs and contrast agents. The remarkable stability of lipid NCs is an important finding of this work. Commonly, nanoemulsions are considered as liquid systems that should not be stable enough *in vivo* and require, for instance, specially designed surface of lipids with long PEG chains [25,36]. However, in the present work, we showed for the first time that nanoemulsion droplets built only from oil (medium chain triglycerides) and a surfactant (Cremophor® ELP) exhibited no signs of disintegration in blood circulation for hours. This result contrasts strongly with the poor capacity of these NCs to keep medium polar molecules like Nile Red, which is rapidly released in biological media [41,57].

Our NCs showed remarkably efficient accumulation in tumors, which can be clearly assigned to the EPR effect originating from the leaky nature of the tumor vesicles [15,58]. The efficiency of the passive EPR tumor accumulation is generally proportional to the circulation

time of the agent in the bloodstream. In this respect, our NCs present dense PEG shell which is known to prolong the circulation time of nanoparticles [59].

Finally, the key finding that has never been shown for lipid NCs is their capacity to accumulate in tumors in nearly intact form. This property is known for polymer nanoparticles, which are established drug delivery vehicles into tumors [60,61], and inorganic nanoparticles, such as quantum dots covered with robust organic shell [9,62]. The capacity of our nano-emulsion droplets to preserve their integrity after accumulation in tumors is particularly remarkable given the liquid nature of their core. This result shows the strong potential of these lipid NCs as nanoscale platform for *in vivo* imaging, drug delivery and image guided surgery.

Acknowledgments

Appendix A. Supplementary data

Supplementary data to this article can be found online at http://dx.doi.org/10.1016/j.jconrel.2016.06.027.

References

[1] D.E. Lee, H. Koo, I.C. Sun, J.H. Ryu, K. Kim, I.C. Kwon, Multifunctional nanoparticles for multimodal imaging and theragnosis, Chem. Soc. Rev. 41 (2012) 2656–2672.
[2] P.D. Howes, R. Chandrawati, M.M. Stevens, Colloidal nanoparticles as advanced biological sensors, Science 346 (2014) 1247390.
[3] A. Reisch, A.S. Klymchenko, Fluorescent Polymer Nanoparticles Based on Dyes: Seeking Brighter Tools for Bioimaging, Small 12 (2016) 1968–1992.
[4] J.-W. Yoo, D.J. Irvine, D.E. Discher, S. Mitragotri, Bio-inspired, bioengineered and biomimetic drug delivery carriers, Nat. Rev. Drug Discov. 10 (2011) 521–535.
[5] D. Peer, J.M. Karp, S. Hong, O.C. FaroKhzad, R. Margalit, R. Langer, Nanocarriers as an emerging platform for cancer therapy, Nat. Nanotechnol. 2 (2007) 751–760.
[6] E. Locatelli, I. Monaco, M.C. Franchini, Hard and soft nanoparticles for image-guided surgery in nanomedicine, J. Nanopart. Res. 17 (2015) 1–17.
[7] L. Bu, B. Shen, Z. Cheng, Fluorescent imaging of cancerous tissues for targeted surgery, Adv. Drug Deliv. Rev. 76 (2014) 21–38.
[8] H.S. Choi, W. Liu, F. Liu, K. Nasr, P. Misra, M.G. Bawendi, et al., Design considerations for tumour-targeted nanoparticles, Nat. Nanotechnol. 5 (2010) 42–47.
[9] Y.M. Zhao, I. van Rooy, S. Hak, F. Fay, J. Tang, C.D. Davies, et al., Near-infrared fluorescence energy transfer imaging of nanoparticle accumulation and dissociation kinetics in tumor-bearing mice, ACS Nano 7 (2013) 10362–10370.
[10] S.S. D'Souza, P.P. DeLuca, Methods to assess in vitro drug release from injectable polymeric particulate systems, Pharm. Res. 23 (2006) 460–474.
[11] D.E. Owens, N.A. Peppas, Opsonization, biodistribution, and pharmacokinetics of polymeric nanoparticles, Int. J. Pharm. 307 (2006) 93–102.
[12] A.E. Nel, L. Maedler, D. Velegol, T. Xia, E.M.V. Hoek, P. Somasundaran, et al., Understanding biophysicochemical interactions at the nano-bio interface, Nat. Mater. 8 (2009) 543–557.
[13] Y. Li, M.S. Budamagunta, J. Luo, W. Xiao, J.C. Voss, K.S. Lam, Probing of the assembly structure and dynamics within nanoparticles during interaction with blood proteins, ACS Nano 6 (2012) 9485–9495.
[14] S. Hak, E. Helgesen, H.H. Hektoen, E.M. Huuse, P.A. Jarzyna, W.J.M. Mulder, et al., The effect of nanoparticle polyethylene glycol surface density on ligand-directed tumor targeting studied in vivo by dual modality imaging, ACS Nano 6 (2012) 5648–5658.
[15] J. Fang, H. Nakamura, H. Maeda, The EPR effect: unique features of tumor blood vessels for drug delivery, factors involved, and limitations and augmentation of the effect, Adv. Drug Deliv. Rev. 63 (2011) 136–151.
[16] W.G. Kreyling, A.M. Abdelmonem, Z. Ali, F. Alves, M. Geiser, N. Haberl, et al., In vivo integrity of polymer-coated gold nanoparticles, Nat. Nanotechnol. 10 (2015) 619–623.
[17] V. Ntziachristos, C. Bremer, R. Weissleder, Fluorescence imaging with near-infrared light: new technological advances that enable in vivo molecular imaging, Eur. Radiol. 13 (2003) 195–208.
[18] J.V. Frangioni, In vivo near-infrared fluorescence imaging, Curr. Opin. Chem. Biol. 7 (2003) 626–634.
[19] J.H. Rao, A. Dragulescu-Andrasi, H.Q. Yao, Fluorescence imaging in vivo: recent advances, Curr. Opin. Biotechnol. 18 (2007) 17–25.
[20] C. Darne, Y.J. Lu, E.M. Sevick-Muraca, Small animal fluorescence and bioluminescence tomography: a review of approaches, algorithms and technology update, Phys. Med. Biol. 59 (2014) R1–R64.
[21] E.A. Jares-Erijman, T.M. Jovin, FRET imaging, Nat. Biotechnol. 21 (2003) 1387–1395.
[22] K.E. Sapsford, L. Berti, I.L. Medintz, Materials for fluorescence resonance energy transfer analysis: beyond traditional donor-acceptor combinations, Angew. Chem. Int. Ed. 45 (2006) 4562–4588.
[23] T. Skajaa, Y. Zhao, D.J. van den Heuvel, H.C. Gerritsen, D.P. Cormode, R. Koole, et al., Quantum dot and Cy5.5LP labeled nanoparticles to investigate lipoprotein biointeractions via Forster resonance energy transfer, Nano Lett. 10 (2010) 5131–5138.
[24] S.W. Morton, X. Zhao, M.A. Quadir, P.T. Hammond, FRET-enabled biological characterization of polymeric micelles, Biomaterials 35 (2014) 3489–3496.
[25] A.L. Laine, J. Gravier, M. Henry, L. Sancey, J. Bejaud, E. Pancani, et al., Conventional versus stealth lipid nanoparticles: formulation and in vivo fate prediction through FRET monitoring, J. Control. Release 188 (2014) 1–8.
[26] S. Hak, N.K. Reitan, O. Haraldseth, Davies CdL. Intravital microscopy in window chambers: a unique tool to study tumor angiogenesis and delivery of nanoparticles, Angiogenesis 13 (2010) 113–130.
[27] H. Chen, S. Kim, W. He, H. Wang, P.S. Low, K. Park, et al., Fast release of lipophilic agents from circulating PEG-PDLLA micelles revealed by in vivo Förster resonance energy transfer imaging, Langmuir 24 (2008) 5213–5217.
[28] Z.Q. Guo, S. Park, J. Yoon, I. Shin, Recent progress in the development of near-infrared fluorescent probes for bioimaging applications, Chem. Soc. Rev. 43 (2014) 16–29.
[29] S.L. Luo, E.L. Zhang, Y.P. Su, T.M. Cheng, C.M. Shi, A review of NIR dyes in cancer targeting and imaging, Biomaterials 32 (2011) 7127–7138.
[30] H. Kobayashi, M. Ogawa, R. Alford, P.L. Choyke, Y. Urano, New strategies for fluorescent probe design in medical diagnostic imaging, Chem. Rev. 110 (2010) 2620–2640.
[31] A. H-w, K.L. Hazelwood, M.W. Davidson, R.E. Campbell, Fluorescent protein FRET pairs for ratiometric imaging of dual biosensors, Nat. Methods 5 (2008) 401–403.
[32] X.F. Zhou, F.Y. Su, H.G. Lu, P. Senechal-Willis, Y.Q. Tian, R.H. Johnson, et al., An FRET-based ratiometric chemosensor for in vitro cellular fluorescence analyses of pH, Biomaterials 33 (2012) 171–180.
[33] K.K. Ng, M. Takada, C.C.S. Jin, G. Zheng, Self-sensing porphysomes for fluorescence-guided photothermal therapy, Bioconjug. Chem. 26 (2015) 345–351.
[34] M.F. Attia, N. Anton, M. Chiper, R. Akasov, H. Anton, N. Messaddeq, et al., Biodistribution of X-ray iodinated contrast agent in nano-emulsions is controlled by the chemical nature of the oily core, ACS Nano 8 (2014) 10537–10550.
[35] X. Li, N. Anton, G. Zuber, M.J. Zhao, N. Messaddeq, F. Hallouard, et al., Iodinated alpha-tocopherol nano-emulsions as non-toxic contrast agents for preclinical X-ray imaging, Biomaterials 34 (2013) 481–491.
[36] N.T. Huynh, C. Passirani, P. Saulnier, J.P. Benoit, Lipid nanocapsules: a new platform for nanomedicine, Int. J. Pharm. 379 (2009) 201–209.
[37] N. Anton, J.-P. Benoit, P. Saulnier, Design and production of nanoparticles formulated from nano-emulsion templates - a review, J. Control. Release 128 (2008) 185–199.
[38] J.M. Gutierrez, C. Gonzalez, A. Maestro, I. Sole, C.M. Pey, J. Nolla, Nano-emulsions: new applications and optimization of their preparation, Curr. Opin. Colloid Interface Sci. 13 (2008) 245–251.
[39] K. Hormann, A. Zimmer, Drug delivery and drug targeting with parenteral lipid nanoemulsions - a review, J. Control. Release 223 (2016) 85–98.
[40] N. Anton, T.F. Vandamme, The universality of low-energy nano-emulsification, Int. J. Pharm. 377 (2009) 142–147.
[41] A.S. Klymchenko, E. Roger, N. Anton, H. Anton, I. Shulov, J. Vermot, et al., Highly lipophilic fluorescent dyes in nano-emulsions: towards bright non-leaking nano-droplets, RSC Adv. 2 (2012) 11876–11886.
[42] J. Gravier, L. Sancey, S. Hirsjaervi, E. Rustique, C. Passirani, J.-P. Benoit, et al., FRET imaging approaches for in vitro and in vivo characterization of synthetic lipid nanoparticles, Mol. Pharm. 11 (2014) 3133–3144.
[43] J. Merian, R. Boisgard, P.-A. Bayle, M. Bardet, B. Tavitian, I. Texier, Comparative biodistribution in mice of cyanine dyes loaded in lipid nanoparticles, Eur. J. Pharm. Biopharm. 93 (2015) 1–10.
[44] V.N. Kilin, H. Anton, N. Anton, E. Steed, J. Vermot, T.E. Vandamme, et al., Counterion-enhanced cyanine dye loading into lipid nano-droplets for single-particle tracking in zebrafish, Biomaterials 35 (2014) 4950–4957.
[45] B.E. Schaafsma, J.S.D. Mieog, M. Hutteman, J.R. Van Der Vorst, P.J.K. Kuppen, C.W.G.M. Löwik, et al., The clinical use of indocyanine green as a near-infrared fluorescent contrast agent for image-guided oncologic surgery, J. Surg. Oncol. 104 (2011) 323–332.
[46] T. Ishizawa, N. Fukushima, J. Shibahara, K. Masuda, S. Tamura, T. Aoki, et al., Real-time identification of liver cancers by using indocyanine green fluorescent imaging, Cancer 115 (2009) 2491–2504.
[47] I. Texier, M. Goutayer, A. Da Silva, L. Guyon, N. Djaker, V. Josserand, et al., Cyanine-loaded lipid nanoparticles for improved in vivo fluorescence imaging, J. Biomed. Opt. 14 (2009) 054005.
[48] S. Preus, L.M. Wilhelmsson, Advances in quantitative FRET-based methods for studying nucleic acids, Chembiochem 13 (2012) 1990–2001.

[49] T. Shibue, M.W. Brooks, R.A. Weinberg, An integrin-linked machinery of cytoskeletal regulation that enables experimental tumor initiation and metastatic colonization, Cancer Cell 24 (2013) 481–498.

[50] M.A. Karreman, L. Mercier, N.L. Schieber, T. Shibue, Y. Schwab, J.G. Goetz, Correlating intravital multi-photon microscopy to 3D electron microscopy of invading tumor cells using anatomical reference points, PLoS One 9 (2014) e114448.

[51] J. Schindelin, I. Arganda-Carreras, E. Frise, V. Kaynig, M. Longair, T. Pietzsch, et al., Fiji: an open-source platform for biological-image analysis, Nat. Methods 9 (2012) 676–682.

[52] T.J. Russin, E.Ï. Altmoğlu, J.H. Adair, P.C. Eklund, Measuring the fluorescent quantum efficiency of indocyanine green encapsulated in nanocomposite particulates, J. Phys. Condens. Matter 22 (2010) 334217.

[53] E. Nir, X. Michalet, K.M. Hamadani, T.A. Laurence, D. Neuhauser, Y. Kovchegov, et al., Shot-noise limited single-molecule FRET histograms: comparison between theory and experiments, J. Phys. Chem. B 110 (2006) 22103–22124.

[54] J.A. Broussard, B. Rappaz, D.J. Webb, C.M. Brown, Fluorescence resonance energy transfer microscopy as demonstrated by measuring the activation of the serine/threonine kinase Akt, Nat. Protoc. 8 (2013) 265–281.

[55] V.V. Shynkar, A.S. Klymchenko, C. Kunzelmann, G. Duportail, C.D. Muller, A.P. Demchenko, et al., Fluorescent biomembrane probe for ratiometric detection of apoptosis, J. Am. Chem. Soc. 129 (2007) 2187–2193.

[56] Y. Kurishita, T. Kohira, A. Ojida, I. Hamachi, Rational design of FRET-based ratiometric chemosensors for in vitro and in cell fluorescence analyses of nucleoside polyphosphates, J. Am. Chem. Soc. 132 (2010) 13290–13299.

[57] G. Bastiat, C.O. Pritz, C. Roider, F. Fouchet, E. Lignieres, A. Jesacher, et al., A new tool to ensure the fluorescent dye labeling stability of nanocarriers: a real challenge for fluorescence imaging, J. Control. Release 170 (2013) 334–342.

[58] S.K. Hobbs, W.L. Monsky, F. Yuan, W.G. Roberts, L. Griffith, V.P. Torchilin, et al., Regulation of transport pathways in tumor vessels: role of tumor type and microenvironment, Proc. Natl. Acad. Sci. U. S. A. 95 (1998) 4607–4612.

[59] J.V. Jokerst, T. Lobovkina, R.N. Zare, S.S. Gambhir, Nanoparticle PEGylation for imaging and therapy, Nanomedicine 6 (2011) 715–728.

[60] R. Devulapally, R. Paulmurugan, Polymer nanoparticles for drug and small silencing RNA delivery to treat cancers of different phenotypes, Wiley Interdiscip. Rev. Nanomed. Nanobiotechnol. 6 (2014) 40–60.

[61] A. Schadlich, H. Caysa, T. Mueller, F. Tenambergen, C. Rose, A. Gopferich, et al., Tumor accumulation of NIR fluorescent PEG PLA nanoparticles: impact of particle size and human xenograft tumor model, ACS Nano 5 (2011) 8710–8720.

[62] X.H. Gao, Y.Y. Cui, R.M. Levenson, L.W.K. Chung, S.M. Nie, In vivo cancer targeting and imaging with semiconductor quantum dots, Nat. Biotechnol. 22 (2004) 969–976.

Integrity of lipid nanocarriers in bloodstream and tumor quantified by near-infrared ratiometric FRET imaging in living mice

Redouane Bouchaala, Luc Mercier, Bohdan Andreiuk, Yves Mély, Thierry Vandamme, Nicolas Anton, Jacky G. Goetz, Andrey S. Klymchenko

Synthesis
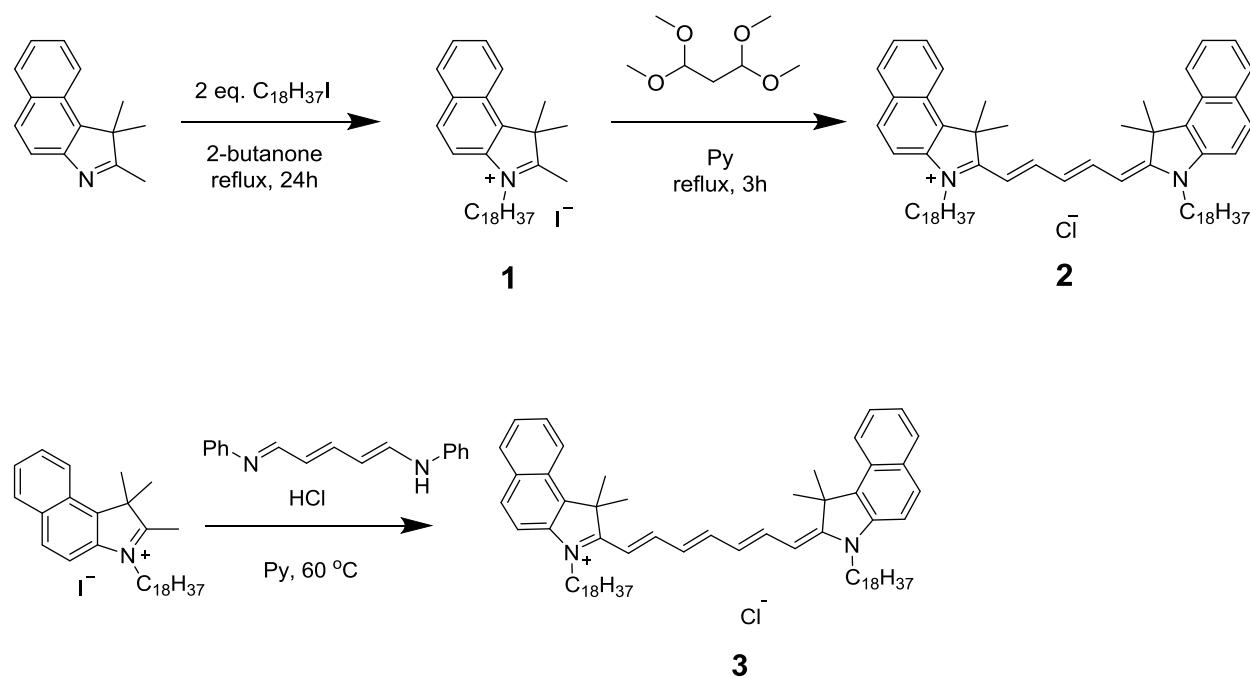
Scheme 1. Synthesis of dioctadecylcyanines 5.5 (**2**) and 7.5 (**3**).
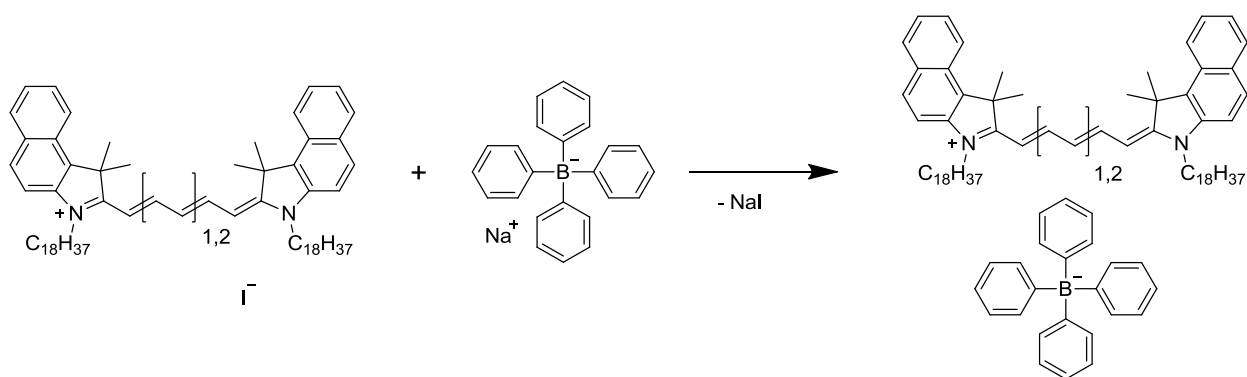
Scheme 2. Synthesis of dioctadecylcyanines 5.5 and 7.5 salts with tetraphenylborate counterion: Cy5.5LP and Cy7.5LP, respectively).
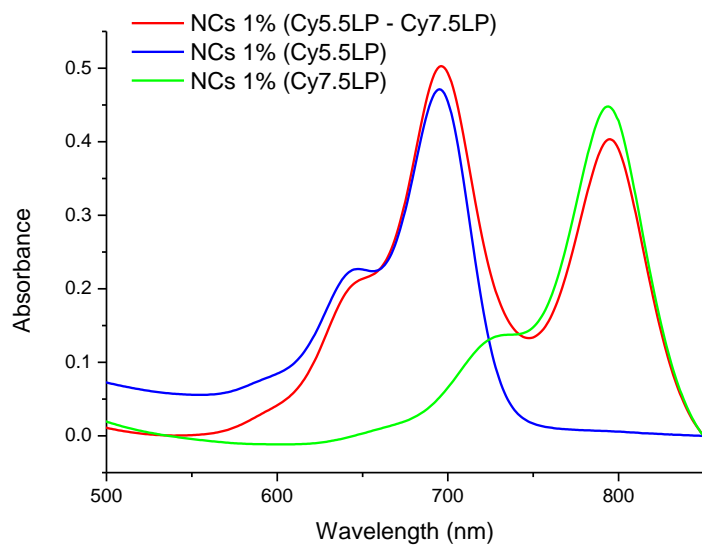
Figure S1. Absorption spectra of NCs encapsulating Cy5.5LP, Cy7.5LP and their mixture. NCs were diluted 500-fold from in water from the original formulation.
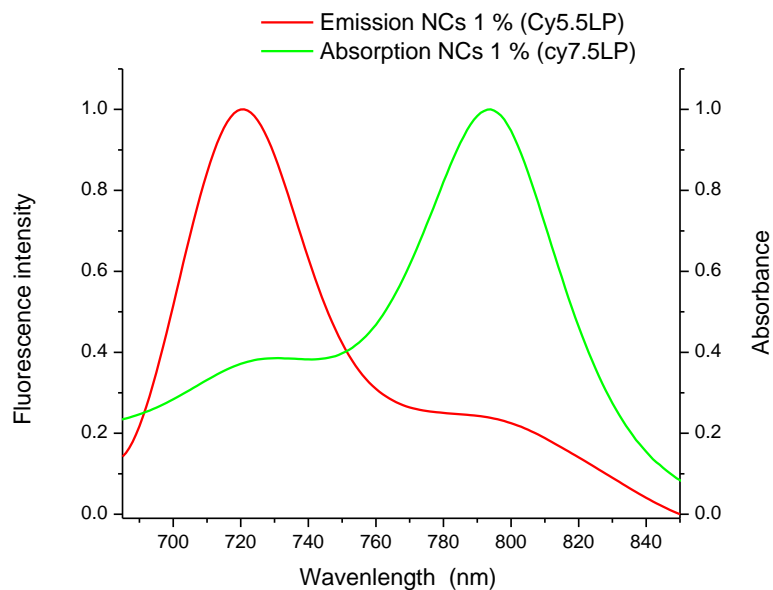
Figure S2. Normalized fluorescence spectrum of NC encapsulating 1% of Cy5.5LP and the absorption spectrum of NC encapsulating 1% of Cy7.5LP showing good spectral overlap, required for FRET. NCs were diluted in water 500-fold from the original formulation.

Table S1. Hydrodynamic diameter and polydispersity index obtained by DLS and the fluorescence quantum yield of lipid nanocarriers encapsulating different NIR dyes.[a]

	Size (nm)	PDI	QY (%)
NC, 1% Cy5.5LP	94	0.165	27
NC, 1% Cy5.5LP / Cy7.5LP	91	0.191	11
NC, 1% Cy7.5LP	90	0.108	5

[a] Statistics by volume was used in the size analysis. PDI is a polydispersity index. QY is a fluorescence quantum yield, measured using DiD dye in methanol (QY = 33 %) as reference [1].
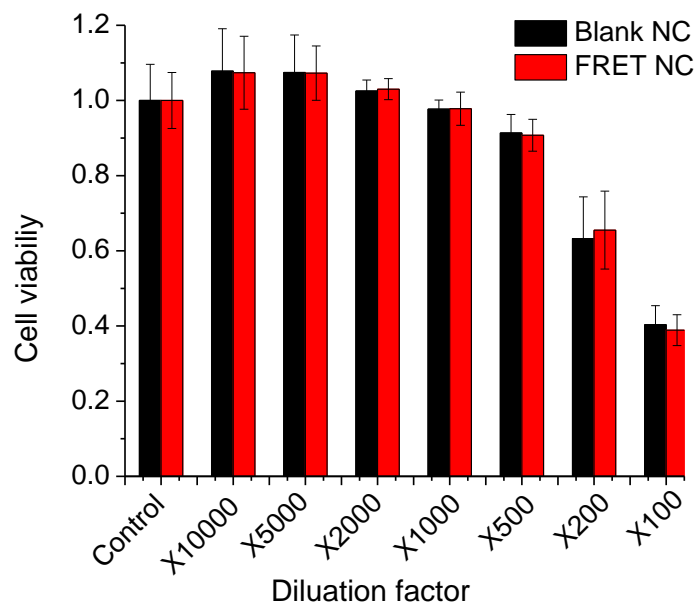
Fig. S3. Cytotoxicity of lipid nanocarriers loaded with FRET pair (Cy5.5LP and Cy7.5LP, 1% each). Cell viability was measured by MTT assay on HeLa cells incubated for 24 h with NCs without and with Cy5.5LP and Cy7.5LP (1% each) at different dilutions from the original formulation. The error bars correspond to standard error of the mean (n = 6).
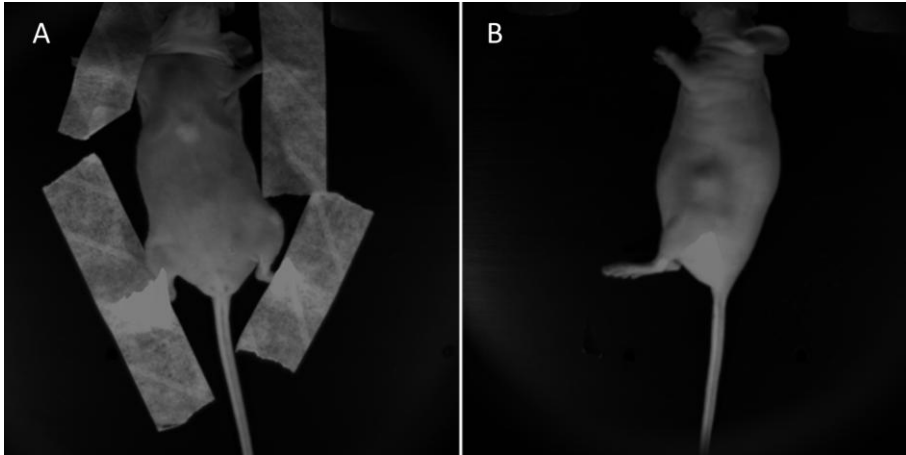
Figure S4. Photos of healthy (A) and tumor-bearing (B) mice which were used in the FRET imaging shown in Figures 3, 4, S3 and S5.
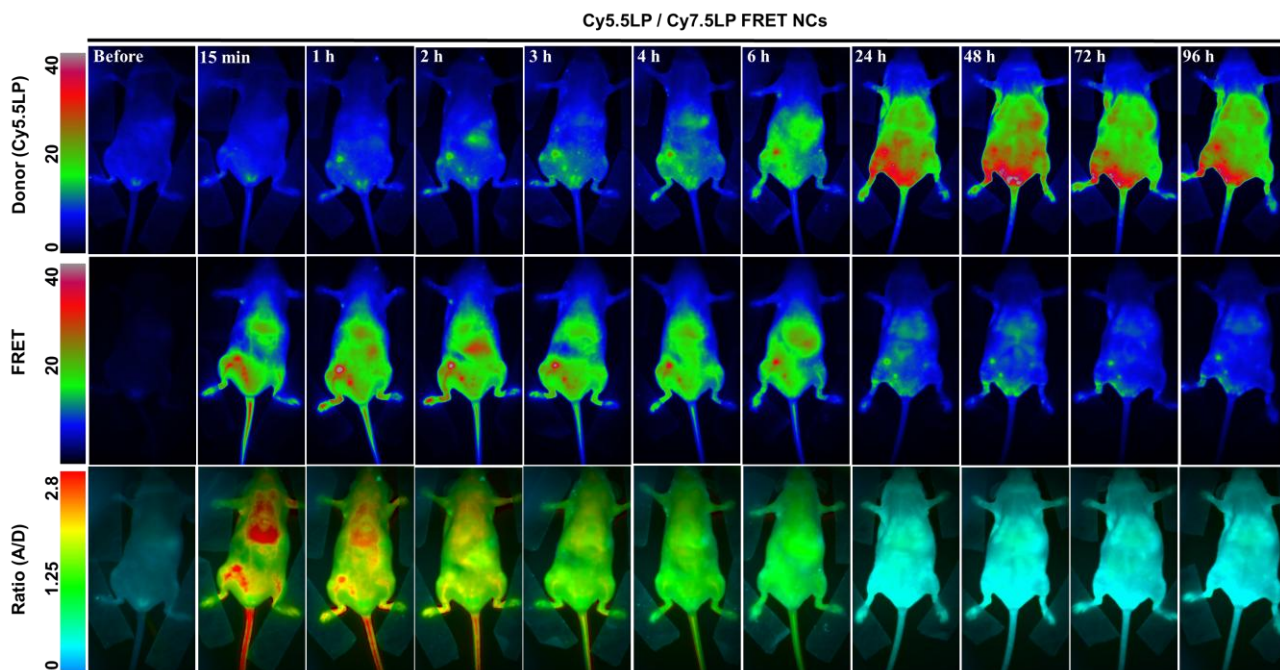
Figure S5. FRET imaging of healthy mice at different times after injection with NIR-FRET lipid nanocarriers. NCs contained 1% of donor Cy5.5LP and acceptor Cy7.5LP. Upper panels present intensity images of the Cy5.5LP channel (700 nm), middle panels present images of Cy7.5LP channel (840 nm), while the lower panels present ratiometric images (acceptor / donor).
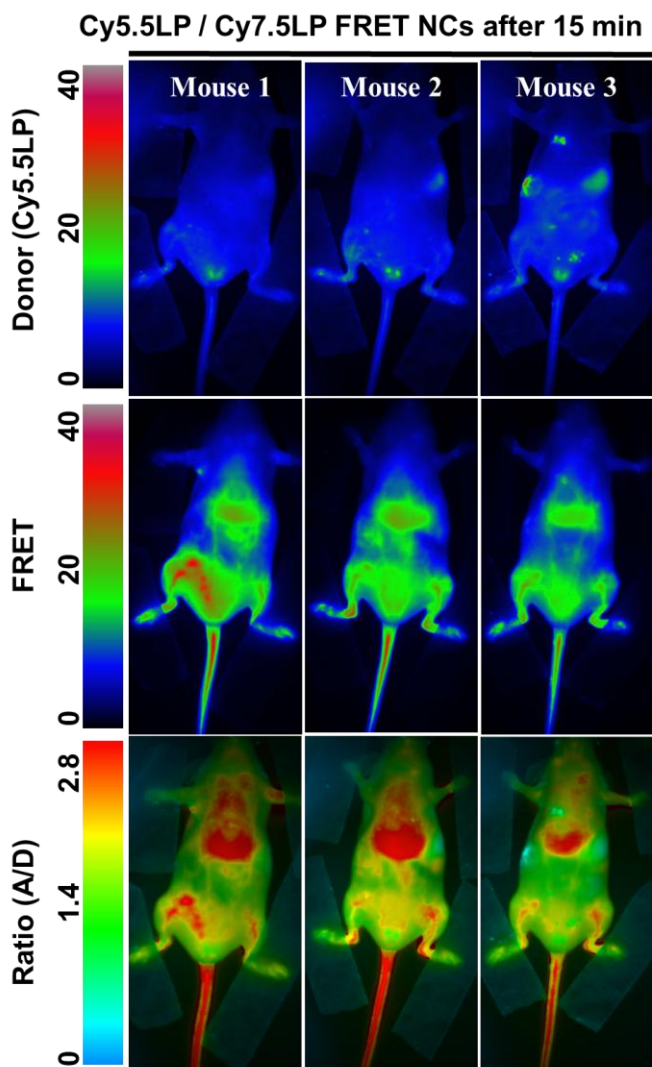
Figure S6. FRET imaging of three different healthy mice at 15 min after injection with NIR-FRET lipid nanocarriers. NCs contained 1% of donor Cy5.5LP and acceptor Cy7.5LP. Upper panels present intensity images of the Cy5.5LP channel (700 nm), middle panels present images of Cy7.5LP channel (840 nm), while the lower panels present ratiometric images (acceptor / donor).
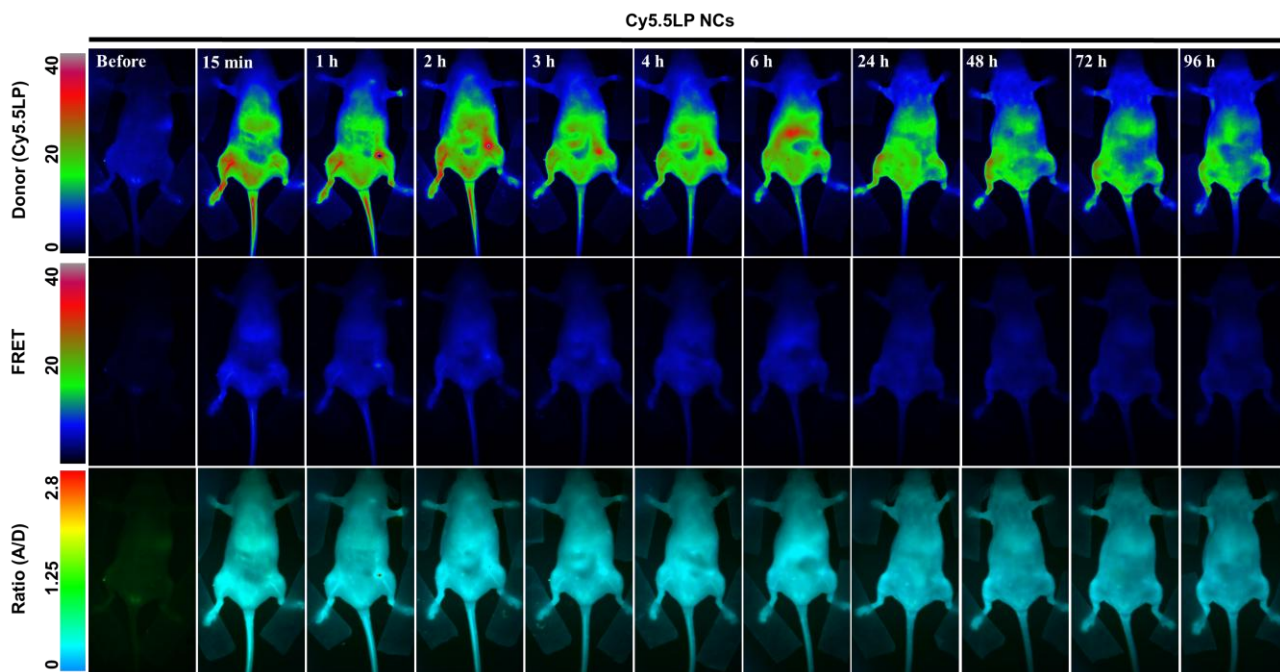
Figure S7. FRET imaging of healthy mice at different times after injected control lipid nanocarriers encapsulating only 1% of Cy5.5LP dye. Upper panels present intensity images of the Cy5.5LP channel (700 nm), middle panels present images of Cy7.5LP channel (840 nm), while the lower panels present ratiometric images (acceptor / donor).
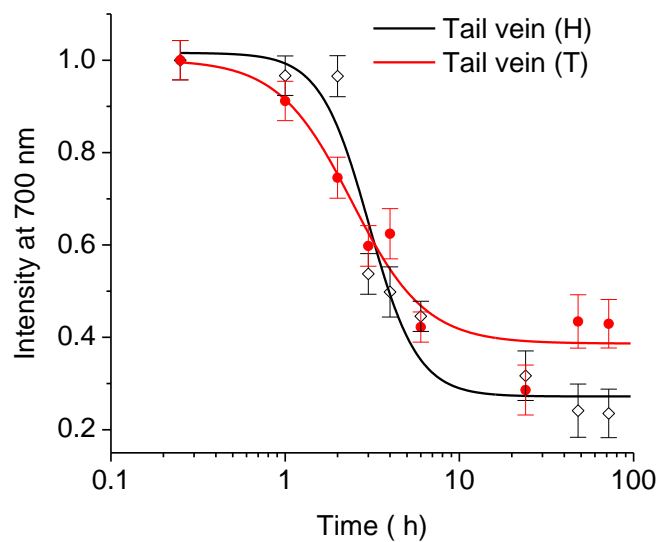
Figure S8. Decay of the fluorescence intensity of the control NCs (Cy5.5LP only) in tail vein of healthy (H) and tumor-bearing (T) mice.
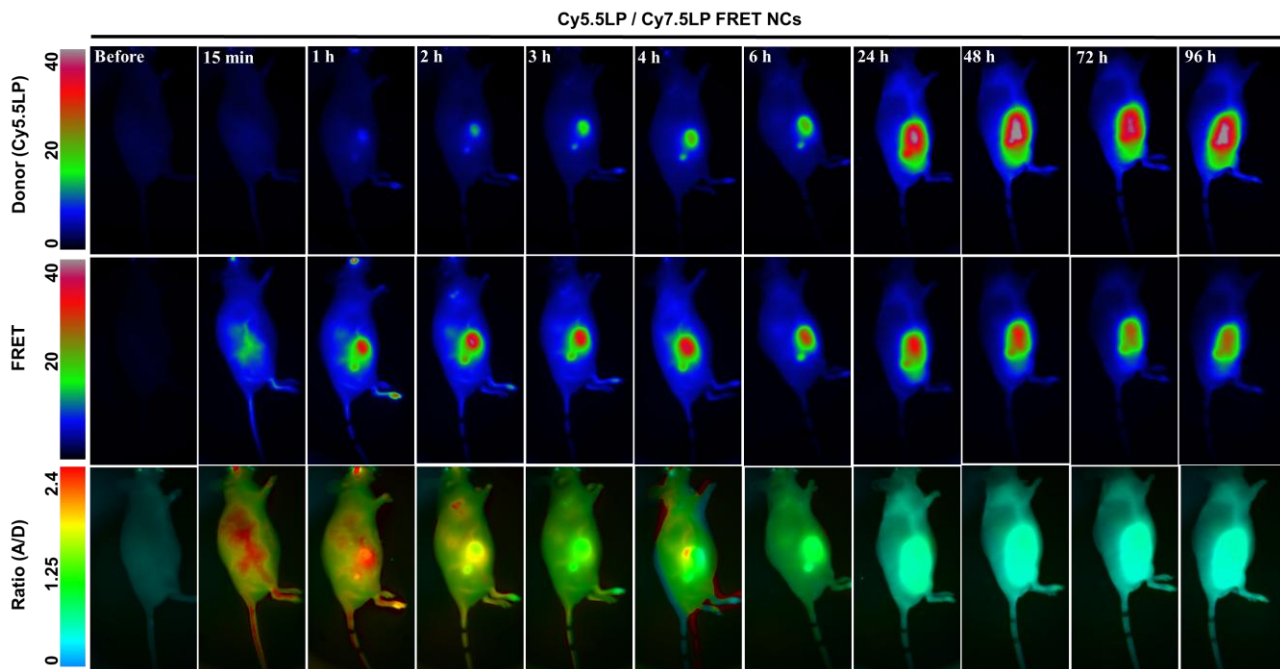
Figure S9. FRET imaging of tumor-bearing mice at different times after injection of FRET lipid nanocarriers. NCs contained 1% of donor Cy5.5LP and acceptor Cy7.5LP. Upper panels present intensity images of the Cy5.5LP channel (700 nm), middle panels present images of Cy7.5LP channel (840 nm), while the lower panels present ratiometric images (acceptor / donor).
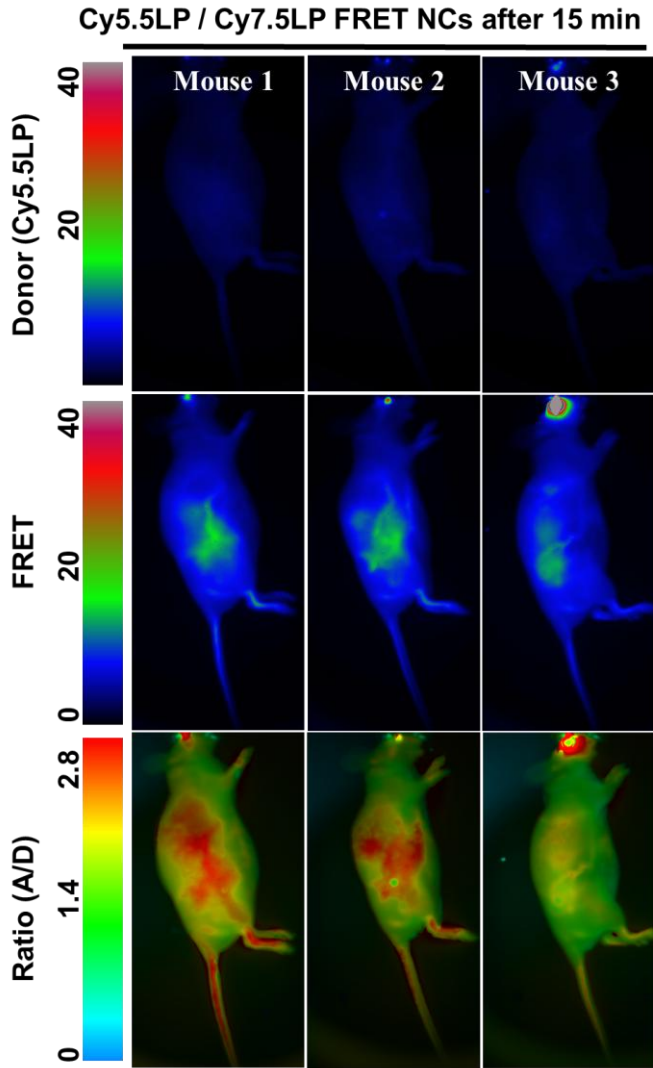
Figure S10. FRET imaging of tumor-bearing mice 15 min after injection with NIR-FRET lipid nanocarriers. NCs contained 1% of donor Cy5.5LP and acceptor Cy7.5LP. Upper panels present intensity images of the Cy5.5LP channel (700 nm), middle panels present images of Cy7.5LP channel (840 nm), while the lower panels present ratiometric images (acceptor / donor).
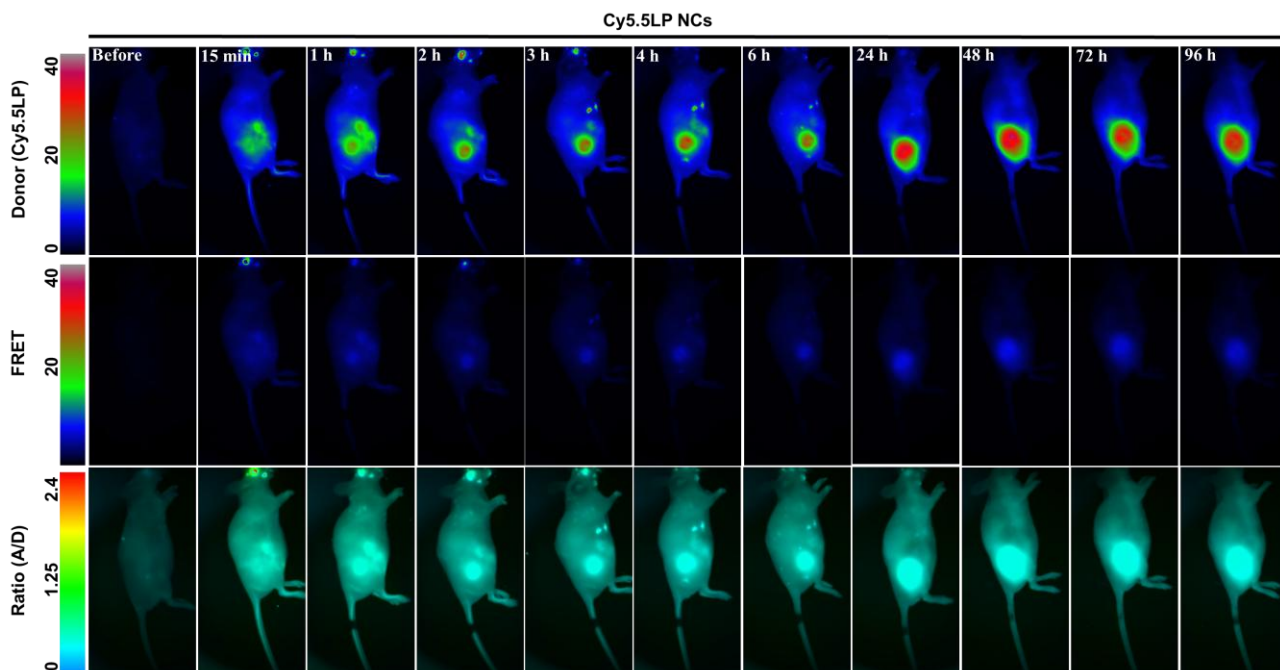
Figure S11. FRET imaging of tumor-bearing nude mice at different times after injected control lipid nanocarriers encapsulating only 1% of Cy5.5LP dye. Upper panels present intensity images of the Cy5.5LP channel (700 nm), middle panels present images of Cy7.5LP channel (840 nm), while the lower panels present ratiometric images (acceptor / donor).
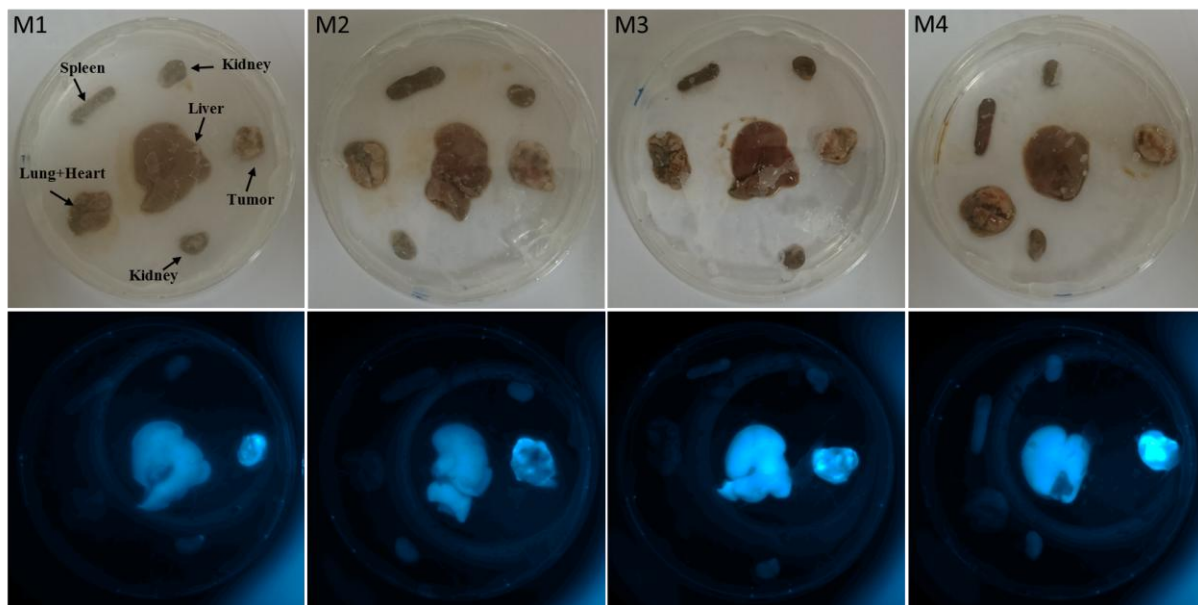
Figure S12. Ambient light photos (A) and NIR fluorescence images of organs of four mice injected with Cy5.5LP NCs 24h earlier. The excitation wavelength was 630 nm, while the emission was detected at 700 nm. Before the injection, NCs solution was diluted 1000-fold in PBS, similarly to all *in vivo* imaging experiments.

References

[1] Texier I, Goutayer M, Da Silva A, Guyon L, Djaker N, Josserand V, et al. Cyanine-loaded lipid nanoparticles for improved in vivo fluorescence imaging. J Biomed. Opt. 2009;14:054005.

2- Fluorescence correlation spectroscopy to study release from lipid nanocarriers (Publication-2)

In nanomedicine field, an optimal release of nanocarriers contents is considered as one of the critical steps in order to ensure an appropriate drug delivery. For that studying the release phenomena is an important challenge that needs to be addressed, with quantitative characterization techniques and methods, capable to operate directly *in situ* in complex biological media. As shown in the first project, FRET is a powerful approach to study integrity and release of cargo. Here, we looked for an alternative method that does not required double labelling of nanoacarriers.

The objective of this study is to develop a simple FCS-based technique for quantification of release from nanocarriers. To this end, we used lipid NCs (LNCs), so-called nanoemulsion droplets, encapsulating as a model cargo the hydrophobic Nile Red derivative NR668. We explored a possibility to study and quantify by FCS the release from LNCs of this model cargo in biological media.

In FCS setup, dye release should affect the LNCs brightness and the quantity of emissive species in solution. However, in this case, the fluorescence of released dye as well as the auto-fluorescence of the medium can alter the measurements of FCS. Starting from this problematic, we introduced fluorescent molecule, calcein, into an external medium, in order to provide us a background fluorescence that could model the emission of the released dye and/or of the autofluorescence of the medium. Two series of experiment were performed, in the first one we kept constant NR668 loading inside LNCs, but increased the calcein concentration, to mimic release of free dye associated with appearance of emissive species in the medium. In the second series, the NR668 loading inside LNCs was increased while keeping constant the concentration of calcein. This would mimic changes in the dye content in the LNCs because of dye leakage. Then, the following FCS parameters were studied: (i) brightness B and (ii) the number of emissive species N and (iii) standard deviation SD of signal fluctuation.

The results suggest that among FCS parameters, the number of fluorescent species N (which is generally used for this type of experiment) and the brightness per particles B are not suitable parameters for the release quantification, because they are affected by the molecules present in

medium in a nonlinear way. The only parameter, which appears useful for leakage quantification is standard deviation SD. It is independent from free small single molecules in solution and depends linearly on the dye content inside LNCs. However, SD value is not an absolute parameter, and would strongly depend on instrumental settings, as well as on the LNCs concentration. Therefore, we introduced a normalized parameter SD/SD_0, where SD_0 represents the standard deviation of signal fluctuation for the 1 wt% NR668 LNCs without any leakage. This new parameter is independent of LNCs concentration and laser power. The obtained dependence of SD/SD_0 was then used against NR668 dyes concentration inside LNCs, as a calibration curve after using linear fit (Figure 1).
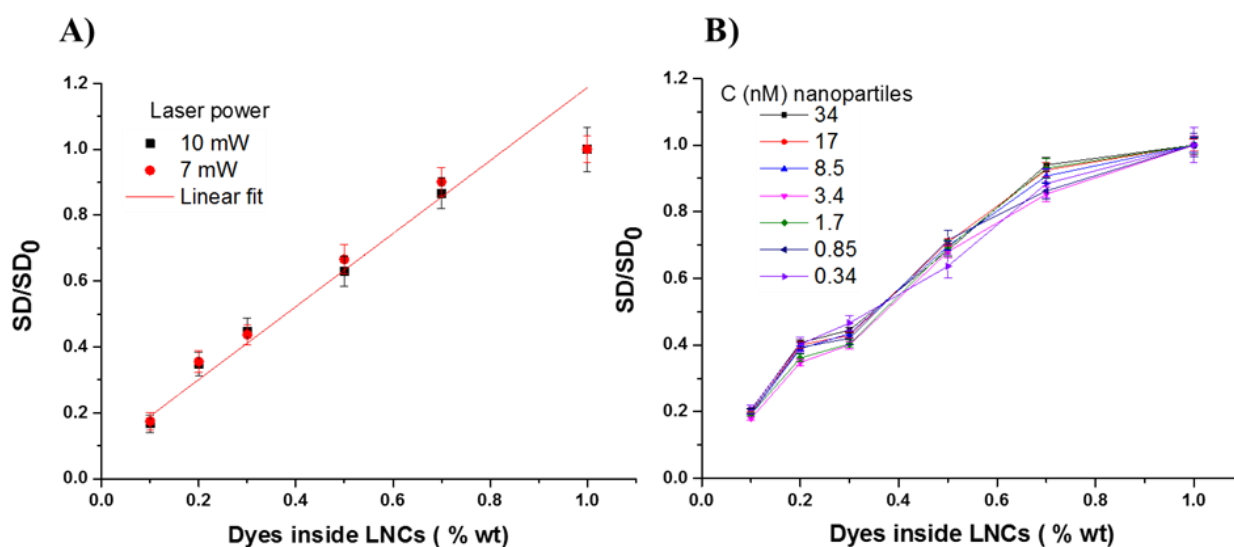
Figure 1. Normalisation of SD/SD0 and calibration. (A) the parameter SD/SD0 in function of NR668 inside LNCs, with laser power change. Calibration curve of SD/SD0 vs NR668 dyes concentration inside LNCs (B) the parameter SD/SD0 in function of NR668 inside LNCs, with variation in LNCs concentrations. Error bars represent the standard error of the mean (n=3).

Finally, a release experiment was performed by incubating 1 wt% NR668 LNCs at 20, 37 and 60°C in three different media: milliQ water, water in the presence of blank nanocarriers or with 10% FBS. The results show that LNCs are very stable in water, whereas in FBS medium, they release their content in a temperature-dependent manner. At 37°C, the release is relatively slow reaching 50% only after 6h of incubation.

This new method of quantification is simple, because it requires only detection of standard deviation of the signal fluctuation, without any analysis of auto-correlation curve. It can be applied for *in situ* release quantification from different nanocarriers.

The full description of the work can be found in the *manuscript* enclosed below.

Fluorescence correlation spectroscopy to study release from lipid nanocarriers

Redouane Bouchaala,[1,3] Ludovic Richert,[1] Nicolas Anton,[2] Thierry Vandamme,[2] Smail Djabi,[3] Yves Mély,[1] Andrey S. Klymchenko[1]

[1] CNRS UMR 7213, Laboratoire de Biophotonique et Pharmacologie, University of Strasbourg,74 route du Rhin, 67401 Illkirch Cedex, France.
[2] CNRS UMR 7199, Laboratoire de Conception et Application de Molécules Bioactives, University of Strasbourg,74 route du Rhin, 67401 Illkirch Cedex, France.
[3] Laboratory of Photonic Systems and Nonlinear Optics, Institute of optics and fine mechanics, University of Setif 1, 19000 Algeria.

Abstract

Understanding the drug release form nanocarriers is fundamental in the development of new effective nanomedicines. However, existing methods, notably dialysis frequently fails to quantifies release of molecules poorly soluble in water and it is not really adapted for in situ measurements in biological media. Here, we have developed a new methodology for quantifying release of fluorescent molecule from lipid nanocarriers (LNCs) using fluorescent correlation spectroscopy (FCS). LNCs, so-called nanoemulsion droplets, encapsulating as a model cargo, the hydrophobic Nile Red derivative NR668, were used as a testing system for release into model biological media. Our studies revealed that standard deviation of fluorescence fluctuation in FCS measurements depends linearly from the loading of the nanocarriers with the dye and it is insensitive to the presence of less bright molecular emissive species in solution. In sharp contrast, classical FCS parameters, such as number and brightness of emissive species are strongly influenced by fluorescence of molecular species in solution. Therefore, only standard deviation of fluorescence fluctuation can directly report on the nanocarriers dye loading without interferences from "parasite" fluorescence because of released dye or auto-fluorescence of the medium. Our method was validated using hydrophobic Nile Red dye, NR668, encapsulated into lipid nanoemulsion. The results suggest that LNCs remain intact in water, whereas in FBS medium, they release their content in a temperature-dependent manner. At 37°C, the release is relatively slow reaching 50% only after 6h of incubation. This method of quantification is simple, because it requires only detection of standard deviation of the signal, so that measurements can be done in principle without any analysis of auto-correlation curve.

Introduction

Nanocarriers technology in the last years gain a lot of interest, because of their possible application as a tools for drug delivery,[1,2] in vivo imaging and image-guided surgery.[3,4] These systems include polymer nanoparticles, lipid-based nanocarriers such as nanoemulsions, liposomes,[5] micelles as well as inorganic nanoparticles. The interest in the studies of the nanocarriers behaviour is increasing; a lot of research has been devoted to novel ways to characterise, fabricate, and explore their properties.[6] One of the most important properties is their ability to encapsulate hydrophobic or hydrophilic molecules, according to their composition and morphology.[7]

Optimal application of nanocarriers (NCs) in the drug delivery requires that the drug is maintained inside the nanocarriers until it reaches the target, such as a tumor, followed by controlled release of the drug inside the target. The most common method to study release of drugs from nanocarriers is dialysis.[8] However, it has limitations when applied to highly hydrophobic drugs poorly soluble in water,[9] and it cannot be really applied to study release directly in cells and animals. Other methods like size exclusion chromatography, continuous flow, flow cytometry were also used,[10] however, they have similar limitations as those of dialysis. Therefore, understanding drug release requires simple and effective assays capable to operate directly in situ in complex biological media. Forster resonance energy transfer (FRET) is the method of choice in this case. Several reports have already shown a strong potential of FRET to study release in biological liquids, cells and even in living animals.[11–15] However, this method requires double labelling of the nanocarriers (i.e. with donor and acceptor). Moreover, it is still challenging to achieve quantitative characterization of the cargo release using FRET-based methods, although some calibration-based approaches were suggested recently. [12]

A much less explored approach to study drug release is fluorescence correlation spectroscopy (FCS).[16] It is a powerful technique used in biological and biophysical research, [17,18] investigation of several fundamental processes like molecular diffusion[19] and interaction of biomolecules,[20,21] and (bio)chemical reaction kinetics,[22] with sensitivity reaching single-molecule level.[23] FCS is based on measuring the fluctuation of fluorescence intensity from emissive species across a small excitation focal volume. Autocorrelation analysis of the intensity provides us information about concentration, diffusion constant and brightness of the fluorescent particles. This technique serves as new tool to characterise nanoparticles specially for measuring size,[24] polydipersity,[25] and to evaluate stability of fluorescent nanoparticles.[26-27]

Also many research used FCS for characterisation of formation of protein corona on gold nanoparticles,[28,29] or interaction of human serum albumin with liposomes.[30] Very few studies shown the use of FCS to study release. Andersen et al used it for quantification of leakage of dyes from unilamellar lipid vesicles, [31] proposing a mathematical framework for the data analysis.

The aim of our studies is to develop a simple FCS-based technique for quantification of release from NCs. To this end, we selected lipid NCs (LNCs), so called nanoemulsion droplets. These systems are composed of substances generally considered as safe (GRAS) and therefore LNCs constitute a promising non-toxic platform for drug delivery.[32] However, the liquid nature of their core raises questions about their stability in vivo and capacity to maintain their cargo until the target. Our recent work as well as those of Texier group showed that LNCs can keep their contents even in vivo and accumulate in tumour in nearly intact form.[12] However, in these cases the cargo should be sufficiently hydrophobic to remain inside the LNCs in the presence of biological media.[11] Therefore, LNCs can be a suitable platform for encapsulation of hydrophobic drugs and contrast agents. In the present work, we explored a possibility to study by FCS release from LNCs of a model cargo, hydrophobic Nile Red derivative NR668. Different parameters of FCS, such as number and brightness of emissive species and standard deviation of the signal fluctuation, were studied as a function of dye loading and the degree of the dye release. Remarkably, only the standard deviation of the signal showed almost linear dependence on the degree of release of the dye with minimal perturbation by the fluorescent species outside of NCs. Here, we propose to use a very simple fluorescence parameter to monitor release of emissive cargo directly in situ in a complex biological context.

Result and discussion

Materials

All chemicals and solvents for synthesis were from Sigma Aldrich. Labrafac WL® (medium chain triglycerides) by Gattefossé (Saint-Priest, France). Kolliphor® HS15 (non-ionic surfactant) obtained from BASF (Ludwigshafen, Germany), Ultrapure water was obtained using a MilliQ® filtration system (Millipore, Saint-Quentin-en-Yvelines, France). Fetal bovine serum (FBS) was acquired from Lonza (Verviers, Belgium) and Gibco-Invitrogen (Grand Island, USA). Dihexylamino-2-(2-ethyl-hexyloxy)-benzo[a]phenoxazin-5- one (NR668) and 4'-Dioctylamino-3-octyloxyflavone (F888) were synthesized as described before.[11]

Formulation and characterisation of lipid nanocarriers LNCs

Dye-loaded nanoemulsions were prepared by spontaneous nano-emulsification.[33] We dissolved the dyes (NR668 or F888) in LabrafacWL® (35 mg) at concentrations of 1% by weight (unless indicated). Then, Kolliphor® HS15 was added (65mg), and the mixture was homogenized under magnetic stirring at 90 °C for 5 min up to complete homogenisation. Finally, nanoemulsions were generated with the addition of ultrapure (Milli-Q) water (230 mg). Size distributions were determined by dynamic light scattering using a Zetasizer Nano series DTS 1060 (Malvern Instruments S.A). In the DLS measurements statistics by volume was used.

Fluorescence spectroscopy

Fluorescence spectra were recorded on a Fluoromax 4 (Jobin Yvon, Horiba) spectrofluorometer. Fluorescence emission spectra were performed at room temperature with 520 nm excitation wavelengths for NR668 dye and 390 nm for F888 dye. Emissions spectra were corrected for lump fluctuations and for wavelength-dependent response of the detector. All fluorescence measurements were done using solutions with absorbance ≤0.1 at the wavelength of excitation.

FRET-based stability test

The stability with time of dyes inside lipid nanocarriers was estimated in three different temperatures 20°, 37°, 60°, by Forster resonance Energy transfer (FRET) between two encapsulated dyes, 0.5 % of F888 (with respect to Labrafac WL®) as energy donor and 0.5 % of NR668 as energy acceptor. The LNCs were diluted 1000 times from the original formulation and incubated in water and 10 % of blank nanocarriers (without encapsulated dyes). The donor in the nanocarriers was excited at 390 nm and the emission spectra were recorded for both donor and acceptor. The semi-quantitative parameter of FRET efficiency was calculated according to the following equation $E=A/(A+D)$,[34] where A and D are the maximum of fluorescence intensity of the acceptor and donor, respectively.

Fluorescence correlation spectroscopy (FCS) and data analysis

FCS measurements were performed on a two-photon platform based on an Olympus IX70 inverted microscope, as described previously. [11] Two-photon excitation at 830 nm (10 mW laser output power) was provided by a mode-locked Tsunami Ti: sapphire laser pumped by a Millenia V solid state laser (Spectra Physics). The measurements were realized in a 96 well plate, using a 200 mL volume per well. The focal spot was set about 20 µm above the coverslip. The

normalized autocorrelation function, G(t) was calculated online by an ALV-5000E correlator (ALV, Germany) from the fluorescence fluctuations, $\delta F(t)$, by $G(\tau) = <\delta F(t)\delta F(t + \tau)>/<F(t)>^2$ where $<F(t)>$. is the mean fluorescence signal, and t is the lag time. Assuming that lipid nanocarriers diffuse freely in a Gaussian excitation volume, the correlation function, $G(\tau)$, calculated from the fluorescence fluctuations was fitted according to Thompson [35] :

$$G(\tau) = \frac{1}{N}\left(1 + \frac{\tau}{\tau_d}\right)^{-1}\left(1 + \frac{1}{s^2}\frac{\tau}{\tau_d}\right)^{\frac{-1}{2}} \tag{1}$$

where τd is the diffusion time, N is the mean number of fluorescent species within the two-photon excitation volume, and S is the ratio between the axial and lateral radius of the excitation volume, B is the brightness par molecules and SD is the standard deviation of signal fluctuation. The excitation volume is about 0.34 fL and S is about 3 to 4. Typical data recording times were 5 min, using dye-loaded LNCs diluted 1: 10 000 from the originally prepared LNCs. Using 6-carboxytetramethylrhodamine (TMR from Sigma-Aldrich) in water as a reference, the hydrodynamic diameter, d, of nanocarriers (LNCs) was calculated as: $d(LNCs) = \tau d(LNCs) / \tau d(TMR) \times d(TMR)$, where d(TMR) is a hydrodynamic diameter of TMR (1.0 nm). Concentration of NCs, C(LNCs), was calculated from the number of species by: $C(LNCs) = N(LNCs)/N(TMR)\times C(TMR)$, where N(LNCs) and N(TMR) are observed number of emissive species for LNCs and TMR samples, respectively and C(TMR) is concentration of TMR (50 nM). The data were obtained based on 20 recorded correlation curves; the recording time for each curve was 10 s for LNCs and 30 s for TMR.

FCS calibration

The calibration of FCS parameters for in situ release quantification were done by measurement of SD, N and B for two different mixing systems. The first one was 1% NR668 LNCs and different concentration of free calcein dyes (0.1, 0.2, 0.5, 1, 2 and 3.6 µM). The second system is mixture between fixed concentration of calcein (0.2 µM) and variable concentration of NR668 inside LNCs (0.1%, 0.2% ,0.4%, 0.6%, 0.8%, 1%). Then obtained values of the SD were normalised with the expression of SD/SD_0, where SD_0 is the standard deviation of initial particles without leakage (1% wt NR668 LNCs). SD/SD_0 was plotted vs % NR668 inside LNCs and the data were fitted with a linear function y=A+B*x where $a = 0.08803$; $b = 0.96141$; y is SD/SD_0 and x is dye content inside LNCs (wt%).

Dye release studies

The release of the NR668 dyes was studied by FCS. Dye-loaded LNCs were diluted 10 000 fold (~1.7 nM) to three different media: water, blank nanocarriers at 1000-fold dilution (10-fold excess with respect to dye-loaded droplets) or 10 % of foetal bovine serum (FBS) in water. Then, samples were incubated at three different temperatures 20, 37, 60°C, for 0.5, 1, 2, 4, and 6 h. SD was measured as a function of time and then converted into SD/SD_0 to obtain quantitative data on the dye release.

Results and discussions

We first wanted to find conditions at which the content of LNCs is released as a function of time. To this end we used FRET, which is a well-established technique for studying stability of nanocarriers. FRET was used to follow the integrity of different nanoparticles in vivo, such as polymeric micelles [13], LNCs[11,12,14,36] and HDL.[37] It acts like a molecular ruler [38] to monitor the proximity between the fluorophores inside LNCs, so that FRET is lost as soon as the dyes are released from the nanocarriers and diluted into the medium. In our case, NR668 was an energy acceptor, while another highly hydrophobic dye F888 was chosen as an energy donor, as shown in our earlier report.[11] Nanoemulsion droplets prepared by spontaneous emulsification showed hydrodynamic diameter of 34 nm and good polydispersity (<0.1) according to DLS. The presence of the dyes did not affect the polydispersity and the size of LNCs. The increase in the loading of the FRET pair resulted in the growth of the relative intensity of the acceptor emission, which is an indication of FRET (Fig 1-A). The highest relative FRET efficiency (~0.75) was obtained for the LNCs with 0.5 wt% of F888 and NR668. This formulation was selected for the release studies.
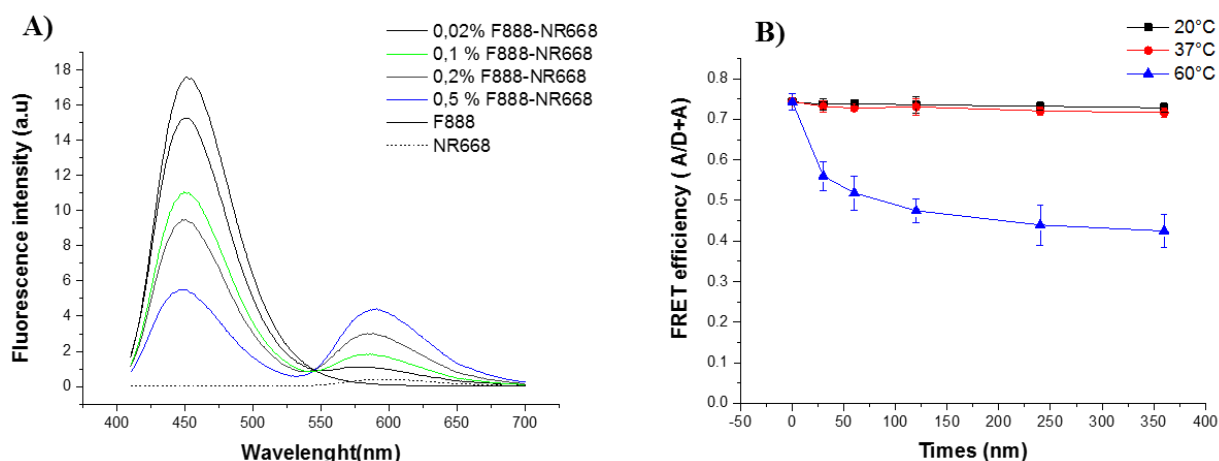
Fig. 1 – (A) Fluorescence spectra of FRET NCs at different concentrations of donor (F888) and acceptor (NR668), encapsulated at a 1: 1 molar ratio. The black solid line corresponds to LNCs containing only the donor. The fluorescence spectra were recorded at 390 nm excitation wavelength. The dotted line corresponds to direct excitation of the acceptor (NR668) at 390 nm. (B) Relative FRET efficiency (A/(D+A)) as a function of time, for a mixture of LNCs (0.5 wt% F888-NR668) and 10-fold excess of blank LNCs for three different temperatures 20, 37 and 60 °C. Error bars represent the standard error of the mean (n = 3).

The release experiments were performed in 10-time excess of blank LNCs, which was our model of the recipient medium for hydrophobic dye molecules. This mixture was incubated at 3 different temperatures (20, 37 and 60°C) and the relative FRET efficiency was measured after 0.5, 1, 2, 4, and 6 h of incubation. As shown in fig 1-B, at 20 and 37°C the FRET efficiency did not change even after 6 h, but at 60°C we observed a decrease in the FRET efficiency already after the first 30 min and continued decreasing within 6h of the experiment. This decline is due to increasing of the distance between the donor and acceptor, which necessary implies that there is a dyes release from our FRET LNCs. These data show that our LNCs can retain the cargo dyes in the release medium even at 37°C at least for 6 h, which is in line with our earlier report realized in serum.[11] Moreover, we found that 60°C is a nice model conditions generating dye release on the time scale of hours. However, it is hard to directly connect FRET efficiency with degree of dyes leakage, unless a dedicated model and corresponding calibrations are realized.

Having set up our model release system, we then explored a possibility to quantify the release using FCS measurements. Since dyes release should affect the nano-droplet brightness and the quantity of emissive species in solution,[27] FCS appears as an promising method to quantify the dye release. Following this logic, the release of hydrophobic dye into the recipient medium should result in the increase in the number of emissive species and decrease in the particle

brightness, as we showed in our earlier work.[11] However, the problem comes when we do not know much about the biological medium, where the dye is released. In this case, the fluorescence of released dye as well as the auto-fluorescence of the medium can alter the measurements of FCS. Therefore, we introduced fluorescent molecule, calcein, into an external medium. It is highly soluble and should provide us a background fluorescence that could model the emission of the released dye and/or of the autofluorescence of the medium. In one series of experiments, we kept constant NR668 loading, but increased the calcein concentration, whereas in the second series, the NR668 loading was increased while keeping the constant concentration of calcein. Increase in the concentration of calcein would mimic release of free dye associated with appearance of emissive species in the medium, while increase in the NR668 loading would mimic changes in the dye content in the LNCs because of dye leakage. To realize FCS measurements, two photon excitation at 830 nm and the emission was collected all over the whole visible spectrum, so that fluorescence signal from NR668 and calcein could be recorded. The following FCS parameters were studied: (i) brightness (B), (ii) the number of emissive species (N) and (iii) standard deviation (SD) of signal fluctuation.

As shown in figure 2A, B, the increase in the calcein concentration increased the N value, but decreased the B value. This was expected because, higher concentrations of calcein should imply increase in the number of emissive species. Moreover, as LNCs containing large number of NR668 are much brighter than single calcein molecules (~74 times brighter according to the FCS measurement of brightness per particles at 10 mW-830 nm of illumination), the increase in the number of less bright species decreased the overall brightness per particle. Remarkably, SD parameter remained unchanged in the broad concentration range of calcein. This parameter did not change probably because again LNCs being much brighter than calcein was the main source of the light fluctuation totally controlling the SD value. On the other hand, SD value showed almost liner dependence on the increase in the NR668 dye loading. Brightness also increased with NR668 loading, although the dependence was clearly not linear with very slow increase at low NR668 loadings followed by faster increase at higher loadings. Remarkably, the number of emissive species showed a complicated behaviour: it rapidly decreased at low dye loadings and then decreased much slower at higher loadings. These complex behaviours of B and N parameters is because at very low dye loading, the contribution of the calcein emission to the auto-correlation curve is still important, increases the overall N values, but decreases B. At higher loading, LNCs become much brighter than calcein, so that start dominating the fluctuation analysis. Nevertheless, even at the highest loading the N and B parameters in the

presence of 0.2 µM calcein were quite different from those for LNCs in miliQ water, whereas SD showed practically the same values for these two conditions (Fig. 2).
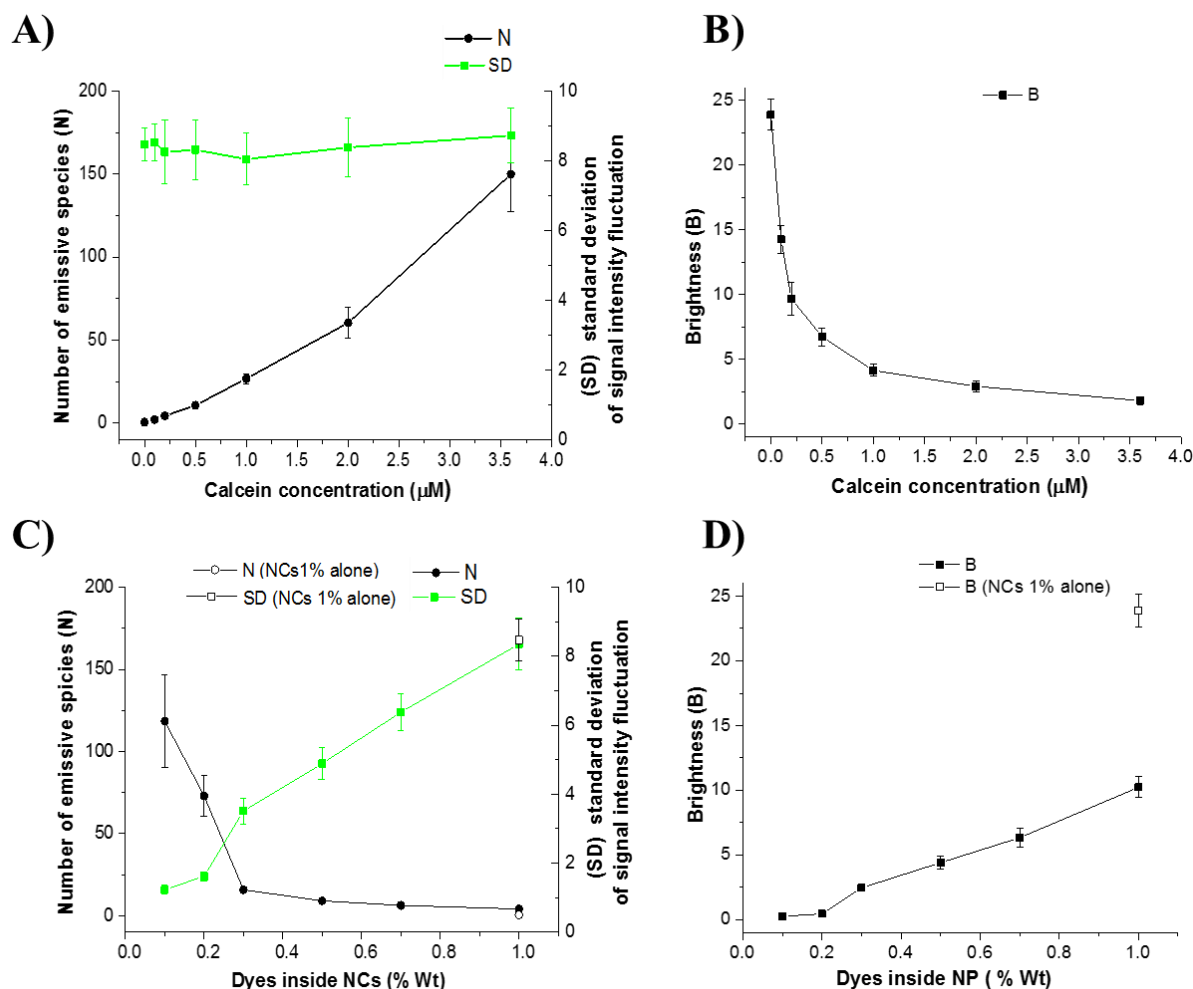
Fig. 2. Signal fluctuation standard deviation and classical FCS parameters recorded for dye-loaded NCs in the presence of calcein in the solution. (A) Emissive species number N and standard deviation SD, as a function of calcein concentration, for a mixture in water of 1 wt% NR668 LNCs diluted 10000 times with different concertation of calcein. (B) Brightness B in function of calcein concentration. (C) Emissive specie number N and standard deviation SD, as a function of NR668 concentration inside LNCs. LNCs are diluted 10000 times in water containing 0.2 µM calcein. (D) Brightness B as a function of NR668 concentration inside LNCs. Error bars represent the standard error of the mean (n = 3). The empty symbols in (C) and (D) represent the parameter N, SD and B for LNCs (NR668) in water.

These two experiments, which model the release of dyes from LNCs suggest that B and N are not suitable parameters for the release quantification, because they are affected by the molecules present in medium with nonlinear way. The only parameter, which appear useful for leakage

quantification is SD. Indeed, it is only affected by the change in the dye content insight bright LNCs, but is practically independent from free small single molecules of calcein in solution, which are much less bright than single LNCs. This means that SD can directly indicate the dye content in LNCs without being influenced by fluorescence of the liberated dye.

However, SD value is not an absolute parameter, and would strongly depend on instrumental settings, such as laser power and instrumental alignment as well as on the LNCs concentration. Therefore, we introduced a normalized parameter SD/SD_0, where SD_0 represent the standard deviation of signal fluctuation for the 1% NR668 LNCs without any leakage. The dependence of SD/SD_0 parameter on the NR668 loading content was verified for different laser powers and concentrations of LNCs.

Thus, dyes-loaded LNCs with different NR668 concentration was measured by FCS setup in function of two laser powers: 7 and 10 mW. Moreover, the same measurements were performed in function of nanocarriers concentration. As shown in the figure 3 (A and B), the parameter SD/SD_0 was not affected by change in the laser power or nanoparticles concentration, showing that it is a robust parameter. The obtained dependence of SD/SD_0 was then then used as a calibration curve after using linear fit (Fig 3-A). It needs to be mentioned that the LNCs point at 1 wt% in fig 3-A is a little deviated from the fit, probably due to some self-quenching of the dyes at the highest loading.
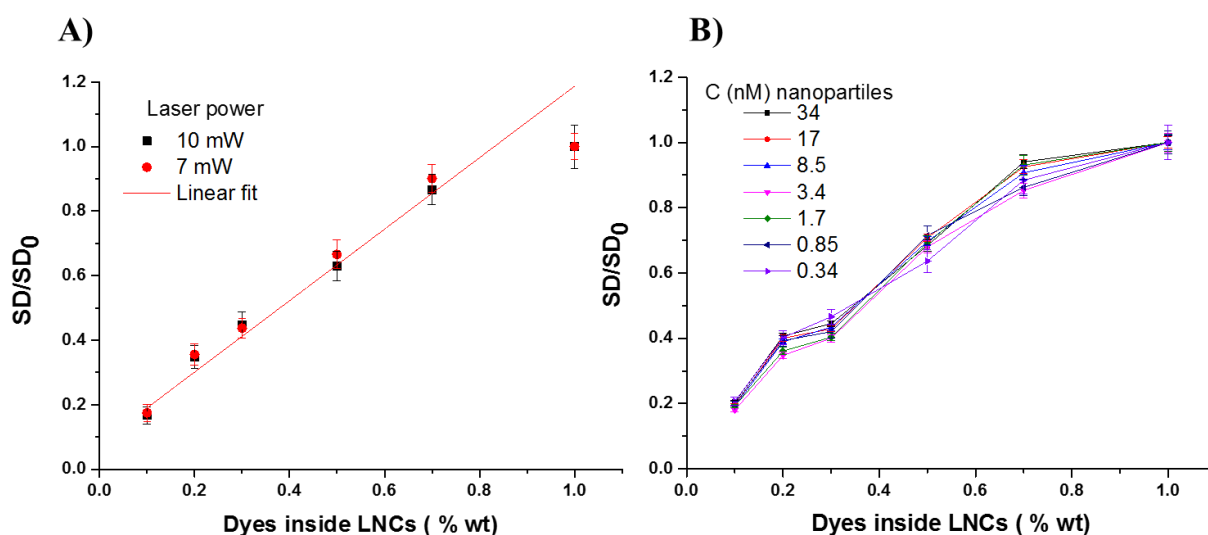
Fig. 3. Normalised parameter SD/SD_0 and its dependence on the dye content inside LNCs. (A) The parameter SD/SD_0 as a function of NR668 inside LNCs, using two different two-photon excitation powers. Linear fit for the obtained data. (B) The parameter SD/SD_0 as a function of NR668 inside LNCs, with variation in LNCs concentrations. Error bars represent the standard error of the mean (n=3).

Then a release experiment was performed by incubating 1 wt% NR668 LNCs at 20, 37 and 60°C in three different media: water alone, in the presence of blank nanocarriers or with 10% FBS.
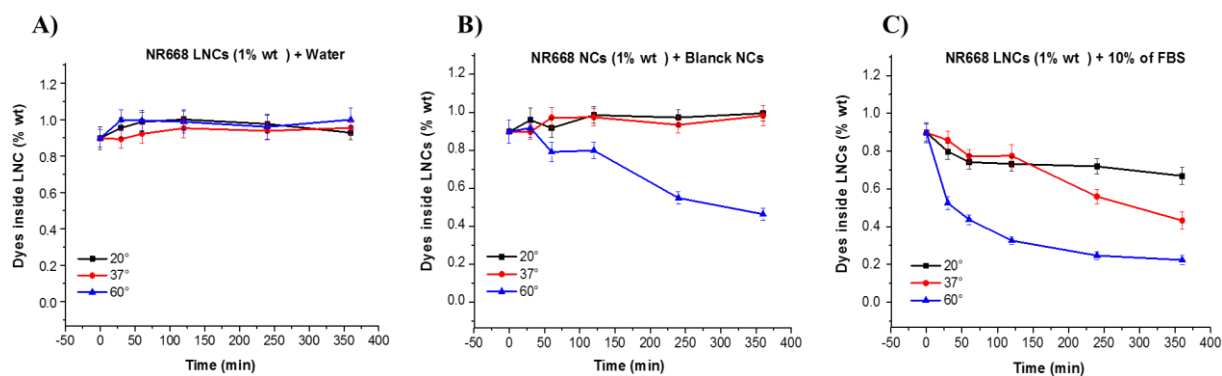
Fig. 4. Quantification of release from 1 % (wt.) dyes LNCs in different media at three different temperatures (20° -37°- 60°) (A) in presence of water. (B) in presence of water and Blank LNCs. (C) in presence of water and 10% FBS. Error bars represent the standard error of the mean (n=3).

Within the course of incubation, NR668 LNCs were very stable in water and there was no release even at 60 °C, because NR668 is very hydrophobic and cannot be released into neat water. In the presence of blank LNCs or FBS, capable to solubilize NR668, we observed the dye release at 60°C with approximatively 50 and 75% release for blank LNCs and FBS, respectively. At 37°C, the dye release was observed only for FBS medium with nearly 50% release after 6h. The results observed in blank LNCs is perfectly in line with our FRET data showing dye release exclusively at 60°C. However, in contrast to our FRET data, our methodology based on FCS enabled quantitative description of the dye release with only one type of dye pay loaded.

Conclusion

In summary, we have developed a new methodology for quantifying release of fluorescent dye from lipid nanocarriers. This assay is based on standard deviation parameter measured by fluorescent correlation spectroscopy. A proof of concept was validated using hydrophobic Nile Red dye, NR668, encapsulated into lipid nanoemulsion. The results suggest that LNCs remain intact in water, whereas in FBS medium, they release their content in a temperature-dependent manner. At 37°C, the release is relatively slow reaching 50% only after 6h of incubation. This method of quantification is simple, because it requires only detection of standard deviation of

the signal. This means that the recording can be done in principle without any analysis of auto-correlation curve. Therefore, we expect this method could be further extended to basic confocal microscopes, where the release kinetics could be directly followed by recording signal fluctuation in the focal spot.

References

(1)   Wei, X.; Wang, Y.; Xiong, X.; Guo, X.; Zhang, L.; Zhang, X.; Zhou, S. Codelivery of a π-π Stacked Dual Anticancer Drug Combination with Nanocarriers for Overcoming Multidrug Resistance and Tumor Metastasis. *Adv. Funct. Mater.* **2016**.

(2)   Torchilin, V. P. Multifunctional, Stimuli-Sensitive Nanoparticulate Systems for Drug Delivery. *Nat. Rev. Drug Discov.* **2014**, *13*, 813–827.

(3)   Hill, T. K.; Abdulahad, A.; Kelkar, S. S.; Marini, F. C.; Long, T. E.; Provenzale, J. M.; Mohs, A. M. Indocyanine Green-Loaded Nanoparticles for Image-Guided Tumor Surgery. *Bioconjug. Chem.* **2015**, *26*, 294–303.

(4)   Hill, T. K.; Mohs, A. M. Image-Guided Tumor Surgery: Will There Be a Role for Fluorescent Nanoparticles? *Wiley Interdiscip. Rev. Nanomedicine Nanobiotechnology* **2016**, *8*, 498–511.

(5)   Pattni, B. S.; Chupin, V. V.; Torchilin, V. P. New Developments in Liposomal Drug Delivery. *Chem. Rev.* **2015**, *115*, 10938–10966.

(6)   Tang, L.; Yang, X.; Yin, Q.; Cai, K.; Wang, H.; Chaudhury, I.; Yao, C.; Zhou, Q.; Kwon, M.; Hartman, J. a.; *et al.* Investigating the Optimal Size of Anticancer Nanomedicine. *Proc. Natl. Acad. Sci.* **2014**, *111*, 15344–15349.

(7)   Zhao, Y.; Fay, F.; Hak, S.; Manuel Perez-Aguilar, J.; Sanchez-Gaytan, B. L.; Goode, B.; Duivenvoorden, R.; de Lange Davies, C.; Bjørkøy, A.; Weinstein, H.; *et al.* Augmenting Drug-Carrier Compatibility Improves Tumour Nanotherapy Efficacy. *Nat. Commun.* **2016**, *7*, 11221.

(8)   Modi, S.; Anderson, B. D. Determination of Drug Release Kinetics from Nanoparticles: Overcoming Pitfalls of the Dynamic Dialysis Method. *Mol. Pharm.* **2013**, *10*, 3076–3089.

(9)   Abouelmagd, S. A.; Sun, B.; Chang, A. C.; Ku, Y. J.; Yeo, Y. Release Kinetics Study of Poorly Water-Soluble Drugs from Nanoparticles: Are We Doing It Right? *Mol. Pharm.* **2015**, *12*, 997–1003.

(10)   Snipstad, S.; Hak, S.; Baghirov, H.; Sulheim, E.; Mørch, Ý.; Lélu, S.; von Haartman, E.; Bäck, M.; Nilsson, K. P. R.; Klymchenko, A. S.; *et al.* Labeling Nanoparticles: Dye Leakage and Altered Cellular Uptake. *Cytom. Part A* **2016**.

(11)   Klymchenko, A. S.; Roger, E.; Anton, N.; Anton, H.; Shulov, I.; Vermot, J.; Mely, Y.; Vandamme, T. F. Highly Lipophilic Fluorescent Dyes in Nano-Emulsions: Towards Bright Non-Leaking Nano-Droplets. *RSC Adv.* **2012**, 11876–11886.

(12)   Bouchaala, R.; Mercier, L.; Andreiuk, B.; Mély, Y.; Vandamme, T.; Anton, N.; Goetz, J. G.; Klymchenko, A. S. Integrity of Lipid Nanocarriers in Bloodstream and Tumor Quantified by near-Infrared Ratiometric FRET Imaging in Living Mice. *J. Control. Release* **2016**, *236*,

57–67.

(13)   Morton, S. W.; Zhao, X.; Quadir, M. A.; Hammond, P. T. FRET-Enabled Biological Characterization of Polymeric Micelles. *Biomaterials* **2014**, *35*, 3489–3496.

(14)   Gravier, J.; Sancey, L.; Hirsjärvi, S.; Rustique, E.; Passirani, C.; Benoît, J. P.; Coll, J. L.; Texier, I. FRET Imaging Approaches for in Vitro and in Vivo Characterization of Synthetic Lipid Nanoparticles. *Mol. Pharm.* **2014**, *11*, 3133–3144.

(15)   Zhao, Y.; van Rooy, I.; Hak, S.; Fay, F.; Tang, J.; Davies, C. de L.; Skobe, M.; Fisher, E. A.; Radu, A.; Fayad, Z. A.; *et al.* Near-Infrared Fluorescence Energy Transfer Imaging of Nanoparticle Accumulation and Dissociation Kinetics in Tumor-Bearing Mice. *ACS Nano* **2013**, *7*, 10362–10370.

(16)   Digman, M. A.; Gratton, E. Lessons in Fluctuation Correlation Spectroscopy. *Annu. Rev. Phys. Chem.* **2011**, *62*, 645–668.

(17)   Pramanik, A.; Widengren, J.; Pramanik, A.; Widengren, J. Fluorescence Correlation Spectroscopy (FCS). In *Encyclopedia of Molecular Cell Biology and Molecular Medicine*; Wiley-VCH Verlag GmbH & Co. KGaA: Weinheim, Germany, 2006.

(18)   Macháň, R.; Wohland, T. Recent Applications of Fluorescence Correlation Spectroscopy in Live Systems. *FEBS Lett.* **2014**, *588*, 3571–3584.

(19)   Schwille, P.; Haupts, U.; Maiti, S.; Webb, W. W. Molecular Dynamics in Living Cells Observed by Fluorescence Correlation Spectroscopy with One- and Two-Photon Excitation. *Biophys. J.* **1999**, *77*, 2251–2265.

(20)   González Bardeci, N.; Angiolini, J. F.; De Rossi, M. C.; Bruno, L.; Levi, V. Dynamics of Intracellular Processes in Live-Cell Systems Unveiled by Fluorescence Correlation Microscopy. *IUBMB Life* **2017**, *69*, 8–15.

(21)   Li, X.; Xing, J.; Qiu, Z.; He, Q.; Lin, J. Quantification of Membrane Protein Dynamics and Interactions in Plant Cells by Fluorescence Correlation Spectroscopy. *Mol. Plant* **2016**, *9*, 1229–1239.

(22)   Abdollah-Nia, F.; Gelfand, M. P.; Van Orden, A. Artifact-Free and Detection-Profile-Independent Higher-Order Fluorescence Correlation Spectroscopy for Microsecond-Resolved Kinetics. 2. Mixtures and Reactions. *J. Phys. Chem. B* **2017**, *121*, 2388–2399.

(23)   Ries, J.; Schwille, P. Fluorescence Correlation Spectroscopy. *BioEssays* **2012**, *34*, 361–368.

(24)   Dominguez-Medina, S.; Chen, S.; Blankenburg, J.; Swanglap, P.; Landes, C. F.; Link, S. Measuring the Hydrodynamic Size of Nanoparticles Using Fluctuation Correlation Spectroscopy. *Annu. Rev. Phys. Chem.* **2016**, *67*, 489–514.

(25)   Pal, N.; Verma, S. D.; Singh, M. K.; Sen, S. Fluorescence Correlation Spectroscopy: An Efficient Tool for Measuring Size, Size-Distribution and Polydispersity of Microemulsion Droplets in Solution. *Anal. Chem.* **2011**, *83*, 7736–7744.

(26)   Reisch, A.; Runser, A.; Arntz, Y.; Mély, Y.; Klymchenko, A. S. Charge-Controlled Nanoprecipitation as a Modular Approach to Ultrasmall Polymer Nanocarriers: Making Bright and Stable Nanoparticles. *ACS Nano* **2015**, *9*, 5104–5116.

(27)   Bouchaala, R.; Anton, N.; Anton, H.; Vandamme, T.; Vermot, J.; Smail, D.; Mély, Y.; Klymchenko, A. S. Light-Triggered Release from Dye-Loaded Fluorescent Lipid Nanocarriers in Vitro and in Vivo. *Colloids Surfaces B Biointerfaces* **2017**, *156*, 414–421.

(28)   Klapper, Y.; Maffre, P.; Shang, L.; Ekdahl, K. N.; Nilsson, B.; Dries, M.; Gerthsen, D.; Nienhaus, G. U.; Hettler, S.; Dries, M.; *et al.* Low Affinity Binding of Plasma Proteins to Lipid-Coated Quantum Dots as Observed by in-Situ Fluorescence Correlation Spectroscopy. *Nanoscale* **2015**, *7*, 9980–9984.

(29)   Nienhaus, G. U.; Maffre, P.; Nienhaus, K. Chapter Four – Studying the Protein Corona on Nanoparticles by FCS. In *Methods in Enzymology*; 2013; Vol. 519, pp. 115–137.

(30)   Kristensen, K.; Urquhart, A.; Thormann, E.; Andresen, T. Binding of Human Serum Albumin to PEGylated Liposomes: Insights into Binding Numbers and Dynamics by Fluorescence Correlation Spectroscopy. *Nanoscale* **2016**.

(31)   Kristensen, K.; Henriksen, J. R.; Andresen, T. L. Quantification of Leakage from Large Unilamellar Lipid Vesicles by Fluorescence Correlation Spectroscopy. *Biochim. Biophys. Acta - Biomembr.* **2014**, *1838*, 2994–3002.

(32)   Anton, N.; Benoit, J. P.; Saulnier, P. Design and Production of Nanoparticles Formulated from Nano-Emulsion Templates-A Review. *J. Control. Release* **2008**, *128*, 185–199.

(33)   Huynh, N. T.; Passirani, C.; Saulnier, P.; Benoit, J. P. Lipid Nanocapsules: A New Platform for Nanomedicine. *Int. J. Pharm.* **2009**, *379*, 201–209.

(34)   Preus, S.; Wilhelmsson, L. M. Advances in Quantitative FRET-Based Methods for Studying Nucleic Acids. *ChemBioChem* **2012**, *13*, 1990–2001.

(35)   Thompson, N. L. Fluorescence Correlation Spectroscopy. In *Topics in Fluorescence Spectroscopy*; Kluwer Academic Publishers: Boston, 2002; pp. 337–378.

(36)   Lainé, A. L.; Gravier, J.; Henry, M.; Sancey, L.; Béjaud, J.; Pancani, E.; Wiber, M.; Texier, I.; Coll, J. L.; Benoit, J. P.; *et al.* Conventional versus Stealth Lipid Nanoparticles: Formulation and in Vivo Fate Prediction through FRET Monitoring. *J. Control. Release* **2014**, *188*, 1–8.

(37)   Skajaa, T.; Zhao, Y.; Van Den Heuvel, D. J.; Gerritsen, H. C.; Cormode, D. P.; Koole, R.; Van Schooneveld, M. M.; Post, J. A.; Fisher, E. A.; Fayad, Z. A.; *et al.* Quantum Dot and Cy5.5 Labeled Nanoparticles to Investigate Lipoprotein Biointeractions via F??rster Resonance Energy Transfer. *Nano Lett.* **2010**, *10*, 5131–5138.

(38)   Wu, M.; Algar, W. R. Concentric Förster Resonance Energy Transfer Imaging. *Anal. Chem.* **2015**, *87*, 8078–8083.

3- Encapsulation and release of molecules in lipid and polymer nanocarriers evaluated by chemical bleaching

Nanocarriers are promising tools for drug delivery, due to their ability to cross the biological barriers, as well as their drug release properties and targeting. In addition, drugs loaded in nanocarriers can be protected from external degradation, besides having their toxicity reduced and efficacy increased.

Lipid and polymeric nanocarriers are composed of biodegradable materials and were extensively investigated as delivery systems in nanomedicine. Their structures give them diverse properties as drug delivery systems in therapeutics. However, for better optimization and selection of the right carriers, we need to provide answers to some important questions concerning nanocarriers and cargos:

- Capacity of the nanocarriers to encapsulate hydrophobic molecules with different level of hydrophobicity.
- Efficiency of the molecule entrapment and repartition among the nanocarriers.
- Effect of the nanocarriers nature, matrix, size and preparation method on the molecule repartition and encapsulation.
- The diffusion of the active molecules inside the nanocarriers.

Addressing these problems could give us information about the stability of these nanocarriers in biological medium, their release rates and profiles and the presence of the burst release phenomena. Moreover, understanding the physical nature of the nanocarriers core (solid or liquid?) is important to predict kinetics of encapsulated molecules release.

In the present work, we tried to answer these questions using different lipid and polymeric nanocarriers. Two dyes were used as a model of drugs: Nile Red and its more hydrophobic version NR668. In drug delivery research, Nile Red has been used and discussed as a model of hydrophobic drug to evaluate the solubilisation and the encapsulation inside nanoparticles [316,317]. Nile Red is highly emissive, displaying solvatochromic properties. It contains a quinoid fragment, which is a potential target for reduction by sodium dithionite $Na_2S_2O_4$ [9].

Based on the reaction of Nile Red bleaching by sodium dithionite $Na_2S_2O_4$, we have developed a technique that can inform us about the physical state of the nanocarriers and the level of encapsulation of the fluorophore (their accessibility). This technique is based on the bleaching of the fluorophore Nile Red (NR) and its hydrophobic analogue (NR668) by sodium dithionite, which bleaching results in a fluorescence inhibition (Figure 1).

Five different lipid and polymer nanocarriers were formulated with NR and NR668 dyes. Nanoemulsion and solid lipid nanoparticles were generated by the spontaneous emulsification of dye-loaded oil (NR 0.2 wt% or NR668 0.5 wt%) and non-ionic surfactant (Kolliphor® HS 15), giving rise to fluorescent PEGylated nanocarriers. Labrafac® oil and Suppocire C ® wax was used for nanoemulsion and solid lipid nanoparticles respectively. PLGA (poly (lactic-co-glycolic acid) and PMMA-MA (poly (methyl methacrylate-co-methacrylic acid)) nanocarriers were obtained through nanoprecipitation of an acetonitrile solution of the polymers and the dyes (NR 0.5 wt% or NR668 0.5 wt% with respect to the polymer) in aqueous phosphate buffer. For PLGA nanocarriers, the pH of the phosphate buffer used was 7.4 and 3.4 to obtain two different sizes. For PMMA-MA pH values used were 7.4 and 6.4. Also, other PLGA nanocarriers were formulated with solvent evaporation methods, using DCM solvent, and ultrasonication process.

★　NR/NR668

　Lipid nanoparticles

　Polymeric nanoparticles
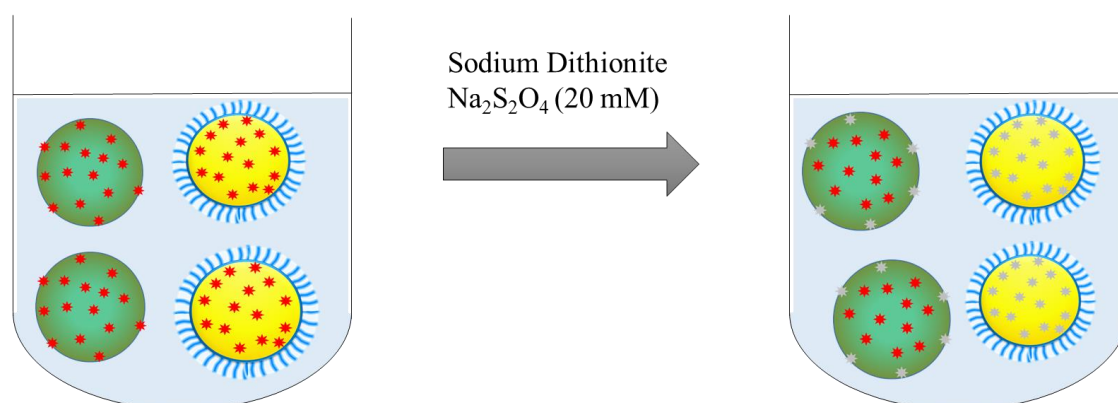
Figure 1. Concept of the reduction experiment by sodium dithionite $Na_2S_2O_4$ with lipid and polymeric nanocarriers encapsulating NR and NR668.

Size of the obtained nanocarriers was measured by DLS (Figure 2). Similar size was obtained with NR or NR668 for each kind of nanocarriers. For lipid systems, nanoemulsion

(LBF NCs) and solid lipid nanoparticles (Sup C NCs) of ~31 nm diameter were formed. PLGA and PMMA-MA NC$_S$ showed a size of 32 and 42 nm, respectively when formed under pH 7.4. For PLGA at pH 3.4 and PMMA-MA at pH 6.4 the nanocarriers were much larger (170-180 nm). In nanoprecipitation methods the pH is an important factor for the size of polymeric nanocarriers, because it controls the charge of the free carboxylate groups and therefore the surface charge of the particles [26]. When formed with solvent evaporation method, the size of PLGA nanocarriers (PLGA SE) was 245-260 nm.
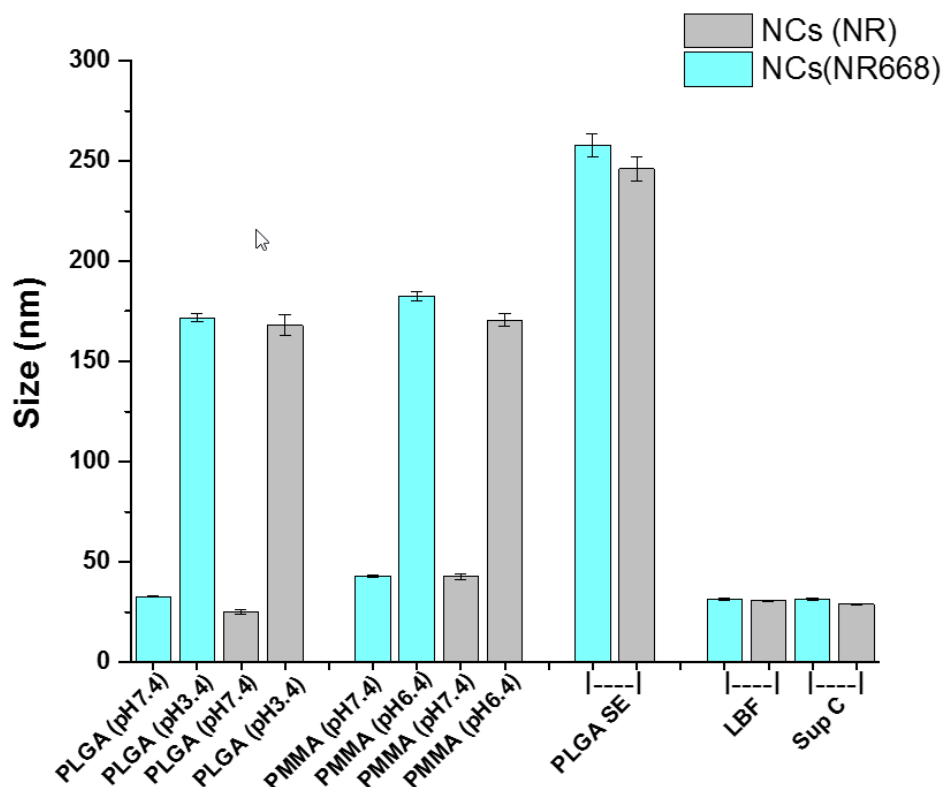
Figure 2. Hydrodynamic diameter of nanocarriers made from different materials as measured by DLS. The size was measured by volume statistics; error bars correspond to standard error of mean (n=3).

For these series of NCs, emissions spectra were measured (Figure 3). In the case of NCs encapsulating NR688 (Figure 3-A), the normalized fluorescence spectra were red shifted for PMMA-MA. It could be due to the more polar environment within the matrix compared to other NCs matrixes. All spectra of NR dye inside NCs (Figure 3-B), except the LBF NCs, were systematically red shifted. We expect that the NR dyes are not well encapsulated and situated near the surface in a more polar environment.

In Figure 3-C, we could see that at the same concentration of 0.5 wt% both small and large PLGA nanocarriers showed very low intensity (~12 time less) compared to PMMA-MA

nanocarriers. This difference is probably caused by the NR668 self-quenching through aggregation inside the porous matrix of PLGA. By contrast, in PMMA-MA matrix, the aggregation caused quenching is less pronounced probably because of more homogenous distribution of the NR668 dyes within the core. The same remark can be made for the Nile Red dye (NR), the difference between matrixes was less pronounced.
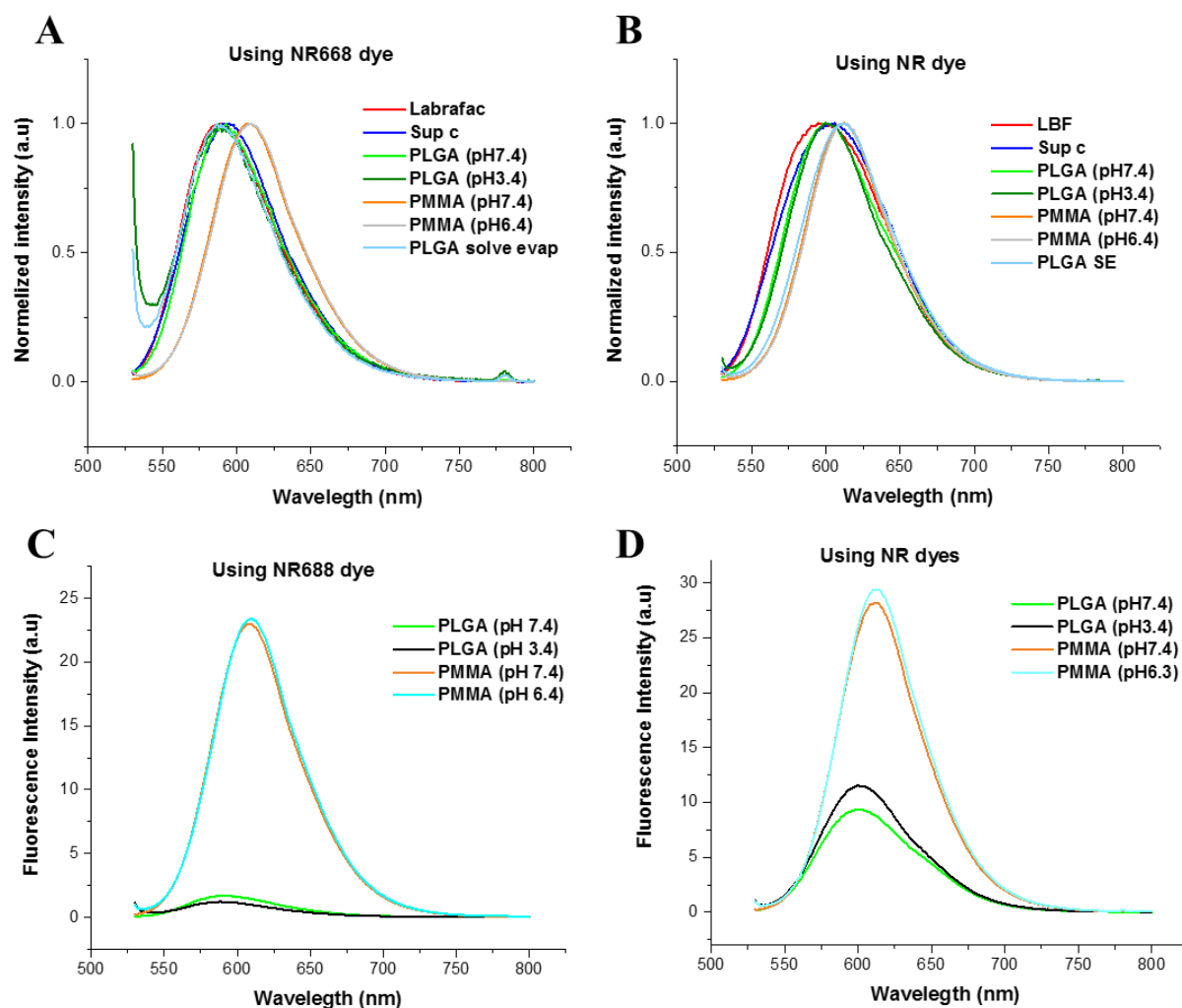
Figure 3. Fluorescence spectra of lipid and polymeric nanocarriers. (A) Normalized spectra of nanocarriers encapsulating NR668. (B) Normalized spectra of nanocarriers encapsulating NR. Emission spectra of PLGA and PMMA encapsulating NR668 (C) and NR (D).

Next step we measured evolution of fluorescence intensity of the nanocarriers in the presence of the reducing agent sodium dithionite $Na_2S_2O_4$. Thus, NR668 and NR dyes should be bleached after reaction with the dithionite and lose their fluorescence. Since sodium dithionite is highly polar dianion and cannot penetrate in the nanoparticles hydrophobic core, it can bleach the fluorophore exclusively on the external side (Fig. 1), as it was shown before for lipid vesicles.[3]
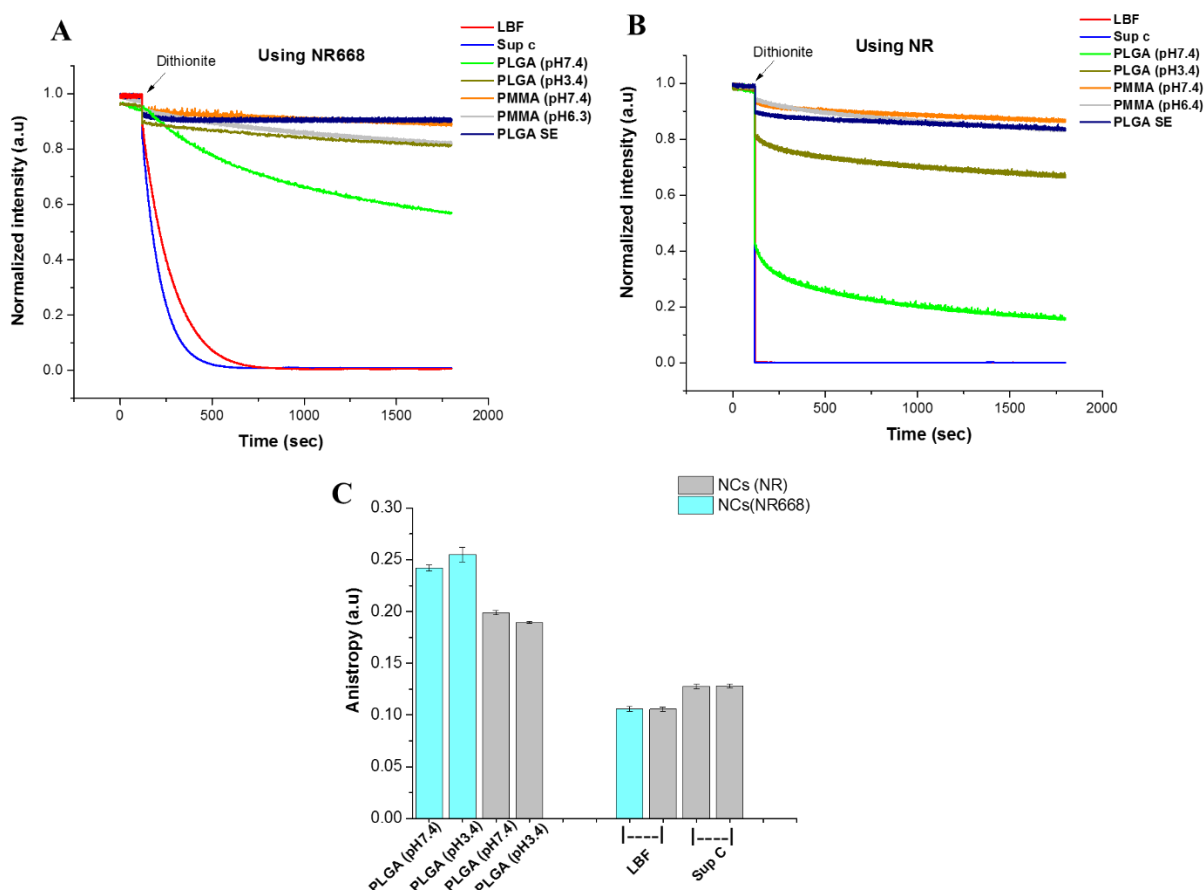
Figure 4. Normalized fluorescence intensity decays kinetics of lipid and polymeric nanocarriers in the presence of sodium dithionite. (A) Nanocarriers encapsulating NR668. (B) nanocarriers encapsulating NR. (C) Fluorescence anisotropy of PLGA, LBF and Sup C nanocarriers.

As shown in Figure 4-A.B, the fluorescence decay kinetics depends strongly on the nanocarrier type and the encapsulated dye. It is clear that for lipid NCs the fluorescence decay is much faster than for polymer NCs. Moreover, in lipid NCs fluorescence drops nearly to zero values, indicating effective bleaching of nearly all encapsulated dyes. In case of LBF NCs this is clearly because of diffusion of the dyes inside the lipid core, so that each dye could reach the NCs surface followed by bleaching.

Generally, for NR the fluorescence decay is much faster than for NR668. In case of Sup C NCs, the decrease in the fluorescence signal can be explained either by the free diffusion of the fluorophore inside the lipid matrix, which means that the matrix is not really solid. Alternatively, one can consider the expulsion of the dyes to the surface after lipid crystallisation, inducing bad encapsulation rapid bleaching of the dye at the surface of NCs. The first hypothesis is more valuable, because the NR668 is very well soluble into the Sup C, and it will be probably hard to expulse this very hydrophobic dye to the surface. Importantly, fluorescence

anisotropy (Figure 4-C) of NR668 inside Sup C NCs is similar to that in the LBF NCs, with a value of 0.12. This means that viscosity of the core of Sup C and LBF NCs is similar. Taking into account that the phase transition temperature of Sup c is 39 °C, we can expect that in form of small nanoparticles and in the presence of large amount of surfactant, Sup C is in the liquid state at room temperature.

In polymer NCs, the fluorescence decay was much slower and incomplete compared to lipid NCs, indicating that the dyes are much better encapsulated inside polymer NCs and cannot freely diffuse in the core. Nevertheless, for small PLGA nanocarriers (PLGA pH 7.4) after 30 min, 40 % of fluorescence decay was observed, suggesting large accessibility of the dye to the dithionite agent. We expect that a significant fraction of NR668 (at least 40%) is located at the NCs surface, allowing relatively fast bleaching by dithionite. The possibility of the fluorophore diffusion within the PLGA core can be excluded, since the phase transition of PLGA is 65 °C and the anisotropy measurement gave a value of 0.25, much larger compared to lipid NCs.

When the small PLGA nanocarriers are substituted with the large size PLGA (prepare at pH 3.4, 170 nm), the accessibility of the NR668 to dithionite is reduced, and just 15 % of the dyes are bleached. This result implies that larger PLGA nanocarriers have better encapsulation and protection for the hydrophobic dyes NR668. It can be explained by smaller surface to volume ratio in larger NCs, which would limit exposure of NR668 to the surface.

Then, in case of PMMA-MA nanocarriers of both sizes only 6% of NR668 signal was lost in the presence of dithionite. This means that PMMA-MA matrix allows better encapsulation and protection of NR668 compared to PLGA matrix. This conclusion is important for drug encapsulation with polymer NCs, in order to avoid the problem of burst release happening with some polymeric nanocarriers. Furthermore, when PLGA NCs is prepared with solvent evaporation method (PLGA SE), they displayed much lower accessibility of the dyes for dithionite as compared to NCs prepared by nanoprecipitation. We expect that when using solvent evaporation method, the dyes are better encapsulated as compared to the nanoprecipitation. Indeed, nanoprecipitation is a very fast, kinetically controlled process, where probably poor encapsulation of the dyes should be higher as compared to the solvent evaporation technique. Larger size of NCs (260 nm) prepared by solvent evaporation could be the second factor favouring better encapsulation of the dyes.

In the case of the less lipophilic Nile Red dye (log P=3-4.5) [318], after addition of dithionite, we observed very fast drop of the fluorescence signal in case of LBF and Sup C nanocarriers. This fluorescence intensity reached zero within 5 seconds, meaning that this kind of molecules are expulsed to the surface of the nanocarriers, making their bleaching very fast. By contrast,

NR668 dye (log P = 9.22) is probably localized in the lipidic core [11], and therefore its interaction with dithionite would require much longer time. For small PLGA NCs the fluorescence loss reached 80% of the initial signal after 30 min, suggesting that at least 80% of the NR dyes are accessible at the surface for dithionite reduction agent. Better molecules encapsulation was found for larger PLGA nanocarriers (170 nm) with just 30 % of fluorescence loss. Similarly, to the NR668, the Nile Red dyes are well protected in case of PMMA-MA NCs, with both sizes as well as in PLGA NCs prepared by solvent evaporation method. For this kind of less lipophilic molecules with log P ~ 3 -4.5, to reach better molecular protection and less burst release, it is much better to use PMMA-MA matrix. Moreover, solvent evaporation method ensures better encapsulation of dyes as compared to the nanoprecipitation. These findings should be important for encapsulation of hydrophobic drugs, such as Paclitaxel, exhibiting very similar Log P values (log P = 4.5).

It should be noted that our method could clearly distinguish liquid core of lipid NCs from the solid core of polymer NCs, because the difference in the dithionite bleaching kinetics was drastic. Finally, to confirm the capacity of this technique to follow the physical state of the nanocarriers within the same polymeric core, we measured fluorescence decay of PLGA (pH 7.4) NCs encapsulating NR668 in the presence dithionite at different temperatures (Figure 5).
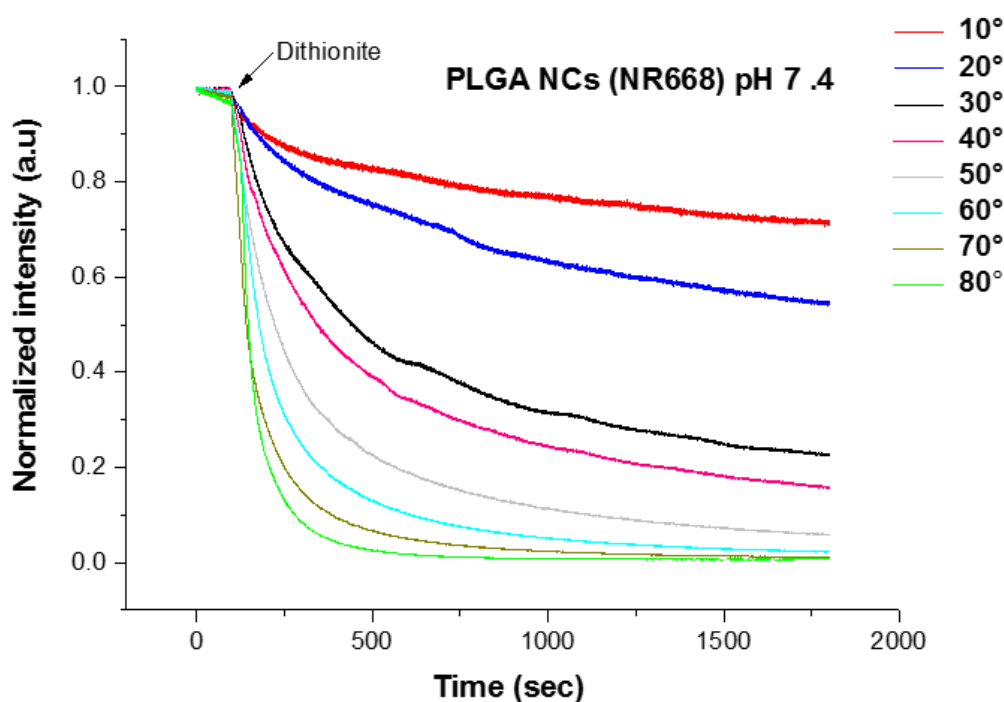
Figure 5. Normalized fluorescence intensity decay kinetics of PLGA nanocarriers (PLGA pH7.4) encapsulating NR668 in the presence of sodium dithionite, at different temperatures.

We could see that the fluorescence decay is much faster for higher temperatures. Higher temperatures favours transition into liquid phase, allowing the NR668 diffusion within the nanocarriers core and thus favouring dithionite bleaching, like in lipid NCs. Indeed, the fluorescence decay kinetics >60°C is similar to that of LBF NCs, which is in agreement with the theoretical PLGA phase transition of 65°C. However, we should note that very fast changes in the kinetics of dithionite bleaching was observed already between 20 and 50°C, which indicates that the polymer starts softening already at this temperature allowing some diffusion of NR668 dye towards particle surface. This observation is very important as it can show that kinetics of release in PLGA NCs is strongly temperature-dependent at physiologically relevant temperatures.

As conclusion, the technique of dithionite bleaching allowed us to determine the parameters that influence the encapsulation of the nanocarriers content (size, preparation method, composition, etc). Moreover, this technique helps to investigate the diffusion of active molecules within the nanocarriers, their accessibility to the surface and, consequently, the release phenomena. Importantly, we could clearly distinguish NCs containing liquid core from those containing solid core, because of dramatic differences in the bleaching kinetics. Moreover, we found that PMMA-MA is much better than PLGA for encapsulation of lipophilic molecules (especially with medium lipophilicity) through a nanoprecipitation protocol.

4- Light-triggered release from dye-loaded fluorescent lipid nanocarriers in vitro and in vivo (Publication-3)

Light is an attractive trigger for release of active molecules from nanocarriers in biological systems. In this work [315], we have described how to use visible light to induce the release of encapsulated fluorophores in lipid nanocarriers (nanoemulsions), similar to those studied in the previous chapters. This study was carried out using 32 nm diameter nanoemulsions droplets synthetized by auto-emulsification process and incorporating NR688, the hydrophobic analogue of the Nile Red (Figure 1).

Figure 1. Concept: lipid nanocarriers and the effect of light on the encapsulated Nile Red derivative NR668.

These nanoparticles do not penetrate into the cells after several hours of incubation at 37 ° C. However, after illumination under a microscope for 30 seconds at the absorption wavelength of NR668 (535 nm), fast accumulation of the fluorophore within the cells was shown. This phenomenon was observed at 1 and 5 wt% of dye loading and characterized by a difference between intracellular and extracellular fluorescence intensity. These results highlight the role of the nanocarriers, which encapsulates NR668 preventing its leakage into the cells, but ensuring its release after the illumination.

The same phenomenon was observed in vivo on zebrafish, where fluorescent probes were released into endothelial cells and tissues after illumination of nanoparticles circulating in the blood. By using fluorescence correlation spectroscopy, we have been able to prove that by illuminating the nanoparticles with defined wavelength and power, a controlled release of the content is obtained (Figure 2). Since this process is inhibited by the presence of sodium sulfite,

an oxygen depleting agent, it can be concluded that the mechanism of light-triggered release is oxygen-dependent, i.e. involves photo-oxidation processes. Nevertheless, we cannot rule out the possibility of a photo-thermal effect, which could also induce the dye release.
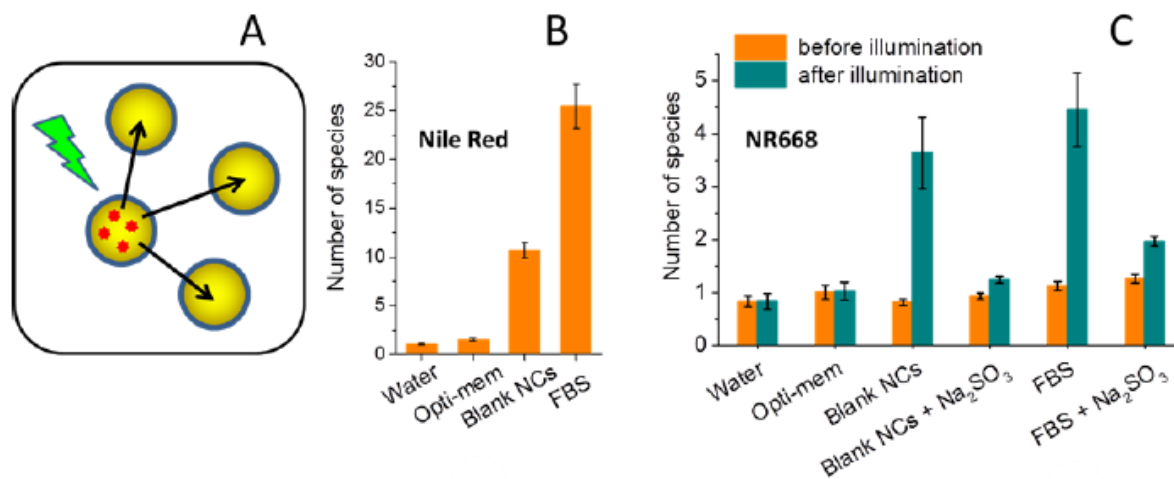
Figure 2. Fluorescence correlation spectroscopy (FCS) study of the light-induced release of fluorophore in model biological media. (A) Photorelease in the presence of blank nano-droplets. (B) Positive control with Red Nile, showing increase in the number of emissive species because of spontaneous dye release into surrounding blank nano-droplets. (C). Monitoring number of fluorescent species variation by FCS for NR668-loaded nano-droplets in different media before and after illumination [315].

Finally, to elucidate whether the whole nanocarriers are delivered or just its content, cells were incubated with a mixture of nano-droplets encapsulating separately NR668 and F888, highly hydrophobic dyes of different color. In this situation, both NR668- and F888-loaded nanocarriers should be detected inside the cells if the whole nanocarriers enter after the illumination. However, it was revealed that only NR668 signal was observed within the cells after illumination, suggesting that laser illumination induced the release of the dye content from NR668-loaded nanocarriers into the cells, but could not really induce internalization of the whole nanocarriers.

Also, we have shown that illumination of NR668 can provoke the release into the cells of another highly hydrophobic dye (F888) co-encapsulated into the lipid nanocarriers. On the basis of these results, dye-loaded lipid nanocarriers appear as a prospective tool for biomedical applications allowing the release of active molecules controlled by illumination.

This work was published in *Colloids and Surfaces B: Biointerfaces;* the article is enclosed below.

135

Light-triggered release from dye-loaded fluorescent lipid nanocarriers *in vitro* and *in vivo*

Redouane Bouchaala [a,b], Nicolas Anton [c], Halina Anton [a], Thierry Vandamme [c], Julien Vermot [d], Djabi Smail [b], Yves Mély [a], Andrey S. Klymchenko [a,*]

[a] CNRS UMR 7213, Laboratoire de Biophotonique et Pharmacologie, University of Strasbourg,74 route du Rhin, 67401 Illkirch Cedex, France
[b] Laboratory of Photonic Systems and Nonlinear Optics, Institute of optics and fine mechanics, University of Setif 1, 19000 Algeria
[c] CNRS UMR 7199, Laboratoire de Conception et Application de Molécules Bioactives, University of Strasbourg,74 route du Rhin, 67401 Illkirch Cedex, France
[d] IGBMC (Institut de Génétique et de Biologie Moléculaire et Cellulaire), Inserm U964, CNRS UMR7104, Université de Strasbourg, 1 rue Laurent Fries, 67404 ILLKIRCH, France

ABSTRACT

Light is an attractive trigger for release of active molecules from nanocarriers in biological systems. Here, we describe a phenomenon of light-induced release of a fluorescent dye from lipid nano-droplets under visible light conditions. Using auto-emulsification process we prepared nanoemulsion droplets of 32 nm size encapsulating the hydrophobic analogue of Nile Red, NR668. While these nano-droplets cannot spontaneously enter the cells on the time scale of hours, after illumination for 30 s under the microscope at the wavelength of NR668 absorption (535 nm), the dye showed fast accumulation inside the cells. The same phenomenon was observed in zebrafish, where nano-droplets initially staining the blood circulation were released into endothelial cells and tissues after illumination. Fluorescence correlation spectroscopy revealed that laser illumination at relatively low power (60 mW/cm²) could trigger the release of the dye into recipient media, such as 10% serum or blank lipid nanocarriers. The photo-release can be inhibited by deoxygenation with sodium sulfite, suggesting that at least in part the release could be related to a photochemical process involving oxygen, though a photo-thermal effect could also take place. Finally, we showed that illumination of NR668 can provoke the release into the cells of another highly hydrophobic dye co-encapsulated into the lipid nanocarriers. These results suggest dye-loaded lipid nano-droplets as a prospective platform for preparation of light-triggered nanocarriers of active molecules.

© 2017 Elsevier B.V. All rights reserved.

1. Introduction

Triggered release of active molecules from nanocarriers has been a subject of intensive research in the last decades [1–6]. Various triggers, such as pH, reductive potential, enzymes, temperature, ultrasound, magnetic field and light have been utilized. Light is particularly attractive in this respect, as it can be focused at a desired position of a specimen with high spatiotemporal resolution. The most common approaches for light controlled release utilize molecules that undergo light-controlled isomerization, photo-polymerization and photo-cleavage [7,8]. Thus, azobenzene *cis*-trans isomerization can trigger release from liposomes [9] polymer vesicles and micelles [10,11] and inorganic porous nanomaterials [12,13]. Photo cleavage reactions in *o*-nitrobenzyl

[14–16], coumarin [17], spiropyran [18,19], malachite green [20], cynnamic acid [21,22] derivatives, etc can produce photo-driven hydrophobicity and charge changes, polymer/lipid fragmentation and de-crosslinking. However, majority of examples of the light-triggered release from nanocarriers reported to date require UV light or two-photon excitation [17,23]. The other approach utilizes surface plasmon and photo-thermal effects, to trigger the cargo release. In this case, most commonly gold nanoparticles, nano-rods or nano-shells, are used in combination with polymer, lipid nanocarrier or thermo-sensitive covalent bonds [24–28]. The plasmon absorption in these nanostructures was successfully tuned, so that they could be activated with almost any desired excitation wavelength from UV up to near-infrared (NIR) region [29,30]. However, photothermal effects using gold nanostrcutures generally require relatively strong illumination powers [31], which can be harmful for the biological sample. Upconverting nanoparticles, which convert NIR light into visible and further produce photochemical effect should be also mentioned, but so far all exam-
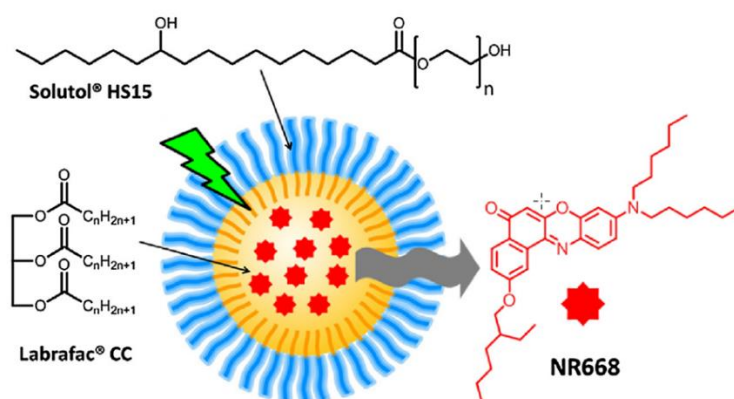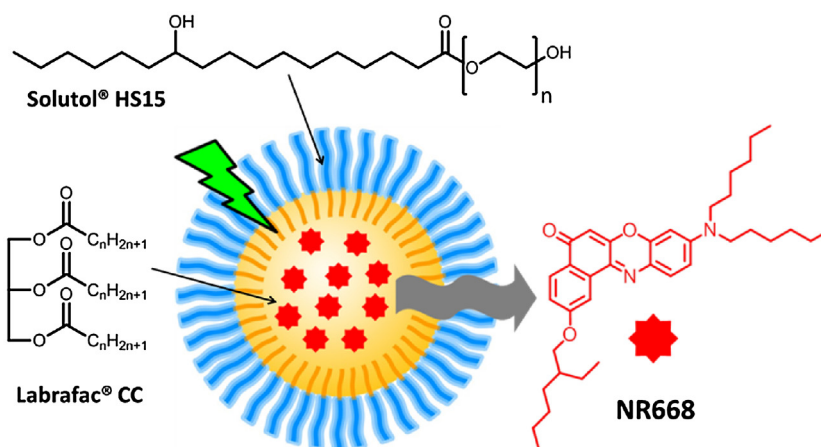
Fig. 1. Concept: lipid nanocarrier and the effect of light on the encapsulated Nile Red derivative NR668.

ples of photo-release with upconversion nanoparticles are limited to inorganic systems [32,33]. In order to develop organic photo-responsive systems one should use dyes encapsulated inside a nanocarrier. In this case, dyes operate as photosensitizers generating highly reactive singlet oxygen and/or as converters of light energy into heat. As photosensitizers, organic dyes, due to their capacity to disrupt biological membranes, were used for photo-chemical delivery into the cells of molecules and nanoparticles [34–37]. The use of organic dyes as triggers of molecular release from a nanocarrier were mainly realized in lipid vesicles, where local photothermal or photochemical effects were proposed as driving mechanisms of photo-release [38–42]. The photothermal effects were also reported for NIR dyes loaded into nanocarriers in cancer therapy applications [43–45].

Lipid nanoemulsions are an important nanocarrier platform, as they can be readily prepared from FDA approved agents and their hydrophobic core can encapsulate drugs and contrast agents [46–50]. Previously, the group of Texier suggested these lipid nanocarriers as imaging agents by loading their core with apolar cyanines [51,52]. We further suggested a particular probe design, using long alkyl chains and bulky hydrophobic counterions, that can increase the dye encapsulation together with preservation of the highly efficient fluorescence [53,54]. Moreover, recent FRET- based studies revealed their high stability *in vitro* and *in vivo* and capacity to enter tumors in the intact form [55,56]. In particular, we showed that the use of highly hydrophobic substituents of Nile Red enables to significantly increase dye loading, preserve good fluorescence efficiency and drastically decrease the dye leakage [53]. However, the question remained: can a strong illumination of a large quantity of dyes confined on the nanoscopic space destabilize lipid droplets? This point was not studied up to now owing to the difficulty to encapsulate a large amount of dyes in these nanoscale reservoirs. Taking recently proposed approaches [53,54], the dye concentration can be increased up to 5 wt% along with conserving their fluorescent properties. This is precisely the point that can open the door to photo-triggered properties. Although Nile Red photosensitizing properties were not described yet, we have shown earlier that large concentrations of Nile Red-based membrane probe (NR12S) can produce some photo-damage on cell membranes [57], which suggests that Nile Red as photo-active molecule to destabilize lipid nanocarriers.

In the present work, we describe an unexpected phenomenon, which is the light-triggered release of nano-droplet content, when encapsulating a hydrophobic Nile Red analogue. We show that the dye release can be observed both in cell culture and *in vivo* on a zebrafish model. The light-induced dye release was validated with different acceptor media, such as blank nanocarriers and 10% serum and it can be inhibited in the presence of oxygen scavenger. Finally, the light-driven release of a co-encapsulated molecule (second encapsulated dye) along with the Nile Red derivative was validated, which proposes the route to light-controlled drug release from lipid nano-droplets.

2. Results and discussion

The idea of light-triggered release from nano-carrier is summarized in Fig. 1. The nano-emulsion droplets can be considered as reservoir with high local concentration of dyes. Our question was whether illumination of this large ensemble of dyes within the small volume of lipid nanocarrier could produce release of its content due to photophysical or photochemical phenomena. As a dye for encapsulation, we selected a derivative of Nile Red bearing long alkyl chains (NR668, Fig. 1). Although this dye is expected to be cell permeant (like parent Nile Red), its high hydrophobicity ensures encapsulation into nano-droplets with minimal leakage effects, which prevents its fast accumulation in the cells [53].

We first prepared nanocarriers by spontaneous emulsification of Solutol, Labrafac and NR668 dye in water, which gave 32 nm particles of low polydispersity index (<0.1) according to dynamic light scattering. The phenomenon of dye release under light illumination was first studied in cell culture. Solutol® (Kolliphor®) HS 15/Labrafac® WL nanoemulsions loaded with hydrophobic Nile Red derivative NR668 was incubated with cells and studied by wide-field fluorescence microscopy. Our earlier works showed that no internalization was observed for the same system even after 2 h of incubation with HeLa cells [53], which showed that these nanocarriers cannot enter the cells on this time scale. Therefore, this system is ideal for testing the effect of light, as no artifacts due to particle internalization or dye leakage into the cells was observed. After 30 min of incubation of the cells with the emulsion of nanocarriers containing 1 wt% of NR668, the cells remained poorly fluorescent, as the fluorescence of the medium was more intense than that of the cells. Moreover, after washing of the cells, no significant fluorescence was detected inside the cells (Fig. S1), which confirmed that NR668 nano-droplets did not spontaneously internalize within this time scale. Then, we illuminated the cells surrounded by NR668-loaded nanocarriers for 30 s at 535 nm (absorption maximum of NR668 in nano-droplets is 526 nm [53]) using the maximal lamp power (~14 W/cm^2 power density at the sample level). The light action resulted in a strong photobleaching of the area of observation. Indeed, it was observed that initially very bright fluorescence field became non-fluorescent after the illumination (Fig. 2). Then,
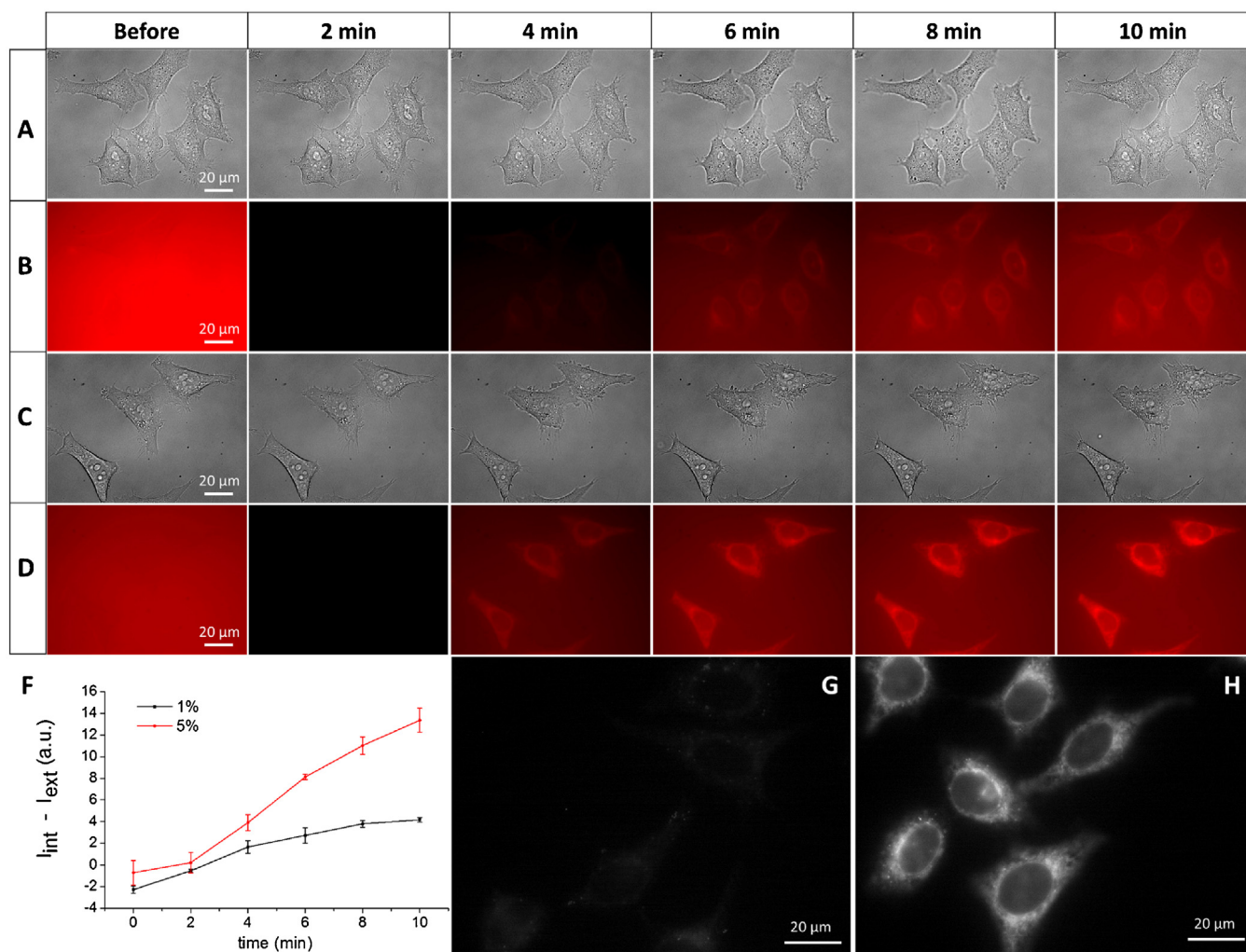
Fig. 2. Release of dye molecules *in vitro*. Brightfield (A and C) and fluorescence (B and D) images of Hela cells in the presence of nanocarrier loaded with at 1% (A, B) or 5% (C, D) of NR668. The first images on the left correspond to samples before illumination, while all others are after illumination for 30 s at 535 nm with 2 min delay for each consecutive image. All the experiments were done at 37 °C. (F): difference between intracellular and extracellular fluorescence intensity, I_{int}-I_{ext}, vs time delay after illumination. The error bars represent the standard deviation of the mean from three independent illumination cycles (n = 3). (G-H) Fluorescence images after washing (from nanocarriers at 5 wt% NR668) showing non-illuminated and illuminated regions.

with time, the fluorescence of the medium started to recover, but surprisingly the fluorescence of the cells increased with time. This phenomenon was observed already at 1 wt% of dye loading and took about 10 min to achieve a clear intracellular staining (Fig. 2A and B), characterized by a significant difference between intracellular and extracellular fluorescence intensity (Fig. 2F). At 5 wt% dye loading (Fig. 2C and D), the cell staining after illumination was much stronger, so that the difference between intracellular and extracellular fluorescence intensity was >3-fold larger compared to that for 1 wt% loading. After cell washing from the nanocarriers, we could find the initially illuminated regions, where the fluorescence inside the cells was many-fold larger than that for the non-illuminated regions (Fig. 2G and H). These experiments clearly showed that nanocarriers, unable to enter the cells in the dark, can deliver the dye after illumination. It should be noted that when NR668 dye without lipid nanocarrier was added directly to the cells from its DMSO stock solution (final DMSO concentration was 1%), the intracellular fluorescence of this dye was observed (Fig. S1). Earlier works showed that its parent analogue Nile Red could also spontaneously internalize [58], which implies that plasma membrane is not really a barrier for these hydrophobic dyes. These results highlight the role of the nanocarrier, which encapsulates NR668

preventing its leakage into the cells, but ensuring its release after the illumination.

Then, we investigated whether the light-induced release can be also realized *in vivo* on zebrafish. Our earlier work showed that NR668-loaded nanocarriers remained in the blood circulation for at least 30 min without dye leakage into the endothelial cells of the vessels and surrounding tissues [53]. Here, we injected nanocarriers containing 5 wt% of NR668 and performed microscopy imaging as a function of time without and with illumination (through 450–490 nm bandpass filter). Without illumination, the red fluorescence of nano-droplets was observed exclusively inside the blood vessels for at least 60 min (Fig. 3A,B), indicating that the nanocarriers remain in the blood circulation without dye leakage into the tissues. By contrast, after the illumination, we could observe a progressive increase of the fluorescence in surrounding tissues between the blood vessels (Fig. 3C-F). The fluorescence intensity, recorded in the tissue areas showed continuous increase in time for the observation period of 60 min (Fig. 3G). Thus, the illumination triggered release of the encapsulated NR668 dye, which then diffused freely into the surrounding tissues.

To understand better the observed phenomenon of release, we performed fluorescence correlation spectroscopy (FCS) of our nanocarriers in different model biological media. FCS is a powerful
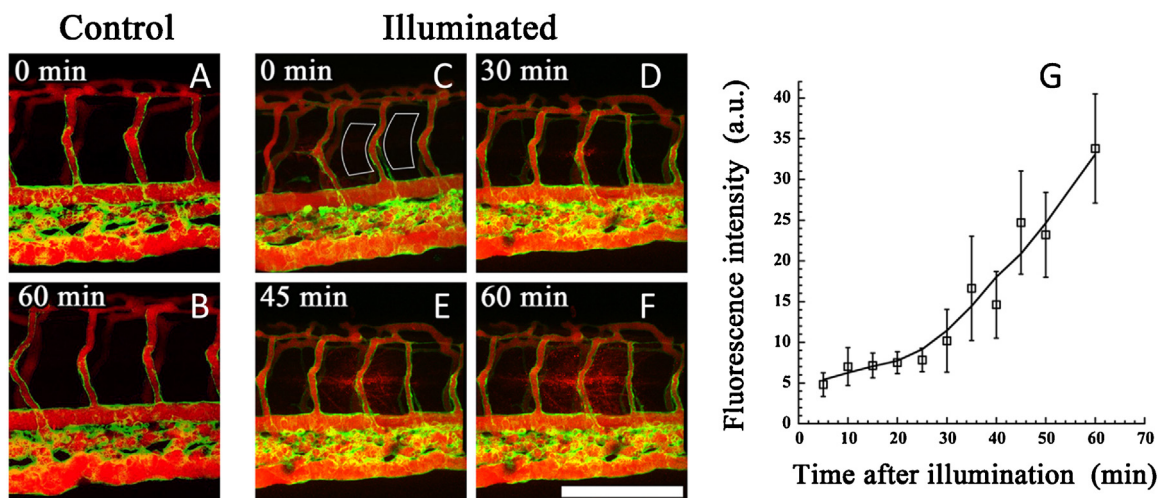
Fig. 3. The photo-induced release of the NR688 dye from the nanoemulsions in the vasculature of living zebrafish embryo. Fluorescence images of tail vasculature (green) containing NR668 nanoemulsions (red). (A,B) Control non-illuminated embryo, showing no leakage of the dye. (C-F) Embryos illuminated for 5 min through 450–490 nm bandpass filter, showing a red fluorescence in the tissues surrounding the vessels. Scale bar is 100 μm. (G) The increase in the fluorescence intensity averaged in the ROIs shown in panel (C) with time. The error bars represent the standard deviation of the mean from two different regions of the embryo ($n = 2$). (For interpretation of the references to colour in this figure legend, the reader is referred to the web version of this article.)

technique to characterize nanoparticles *in situ*, which can provide information about size, concentration and brightness of particles [53,59,60]. According to our FCS data, the particle size, measured from the diffusion correlation time of the emissive species was 33 nm (Table S1). This value is remarkably close to the hydrodynamic diameter obtained for these nanocarriers by DLS (32 nm). Moreover, the particles concentration for this sample at 1:10000 dilution, evaluated from the number of emissive species per focal volume, was 1.7 nM. Basic calculation based on known total lipid concentration in the used nanoemulsion ($1.1 \times 10^{-3}\%$) and the mass of a single 33-nm nano-droplet (1.9×10^{-17} g, assuming density of the droplet of 1 g/ml), we could estimate that the concentration of nanocarriers should be around 1.0 nM. The correspondence of the theoretical and experimental values of the particle concentration and the match of the particle size obtained from DLS and FCS suggest that after this 10000-fold dilution the nanocarriers remained practically intact.

In order to monitor the photo-release of the dye, we studied the number of emissive species, which, according to our earlier studies, is an important indicator of the dye release [53]. Indeed, if the dyes are released into the acceptor medium (blank particles or serum), the number of emissive species should increase (Fig. 4A). For example, in control experiments without illumination, Nile Red encapsulated into the nanocarriers showed a low number of emissive species in water and Opti-MEM, where poorly soluble Nile Red cannot really escape (Fig. 4B). On the other hand, in the presence of blank nanocarriers or fetal bovine serum (FBS), the number of emissive species increased drastically, showing that Nile Red leaked from nanocarriers and distributed in the recipient medium. By contrast, the number of emissive species for the NR668-loaded nanocarriers was low for all four studied media (Fig. 4C) and the size of emissive species remained stable (Table S1). These results confirmed our earlier data on the high stability of NR668-loaded nanocarriers against leakage [53]. After illumination with the laser at 532 nm (power density 60 mW/cm^2) the number of emissive species grew drastically in the presence blank nanocarriers and FBS, but did not change in water and Opti-MEM. The number of emissive species in the media with blank nanocarriers or FBS grew gradually on increase in the time of illumination (Fig. 4D). These results suggest that the dye photo-release is light-dose dependent and it requires a biological medium containing hydrophobic microen-

vironment. This was expected, because NR668 is highly apolar (log P = 9.22 [53]) and practically insoluble in water. Moreover, as the number and the size (Table S1) of emissive species in water did not change after illumination, we could conclude that illumination did not split the nanocarriers into multiple species. Therefore, the observed photo-release in the presence of the acceptor medium as well as in cell and zebrafish embryo is probably related to the light-triggered dye leakage from the nanocarriers into the surrounding hydrophobic microenvironment. The illumination also produced a drop in the total fluorescence intensity (Fig. 4E), indicating the photobleaching of the dye. The latter indicates that NR668 underwent photochemical transformation, which could explain the destabilization of the nanocarrier with further release of the dyes into the medium. Photobleaching of dyes is commonly associated with generation of singlet oxygen that further oxidize the dye or other components of the nanocarrier. Therefore, we repeated our FCS experiments in the presence of sodium sulfite. The latter is a reductive deoxygenating agent, which depletes oxygen through oxidation into a sulfate anion [61–63]. Remarkably, sodium sulfite drastically decreased the release of the dye under illumination in the presence of blank nanocarriers and serum, as it can be seen from only small change in the number of emissive species (Fig. 4C). Moreover, sodium sulfite did not show a significant influence on the fluorescence intensity of the samples before illumination (Table S1), indicating that it did not act as quencher through electron transfer or other mechanisms. Overall, these results suggest that the key mechanism that drives the dye release is linked to the photo-oxidation that could destabilize the nanocarriers.

The important question is whether illumination of NR668 can trigger release of other molecules form the nanocarriers. To this end, we encapsulated into our lipid nano-droplets a second dye, F888, which was also reported previously to remain inside the droplets without dye leakage [53], similarly to NR668. Importantly, the maxima of absorption and emission of F888 in nano-droplets at 1 wt% loading (388 and 455 nm, respectively) are well separated from those of NR668 (526 and 592 nm) [53], which should allow selective excitation and detection of three two dyes by fluorescence microscopy. We incubated the dually labeled nanocarriers with cells for 15 min and then illuminated them for 30 s at 535 nm. Before illumination, the intracellular fluorescence was weak confirming no leakage of the encapsulated dyes in the presence of cells
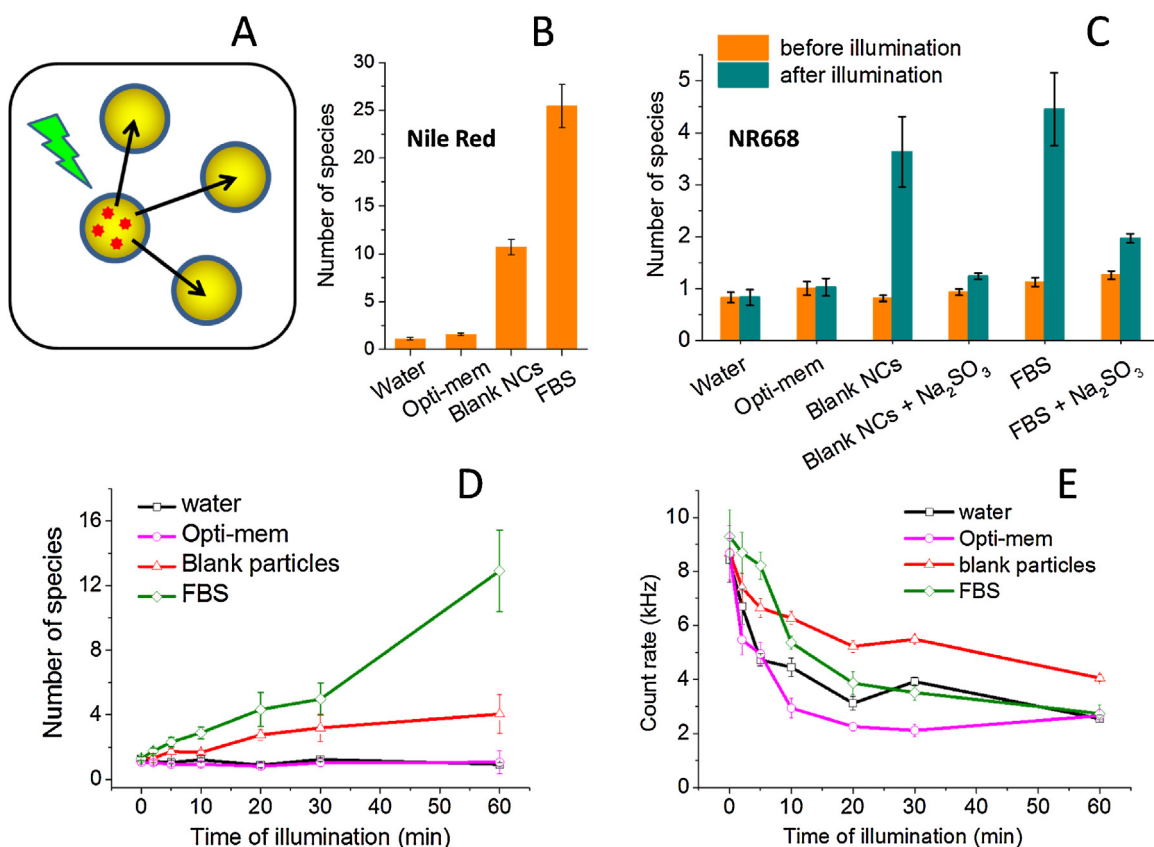
Fig. 4. Fluorescence correlation spectroscopy (FCS) studies of the light-induced dye release into model biological media. (A) Scheme explaining the effect of the dye release on the number of the emissive species. (B) Control experiment showing Nile Red dye release from nanocarriers into blank nanocarriers (NCs) and 10% serum (FBS), which was recorded as number of emissive species. (C) The effect of 30 min illumination by 532-nm laser (power density 60 mW/cm^2) on lipid nanocarriers loaded with NR668 in different media: water, Opti-MEM, blank nanocarriers and FBS. Presence of oxygen-depleting agent sodium sulfite was also tested. (D) Effect of laser illumination time on the number of emissive species and the total fluorescence intensity of NR668-loaded lipid nanocarriers in different media. The error bars in (B-E) represent the standard deviation of the mean ($n = 20$ recorded correlation curves).

(Fig. 5A and B). After illumination, the fluorescence recorded at the NR668 channel showed expected behavior, where the total fluorescence decreased significantly after illumination, and then increased inside the cells in the time period of 10 min (Fig. 5B). Importantly, the intracellular fluorescence recorded at the channel corresponding to F888 dye (shown in green) increased after illumination and continued increasing together with that of NR668 (Fig. 5A). Importantly, the background fluorescence in the F888 channel did not change after illumination, because this illumination cannot excite F888 dye. In the control experiment, we incubated the cells with only F888-loaded nanocarriers. After 30 s illumination at 535 nm, we found no changes in fluorescence inside the cells (Fig. S2), so that NR668 was absolutely required to induce release of F888 dye. These results showed that illumination that excites selectively NR668 dye inside nano-droplets can trigger the release of the second encapsulated dye F888. Thus, a prototype of a photo-release system is developed, where illumination of nanocarriers could induce the release of a molecule of interest, for instance in the drug delivery applications.

Finally, to clarify whether the whole nanocarrier is delivered or just its content, we incubated the cells with a mixture of nano-droplets containing separately NR668 and F888. In this case, if the whole nanocarriers enter after the illumination, then both NR668- and F888-loaded nanocarriers should be detected inside the cells. However, it was found that after illumination, only the NR668 signal was observed inside the cells, whereas the F888 signal remained low (Fig. 5C and D). This suggested that light illumination triggered the release of the dye content from NR668-loaded

nanocarriers into the cells, but could not really induce internalization of the whole nanocarrier. Moreover, the fact that F888 did not enter the cells after illumination also suggested that the photo-release process did not disrupt the cell plasma membranes. This feature is important in the development of photo-release systems with minimal photo-damaging effects. Together with the FCS data, these observations suggest that the light acts at the level of the nano-droplet, producing destabilization and further cargo release into the cells. In this respect the described phenomenon is close to the light-triggered release from lipid vesicles, which was explained by photo-thermal or photochemical mechanisms [38–42]. The described phenomenon is also relevant to photochemical internalization [34–37], however, in the latter case light acts mainly at the level of cell membranes.

3. Conclusions

In the present work, a phenomenon of light-induced release from lipid nano-droplets under visible light conditions is described for the first time. It was observed using nanoemulsion droplets of 32 nm size encapsulating hydrophobic the analogue of Nile Red, NR668. These nanocarriers did not enter the cells after several hours of incubation at 37 °C, however, after illumination for 30 s under the microscope at the wavelength of NR668 absorption (535 nm), fast accumulation of the released dyes inside the cells was observed. The light-triggered release was also validated *in vivo* on zebrafish, where nano-droplets showing stable emission in the blood circulation, stained surrounding tissues after illumina-
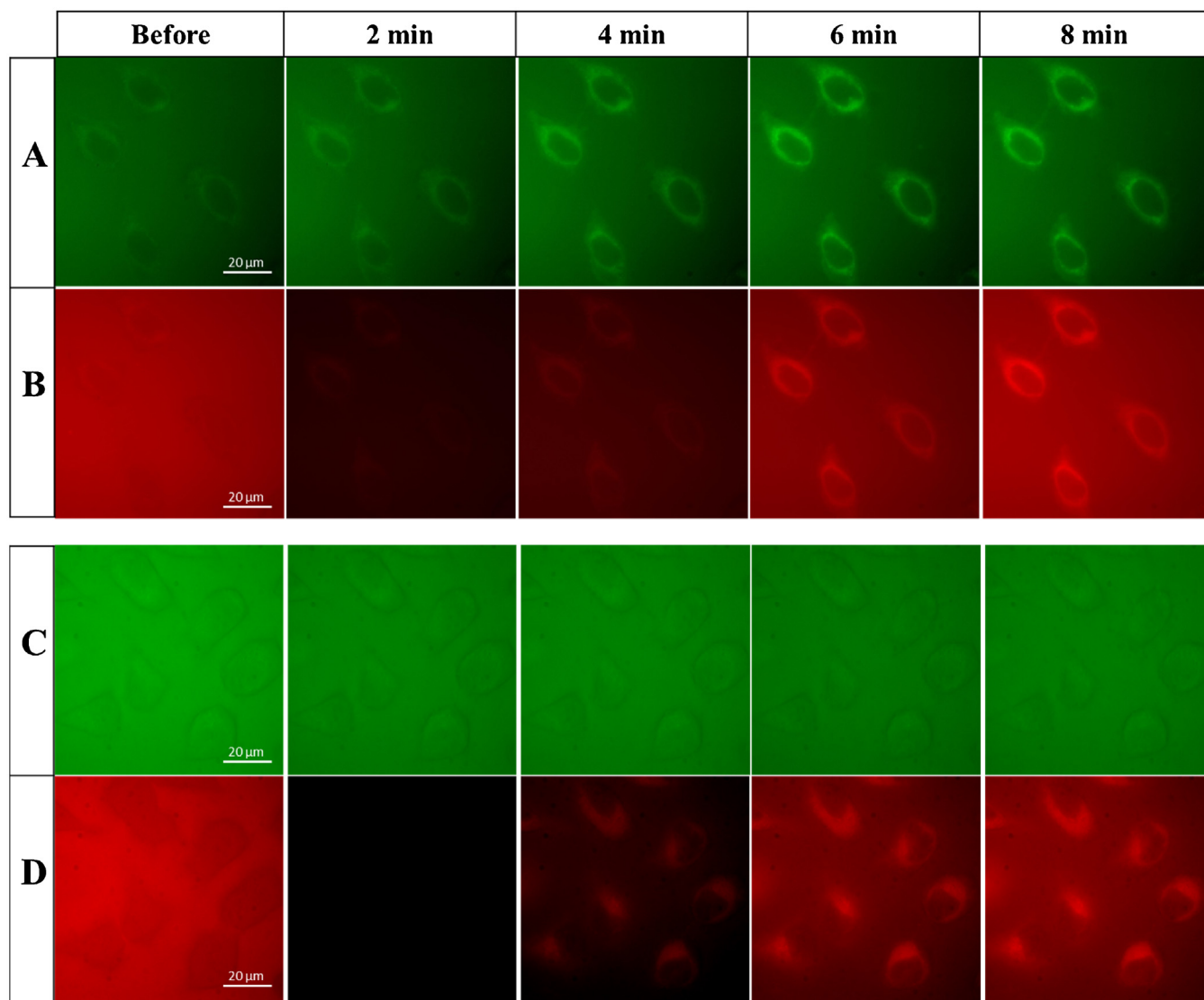
Fig. 5. Fluorescence imaging of HeLa cells incubated for 15 min at 37 °C with nanocarrier before and after illumination at 535 nm for 30 s. Images were taken every 2 min. (A and B) Nanocarriers encapsulating both dyes F888-NR668 (1 wt% each). (C and G) Mixture of nanocarriers encapsulating separately F888 (1 wt%) and NR668 (1 wt%) dyes (1:1, v:v). F888 channel: excitation 360/40 nm and emission 470/40 nm. NR668 channel: excitation 535/50 nm and emission 610/75 nm.

tion. Using fluorescence correlation spectroscopy, we showed that laser illumination at relatively low power (60 mW/cm^2) triggered dye release into 10% serum or blank lipid nanocarriers. As this process is inhibited by the deoxygenating agent sodium sulfite, we can conclude that the mechanism is linked to oxygen-dependent photochemistry, which destabilizes the nanocarrier. Nevertheless, we cannot exclude that a photo-thermal effect could also take part, as proposed in some recent literature for NIR dyes. Finally, we showed that illumination of NR668 can induce the release of another highly hydrophobic dye from the lipid nanocarriers, which was observed as accumulation of both dyes inside living cells. Based on these results, dye-loaded lipid nano-droplets emerge as a promising platform for light-triggered release of active molecules in biomedical applications. We expect that this concept could be readily extended to other dyes, which could induce under light stimulus the release of drugs from nano-droplets.

4. Materials and methods

4.1. Materials

All chemicals and solvents were purchased from Sigma-Aldrich. Kolliphor® HS15 non-ionic surfactant (mixture of polyethylene glycol 660 hydroxystearate and free polyethylene glycol 660 and) obtained from BASF (Ludwigshafen, Germany) was a kind gift from Laserson (Etampes, France), Labrafac® WL (medium chain triglycerides) was obtained from Gattefossé (Saint-Priest, France). MilliQ-water (Millipore) was used in all experiments. Culture reagents were obtained from Sigma (St. Louis, USA), Lonza (Verviers, Belgium) and Gibco-Invitrogen (Grand Island, USA). Opti-MEM® reduced serum medium was from Gibco. Dihexylamino-2-(2-ethyl-hexyloxy)-benzo[a]phenoxazin-5- one (NR668) and 4′-Dioctylamino-3-octyloxyflavone (F888) were synthesized as described before [53].

4.2. Formulation and characterization of lipid nanoparticle

Lipid nanocarriers were prepared by spontaneous nano-emulsification. Briefly, NR668 or F888 was solubilised in Labrafac® WL. Then, Kolliphor® HS 15 was added and the mixture was homogenized under magnetic stirring at 90° C. Nano-droplets of 32 nm diameter were prepared by adding 230 mg of ultrapure water to a mixture of 35 mg of Labrafac® WL and 65 mg of Kolliphor® HS 15 under intense stirring.

The size distribution of the nanoemulsions was determined by dynamic light scattering on a Zetasizer® Nano series DTS 1060 (Malvern Instruments S.A., Worcestershire, UK) and by FCS (home-built setup, see below). In the DLS measurements statistics by volume was used.

4.3. Cell culture

HeLa cells were cultured in Dulbecco's modified Eagle medium (D-MEM, high glucose, Gibco-invitrogen) supplemented with 10% (v/v) fetal bovine serum (FBS, Lonza), 1% antibiotic solution (penicillin-streptomycin, Gibco-invitrogen) in a humidified incubator with 5% CO_2 at 37°C. Cells plated on a 75 cm^2 flask at a density of 10^6 cells/flask were harvested at 80% confluence with trypsin–EDTA (Sigma) and seeded onto a chambered cover-glass (IBiDi) at a density of 0.1×10^6 cells/IBiDi. After 24 h, cells in the IBiDi dishes were washed 2 times with PBS (phosphate buffer saline) (Lonza). Then, a solution of dye-loaded nano-droplets diluted at 1: 1000 in Opti-MEM was added. Microscopy images were taken after 30-min incubation at 37°C, unless indicated.

4.4. Microscopy

Fluorescence images were taken on a Leica DMIRE2 inverted microscope equipped with a Leica DC350FX CCD camera and a thermostated chamber (Life Imaging Services, Basel Switzerland) for maintaining the temperature at 37°C. Cy3 filter cube (excitation 535/50 nm, emission 610/75 nm) and DAPI filter cube (excitation 360/40 nm, emission 470/40 nm) were used for detection of NR668 and F888, respectively. A 63× HCX PLAPO (1.32 NA) was used as an objective. In the photo-release studies, the illumination for 30 s was done using the same Cy3 filter cube at ~14 W/cm^2 power density of light.

4.5. Fluorescence correlation spectroscopy (FCS) and dye release

FCS measurements were performed on a two-photon platform including an Olympus IX70 inverted microscope. Two-photon excitation at 830 nm (10 mW laser output power) was provided by a mode-locked Tsunami Ti: sapphire laser pumped by a Millenia V solid state laser (Spectra Physics). The measurements were realized in an 96 well plate, using a 50 uL volume per well. The focal spot was set about 20 μm above the plate. The normalized auto-correlation function, G(t) was calculated online by an ALV-5000E correlator (ALV, Germany) from the fluorescence fluctuations, δF(t), by $G(\tau) = <\delta F(t)\,\delta F(t+\tau)>/<F(t)>^2$ where $<F(t)>$ is the mean fluorescence signal, and τ is the lag time. Assuming that lipid nanoparticle diffuse freely in a Gaussian excitation volume, the correlation function, $G(\tau)$, calculated from the fluorescence fluctuations was fitted according to Thompson [64]:

$$G(\tau) = \frac{1}{N}\left(1+\frac{\tau}{\tau_d}\right)^{-1}\left(1+\frac{1}{s^2}\frac{\tau}{\tau_d}\right)^{-1/2} \quad (1)$$

where τ_d is the diffusion (correlation) time, N is the mean number of fluorescent species within the two-photon excitation volume, and S is the ratio between the axial and lateral radii of the excitation volume. The excitation volume is about 0.34 fL and S is about

3–4. Typical data recording times were 5 min, using dye-loaded lipid nanoparticle diluted 1: 10 000 from the originally prepared nanoparticle. Using 6-carboxytetramethylrhodamine (TMR from Sigma-Aldrich) in water as a reference, the hydrodynamic diameter, d, of nanocarriers (NCs) was calculated as: $d_{NCs} = \tau_{d(NCs)}/\tau_{d(TMR)} \times d_{TMR}$, where d_{TMR} is a hydrodynamic diameter of TMR (1.0 nm). Concentration of NCs was calculated from the number of species by: $C_{NCs} = N_{NCs}/N_{TMR} \times C_{TMR}$, using a TMR concentration of 50 nM. The data were obtained based on 20 recorded correlation curves; the recording time for each curve was 10 s for NCs and 30 s for TMR.

For the dye release studies by FCS, dye-loaded nano-droplets were diluted 10 000 fold to four different media: water, Opti-mem, blank nanocarriers at 1000-fold dilution (10-fold excess with respect to dye-loaded droplets) and 10% of FBS in water (serum). Each sample was placed into special 50 μl cuvette and the whole sample was illuminated with 532-nm laser at ~60 mW/cm^2 power density for different time (10 and 30 s, 10, 20 30 and 60 min) and we measure number of species and total count rate.

4.6. In vivo studies in zebrafish

Zebrafish were kept at 28 °C and bred under standard conditions. The transgenic line, Tg(flk1:eGFP) [65], expressing eGFP specifically in the endothelial cells, was used in order to visualize the vasculature. For the angiography, the embryos, 3 days after fertilization, were anaesthetized in egg water containing 0.04% tricaine and 0.05% phenyl thiourea (Sigma-Aldrich) and immobilized in 0.8% low melting point agarose (Sigma). The injections were performed using a Nanoject microinjector (Drummond Scientific, Broomal, PA, USA). The glass capillary was filled with NR668-loaded nanocarriers (5 wt% in oil) in 5 mM HEPES (1000-fold dilution) and 2.3 nL were injected in the sinus venosus of the embryos. The nanocarriers were immediately distributed in all the vasculature. The injected embryos were placed on the microscope stage and imaged within 5 min after injection. Intravital confocal microscopy was performed on a Leica SP5 fixed stage direct microscope with a 25× (NA 0.95) and 10× (NA 0.3) water immersion objectives. 488 nm argon laser line was used to excite both eGFP and the NR668 dyes, and their emission was detected by two separate PMTs in the spectral range 500–530 nm and 620–650 nm, respectively. At these conditions, no cross-talk between the channels was observed. The illuminations for the light-driven release were performed with a xenon lamp in epifluorescence mode using a 450–490 nm band pass filter. Confocal z-stacks and time lapses were recorded and treated by the ImageJ software (rsbweb.nih.gov/ij/). The embryos were imaged during one hour post injection and no toxicity due to the injection or to the illumination was observed. All experiments performed with zebrafish complied with the European directive 86/609/CEE and IGBMC guidelines validated by the regional committee of ethics.

Appendix A. Supplementary data

Supplementary data associated with this article can be found, in the online version, at http://dx.doi.org/10.1016/j.colsurfb.2017.05.035.

References

[1] E. Fleige, M.A. Quadir, R. Haag, Adv. Drug Deliv. Rev. 64 (2012) 866–884.
[2] S. Kaur, C. Prasad, B. Balakrishnan, R. Banerjee, Biomater. Sci. 3 (2015) 955–987.
[3] V.P. Torchilin, Nat. Rev. Drug Discov. 13 (2014) 813–827.
[4] S. Mura, J. Nicolas, P. Couvreur, Nat. Mater. 12 (2013) 991–1003.
[5] J. Liu, C. Detrembleur, S. Mornet, C. Jerome, E. Duguet, J. Mater. Chem. B 3 (2015) 6117–6147.
[6] S. Swaminathan, J. Garcia-Amoros, A. Fraix, N. Kandoth, S. Sortino, F.M. Raymo, Chem. Soc. Rev. 43 (2014) 4167–4178.
[7] N. Fomina, J. Sankaranarayanan, A. Almutairi, Adv. Drug Deliv. Rev. 64 (2012) 1005–1020.
[8] J. Olejniczak, C.-J. Carling, A. Almutairi, J. Controlled Release 219 (2015) 18–30.
[9] K. Kano, Y. Tanaka, T. Ogawa, M. Shimomura, Y. Okahata, T. Kunitake, Chem. Lett. (1980) 421–424.
[10] Y. Wang, P. Han, H. Xu, Z. Wang, X. Zhang, A.V. Kabanov, Langmuir 26 (2010) 709–715.
[11] G. Wang, X. Tong, Y. Zhao, Macromolecules 37 (2004) 8911–8917.
[12] S. Angelos, E. Choi, F. Vo, L.D. Cola, J.I. Zink, P. Institut, J. Phys. Chem. C 111 (2007) 6589–6592.
[13] Y. Tian, Y. Kong, X.J. Li, J. Wu, A.C.T. Ko, M. Xing, Colloid Surf. B-Biointerfaces 134 (2015) 147–155.
[14] J.Q. Jiang, X. Tong, D. Morris, Y. Zhao, Macromolecules 39 (2006) 4633–4640.
[15] N. Fomina, C. McFearin, M. Sermsakdi, O. Edigin, A. Almutairi, J. Am. Chem. Soc. 132 (2010) 9540–9542.
[16] X. Zhao, M. Qi, S. Liang, K. Tian, T. Zhou, X. Jia, J. Li, P. Liu, ACS Appl. Mater. Interfaces 8 (2016) 22127–22134.
[17] J. Babin, M. Pelletier, M. Lepage, J.-F. Allard, D. Morris, Y. Zhao, Angew. Chem. Int. Ed. 48 (2009) 3329–3332.
[18] H.-I. Lee, W. Wu, J.K. Oh, L. Mueller, G. Sherwood, L. Peteanu, T. Kowalewski, K. Matyjaszewski, Angew. Chem. Int. Ed. 46 (2007) 2453–2457.
[19] Q.J. Xing, N.J. Li, D.Y. Chen, W.W. Sha, Y. Jiao, X.X. Qi, Q.F. Xu, J.M. Lu, J. Mater. Chem. B 2 (2014) 1182–1189.
[20] R.M. Uda, Y. Kato, M. Takei, Colloid Surf. B-Biointerfaces 146 (2016) 716–721.
[21] M. Wang, J.-C. Kim, Int. J. Pharm. 468 (2014) 243–249.
[22] D. Shi, M. Matsusaki, M. Akashi, J. Controlled Release 149 (2011) 182–189.
[23] N. Fomina, C.L. McFearin, M. Sermsakdi, J.M. Morachis, A. Almutairi, Macromolecules 44 (2011) 8590–8597.
[24] L. Dykman, N. Khlebtsov, Chem. Soc. Rev. 41 (2012) 2256–2282.
[25] A.B.S. Bakhtiari, D. Hsiao, G. Jin, B.D. Gates, N.R. Branda, Angew. Chem. (International ed. in English) 48 (2009) 4166–4169.
[26] Y. Cheng, T.L. Doane, C.-H. Chuang, A. Ziady, C. Burda, Small (Weinheim an der Bergstrasse Germany) 10 (2014) 1799–1804.
[27] L. Paasonen, T. Laaksonen, C. Johans, M. Yliperttula, K. Kontturi, A. Urtti, J. Controlled Release 122 (2007) 86–93.
[28] W.-C. Jeong, S.-H. Kim, S.-M. Yang, ACS Appl. Mater. Interfaces 6 (2014) 826–832.
[29] X.H. Huang, I.H. El-Sayed, W. Qian, M.A. El-Sayed, J. Am. Chem. Soc. 128 (2006) 2115–2120.
[30] E. Ju, Z. Li, Z. Liu, J. Ren, X. Qu, ACS Appl. Mater. Interfaces 6 (2014) 4364–4370.
[31] Z. Qin, J.C. Bischof, Chem. Soc. Rev. 41 (2012) 1191–1217.
[32] B. Yan, J.-C. Boyer, D. Habault, N.R. Branda, Y. Zhao, J. Am. Chem. Soc. 134 (2012) 16558–16561.
[33] Y. Yang, F. Liu, X. Liu, B. Xing, Nanoscale 5 (2013) 231–238.
[34] H.L. Lu, W.J. Syu, N. Nishiyama, K. Kataoka, P.S. Lai, J. Controlled Release 155 (2011) 458–464.
[35] P.K. Selbo, A. Weyergang, A. Høgset, O.J. Norum, M.B. Berstad, M. Vikdal, K. Berg, J. Controlled Release 148 (2010) 2–12.
[36] S. Febvay, D.M. Marini, A.M. Belcher, D.E. Clapham, Nano Lett. 10 (2010) 2211–2219.
[37] A. Høgset, L. Prasmickaite, P.K. Selbo, M. Hellum, B.Ø. Engesæter, A. Bonsted, K. Berg, Adv. Drug Deliv. Rev. 56 (2004) 95–115.
[38] V.C. Anderson, D.H. Thompson, Biochim. Biophys. Acta 1109 (1992) 33–42.
[39] S.J. Leung, M. Romanowski, Theranostics 2 (2012) 1020–1036.
[40] S. Guha, S.K. Shaw, G.T. Spence, F.M. Roland, B.D. Smith, Langmuir 31 (2015) 7826–7834.
[41] K.A. Dendramis, D.T. Chiu, J. Am. Chem. Soc. 131 (2009) 16771–16778.
[42] A. Rodriguez-Pulido, A.I. Kondrachuk, D.K. Prusty, J. Gao, M.A. Loi, A. Herrmann, Angew. Chem. Int. Ed. 52 (2013) 1008–1012.
[43] J. Yu, D. Javier, M.A. Yaseen, N. Nitin, R. Richards-Kortum, B. Anvari, M.S. Wong, J. Am. Chem. Soc. 132 (2010) 1929–1938.
[44] G.T. Spence, G.V. Hartland, B.D. Smith, Chem. Sci. 4 (2013) 4240–4244.
[45] G. Chen, K. Wang, Y. Zhou, L. Ding, A. Ullah, Q. Hu, M. Sun, D. Oupický, ACS Appl. Mater. Interfaces 8 (2016) 25087–25095.
[46] D.J. McClements, Y. Li, Adv. Colloid Interface Sci. 159 (2010) 213–228.
[47] M.M. Fryd, T.G. Mason, Ann. Rev. Phys. Chem. 63 (2012) 493–518.
[48] D.J. McClements, Emulsion design to improve the delivery of functional lipophilic components, in: M.P. Doyle, T.R. Klaenhammer (Eds.), Annual Review of Food Science and Technology, vol. 1, 2010, pp. 241–269.
[49] A. Gianella, P.A. Jarzyna, V. Mani, S. Ramachandran, C. Calcagno, J. Tang, B. Kann, W.J.R. Dijk, V.L. Thijssen, A.W. Griffioen, G. Storm, Z.A. Fayad, W.J.M. Mulder, ACS Nano 5 (2011) 4422–4433.
[50] N. Anton, J.-P. Benoit, P. Saulnier, J. Controlled Release 128 (2008) 185–199.
[51] M. Goutayer, S. Dufort, V. Josserand, A. Royere, E. Heinrich, F. Vinet, J. Bibette, J.L. Coll, I. Texier, Eur. J. Pharm. Biopharm. 75 (2010) 137.
[52] I. Texier, M. Goutayer, A.D. Silva, L. Guyon, N. Djaker, I. Veronique Josserand, E. Neumann, J. Bibette, F. Vinet, J. Biomed. Opt. 14 (2009).
[53] A.S. Klymchenko, E. Roger, N. Anton, H. Anton, I. Shulov, J. Vermot, Y. Mely, T.F. Vandamme, RSC Adv. 2 (2012) 11876–11886.
[54] V.N. Kilin, H. Anton, N. Anton, E. Steed, J. Vermot, T.E. Vandamme, Y. Mely, A.S. Klymchenko, Biomaterials 35 (2014) 4950–4957.
[55] J. Gravier, L. Sancey, S. Hirsjaervi, E. Rustique, C. Passirani, J.-P. Benoit, J.-L. Coll, I. Texier, Mol. Pharm. 11 (2014) 3133–3144.
[56] R. Bouchaala, L. Mercier, B. Andreiuk, Y. Mély, T. Vandamme, N. Anton, J.G. Goetz, A.S. Klymchenko, J. Controlled Release 236 (2016) 57–67.
[57] Z. Darwich, A.S. Klymchenko, D. Dujardin, Y. Mely, RSC Adv. 4 (2014) 8481–8488.
[58] O.A. Kucherak, S. Oncul, Z. Darwich, D.A. Yushchenko, Y. Arntz, P. Didier, Y. Mely, A.S. Klymchenko, J. Am. Chem. Soc. 132 (2010) 4907.
[59] E. Haustein, P. Schwille, Fluorescence correlation spectroscopy: novel variations of an established technique Annu. Rev. Biophys. Biomol. Struct., vol. 36, 2007, pp. 151–169.
[60] D. Woll, RSC Adv. 4 (2014) 2447–2465.
[61] M.E.D. Garcia, A. Sanzmedel, Anal. Chem. 58 (1986) 1436–1440.
[62] M.A. Filatov, S. Baluschev, K. Landfester, Chem. Soc. Rev. 45 (2016) 4668–4689.
[63] S.H.C. Askes, N.L. Mora, R. Harkes, R.I. Koning, B. Koster, T. Schmidt, A. Kros, S. Bonnet, Chem. Commun. 51 (2015) 9137–9140.
[64] N.L. Thompson, in: J.R. Lakowicz (Ed.), Topics in Fluorescence Spectroscopy Techniques, vol. 1, Plenum Press, New York, 1991, p. 337.
[65] S.-W. Jin, D. Beis, T. Mitchell, J.-N. Chen, D.Y.R. Stainier, Development (Cambridge England) 132 (2005) 5199–5209.

Supplementary Material

Light-triggered release from dye-loaded fluorescent lipid nanocarriers *in vitro* and *in vivo*

Redouane Bouchaala, Nicolas Anton, Halina Anton, Thierry Vandamme, Julien Vermot, Djabi Smail, Yves Mély, Andrey S. Klymchenko
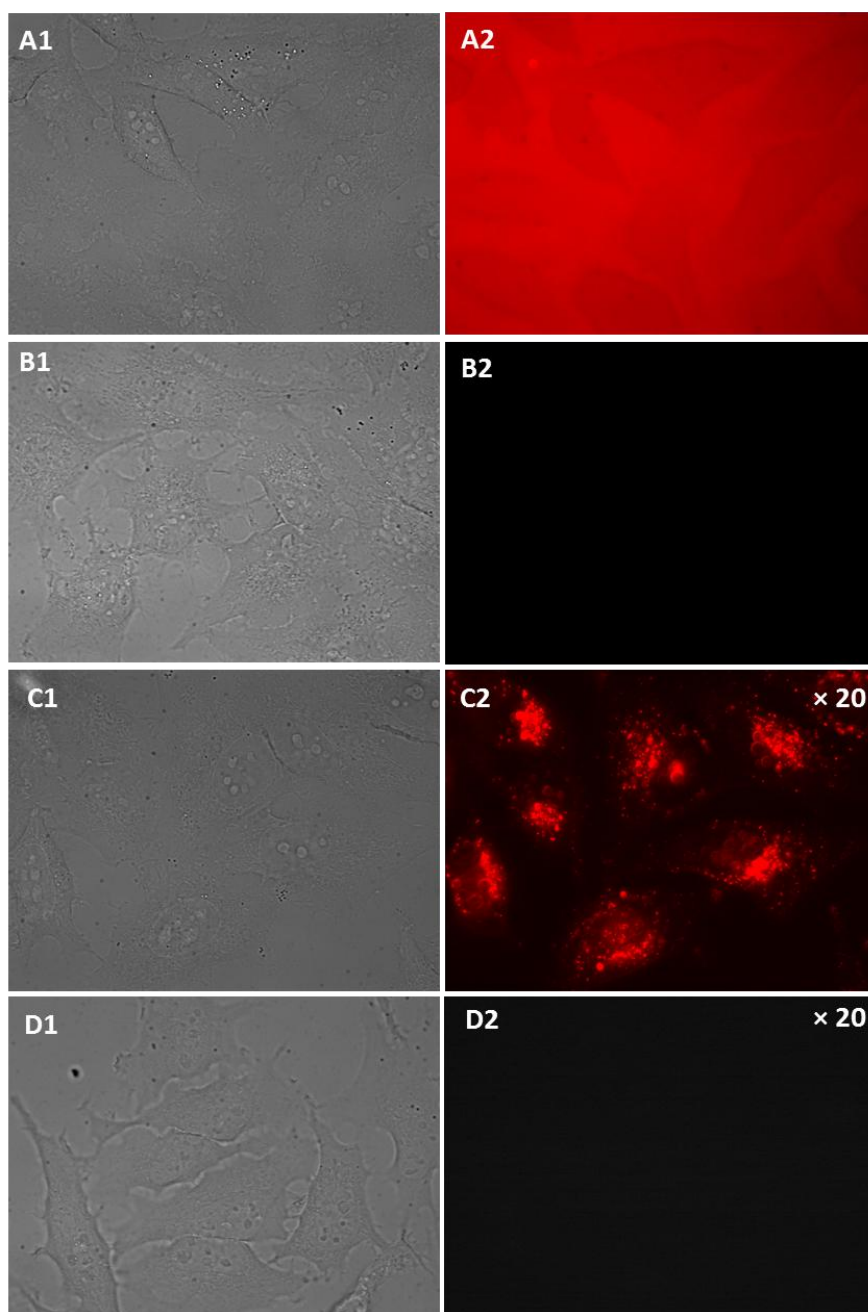
Figure S1. Bright field and fluorescence images of Hela cells. (A1-A2) NR668 nanocarriers incubated for 15 min with HeLa cells. (B1-B2) NR668 nanocarriers incubated for 15 min with cells then washed by PBS. (C1-C2) NR668 without nanocarriers (added from DMSO) incubated for 15 min with cells. The signal in C2 is multiplied 20-fold for visibility. All experiments were done at 37 °C. (D1-D2) Control image of HeLa cells without NR888 using the same microscopy settings. The size of the images was 140 × 105 μm.

Before	2 min	4 min	6 min	8 min
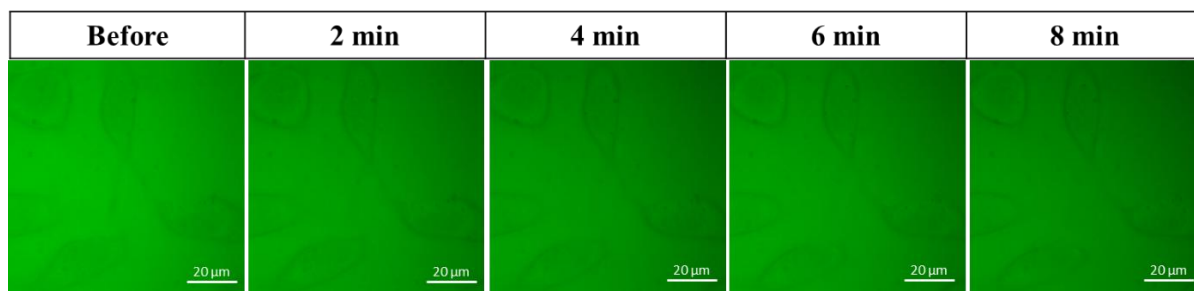
Figure S2. Fluorescence imaging of HeLa cells incubated for 15 min at 37 °C with F888-loaded nanocarrier (at 1 wt%) before and after illumination for 30 s. Each figure was taken every 2 min.

Table S1. FCS data of nanoemulsions in different media before and after illumination.[a]

Sample	Cps (kHz)	N	τ_d (ms)	Chi2	Brightness (kHz)	C (nM)	Size (nm)
Before illumination							
Water	32.1	0.82	1.35	0.999	38.8	1.7	33
Blank NCs	33.8	0.81	1.31	0.999	40.5	1.7	32
Blank NCs + Na$_2$SO$_3$	29.8	0.92	1.41	0.999	32.1	1.9	34
Opti-MEM	33.1	1.00	1.41	0.999	32.0	2.1	34
FBS	29.6	1.12	1.38	0.999	26.3	2.3	33
FBS + Na$_2$SO$_3$	32.1	1.26	1.42	0.999	25.6	2.6	34
After illumination							
Water	10.2	0.83	1.37	0.999	12.3	1.7	33
Blank NCs	18.6	3.63	1.28	0.998	5.11	7.5	31
Blank NCs + Na$_2$SO$_3$	13.6	1.23	1.43	0.999	11.0	2.6	34
Opti-MEM	12.1	1.02	1.39	0.998	11.9	2.1	33
FBS	17.2	4.45	1.30	0.996	3.86	9.2	31
FBS + Na$_2$SO$_3$	16.4	1.96	1.34	0.998	8.32	4.1	32
TMR (rhodamine)	67.0	24.08	0.0417	0.998	2.77	50	1.0

[a] The effect of 30 min illumination by 532-nm laser (power density 60 mW/cm^2) on lipid nanocarriers (NCs) loaded with NR668 in different media: water, Opti-MEM, emulsion of blank nanocarriers and FBS. In some samples oxygen depleting agent sodium sulphide (Na$_2$SO$_3$) was used. Cps: count rate. N: the mean number of emissive species within the two-photon excitation volume. Chi2: the goodness of the fit. τ_d: diffusion (correlation) time. C: concentration of emissive species. Size: the hydrodynamic diameter of NCs (d_{NCs}) was calculated as: $d_{NCs} = \tau_{d(NCs)} / \tau_{d(TMR)} \times d_{TMR}$, where d_{TMR} is a hydrodynamic diameter of TMR (1.0 nm). Each value is the mean of 20 recorded correlation curves (the recording time for each curve was 10 s for NCs and 30 s for TMR).

PART III

Conclusion and perspectives

Conclusion and perspectives

The aim of my PhD project was dedicated to the development of fluorescence methods for characterization of lipid nanocarrier integrity and the release of actives molecules in vitro and in vivo.

In the first part of my work, Förster resonance energy transfer (FRET) technique was used to follow the integrity of lipid nanocarriers and they release in vitro and in vivo. To address this problem, we developed lipid nanocarriers (nanoemulsions) of 100 nm size encapsulating lipophilic near-infrared cyanine 5.5 and 7.5 dyes. The excellent brightness and efficient FRET inside the nanocarriers enabled for the first time quantitative fluorescence ratiometric imaging of nanocarriers integrity directly in the blood circulation, liver and tumor xenografts of living mice, using a whole-animal imaging set-up. The results revealed that in blood circulation of healthy mice, the integrity of the nanocarriers is preserved at 93% 6h post-administration. Through enhanced permeability and retention (EPR) effect, they accumulate rapidly in tumors while preserving their integrity (77% after 2h), and further disintegrate in liver with a half-life of 4.4h. Thus, nanoemulsions can be promising candidates for drug delivery and cancer targeting because they can deliver the cargo up to the targeted tumor before getting disassembled.

Then, based on fluorescence correlation spectroscopy (FCS) analysis, we developed a simple method for the *in vitro* release quantification from lipid nanocarriers (NCs). A modified Nile Red (NR668) dye was encapsulated inside the nanocarriers as model for hydrophobic drug. Initially, we made a calibration, where the important FCS parameters for the quantification of dye release were identified. As a result, we showed that standard deviation of the signal fluctuation is a key parameter for FCS quantification. Unlike classical FCS parameters, such as correlation time, number and brightness of the emissive species, the standard deviation depended exclusively on the dye content inside nano-droplets, being independent from the presence of emissive species. Moreover, we introduced a normalized parameter of standard deviation which was independent from the nanocarrier concentration and the laser power. Then, using different media, an evaluation of the NR668 release from NCs at different temperatures was performed. We showed that NCs were intact in water, but showed slow dye release at 37 °C in 10% Foetal bovine serum (FBS), and at 60° the release in FBS was the fastest reaching

75 % after 6h. Our new approach is quantitative, universal and very easy to apply to other nanocarrier systems. Moreover, as our method requires simple recording of the fluctuation of the signal (standard deviation of the fluctuation) without building an auto-correlation curve, we expect that our method could be extended to a conventional confocal microscope. This means that evaluation of the release from NCs would become really simple and accessible for any laboratory having confocal fluorescence microscope without a dedicated FCS module. However, additional work is needed to validate this idea.

The next step of the project was to understand the encapsulation of hydrophobic molecules inside lipid and polymeric nanocarriers. For this purpose, a new method was developed based on the chemical bleaching of a fluorescent dye by sodium dithionite $Na_2S_2O_4$. The Nile Red and NR668 dyes were encapsulated into different nanocarriers: liquid lipid nanocarriers, solid lipid nanocarriers, PLGA and PMMA-MA nanocarriers. The effect of lipid and polymer matrix on the chemical bleaching of encapsulated dyes was studied, in addition to the effects of the size and the preparation methods. The bleaching process monitored from the fluorescence intensity of encapsulated dyes was much faster in lipid NCs compared to polymer NCs, independently of the dye used. We concluded that all lipid NCs tested in our work present liquid core, so that the encapsulated dyes can freely diffuse towards the particle surface resulting in rapid beaching of all dyes inside NCs. However, we also found that NR668 was bleached significantly slower than Nile Red, indicating that molecules of higher hydrophobicity are much less assessable to the aqueous medium. Therefore, one should expect much slower release of NR668 to the biological medium compared to Nile Red. Indeed, our FCS as well as FRET studies confirm this conclusion. Secondly, in all polymer NCs, the bleaching was much slower than in lipid NCs, suggesting that encapsulated dyes cannot diffuse in the solid matrix to the particle surface and, therefore, they are better protected from the bleaching agent. Moreover, the bleaching reaction was the fastest in case of smaller sized PLGA NCs, probably because they present higher surface to volume ratio. Moreover, our bleaching methodology revealed than PLGA NCs prepared by solvent evaporation are bleached much slower than those prepared by nanoprecipitation. The difference between the methods was especially drastic for less hydrophobic Nile Red, indicating much better encapsulation of dyes using solvent evaporation method. Unlike solvent evaporation, nanoprecipitation is a kinetically controlled process, and, therefore, some fraction of the dye may not have enough time to be encapsulated into newly formed particles. Finally, PMMA-MA based NCs displayed much slower bleaching reaction, suggesting that nanoprecipitation of PMMA-MA NCs provides much better encapsulation of

dyes compared to PLGA NCs. Thus, our methodology can detect differences between different NCs. In particular, it can distinguish solid vs liquid core NCs and it can show which formulation ensures better encapsulation of the dyes with minimal diffusion to the surface. This means that the bleaching method could evaluate the resistance of NCs against burst release and allow prediction of release profile in biological media. We expect that the proposed method could be extended to other nanocarriers. However, for the moment this method is still not quantitative and therefore, it would be important to extract quantitative information from the fluorescence decay kinetics in order to evaluate the degree of encapsulation and burst release.

Finally, I investigated the possibility of using light as trigger for controlled release of active molecules from lipid nanocarriers in vitro and in vivo in zebrafish. As a model of active molecules, NR668 the hydrophobic analogue of the Nile Red, was encapsulated into nanoemulsion droplets. Then, visible light was used to induce the release of encapsulated fluorophores in lipid nanocarriers. The release of the fluorophore and further accumulation into the cells was shown to be light-dependent. According to fluorescence correlation spectroscopy (FCS), this release is related to a photochemical process involving oxygen. In addition, we showed that illumination of NR668 can provoke the release into the cells of another highly hydrophobic dye co-encapsulated into the lipid nanocarriers. This system appears as promising platform for light-triggered release of active molecules in biomedical applications. We expect that other dyes encapsulated at large concentration could show similar light-triggered release from lipid NCs, so that the light-triggered release could be in principle achieved for different excitation wavelengths.

Obtained results suggest that nanoemulsion-based lipid nanocarriers have a great potential as drug delivery carriers. Large variety of therapeutics molecules could be encapsulated, and delivered by the EPR effect. Also, they display a very good stability and biodistribution in vivo. Nanoemulsions can be a platform for controlled triggered release of active molecules, with a variety of stimulus. Moreover, surface modifications of lipid nanocarriers may be considered for targeting applications. However, at the moment it remains a challenge before the surfactants at the surface of nanoemulsion droplets are quite mobile and can easily detach from the surface in biological media. Finally, the developed fluorescence techniques provided suitable tools to overcoming the challenges and the difficulties of obtaining rapid quantitative characterization of nanocarriers such as stability and cargo release directly in biological medium. In addition, these new methods can be applied to a variety of organic and inorganic nanocarriers and could become standard benchmarks for evaluation of nanocarriers.

PART IV

Materials and Methods

1- Materials

All chemicals and solvents for synthesis were from Sigma Aldrich. Cremophor ELP® (Kolliphor ELP®), Kolliphor® HS15 non-ionic surfactant (mixture of polyethylene glycol 660 hydroxystearate and free polyethylene glycol 660 and) were from BASF (Ludwigshafen, Germany). Labrafac WL® (medium chain triglycerides) and Suppocire C® were from Gattefossé (Saint-Priest, France). Ultrapure water was obtained using a MilliQ® filtration system (Millipore, Saint-Quentin-en-Yvelines, France). Foetal bovine serum (FBS) was acquired from Lonza (Verviers, Belgium) and Gibco-Invitrogen (Grand Island, USA). Culture reagents were obtained from Sigma (St. Louis, USA), Lonza (Verviers, Belgium) and Gibco-Invitrogen (Grand Island, USA). Opti-MEM® reduced serum medium was from Gibco. Nile Red and Calcein dyes were purchased from sigma Aldrich. Sodium hydrosulfite from Alfa Aesar.

Poly(D,L-lactide-co-glycolide) (PLGA, lactide 50 mol %, glycolide 50 mol %, acid terminated, Mn 24 000, PDI 1.7, and Mn 8800, PDI 1.7), poly-(methyl methacrylate-co-methacrylic acid) (PMMA-MA, 1.3% methacrylic acid, Mn ∼15 000, Mw∼34 000) were purchased from Sigma-Aldrich. Sodium phosphate monobasic (>99.0%, Sigma-Aldrich) and sodium phosphate dibasic dihydrate (>99.0%, Sigma-Aldrich) were used to prepare 20 mM phosphate buffer solutions.

2- Methods

2.1- Synthesis of NR668 and F888

The synthesis of 4'-Dioctylamino-3-octyloxyflavone (**F888**) and 9-Dihexylamino-2-(2-ethyl-hexyloxy)-benzo[a]phenoxazin-5- one (**NR668**). was performed by Ievgen Shulov as described in ref [1].
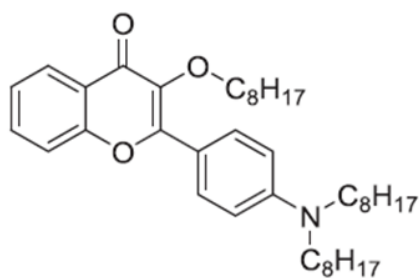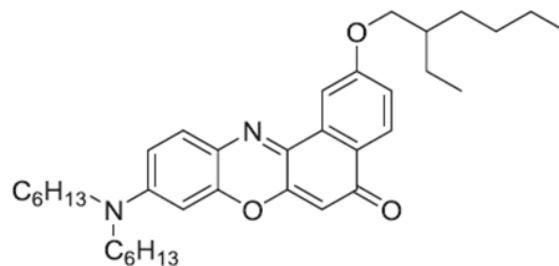
F888   **NR668**

2.2- Synthesis of Cy5.5LP and Cy7.5LP

The synthesis of Dioctadecylcyanine 5.5 tetraphenylborate (**Cy5.5LP**) and Dioctadecylcyanine 7.5 tetraphenylborate (**Cy7.5LP**) was performed by Bohdan Andreiuk.

Cy5.5LP   **Cy7.5LP**

<u>1,1,2-trimethyl-3-octadecyl-1H-benzo[e]indol-3-ium iodide (1).</u> 250 mL round-bottom flask equipped with magnetic stirring bar was charged with 1,1,2-Trimethylbenz[e]indole (1 eq., 6.88 g, 32.9 mmol) and 1-iodooctadecane (2 eq., 25 g, 65.7 mmol), 100 mL of 2-butanone was added subsequently. Reaction mixture was refluxed for 24h, then cooled down to r.t. Reaction mixture was cooled down to r.t., diethyl ether was added and formed solid part was filtered off and washed with 100 mL of diethyl ether. Obtained crystals of crude product were re-dissolved in DCM and precipitated back while by adding diethyl ether, afterwards filtered and washed with diethyl ether. Product was obtained as slightly green crystals in 76% yield (14.73g).

^{1}H NMR (400 MHz, CDCl$_3$) δ 8.10 (d, J = 8.7 Hz, 1H), 8.08 (dd, J = 8.0, 1.1 Hz, 1H), 8.04 (dd, J = 8.2, 1.3 Hz, 1H), 7.76 (d, J = 8.9 Hz, 1H), 7.72 (ddd, J = 8.3, 6.9, 1.4 Hz, 1H), 7.65 (ddd, J = 8.1, 6.9, 1.2 Hz, 1H), 4.78 (t, J = 7.7 Hz, 2H), 3.19 (s, 3H), 1.97 (p, J = 7.8 Hz, 2H), 1.87 (s, 6H), 1.52 – 1.41 (m, 2H), 1.40 – 1.30 (m, 2H), 1.28 – 1.19 (m, 26H), 0.85 (t, J = 7.0 Hz, 3H).

^{13}C NMR (100 MHz, CDCl$_3$) δ 195.25, 138.34, 137.29, 133.82, 131.56, 130.17, 128.77, 127.97, 127.74, 122.96, 112.59, 56.04, 50.56, 32.00, 29.77, 29.76, 29.73, 29.70, 29.65, 29.55, 29.43, 29.41, 29.24, 28.26, 26.92, 22.85, 22.76, 17.03, 14.18.

HRMS (m/z): [M]$^+$ calcd for C$_{33}$H$_{52}$N 462.40943; found 462.40854.

<u>Dioctadecylcyanine 5.5 chloride (2).</u>1,1,2-trimethyl-3-octadecyl-1H-benzo[e]indol-3-ium iodide (1) (1 eq., 2 g, 3.39 mmol) was placed in 50 mL round-bottom flask. 10 mL of dry pyridine was added via syringe. Then, 1,1,3,3-tetramethoxypropane (1.5 eq., 0.835 g, 0.838

mL, 5.09 mmol) was quickly added dropwise to the boiling solution of indoleninium salt using syringe. Reaction mixture was stirred under reflux for 3h. After cooling down to room temperature solvent was removed under reduced pressure. To the obtained residue 50 mL of dichloromethane were added. Obtained solution was washed three times with 1N HCl, then with brine and water. The crude product was purified by flash column chromatography on silica gel using ethyl acetate/dichloromethane (9:1) mixture as eluent. Cyanine was obtained as dark blue-greenish viscous oil in 76% yield (2.8 g).

^{1}H NMR (400 MHz, CDCl$_3$) δ 8.55 (t, J = 13.0 Hz, 2H), 8.20 (d, J = 8.5 Hz, 2H), 7.90 (d, J = 8.6 Hz, 4H), 7.64 – 7.54 (m, 2H), 7.44 (t, J = 7.5 Hz, 2H), 7.32 (d, J = 8.8 Hz, 2H), 6.74 (t, J = 12.4 Hz, 1H), 6.24 (d, J = 13.7 Hz, 2H), 4.14 (t, J = 7.5 Hz, 4H), 2.12 (s, 12H), 1.83 (p, J = 7.6 Hz, 4H), 1.46 (p, J = 7.6, 7.0 Hz, 4H), 1.40 – 1.33 (m, 4H), 1.30 – 1.18 (m, 52H), 0.85 (t, J = 6.7 Hz, 6H).

^{13}C NMR (100 MHz, CDCl$_3$) δ 174.60, 153.33, 139.40, 134.46, 131.81, 130.44, 129.94, 128.32, 127.83, 125.11, 122.65, 110.44, 103.10, 51.53, 44.64, 32.00, 29.79, 29.77, 29.74, 29.70, 29.66, 29.55, 29.48, 29.44, 27.93, 27.80, 27.08, 22.77, 14.21.

HRMS (m/z): [M]$^{+}$ calcd for C$_{69}$H$_{103}$N$_2$ 959.81158; found 959.8098.

Dioctadecylcyanine 7.5 chloride (**3**).1,1,2-trimethyl-3-octadecyl-1H-benzo[e]indol-3-ium iodide (1) (2.2 eq., 1029 mg, 1.75 mmol) and glutaconaldehydedianil hydrochloride (1 eq., 226 mg, 0.794 mmol) were mixed in 10ml of pyridine, afterwards Ac$_2$O (13.4 eq., 1087 mg, 1 mL, 10.6 mmol) was added and the reaction mixture was heated to 60 ºC while stirring and left for 3h. After reaction was finished, solvents were evaporated at vacuum, and the crude product was dissolved in DCM, washed with 0.1 N HCl (3 times), brine and water. DCM layer was dried over Na$_2$SO$_4$, the solvent was evaporated and the product was purified by column chromatography on silica (gradient DCM/MeOH 99/1 - 95/5). Product was obtained as a green solid (926 mg, 0.906 mmol, 52 %)

^{1}H NMR (400 MHz, CDCl$_3$): δ 8.16 (d, J=8Hz, 2H), 8.06 (t, J=12Hz, 2H), 7.97 (bs, 1H), 7.92 (d, J=8Hz, 4H), 7.61 (t, J=7Hz, 2H), 7.46 (t, J=7Hz, 2H), 7.35 (d, J=9Hz, 2H), 6.67 (t, J=12Hz, 2H), 6.25 (d, J=12Hz, 2H), 4.14 (bs, 4H), 2.04 (s, 12H), 1.87 (m, J=7Hz, 4H), 1.49 (m, J=7Hz, 4H), 1.39 (m, J=7Hz, 4H), 1.26 (bs, 52H), 0.88 (t, J=7Hz, 6H)

^{13}C NMR (100 MHz, CDCl$_3$): δ 173.07, 157.04, 151.02, 139.74, 133.98, 131.83, 130.59, 130.09, 128.41, 127.87, 126.27, 125.06, 122.47, 110.56, 103.39, 51.155, 44.76, 32.06, 29.842, 29.807, 29.76, 29.72, 29.60, 29.53, 29.50, 27.86, 27.14, 22.82, 14.26

HRMS (m/z): [M]$^+$ calcd. For C$_{71}$H$_{105}$N$_2$$^+$ 985.8272; found 985.8290.

<u>Dioctadecylcyanine 5.5 tetraphenylborate (Cy5.5LP).</u>

Dioctadecylcyanine 5.5 chloride (1 eq., 100 mg, 0.1 mmol) was dissolved in 5 mL of DCM, sodium tetraphenylborate (3 eq., 103 mg, 0.301 mmol) was added and the dispersion was sonicated for 5 min. TLC control has shown full conversion. Afterwards, the mixture was purified on a silica column, eluent DCM/MeOH 95/5 (product goes almost with front). Dioctadecylcyanine 5.5 tetraphenylborate (109.2 mg, 0.085 mmol, 85 %) was obtained as blue-green viscous oil and used without further characterisation.

<u>Dioctadecylcyanine 7.5 tetraphenylborate (Cy7.5LP).</u>

Dioctadecylcyanine 7.5 chloride (1 eq., 200 mg, 0.18 mmol) was dissolved in 5 mL of DCM, sodium tetraphenylborate (3 eq., 184 mg, 0.539 mmol) was added and the dispersion was sonicated for 5 min. TLC control has shown full conversion. Afterwards, the mixture was purified on a silica column, eluent DCM/MeOH 95/5 (product goes almost with front). Dioctadecylcyanine 7.5 tetraphenylborate (218 mg, 0.167 mmol, 93 %) was obtained as green viscous oil and used without further characterisation.

2.3- Preparation of lipid nanocarriers

Cy5.5LP and Cy7.5LP loaded lipid nanocarriers were produced by spontaneous nano-emulsification. Briefly, the dyes were firstly dissolved in Labrafac WL$^®$ (56 mg) at concentrations ranging from 0.1 to 1% by weight. Then, Cremophor ELP$^®$ (also called Kolliphor ELP$^®$) was added (44 mg), and the mixture was homogenized under magnetic stirring at 37°C for 10 minutes up to complete homogenisation. Finally, nanoemulsions were generated with the addition of ultrapure (Milli-Q) water (230 mg).

Spontaneous nano-emulsification was also used for the preparation of NR668 or F888 nanocarriers. The dyes (NR668 or F888) in LabrafacWL® (35 mg) at concentrations of 1% by weight (unless indicated). Then, Kolliphor® HS 15S was added (65mg), and the mixture was homogenized under magnetic stirring at 90 °C for 5 min up to complete homogenisation. Finally, nanocarriers were generated with the addition of ultrapure (Milli-Q) water (230 mg).

Solid lipid nanocarriers with the wax Suppocire C® (SupC) encapsulated NR688 was prepared with the same protocol.

2.4- Preparation of polymer nanoparticles

PLGA and PMMA-MA nanocarriers was prepared by nanoprecipitation methods. Stock solutions of polymers in acetonitrile were prepared at a concentration of 10 mg/ml. These solutions were then diluted with acetonitrile containing desired amount of dye, to the concentration of 1 or 2 mg/ml. 50 µL of the polymer solutions were then added quickly using a micropipette and under shaking (Thermomixer comfort, Eppendorf, 1000 rpm) to 450 µL of water or buffer. PLGA and PMMA-MA based nanoparticles were prepared at 21°C. The particles solution was then quickly diluted 5-fold with the same buffer. For varying the size of NCs the value of pH of buffer was changed from 7.4 to 6.4 for PMMA-MA and 3.4 for PLGA.

For PLGA SE, the single-emulsion (O/W) solvent evaporation method was adopted. Briefly, 20 mg of PLGA was dissolved into 2.5 ml of dichloromethane containing NR668 dye. This organic phase was added to 6 ml of 0.5% polyvinyl alcohol (PVA) aqueous solution and sonicated at 40 W using a probe sonicator for 5 min in an ice bath. Organic solvent was evaporated under vacuum evaporation. The nanosuspension was then centrifuged for 5 min at 10000×g to separate unloaded material and remove Ti-particles.

2.5- Nanocarriers size characterization

Dynamic light scattering measurements were performed on a Zetasizer Nano series DTS 1060 (Malvern Instruments S.A.). with a laser source of 633 nm. The size was calculated by volume statistics.

2.6- Fluorescence spectroscopy

Absorption and fluorescence spectra were recorded on a Cary 4 spectrophotometer (Varian) and a Fluoromax 4 (Jobin Yvon, Horiba) spectrofluorometer, respectively. Fluorescence emission spectra were performed at room temperature with 670 and 760 nm excitation wavelengths for Cy5.5LP and Cy7.5LP loaded nanocarriers, respectively. 520 nm excitation wavelengths was used for NR668 loaded nanocarriers and 390 nm for F888. The emission spectra were corrected from for the wavelength-dependent response of the detector. All fluorescence measurements were done using solutions with absorbance ≤ 0.1 at the wavelength of excitation. For NCs (Cy5.5LP - Cy7.5LP) , the relative fluorescence quantum yield was

measured using DiD dye in methanol (QY = 33%) as reference using excitation at 630 nm [47]. Anisotropy was measured on a Fluorolog spectrofluorometer (Jobin Yvon, Horiba) on a T-configuration.

2.7- FRET-based stability test

The stability of lipid nanocarriers was estimated using Forster resonance energy transfer (FRET) between two encapsulated dyes. 1 wt% of Cy5.5LP (with respect to Labrafac WL$^®$) as energy donor and 1 wt% of Cy7.5LP as energy acceptor were used. The nanoemulsion was diluted 10000 times from the original formulation and incubated in water and 100 % of foetal bovine serum (FBS). High dilution was needed to avoid saturation of serum by lipids of NCs. The donor in the nanocarriers was excited at 670 nm. The semi-quantitative parameter of FRET efficiency was calculated according to the following equation E = A/(A+D) [48], where A and D are the maximum of fluorescence intensity of the acceptor and donor, respectively. In case of nanocarriers containing 0.5 wt% of F888 as energy donor and 0.5 wt% of NR668 as energy acceptor, the NCs were diluted 1000 times from the original formulation and incubated in water and 10% of blank nanocarriers (without dyes). The donor in the nanocarriers was excited at 390 nm and the emission was measured for both donor and acceptor dyes.

2.8- Fluorescence correlation spectroscopy (FCS) and dyes release

FCS measurements of lipid NCs loaded with NR668 and Nile Red were performed on a two-photon platform including an Olympus IX70 inverted microscope. Two-photon excitation at 830 nm (7 to 10 mW laser output power) was provided by a mode-locked Tsunami Ti: sapphire laser pumped by a Millenia V solid state laser (Spectra Physics). The measurements were realized in a 96 well plate, using a 50 µL volume per well for light trigger release studies and 200 µL for the others. The focal spot was set about 20 µm above the plate. The normalized autocorrelation function, G(t) was calculated online by an ALV-5000E correlator (ALV, Germany) from the fluorescence fluctuations, $\delta F(t)$, by $G(\tau) = < \delta F(t)\, \delta F(t + \tau) > / < F(t) >^2$ where $< F(t) >$ is the mean fluorescence signal, and τ is the lag time. Assuming that lipid nanoparticle diffuse freely in a Gaussian excitation volume, the correlation function, $G(\tau)$, calculated from the fluorescence fluctuations was fitted according to Thompson [64]:

$$G(\tau) = \frac{1}{N}\left(1 + \frac{\tau}{\tau_d}\right)^{-1}\left(1 + \frac{1}{s^2}\,\frac{\tau}{\tau_d}\right)^{\frac{-1}{2}}$$

where τ_d is the diffusion (correlation) time, N is the mean number of fluorescent species within the two-photon excitation volume, and S is the ratio between the axial and lateral radii of the excitation volume. The excitation volume was about 0.34 fL and S was about 3 to 4. Typical data recording using dye-loaded lipid NCs diluted 1 : 10 000 from the originally prepared formulatrion. Using 6-carboxytetramethylrhodamine (TMR from Sigma-Aldrich) in water as a reference, the hydrodynamic diameter, d, of nanocarriers (NCs) was calculated as: $d_{NCs} = \tau_{d(NCs)}$ / $\tau_{d(TMR)} \times d_{TMR}$, where d_{TMR} is a hydrodynamic diameter of TMR (1.0 nm). Concentration of NCs was calculated from the number of species by: $C_{NCs} = N_{NCs}/N_{TMR} \times C_{TMR}$, where N_{NCs} and N_{TMR} are numbers of emissive species for NCs and TMR, respectively,   and C_{TMR} is a TMR concentration of 50 nM. The data were obtained based on 20 recorded correlation curves; the recording time for each curve was 10 s for NCs and 30 s for TMR.

For release studies, dye-loaded nanocarriers were diluted 10 000 fold (1.7 nM) to four different media: water, Opti-mem, blank nanocarriers at 1000-fold dilution (10-fold excess with respect to dye-loaded droplets) and 10 % of FBS in water (serum).

For light-trigger release studies, the NCs were placed into special 50 µL cuvette and the whole sample was illuminated with 532-nm laser at ~60 mW/cm^2 power density for different time (10 and 30 s, 10, 20 30 and 60 min) and we measured number of species (N) and total count rate (CPS).

For the in situ release quantification studies, a calibration of FCS parameter was done by measurement of SD, N and B for two different mixing system, the first one was 1 wt% NR668 NCs and different concentration of free calcein dyes (0.1, 0.2, 0.5, 1 and 2 µM, 3.6µM). The second system is mixture between fixed concentration of calcein (0.2µM) and variable concentration of NR668 inside NCs (0.1, 0.2 ,0.4, 0.6, 0.8 and 1%). then obtained values of the SD/SD$_0$ were plotted vs % NR668 inside NCs and the data were fitted with a linear function y=A+B*x where a = 0.08803; b = 0.96141; y is SD/SD0 and x is dye content inside LNCs (wt%).

2.9- Microscopy

For light-triggered release studies, fluorescence images were taken on a Leica DMIRE2 inverted microscope equipped with a Leica DC350FX CCD camera and a thermostatic chamber (Life Imaging Services, Basel Switzerland) for maintaining the temperature at 37◦C. Cy3 filter cube (excitation 535/50 nm, emission 610/75 nm) and DAPI filter cube (excitation 360/40 nm, emission 470/40 nm) were used for detection of NR668 and F888, respectively. A 63× HCX

PLAPO (1.32 NA) was used as an objective. To induce photo-release, the illumination for 30 s was done using the same Cy3 filter cube at $\sim$14 W/cm^2 power density of light.

2.10- Cellular studies

HeLa cells (ATCC® CCL-2) were grown in Dulbecco's modified Eagle's medium (DMEM, Gibco-Invitrogen), supplemented with 10% fetal bovine serum (FBS, Lonza) and 1% antibiotic solution (penicillin streptomycin, Gibco-Invitrogen) at 37 °C in a humidified atmosphere containing 5% CO2. Cells plated on a 75 cm^2 flask at a density of 10^6 cells/flask were harvested at 80% confluence with trypsin–EDTA (Sigma). For microscopy imaging Hela cells were seeded onto a chambered cover-glass (IBiDi) at a density of 0.1×10^6 cells/IBiDi. After 24 h, cells in the IBiDi dishes were washed 2 times with PBS (phosphate buffer saline) (Lonza). Then, a solution of dye-loaded (NR668 or F888) nanocarriers diluted at 1 : 1000 in Opti-MEM (Gibco-Invitrogen) was added. Microscopy images were taken after 30-min incubation at 37∘C, unless indicated.

For cytotoxicity, in 96-well plates, HeLa cells were seeded at a concentration of 1×10^4 cells per well in 200 µL of the DMEM growth medium and then incubated overnight at 37 °C in humidified atmosphere containing 5% CO2. Next, we added the lipid nanocarriers (1% Cy5.5LP–Cy7.5LP), by substituting the culture medium for a similar one containing variable dilutions of the nanocarriers. After incubation for 24 h, the medium was removed. Then, the wells were filled with cell culture medium containing MTT (3-(4,5-dimethylthiazol-2-yl)-2,5-diphenyltetrazolium bromide), incubated for 4 h at 37 °C, and the formazan crystals formed were dissolved by adding 100 µL of DMSO and shaked for 10 min. We measure the absorbance at 570 nm with a microplate reader (Xenius, Safas). Experiments were carried out in triplicate, and expressed as a percentage of viable cells compared to the control group.

2.11- In vivo studies in zebrafish

The transgenic line of zebrafish, Tg (flk1: eGFP) [65], expressing eGFP specifically in the endothelial cells, was used in order to visualize the vasculature. For the angiography, the embryos, 3 days after fertilization, were anaesthetized in egg water containing 0.05% phenyl thiourea and 0.04% tricaine then immobilized in 0.8% low melting point agarose. The injections were performed using a Nanoject micro injector (Drummond Scientific, Broomal, PA, USA). The glass capillary was filled with NR668-loaded nanocarriers (5 wt%) in 5 mM HEPES (1000-fold dilution) and 2.3 nL were injected in the sinus venous of the embryos. The nanocarriers

were immediately distributed in all the vasculature. The injected embryos were placed on the microscope stage and imaged within 5 min after injection. Intravital confocal microscopy was performed on a Leica SP5 fixed stage direct microscope with a 25× (NA 0.95) and 10× (NA 0.3) water immersion objectives. 488 nm argon laser line was used to excite both eGFP and the NR668 dyes, and their mission was detected by two separate PMTs in the spectral range 500–530 nm and 620–650 nm, respectively. The illuminations for the light-driven release were performed with a xenon lamp in epifluorescence mode using a 450–490 nm band pass filter. Confocal z-stacks and time lapses were recorded and treated by the Image J software (rsbweb.nih.gov/ij/). The embryos were imaged during one-hour post injection. All experiments performed with zebrafish complied with the European directive 86/609/CEE and IGBMC guidelines validated by the regional committee of ethics.

2.12- Subcutaneous tumor grafting and administration of FRET nanocarriers

Adult (10 months) immuno-deficient mice (NMRI-Foxn1nu/ Fox1nu, Janvier labs, 1) were anesthetized via gas anaesthesia (isoflurane) system prior to tumor cell grafting. Anesthetized mice were injected subcutaneously (in the flank) with 100 µL of a solution made of 50% PBS and 50% Matrigel containing 1.10^6 of D2A1 (murine mammary carcinoma) cells [49]. Tumors were grown over a period of 20 days before administrating lipid nanocarriers. The mouse studies were performed according to the Guide for Care and Use of Laboratory Animals (E67-6-482-21) and the European Directive with approval of the regional ethical committee (CREMEAS de Strasbourg, AL/73/80/02/13). Mice received food and water ad libitum; they were checked daily and tumor growth never exceeded 20 days, leading to low-size tumors with no impact on the animal's health. All efforts were made to minimize suffering and euthanasia was performed using CO2. General health status was monitored regularly by independent observers. Sacrifice of the animal was effectuated when reaching limit ethical endpoints. Before administration of the nanocarriers solution, mice were anesthetized by intraperitoneal injection of a mixture of ketamine (100 mg/kg) and xylazine (10mg/kg). The nanocarriers were administrated by retro-orbital injection (100 µL) as previously performed for other purposes [50].

2.13- In vivo whole animal FRET imaging

Whole- and live-animal imaging of the FRET signal in healthy and tumor-bearing mice was performed by using a luminograph (Night Owl, Berthold Technologies). Anesthetized mice (isoflurane) were placed repeatedly in the luminograph, and positioned either on the flank or the back. Mice were imaged using a halogen lamp, (75 W, 340–750 nm) and emission of the two dyes was collected separately using separate filters sets (630/700 nm for Cy5.5LP, and 630/820 nm for Cy7.5LP). The experiments with healthy and tumor bearing mice were repeated three times.

2.14- Calibration of the ratiometric response of NCs to disintegration

To calibrate the ratiometric response of NCs to disintegration in our in vivo imaging setup, we model the disintegration NCs by mixing intact FRET NCs with NCs containing separately donor and acceptor at low concentration, with the preservation of the same concentration of dyes: 100% integrity corresponds to FRET NCs (1% of Cy5.5LP and 1% of Cy7.5LP) diluted in PBS 1000-fold from the original formulation, while 0% integrity corresponds to a mixture of NCs containing separately donor (0.1% of Cy5.5LP) and acceptor (0.1% Cy7.5LP), both diluted at 100-fold in PBS. Intermediate mixtures were made, where the level of integrity (%) is defined as the fraction of Cy5.5LP/Cy7.5LP dyes in the FRET NCs with respect to the total amount of these dyes. They were placed into 96-well plate and imaged using the NightOwl setup. The measurements were done in triplicate. The obtained values of the A/(A+D) ratio were plotted *vs* % of integrity and the data were fit with an exponential function (1):

$$y = a + be^{c*x} \qquad\qquad (1)$$

Where $a = 0.14572$; $b = 0.1254$; $c = 0.01748$, y is A/(A+D) and x is FRET pair concentration (wt. %). As another model of the complete disintegration of NCs, solution FRET NCs diluted 1000-fold in dioxane was placed into 1 ml Eppendorf® tube and imaged by the NightOwl setup.

2.15- Image analysis of the FRET signal in living mice

The ratiometric images were built using a homemade plugin (developed by Romain Vauchelles) under ImageJ that divides the image of the 840 nm channel by that of the 700 nm channel. For each pixel, a pseudo colour scale is used for coding the ratio, while the intensity is defined by the integral intensity recorded for both channels at the corresponding pixel. Image analysis was performed by using the Fiji software [51]. The tail vein, liver and tumor were manually

delimitated and the mean intensity of the delimitated region was determined for each respective time point and channel for three healthy and three tumor-bearing mice. For both donor and acceptor channels, the signal was corrected for the background using the mice before injection (in the corresponding region of interest). Then the corrected values of A/(A+D) were converted into the FRET pair. The obtained values of FRET pair concentration were then plotted vs time and fitted using a logistic function : $y = a_2 + \frac{(a_1 - a_2)}{(1 + (\frac{x}{x_0})^p}$ where y is the FRET pair concentration (wt%); x is time; other parameters were calculated during the fitting procedure. This fit was further used to calculate the integrity half-life.

2.16- Statistical analysis

In case of animals experiments, Student's t-test was used to evaluate the statistical significance between two sample groups. The differences between the results were considered to be significant when the p-values were less than 0.05.

2.17- Bleaching of Nile Red and NR668 with Sodium Dithionite

Chemical bleaching kinetics was recorded as fluorescence intensity using Fluoromax 4 (Jobin Yvon, Horiba) spectrofluorometer. Excitation wavelength was 520 nm, while emission wavelength was 590 nm. A 0.5 M stock solution of sodium dithionite $Na_2S_2O_4$ miliQ water was used for the experiments. After 2 min of recording, to 1 mL aqueous solution of dyes loaded nanocarriers in a quartz cuvette under magnetic stirring was added an aliquot of the stock solution of dithionite to a final concentration 20 mM. Then fluorescence intensity was recorded as a function of time over 30 min while stirring.

References

[1]   J.R. Lakowicz, Principles of Fluorescence Spectroscopy Principles of Fluorescence Spectroscopy, 2006. doi:10.1007/978-0-387-46312-4.

[2]   http://www.ibs.fr/recherche/groupes-de-recherche/groupe-dynamique-et-cinetique-des-processus-moleculaires-m-weik/pixel/photophysique-des-proteines, (n.d.).

[3]   W. BECKER, Fluorescence lifetime imaging - techniques and applications, J. Microsc. 247 (2012) 119–136. doi:10.1111/j.1365-2818.2012.03618.x.

[4]   M. Sauer, J. Hofkens, J. Enderlein, Handbook of Fluorescence Spectroscopy and Imaging, 2011. doi:10.1002/9783527633500.

[5]   J.R. Lakowicz, I. Gryczynski, Z. Gryczynski, J.D. Dattelbaum, Anisotropy-Based Sensing with Reference Fluorophores, Anal. Biochem. 267 (1999) 397–405. doi:10.1006/abio.1998.3029.

[6]   R.Y. Tsien, THE GREEN FLUORESCENT PROTEIN, Annu. Rev. Biochem. 67 (1998) 509–544. doi:10.1146/annurev.biochem.67.1.509.

[7]   H. Zhu, J. Fan, J. Du, X. Peng, Fluorescent Probes for Sensing and Imaging within Specific Cellular Organelles, Acc. Chem. Res. 49 (2016) 2115–2126. doi:10.1021/acs.accounts.6b00292.

[8]   K.P. Carter, A.M. Young, A.E. Palmer, Fluorescent Sensors for Measuring Metal Ions in Living Systems, Chem. Rev. 114 (2014) 4564–4601. doi:10.1021/cr400546e.

[9]   O.A. Kucherak, S. Oncul, Z. Darwich, D.A. Yushchenko, Y. Arntz, P. Didier, Y. Mély, A.S. Klymchenko, Switchable nile red-based probe for cholesterol and lipid order at the outer leaflet of biomembranes, J. Am. Chem. Soc. 132 (2010) 4907–4916. doi:10.1021/ja100351w.

[10]   L.D. Lavis, R.T. Raines, Bright Ideas for Chemical Biology, ACS Chem. Biol. 3 (2008) 142–155. doi:10.1021/cb700248m.

[11]   M.S.T. Gon?alves, Fluorescent Labeling of Biomolecules with Organic Probes, Chem. Rev. 109 (2009) 190–212. doi:10.1021/cr0783840.

[12]   M. Beija, C.A.M. Afonso, J.M.G. Martinho, J. Nicolas, G.J. Chen, R. Wallis, D.A. Mitchell, B.R.G. Johnson, S.D. Evans, D.M. Haddleton, C. Huang, Synthesis and applications of Rhodamine derivatives as fluorescent probes, Chem. Soc. Rev. 38 (2009) 2410. doi:10.1039/b901612k.

[13]   R. Ziessel, G. Ulrich, A. Harriman, R. Ziessel, B. Donnio, C. Bourgogne, D. Guillon, P. Retailleau, R. Ziessel, K. Burgess, J.S. Lindsey, The chemistry of Bodipy: A new El Dorado for fluorescence tools, New J. Chem. 31 (2007) 496. doi:10.1039/b617972j.

[14]   Yuhui Lin,   and Ralph Weissleder, C.-H. Tung*, Novel Near-Infrared Cyanine Fluorochromes: Synthesis, Properties, and Bioconjugation, (2002). doi:10.1021/BC0155723.

[15]   † Amaresh Mishra, Rajani K. Behera, Pradipta K. Behera, and Bijaya K. Mishra, G.B. Behera*, Cyanines during the 1990s: A Review, (2000). doi:10.1021/CR990402T.

[16]   https://www.lumiprobe.com/tech/cyanine-dyes, (n.d.).

[17]   *,†,‡ Andrey S. Klymchenko, ‡ and Vasyl G. Pivovarenko, § Alexander P. Demchenko†, Elimination of the Hydrogen Bonding Effect on the Solvatochromism of 3-Hydroxyflavones, (2003). doi:10.1021/JP027315G.

[18]   M.A. Rizzo, G.H. Springer, B. Granada, D.W. Piston, An improved cyan fluorescent protein variant useful for FRET, Nat. Biotechnol. 22 (2004) 445–449. doi:10.1038/nbt945.

[19]   A.S. Klymchenko, T. Ozturk, V.G. Pivovarenko, A.P. Demchenko, A 3-hydroxychromone with dramatically improved fluorescence properties, Tetrahedron Lett. 42 (2001) 7967–7970. doi:10.1016/S0040-4039(01)01723-3.

[20]   A.S. Klymchenko, Solvatochromic and Fluorogenic Dyes as Environment-Sensitive Probes: Design and Biological Applications, Acc. Chem. Res. 50 (2017) 366–375. doi:10.1021/acs.accounts.6b00517.

[21]   R.M.-M. and, F. Sancenón, Fluorogenic and Chromogenic Chemosensors and Reagents for Anions, (2003). doi:10.1021/CR010421E.

[22]   R. Kreder, K.A. Pyrshev, Z. Darwich, O.A. Kucherak, Y. M?ly, A.S. Klymchenko, Solvatochromic Nile Red Probes with FRET Quencher Reveal Lipid Order Heterogeneity in Living and Apoptotic Cells, ACS Chem. Biol. 10 (2015) 1435–1442. doi:10.1021/cb500922m.

[23]   A.P. Alivisatos, W. Gu, C. Larabell, Quantum Dots as Cellular Probes, Annu. Rev. Biomed. Eng. 7 (2005) 55–76. doi:10.1146/annurev.bioeng.7.060804.100432.

[24]   A.P. Demchenko, Introduction to Fluorescence Sensing, Springer International Publishing, Cham, 2015. doi:10.1007/978-3-319-20780-3.

[25]   H. Kobayashi, M. Ogawa, R. Alford, P.L. Choyke, Y. Urano, New Strategies for Fluorescent Probe Design in Medical Diagnostic Imaging, Chem. Rev. 110 (2010) 2620–2640. doi:10.1021/cr900263j.

[26]   D.J. Irvine, M.A. Purbhoo, M. Krogsgaard, M.M. Davis, Direct observation of ligand recognition by T cells, Nature. 419 (2002) 845–849. doi:10.1038/nature01076.

[27]   V.J. Pansare, S. Hejazi, W.J. Faenza, R.K. Prud'homme, Review of Long-Wavelength Optical and NIR Imaging Materials: Contrast Agents, Fluorophores, and Multifunctional Nano Carriers, Chem. Mater. 24 (2012) 812–827. doi:10.1021/cm2028367.

[28]   A. Adan, G. Alizada, Y. Kiraz, Y. Baran, A. Nalbant, Flow cytometry: basic principles and applications, Crit. Rev. Biotechnol. 37 (2017) 163–176. doi:10.3109/07388551.2015.1128876.

[29]   C.E. Aitken, R.A. Marshall, J.D. Puglisi, F. Koberling, M. Patting, R. Erdmann, R. Erdmann, An Oxygen Scavenging System for Improvement of Dye Stability in Single-Molecule Fluorescence Experiments, Biophys. J. 94 (2008) 1826–1835. doi:10.1529/biophysj.107.117689.

[30] M. Fern?ndez-Su?rez, A.Y. Ting, Fluorescent probes for super-resolution imaging in living cells, Nat. Rev. Mol. Cell Biol. 9 (2008) 929–943. doi:10.1038/nrm2531.

[31] P.P. Mondal, Temporal resolution in fluorescence imaging, Front. Mol. Biosci. 1 (2014) 1–10. doi:10.3389/fmolb.2014.00011.

[32] A.C. Croce, G. Bottiroli, New light in flavin autofluorescence, Eur. J. Histochem. 59 (2015) 317–318. doi:10.4081/ejh.2015.2576.

[33] B. del Rosal, D.H. Ortgies, N. Fern??ndez, F. Sanz-Rodr??guez, D. Jaque, E.M. Rodr??guez, Overcoming Autofluorescence: Long-Lifetime Infrared Nanoparticles for Time-Gated In Vivo Imaging, Adv. Mater. (2016) 1–6. doi:10.1002/adma.201603583.

[34] S. Diao, J.L. Blackburn, G. Hong, A.L. Antaris, J. Chang, J.Z. Wu, B. Zhang, K. Cheng, C.J. Kuo, H. Dai, Fluorescence imaging in Vivo at wavelengths beyond 1500 nm, Angew. Chemie - Int. Ed. 54 (2015) 14758–14762. doi:10.1002/anie.201507473.

[35] P. Reineck, B.C. Gibson, Near-Infrared Fluorescent Nanomaterials for Bioimaging and Sensing, Adv. Opt. Mater. (2016). doi:10.1002/adom.201600446.

[36] T.M. Liu, J. Conde, T. Lipiński, A. Bednarkiewicz, C.C. Huang, Smart NIR linear and nonlinear optical nanomaterials for cancer theranostics: Prospects in photomedicine, Prog. Mater. Sci. 88 (2017) 89–135. doi:10.1016/j.pmatsci.2017.03.004.

[37] Easwaran Arunkumar, Christopher C. Forbes, and Bruce C. Noll, B.D. Smith*, Squaraine-Derived Rotaxanes: Sterically Protected Fluorescent Near-IR Dyes, (2005). doi:10.1021/JA042404N.

[38] https://www.drugs.com/pro/ic-green.html, (n.d.).

[39] N. Anton, J.P. Benoit, P. Saulnier, Design and production of nanoparticles formulated from nano-emulsion templates-A review, J. Control. Release. 128 (2008) 185–199. doi:10.1016/j.jconrel.2008.02.007.

[40] S. Hirsjärvi, S. Dufort, J. Gravier, I. Texier, Q. Yan, J. Bibette, L. Sancey, V. Josserand, C. Passirani, J.-P. Benoit, J.-L. Coll, Influence of size, surface coating and fine chemical composition on the in vitro reactivity and in vivo biodistribution of lipid nanocapsules versus lipid nanoemulsions in cancer models, Nanomedicine Nanotechnology, Biol. Med. 9 (2013) 375–387. doi:10.1016/j.nano.2012.08.005.

[41] †,⊥ Sergey K. Poznyak, *‡,§,⊥ Dmitri V. Talapin, ‡,‖ and Elena V. Shevchenko, H. Weller‡, Quantum Dot Chemiluminescence, (2004). doi:10.1021/NL049713W.

[42] D. Deli-, A. Sukhanova, I. Nabiev, Accepted Manuscript, (n.d.).

[43] P. Zrazhevskiy, X. Gao, ARTICLE Quantum dot imaging platform for single-cell molecular profiling, Nat. Commun. 4 (2013). doi:10.1038/ncomms2635.

[44] M.P. Clausen, E.C. Arnspang, B. Ballou, J.E. Bear, B.C. Lagerholm, Simultaneous multi-species tracking in live cells with quantum dot conjugates, PLoS One. 9 (2014). doi:10.1371/journal.pone.0097671.

[45] M. ?V. Yezhelyev, A. Al-Hajj, C. Morris, A. ?I. Marcus, T. Liu, M. Lewis, C. Cohen, P. Zrazhevskiy, J. ?W. Simons, A. Rogatko, S. Nie, X. Gao, R. ?M. O'Regan, In Situ

Molecular Profiling of Breast Cancer Biomarkers with Multicolor Quantum Dots, Adv. Mater. 19 (2007) 3146–3151. doi:10.1002/adma.200701983.

[46]   L. Zhou, J. Yan, L. Tong, X. Han, X. Wu, P. Guo, Quantum Dot-based Immunohistochemistry for Pathological Applications, Cancer Transl. Med. 2 (2016) 21. doi:10.4103/2395-3977.177562.

[47]   B.A. Kairdolf, X. Qian, S. Nie, Bioconjugated Nanoparticles for Biosensing, in Vivo Imaging, and Medical Diagnostics, Anal. Chem. (2017) acs.analchem.6b04873. doi:10.1021/acs.analchem.6b04873.

[48]   J. Wang, W.H. Yong, Y. Sun, P.T. Vernier, H.P. Koeffler, M.A. Gundersen, L. Marcu, Receptor-targeted quantum dots: fluorescent probes for brain tumor diagnosis, J. Biomed. Opt. 12 (2007) 44021. doi:10.1117/1.2764463.

[49]   G. Hong, J.C. Lee, J.T. Robinson, U. Raaz, L. Xie, N.F. Huang, J.P. Cooke, H. Dai, Multifunctional in vivo vascular imaging using near-infrared II fluorescence., Nat. Med. 18 (2012) 1841–6. doi:10.1038/nm.2995.

[50]   C. Li, Y. Zhang, M. Wang, Y. Zhang, G. Chen, L. Li, D. Wu, Q. Wang, In vivo real-time visualization of tissue blood flow and angiogenesis using Ag2S quantum dots in the NIR-II window, Biomaterials. 35 (2014) 393–400. doi:10.1016/j.biomaterials.2013.10.010.

[51]   M.-X. Zhao, B.-J. Zhu, The Research and Applications of Quantum Dots as Nano-Carriers for Targeted Drug Delivery and Cancer Therapy., Nanoscale Res. Lett. 11 (2016) 207. doi:10.1186/s11671-016-1394-9.

[52]   E. Oh, R. Liu, A. Nel, K.B. Gemill, M. Bilal, Y. Cohen, I.L. Medintz, Meta-analysis of cellular toxicity for cadmium-containing quantum dots, Nat Nano. 11 (2016) doi:10.1038/nnano.2015.338. doi:10.1038/nnano.2015.338.

[53]   K.M. Tsoi, Q. Dai, B.A. Alman, W.C.W. Chan, Are Quantum Dots Toxic? Exploring the Discrepancy Between Cell Culture and Animal Studies, Acc. Chem. Res. 46 (2013) 662–671. doi:10.1021/ar300040z.

[54]   W.-C. Law, K.-T. Yong, I. Roy, H. Ding, R. Hu, W. Zhao, P.N. Prasad, Aqueous-Phase Synthesis of Highly Luminescent CdTe/ZnTe Core/Shell Quantum Dots Optimized for Targeted Bioimaging, Small. 5 (2009) 1302–1310. doi:10.1002/smll.200801555.

[55]   D. Yang, P. Ma, Z. Hou, Z. Cheng, C. Li, J. Lin, D.Z. Chi, T.S.A. Hor, P. Zhang, G.K. Liu, Y. Han, X.G. Liu, S.H. Choi, H.S. Park, S.Y. Yoon, Y.D. Suh, S.H. Lee, T. Hyeon, Y.D. Suh, T. Hyeon, Current advances in lanthanide ion (Ln $^{3+}$)-based upconversion nanomaterials for drug delivery, Chem. Soc. Rev. 44 (2015) 1416–1448. doi:10.1039/C4CS00155A.

[56]   F. Auzel, Upconversion and Anti-Stokes Processes with f and d Ions in Solids, (2003). doi:10.1021/CR020357G.

[57]   B. Zhou, B. Shi, D. Jin, X. Liu, Controlling upconversion nanocrystals for emerging applications, Nat. Nanotechnol. 10 (2015) 924–936. doi:10.1038/nnano.2015.251.

[58]   C. Wang, H. Tao, L. Cheng, Z. Liu, Near-infrared light induced in?vivo photodynamic therapy of cancer based on upconversion nanoparticles, Biomaterials. 32 (2011) 6145–6154. doi:10.1016/j.biomaterials.2011.05.007.

[59]   N.M. Idris, M.K. Gnanasammandhan, J. Zhang, P.C. Ho, R. Mahendran, Y. Zhang, In vivo photodynamic therapy using upconversion nanoparticles as remote-controlled nanotransducers, Nat. Med. 18 (2012) 1580–1585. doi:10.1038/nm.2933.

[60]   J. Liu, W. Bu, L. Pan, J. Shi, NIR-triggered anticancer drug delivery by upconverting nanoparticles with integrated azobenzene-modified mesoporous silica, Angew. Chemie - Int. Ed. 52 (2013) 4375–4379. doi:10.1002/anie.201300183.

[61]   Y. Yang, F. Liu, X. Liu, B. Xing, J.C. Hummelen, H. Zhu, X. Chen, W. Liu, D. Graham, N.J. Wheate, B.G. Xing, S. Lee, X. Chen, NIR light controlled photorelease of siRNA and its targeted intracellular delivery based on upconversion nanoparticles, Nanoscale. 5 (2013) 231–238. doi:10.1039/C2NR32835F.

[62]   R. Zhang, R. Yao, B. Ding, Y. Shen, S. Shui, L. Wang, Y. Li, X. Yang, W. Tao, Fabrication of Upconverting Hybrid Nanoparticles for Near-Infrared Light Triggered Drug Release, 2014 (2014). doi:10.1155/2014/169210.

[63]   L. Cheng, K. Yang, S. Zhang, M. Shao, S. Lee, Z. Liu, Highly-sensitive multiplexed in vivo imaging using pegylated upconversion nanoparticles, Nano Res. 3 (2010) 722–732. doi:10.1007/s12274-010-0036-2.

[64]   S.H. Voon, L.V. Kiew, H.B. Lee, S.H. Lim, M.I. Noordin, A. Kamkaew, K. Burgess, L.Y. Chung, In vivo studies of nanostructure-based photosensitizers for photodynamic cancer therapy, Small. 10 (2014) 4993–5013. doi:10.1002/smll.201401416.

[65]   G. Hong, S. Diao, A.L. Antaris, H. Dai, Carbon Nanomaterials for Biological Imaging and Nanomedicinal Therapy, Chem. Rev. 115 (2015) 10816–10906. doi:10.1021/acs.chemrev.5b00008.

[66]   H. Gong, R. Peng, Z. Liu, Carbon nanotubes for biomedical imaging: The recent advances, Adv. Drug Deliv. Rev. 65 (2013) 1951–1963. doi:10.1016/j.addr.2013.10.002.

[67]   M. Karimi, N. Solati, A. Ghasemi, M.A. Estiar, M. Hashemkhani, P. Kiani, E. Mohamed, A. Saeidi, M. Taheri, P. Avci, A.R. Aref, M. Amiri, F. Baniasadi, M.R. Hamblin, Carbon nanotubes part II: a remarkable carrier for drug and gene delivery, Expert Opin. Drug Deliv. 12 (2015) 1089–1105. doi:10.1517/17425247.2015.1004309.

[68]   C. Liang, S. Diao, C. Wang, H. Gong, T. Liu, G. Hong, X. Shi, H. Dai, Z. Liu, Tumor Metastasis Inhibition by Imaging-Guided Photothermal Therapy with Single-Walled Carbon Nanotubes, Adv. Mater. 26 (2014) 5646–5652. doi:10.1002/adma.201401825.

[69]   M. Ema, M. Gamo, K. Honda, A review of toxicity studies of single-walled carbon nanotubes in laboratory animals, Regul. Toxicol. Pharmacol. 74 (2016) 42–63. doi:10.1016/j.yrtph.2015.11.015.

[70]   F. Tian, D. Cui, H. Schwarz, G.G. Estrada, H. Kobayashi, Cytotoxicity of single-wall carbon nanotubes on human fibroblasts, Toxicol. Vitr. 20 (2006) 1202–1212. doi:10.1016/j.tiv.2006.03.008.

[71]   R.M. Reilly, Carbon Nanotubes: Potential Benefits and Risks of Nanotechnology in Nuclear Medicine, J. Nucl. Med. 48 (2007) 1039–1042. doi:10.2967/jnumed.107.041723.

[72]   H. Kim, K. Chung, S. Lee, D.H. Kim, H. Lee, Near-infrared light-responsive

nanomaterials for cancer theranostics, Wiley Interdiscip. Rev. Nanomedicine Nanobiotechnology. 8 (2016) 23–45. doi:10.1002/wnan.1347.

[73] X. Yang, M. Yang, B. Pang, M. Vara, Y. Xia, Gold Nanomaterials at Work in Biomedicine, Chem. Rev. 115 (2015) 10410–10488. doi:10.1021/acs.chemrev.5b00193.

[74] M. Li, S.K. Cushing, N. Wu, Plasmon-enhanced optical sensors: a review., Analyst. 140 (2014) 386–406. doi:10.1039/c4an01079e.

[75] S. Her, D.A. Jaffray, C. Allen, Gold nanoparticles for applications in cancer radiotherapy: Mechanisms and recent advancements, Adv. Drug Deliv. Rev. (2015). doi:10.1016/j.addr.2015.12.012.

[76] J. Hu, F. Rivero, R.A. Torres, H. Loro Ramírez, E.M. Rodríguez, F. Alfonso, J. García Solé, D. Jaque, Dynamic single gold nanoparticle visualization by clinical intracoronary optical coherence tomography, J. Biophotonics. 10 (2017) 674–682. doi:10.1002/jbio.201600062.

[77] C. Kim, E.C. Cho, J. Chen, K.H. Song, L. Au, C. Favazza, Q. Zhang, C.M. Cobley, F. Gao, Y. Xia, L. V. Wang, *In Vivo* Molecular Photoacoustic Tomography of Melanomas Targeted by Bioconjugated Gold Nanocages, ACS Nano. 4 (2010) 4559–4564. doi:10.1021/nn100736c.

[78] P. Mok, S. Leow, A. Koh, H. Mohd Nizam, S. Ding, C. Luu, R. Ruhaslizan, H. Wong, W. Halim, M. Ng, R. Idrus, S. Chowdhury, C. Bastion, S. Subbiah, A. Higuchi, A. Alarfaj, K. Then, Micro-Computed Tomography Detection of Gold Nanoparticle-Labelled Mesenchymal Stem Cells in the Rat Subretinal Layer, Int. J. Mol. Sci. 18 (2017) 345. doi:10.3390/ijms18020345.

[79] M.A. Mackey, M.R.K. Ali, L.A. Austin, R.D. Near, M.A. El-Sayed, The Most Effective Gold Nanorod Size for Plasmonic Photothermal Therapy: Theory and *In Vitro* Experiments, J. Phys. Chem. B. 118 (2014) 1319–1326. doi:10.1021/jp409298f.

[80] M. Sun, D. Peng, H. Hao, J. Hu, D. Wang, K. Wang, J. Liu, X. Guo, Y. Wei, W. Gao, Thermally Triggered in Situ Assembly of Gold Nanoparticles for Cancer Multimodal Imaging and Photothermal Therapy, ACS Appl. Mater. Interfaces. 9 (2017) 10453–10460. doi:10.1021/acsami.6b16408.

[81] N. Zhang, H. Chen, A.-Y. Liu, J.-J. Shen, V. Shah, C. Zhang, J. Hong, Y. Ding, Gold conjugate-based liposomes with hybrid cluster bomb structure for liver cancer therapy, Biomaterials. 74 (2016) 280–291. doi:10.1016/j.biomaterials.2015.10.004.

[82] M.-P.N. Bui, S. Ahmed, A. Abbas, Single-Digit Pathogen and Attomolar Detection with the Naked Eye Using Liposome-Amplified Plasmonic Immunoassay, Nano Lett. 15 (2015) 6239–6246. doi:10.1021/acs.nanolett.5b02837.

[83] F. Tang, L. Li, D. Chen, Mesoporous Silica Nanoparticles: Synthesis, Biocompatibility and Drug Delivery, Adv. Mater. 24 (2012) 1504–1534. doi:10.1002/adma.201104763.

[84] S.-H. Wu, C.-Y. Mou, H.-P. Lin, V.S.Y. Lin, Y. Yamauchi, T. Okubo, R.C. Brown, V.S.Y. Lin, C.Y. Chen, Synthesis of mesoporous silica nanoparticles, Chem. Soc. Rev. 42 (2013) 3862. doi:10.1039/c3cs35405a.

[85] P. Huang, Y. Chen, H. Lin, L. Yu, L. Zhang, L. Wang, Y. Zhu, J. Shi, Molecularly

organic/inorganic hybrid hollow mesoporous organosilica nanocapsules with tumor-specific biodegradability and enhanced chemotherapeutic functionality, Biomaterials. 125 (2017) 23–37. doi:10.1016/j.biomaterials.2017.02.018.

[86]   N. Song, Y.-W. Yang, Molecular and supramolecular switches on mesoporous silica nanoparticles, Chem. Soc. Rev. 44 (2015) 3474–3504. doi:10.1039/C5CS00243E.

[87]   H.M. Teow, Z. Zhou, M. Najlah, S.R. Yusof, N.J. Abbott, A. D?Emanuele, Delivery of paclitaxel across cellular barriers using a dendrimer-based nanocarrier, Int. J. Pharm. 441 (2013) 701–711. doi:10.1016/j.ijpharm.2012.10.024.

[88]   E. Abbasi, S. Aval, A. Akbarzadeh, M. Milani, H. Nasrabadi, S. Joo, Y. Hanifehpour, K. Nejati-Koshki, R. Pashaei-Asl, S.W. Joo, Y. Hanifehpour, Dendrimers: synthesis, applications, and properties, Nanoscale Res. Lett. 9 (2014) 247. doi:10.1186/1556-276X-9-247.

[89]   R. Jevprasesphant, The influence of surface modification on the cytotoxicity of PAMAM dendrimers, Int. J. Pharm. 252 (2003) 263–266. doi:10.1016/S0378-5173(02)00623-3.

[90]   H.-J. Hsu, J. Bugno, S. Lee, S. Hong, Dendrimer-based nanocarriers: a versatile platform for drug delivery, Wiley Interdiscip. Rev. Nanomedicine Nanobiotechnology. (2016) 1–21. doi:10.1002/wnan.1409.

[91]   L. van Zuylen, M.O. Karlsson, J. Verweij, E. Brouwer, P. de Bruijn, K. Nooter, G. Stoter, A. Sparreboom, Pharmacokinetic modeling of paclitaxel encapsulation in Cremophor EL micelles, Cancer Chemother. Pharmacol. 47 (2001) 309–318. doi:10.1007/s002800000215.

[92]   D. Kessel, Properties of cremophor EL micelles probed by fluorescence., Photochem. Photobiol. 56 (1992) 447–51. http://www.ncbi.nlm.nih.gov/pubmed/1454875 (accessed June 24, 2017).

[93]   W.H. Jian, T.W. Yu, C.J. Chen, W.C. Huang, H.C. Chiu, W.H. Chiang, Indocyanine Green-Encapsulated Hybrid Polymeric Nanomicelles for Photothermal Cancer Therapy, Langmuir. 31 (2015) 6202–6210. doi:10.1021/acs.langmuir.5b00963.

[94]   S. Movassaghian, O.M. Merkel, V.P. Torchilin, Applications of polymer micelles for imaging and drug delivery, Wiley Interdiscip. Rev. Nanomedicine Nanobiotechnology. 7 (2015) 691–707. doi:10.1002/wnan.1332.

[95]   H.M. Burt, X. Zhang, P. Toleikis, L. Embree, W.L. Hunter, Development of copolymers of poly(d,l-lactide) and methoxypolyethylene glycol as micellar carriers of paclitaxel, Colloids Surfaces B Biointerfaces. 16 (1999) 161–171. doi:10.1016/S0927-7765(99)00067-3.

[96]   Z. Jin, M. Jin, C. Jiang, X. Yin, S. Jin, X. Quan, Z. Gao, Evaluation of doxorubicin-loaded pH-sensitive polymeric micelle release from tumor blood vessels and anticancer efficacy using a dorsal skin-fold window chamber model, Acta Pharmacol. Sin. 35 (2014) 839–845. doi:10.1038/aps.2014.12.

[97]   T. Thambi, V.G. Deepagan, H. Ko, Y.D. Suh, G.-R. Yi, J.Y. Lee, D.S. Lee, J.H. Park, S.C. Lee, G.-R. Yi, J.Y. Lee, D.S. Lee, J.H. Park, Biostable and bioreducible polymersomes for intracellular delivery of doxorubicin, Polym. Chem. 5 (2014) 4627–4634. doi:10.1039/C4PY00567H.

[98] V.G. Deepagan, S. Kwon, D.G. You, V.Q. Nguyen, W. Um, H. Ko, H. Lee, D.G. Jo, Y.M. Kang, J.H. Park, In situ diselenide-crosslinked polymeric micelles for ROS-mediated anticancer drug delivery, Biomaterials. 103 (2016) 56–66. doi:10.1016/j.biomaterials.2016.06.044.

[99] M. Guo, H. Mao, Y. Li, A. Zhu, H. He, H. Yang, Y. Wang, X. Tian, C. Ge, Q. Peng, X. Wang, X. Yang, X. Chen, G. Liu, H. Chen, Dual imaging-guided photothermal/photodynamic therapy using micelles, Biomaterials. 35 (2014) 4656–4666. doi:10.1016/j.biomaterials.2014.02.018.

[100] S. Sreejith, J. Joseph, M. Lin, N.V. Menon, P. Borah, H.J. Ng, Y.X. Loong, Y. Kang, S.W.K. Yu, Y. Zhao, Near-Infrared Squaraine Dye Encapsulated Micelles for in Vivo Fluorescence and Photoacoustic Bimodal Imaging, ACS Nano. 9 (2015) 5695–5704. doi:10.1021/acsnano.5b02172.

[101] I. Shulov, R. V Rodik, Y. Arntz, A. Reisch, V.I. Kalchenko, A.S. Klymchenko, Protein-Sized Bright Fluorogenic Nanoparticles Based on Cross-Linked Calixarene Micelles with Cyanine Corona., Angew. Chem. Int. Ed. Engl. 55 (2016) 15884–15888. doi:10.1002/anie.201609138.

[102] M. Elsabahy, K.L. Wooley, E. Themistou, Y. Yap, Z.A. Wintrob, P. Alexandridis, A.C. Ceacareanu, C. Cheng, R.H. Grubbs, K.L. Wooley, M. Chan, H. Li, N.S. Yew, S.H. Cheng, A.C. Boyd, J.C. Davies, U. Griesenbach, D.J. Porteous, D.N. Sheppard, F.M. Munkonge, E.W. Alton, D.R. Gill, Design of polymeric nanoparticles for biomedical delivery applications, Chem. Soc. Rev. 41 (2012) 2545. doi:10.1039/c2cs15327k.

[103] H.K. Makadia, S.J. Siegel, Poly Lactic-co-Glycolic Acid (PLGA) as Biodegradable Controlled Drug Delivery Carrier., Polymers (Basel). 3 (2011) 1377–1397. doi:10.3390/polym3031377.

[104] J.P. Rao, K.E. Geckeler, Polymer nanoparticles: Preparation techniques and size-control parameters, Prog. Polym. Sci. 36 (2011) 887–913. doi:10.1016/j.progpolymsci.2011.01.001.

[105] Z. Tian, A.D. Shaller, A.D.Q. Li, Twisted perylene dyes enable highly fluorescent and photostable nanoparticles., Chem. Commun. (Camb). (2009) 180–2. doi:10.1039/b815507k.

[106] Franca Tiarks, * and Katharina Landfester, M. Antonietti, Preparation of Polymeric Nanocapsules by Miniemulsion Polymerization, (2001). doi:10.1021/LA001276N.

[107] F. Candau, M. Pabon, J.-Y. Anquetil, Polymerizable microemulsions: some criteria to achieve an optimal formulation, Colloids Surfaces A Physicochem. Eng. Asp. 153 (1999) 47–59. doi:10.1016/S0927-7757(98)00425-7.

[108] A. Reisch, A.S. Klymchenko, Fluorescent Polymer Nanoparticles Based on Dyes: Seeking Brighter Tools for Bioimaging, Small. 12 (2016) 1968–1992. doi:10.1002/smll.201503396.

[109] N. Mendoza-Mu?oz, S. Alcal?-Alcal?, D. Quintanar-Guerrero, Preparation of Polymer Nanoparticles by the Emulsification-Solvent Evaporation Method: From Vanderhoff?s Pioneer Approach to Recent Adaptations, in: Polym. Nanoparticles Nanomedicines, Springer International Publishing, Cham, 2016: pp. 87–121. doi:10.1007/978-3-319-

41421-8_4.

[110] C.E. Mora-Huertas, H. Fessi, A. Elaissari, Influence of process and formulation parameters on the formation of submicron particles by solvent displacement and emulsification–diffusion methods, Adv. Colloid Interface Sci. 163 (2011) 90–122. doi:10.1016/j.cis.2011.02.005.

[111] A. Reisch, A. Runser, Y. Arntz, Y. Mély, A.S. Klymchenko, Charge-controlled nanoprecipitation as a modular approach to ultrasmall polymer nanocarriers: Making bright and stable nanoparticles, ACS Nano. 9 (2015) 5104–5116. doi:10.1021/acsnano.5b00214.

[112] X. Zhu, J. Wu, W. Shan, W. Tao, L. Zhao, J.M. Lim, M. D'Ortenzio, R. Karnik, Y. Huang, J. Shi, O.C. Farokhzad, Polymeric Nanoparticles Amenable to Simultaneous Installation of Exterior Targeting and Interior Therapeutic Proteins, Angew. Chemie - Int. Ed. 55 (2016) 3309–3312. doi:10.1002/anie.201509183.

[113] M. Tripathy, E.S. McGarrity, M.E. Mackay, J.-U. Sommer, R. Serban, D.E. Shumaker, C.S. Woodward, S.Z.D. Cheng, Y. Li, V. Pryamitsyn, V. Ganesan, J. Ilavsky, P. Thiyagarajan, R.H. Colby, J.F. Douglas, Self-assembly of polymer-linked nanoparticles and scaling behavior in the assembled phase, Soft Matter. 13 (2017) 2475–2482. doi:10.1039/C7SM00230K.

[114] O.C. Farokhzad, J. Cheng, B.A. Teply, I. Sherifi, S. Jon, P.W. Kantoff, J.P. Richie, R. Langer, Targeted nanoparticle-aptamer bioconjugates for cancer chemotherapy in vivo, Proc. Natl. Acad. Sci. 103 (2006) 6315–6320. doi:10.1073/pnas.0601755103.

[115] J. Shi, P.W. Kantoff, R. Wooster, O.C. Farokhzad, Cancer nanomedicine: progress, challenges and opportunities, Nat. Publ. Gr. (2016). doi:10.1038/nrc.2016.108.

[116] C. Corbo, R. Molinaro, M. Tabatabaei, O.C. Farokhzad, M. Mahmoudi, Personalized protein corona on nanoparticles and its clinical implications, Biomater. Sci. (2017). doi:10.1039/C6BM00921B.

[117] N. Kamaly, B. Yameen, J. Wu, O.C. Farokhzad, Degradable Controlled-Release Polymers and Polymeric Nanoparticles: Mechanisms of Controlling Drug Release, Chem. Rev. 116 (2016) 2602–2663. doi:10.1021/acs.chemrev.5b00346.

[118] C.J. Hu, R.H. Fang, K. Wang, B.T. Luk, S. Thamphiwatana, D. Dehaini, P. Nguyen, P. Angsantikul, C.H. Wen, A. V Kroll, C. Carpenter, M. Ramesh, V. Qu, S.H. Patel, J. Zhu, W. Shi, F.M. Hofman, T.C. Chen, W. Gao, K. Zhang, S. Chien, L. Zhang, Nanoparticle biointerfacing by platelet membrane cloaking., Nature. 526 (2015) 118–21. doi:10.1038/nature15373.

[119] A. Reisch, P. Didier, L. Richert, S. Oncul, Y. Arntz, Y. Mély, A.S. Klymchenko, Collective fluorescence switching of counterion-assembled dyes in polymer nanoparticles, Nat. Commun. 5 (2014) 4089. doi:10.1038/ncomms5089.

[120] G.T. Dempsey, J.C. Vaughan, K.H. Chen, M. Bates, X. Zhuang, Evaluation of fluorophores for optimal performance in localization-based super-resolution imaging, Nat. Methods. 8 (2011) 1027–1036. doi:10.1038/nmeth.1768.

[121] D. Van Der Zwaag, N. Vanparijs, S. Wijnands, R. De Rycke, B.G. De Geest, L. Albertazzi, Super Resolution Imaging of Nanoparticles Cellular Uptake and Trafficking,

ACS Appl. Mater. Interfaces. 8 (2016) 6391–6399. doi:10.1021/acsami.6b00811.

[122] A.D. Bangham, M.M. Standish, J.C. Watkins, Diffusion of univalent ions across the lamellae of swollen phospholipids., J. Mol. Biol. 13 (1965) 238–52. http://www.ncbi.nlm.nih.gov/pubmed/5859039 (accessed June 28, 2017).

[123] Y. Panahi, M. Farshbaf, M. Mohammadhosseini, M. Mirahadi, R. Khalilov, S. Saghfi, A. Akbarzadeh, Recent advances on liposomal nanoparticles: synthesis, characterization and biomedical applications, Artif. Cells, Nanomedicine, Biotechnol. 1401 (2017) 1–12. doi:10.1080/21691401.2017.1282496.

[124] M. Al-Remawi, A. Elsayed, I. Maghrabi, M. Hamaidi, N. Jaber, Chitosan/lecithin liposomal nanovesicles as an oral insulin delivery system, Pharm. Dev. Technol. 22 (2017) 390–398. doi:10.1080/10837450.2016.1213745.

[125] E. Veneti, R.S. Tu, D.T. Auguste, RGD-Targeted Liposome Binding and Uptake on Breast Cancer Cells Is Dependent on Elastin Linker Secondary Structure, Bioconjug. Chem. 27 (2016) 1813–1821. doi:10.1021/acs.bioconjchem.6b00205.

[126] E.M. Davidson, S. Haroutounian, L. Kagan, M. Naveh, A. Aharon, Y. Ginosar, A Novel Proliposomal Ropivacaine Oil, Anesth. Analg. 122 (2016) 1663–1672. doi:10.1213/ANE.0000000000001200.

[127] Y. Lee, D.H. Thompson, Stimuli-responsive liposomes for drug delivery, (2017). doi:10.1002/wnan.1450.

[128] J.M. Caster, A.N. Patel, T. Zhang, A. Wang, Investigational nanomedicines in 2016: a review of nanotherapeutics currently undergoing clinical trials, Wiley Interdiscip. Rev. Nanomedicine Nanobiotechnology. 9 (2017) e1416. doi:10.1002/wnan.1416.

[129] Y. (Chezy) Barenholz, Doxil® — The first FDA-approved nano-drug: Lessons learned, J. Control. Release. 160 (2012) 117–134. doi:10.1016/j.jconrel.2012.03.020.

[130] U. Bulbake, S. Doppalapudi, N. Kommineni, W. Khan, Liposomal formulations in clinical use: An updated review, Pharmaceutics. 9 (2017) 1–33. doi:10.3390/pharmaceutics9020012.

[131] D. Mellal, A. Zumbuehl, Exit-strategies – smart ways to release phospholipid vesicle cargo, J. Mater. Chem. B. 2 (2014) 247. doi:10.1039/c3tb21086c.

[132] C. Zhan, W. Wang, J.B. McAlvin, S. Guo, B.P. Timko, C. Santamaria, D.S. Kohane, Phototriggered Local Anesthesia, Nano Lett. 16 (2016) 177–181. doi:10.1021/acs.nanolett.5b03440.

[133] A. H?gset, Photochemical internalisation in drug and gene delivery, Adv. Drug Deliv. Rev. 56 (2004) 95–115. doi:10.1016/j.addr.2003.08.016.

[134] S. Guha, S.K. Shaw, G.T. Spence, F.M. Roland, B.D. Smith, Clean Photothermal Heating and Controlled Release from Near-Infrared Dye Doped Nanoparticles without Oxygen Photosensitization, Langmuir. 31 (2015) 7826–7834. doi:10.1021/acs.langmuir.5b01878.

[135] T. Lajunen, L.S. Kontturi, L. Viitala, M. Manna, O. Cramariuc, T. R??g, A. Bunker, T. Laaksonen, T. Viitala, L. Murtom??ki, A. Urtti, Indocyanine Green-Loaded Liposomes

for Light-Triggered Drug Release, Mol. Pharm. 13 (2016) 2095–2107. doi:10.1021/acs.molpharmaceut.6b00207.

[136] H.J. Yoon, H.S. Lee, J.Y. Lim, J.H. Park, Liposomal Indocyanine Green for Enhanced Photothermal Therapy, ACS Appl. Mater. Interfaces. 9 (2017) 5683–5691. doi:10.1021/acsami.6b16801.

[137] C. Schwarz, W. Mehnert, J.S. Lucks, R.H. Müller, Solid lipid nanoparticles (SLN) for controlled drug delivery. I. Production, characterization and sterilization, J. Control. Release. 30 (1994) 83–96. doi:10.1016/0168-3659(94)90047-7.

[138] C. Freitas, J.S. Lucks, R.H. Müller, P238 effect of storage conditions on long-term stability of "solid lipid nanoparticles" (SLN) in aqueous dispersion, Eur. J. Pharm. Sci. 2 (1994) 178. doi:10.1016/0928-0987(94)90411-1.

[139] W. Mehnert, Solid lipid nanoparticles Production, characterization and applications, Adv. Drug Deliv. Rev. 47 (2001) 165–196. doi:10.1016/S0169-409X(01)00105-3.

[140] K. Jores, W. Mehnert, M. Drechsler, H. Bunjes, C. Johann, K. Mäder, Investigations on the structure of solid lipid nanoparticles (SLN) and oil-loaded solid lipid nanoparticles by photon correlation spectroscopy, field-flow fractionation and transmission electron microscopy, J. Control. Release. 95 (2004) 217–227. doi:10.1016/j.jconrel.2003.11.012.

[141] S. Mukherjee, S. Ray, R.S. Thakur, Solid lipid nanoparticles: a modern formulation approach in drug delivery system., Indian J. Pharm. Sci. 71 (2009) 349–58. doi:10.4103/0250-474X.57282.

[142] R. Müller, Solid lipid nanoparticles (SLN) for controlled drug delivery – a review of the state of the art, Eur. J. Pharm. Biopharm. 50 (2000) 161–177. doi:10.1016/S0939-6411(00)00087-4.

[143] E.B. Souto, C. Anselmi, M. Centini, R.H. Müller, Preparation and characterization of n-dodecyl-ferulate-loaded solid lipid nanoparticles (SLN®), Int. J. Pharm. 295 (2005) 261–268. doi:10.1016/j.ijpharm.2005.02.005.

[144] M. Muchow, P. Maincent, R.H. Müller, Lipid Nanoparticles with a Solid Matrix (SLN®, NLC®, LDC®) for Oral Drug Delivery, Drug Dev. Ind. Pharm. 34 (2008) 1394–1405. doi:10.1080/03639040802130061.

[145] N. Centre, T. Electrochemistry, Solid lipid nanoparticles as attractive drug vehicles : Composition , properties and therapeutic strategies, 68 (2016) 982–994. doi:10.1016/j.msec.2016.05.119.

[146] N. Matougui, L. Boge, A.C. Groo, A. Umerska, L. Ringstad, H. Bysell, P. Saulnier, Lipid-based nanoformulations for peptide delivery, Int. J. Pharm. 502 (2016) 80–97. doi:10.1016/j.ijpharm.2016.02.019.

[147] R. Dal Magro, F. Ornaghi, I. Cambianica, S. Beretta, F. Re, C. Musicanti, R. Rigolio, E. Donzelli, A. Canta, E. Ballarini, G. Cavaletti, P. Gasco, G. Sancini, ApoE-modified solid lipid nanoparticles: A feasible strategy to cross the blood-brain barrier, J. Control. Release. 249 (2017) 103–110. doi:10.1016/j.jconrel.2017.01.039.

[148] N. Gandomi, R. Varshochian, F. Atyabi, M.H. Ghahremani, M. Sharifzadeh, M. Amini, R. Dinarvand, Solid lipid nanoparticles surface modified with anti-Contactin-2 or anti-

Neurofascin for brain-targeted delivery of medicines, Pharm. Dev. Technol. 22 (2017) 426–435. doi:10.1080/10837450.2016.1226901.

[149] M. Nooli, N. Chella, H. Kulhari, N.R. Shastri, R. Sistla, Solid lipid nanoparticles as vesicles for oral delivery of olmesartan medoxomil: formulation, optimization and *in vivo* evaluation, Drug Dev. Ind. Pharm. 43 (2017) 611–617. doi:10.1080/03639045.2016.1275666.

[150] D. Kaklotar, P. Agrawal, A. Abdulla, R.P. Singh, A.K. Mehata, S. Singh, B. Mishra, B.L. Pandey, A. Trigunayat, M.S. Muthu, Transition from passive to active targeting of oral insulin nanomedicines: enhancement in bioavailability and glycemic control in diabetes, Nanomedicine. 11 (2016) 1465–1486. doi:10.2217/nnm.16.43.

[151] L. Arana, C. Salado, S. Vega, O. Aizpurua-Olaizola, I. de la Arada, T. Suarez, A. Usobiaga, J.L.R. Arrondo, A. Alonso, F.M. Goñi, I. Alkorta, Solid lipid nanoparticles for delivery of Calendula officinalis extract, Colloids Surfaces B Biointerfaces. 135 (2015) 18–26. doi:10.1016/j.colsurfb.2015.07.020.

[152] J. Pardeike, A. Hommoss, R.H. Müller, Lipid nanoparticles (SLN, NLC) in cosmetic and pharmaceutical dermal products, Int. J. Pharm. 366 (2009) 170–184. doi:10.1016/j.ijpharm.2008.10.003.

[153] P.S. Apaolaza, A. del Pozo-Rodríguez, M.A. Solinís, J.M. Rodríguez, U. Friedrich, J. Torrecilla, B.H.F. Weber, A. Rodríguez-Gascón, Structural recovery of the retina in a retinoschisin-deficient mouse after gene replacement therapy by solid lipid nanoparticles, Biomaterials. 90 (2016) 40–49. doi:10.1016/j.biomaterials.2016.03.004.

[154] R.H. Müller, M. Radtke, S.A. Wissing, Solid lipid nanoparticles (SLN) and nanostructured lipid carriers (NLC) in cosmetic and dermatological preparations, Adv. Drug Deliv. Rev. 54 (2002) S131–S155. doi:10.1016/S0169-409X(02)00118-7.

[155] R.. Müller, M. Radtke, S.. Wissing, Nanostructured lipid matrices for improved microencapsulation of drugs, Int. J. Pharm. 242 (2002) 121–128. doi:10.1016/S0378-5173(02)00180-1.

[156] V. Jenning, A.F. Thünemann, S.H. Gohla, Characterisation of a novel solid lipid nanoparticle carrier system based on binary mixtures of liquid and solid lipids, Int. J. Pharm. 199 (2000) 167–177. doi:10.1016/S0378-5173(00)00378-1.

[157] F. Tamjidi, M. Shahedi, J. Varshosaz, A. Nasirpour, Nanostructured lipid carriers (NLC): A potential delivery system for bioactive food molecules, Innov. Food Sci. Emerg. Technol. 19 (2013) 29–43. doi:10.1016/j.ifset.2013.03.002.

[158] W.A. Kasongo, J. Pardeike, R.H. Müller, R.B. Walker, Selection and Characterization of Suitable Lipid Excipients for use in the Manufacture of Didanosine-Loaded Solid Lipid Nanoparticles and Nanostructured Lipid Carriers, J. Pharm. Sci. 100 (2011) 5185–5196. doi:10.1002/jps.22711.

[159] A. Babazadeh, B. Ghanbarzadeh, H. Hamishehkar, Formulation of food grade nanostructured lipid carrier (NLC) for potential applications in medicinal-functional foods, J. Drug Deliv. Sci. Technol. 39 (2017) 50–58. doi:10.1016/j.jddst.2017.03.001.

[160] J.C. Schwarz, N. Baisaeng, M. Hoppel, M. Löw, C.M. Keck, C. Valenta, Ultra-small NLC for improved dermal delivery of coenyzme Q10, Int. J. Pharm. 447 (2013) 213–

217. doi:10.1016/j.ijpharm.2013.02.037.

[161] T. Courant, E. Bayon, H.L. Reynaud-Dougier, C. Villiers, M. Menneteau, P.N. Marche, F.P. Navarro, Tailoring nanostructured lipid carriers for the delivery of protein antigens: Physicochemical properties versus immunogenicity studies, Biomaterials. 136 (2017) 29–42. doi:10.1016/j.biomaterials.2017.05.001.

[162] I. Texier, M. Goutayer, A. Da Silva, L. Guyon, N. Djaker, V. Josserand, E. Neumann, J. Bibette, F. Vinet, Cyanine-loaded lipid nanoparticles for improved in vivo fluorescence imaging, J. Biomed. Opt. 14 (2009) 54005. doi:10.1117/1.3213606.

[163] J. Gravier, F.P. Navarro, T. Delmas, F. Mittler, A.-C. Couffin, F. Vinet, I. Texier, Lipidots: competitive organic alternative to quantum dots for in vivo fluorescence imaging, J. Biomed. Opt. 16 (2011) 96013. doi:10.1117/1.3625405.

[164] F.P. Navarro, M. Berger, S. Guillermet, V. Josserand, L. Guyon, E. Neumann, F. Vinet, I. Texier, Lipid nanoparticle vectorization of IndoCyanine Green improves fluorescence imaging for tumor diagnosis and lymph node resection, J. Biomed. Nanotechnol. 8 (2012) 730–741. doi:10.1166/jbn.2012.1430.

[165] A. Jacquart, M. Kéramidas, J. Vollaire, R. Boisgard, G. Pottier, E. Rustique, F. Mittler, F.P. Navarro, J. Boutet, J.-L. Coll, I. Texier, LipImage™ 815: novel dye-loaded lipid nanoparticles for long-term and sensitive in vivo near-infrared fluorescence imaging., J. Biomed. Opt. 18 (2013) 101311. doi:10.1117/1.JBO.18.10.101311.

[166] Q. Cabon, D. Sayag, I. Texier, F. Navarro, R. Boisgard, D. Virieux-Watrelot, F. Ponce, C. Carozzo, Evaluation of intraoperative fluorescence imaging–guided surgery in cancer-bearing dogs: a prospective proof-of-concept phase II study in 9 cases, Transl. Res. 170 (2016) 73–88. doi:10.1016/j.trsl.2015.12.001.

[167] D. Sayag, Q. Cabon, I. Texier, F.P. Navarro, R. Boisgard, D. Virieux-Watrelot, C. Carozzo, F. Ponce, Phase-0/phase-I study of dye-loaded lipid nanoparticles for near-infrared fluorescence imaging in healthy dogs, Eur. J. Pharm. Biopharm. 100 (2016) 85–93. doi:10.1016/j.ejpb.2016.01.001.

[168] B. Heurtault, P. Saulnier, B. Pech, J.-E. Proust, J.-P. Benoit, A novel phase inversion-based process for the preparation of lipid nanocarriers., Pharm. Res. 19 (2002) 875–80. http://www.ncbi.nlm.nih.gov/pubmed/12134960 (accessed July 11, 2017).

[169] A. Lamprecht, Y. Bouligand, J.-P. Benoit, New lipid nanocapsules exhibit sustained release properties for amiodarone., J. Control. Release. 84 (2002) 59–68. http://www.ncbi.nlm.nih.gov/pubmed/12399168 (accessed July 11, 2017).

[170] I. Minkov, T. Ivanova, I. Panaiotov, J. Proust, P. Saulnier, Reorganization of lipid nanocapsules at air–water interface, Colloids Surfaces B Biointerfaces. 45 (2005) 14–23. doi:10.1016/j.colsurfb.2005.03.009.

[171] I. Minkov, T. Ivanova, I. Panaiotov, J. Proust, P. Saulnier, Reorganization of lipid nanocapsules at air–water interface, Colloids Surfaces B Biointerfaces. 44 (2005) 197–203. doi:10.1016/j.colsurfb.2005.07.001.

[172] N.T. Huynh, C. Passirani, P. Saulnier, J.P. Benoit, Lipid nanocapsules: A new platform for nanomedicine, Int. J. Pharm. 379 (2009) 201–209. doi:10.1016/j.ijpharm.2009.04.026.

[173] S. Peltier, J.-M. Oger, F. Lagarce, W. Couet, J.-P. Benoît, Enhanced Oral Paclitaxel Bioavailability After Administration of Paclitaxel-Loaded Lipid Nanocapsules, Pharm. Res. 23 (2006) 1243–1250. doi:10.1007/s11095-006-0022-2.

[174] M.M. Eissa, R.M. El-Moslemany, A.A. Ramadan, E.I. Amer, M.Z. El-Azzouni, L.K. El-Khordagui, Miltefosine Lipid Nanocapsules for Single Dose Oral Treatment of Schistosomiasis Mansoni: A Preclinical Study, PLoS One. 10 (2015) e0141788. doi:10.1371/journal.pone.0141788.

[175] E. Roger, F. Lagarce, J.-P. Benoit, The gastrointestinal stability of lipid nanocapsules, Int. J. Pharm. 379 (2009) 260–265. doi:10.1016/j.ijpharm.2009.05.069.

[176] E. Roger, J.-C. Gimel, C. Bensley, A.S. Klymchenko, J.-P. Benoit, Lipid nanocapsules maintain full integrity after crossing a human intestinal epithelium model, J. Control. Release. 253 (2017) 11–18. doi:10.1016/j.jconrel.2017.03.005.

[177] D.J. McClements, P. Gayet, J.P. Benoit, P. Saulnier, J.M. Gao, G. Mustafa, S. Shafiq, Nanoemulsions versus microemulsions: terminology, differences, and similarities, Soft Matter. 8 (2012) 1719–1729. doi:10.1039/C2SM06903B.

[178] S. Tan, J. Stanslas, M. Basri, A. Karjiban R.A., B. Kirby, D. Sani, H. Basri, Nanoemulsion-based Parenteral Drug Delivery System of Carbamazepine: Preparation, Characterization, Stability Evaluation and Blood-Brain Pharmacokinetics, Curr. Drug Deliv. 12 (2015) 795–804. doi:10.2174/1567201812666150901112544.

[179] P.E. Makidon, S.S. Nigavekar, A.U. Bielinska, N. Mank, A.M. Shetty, J. Suman, J. Knowlton, A. Myc, T. Rook, J.R. Baker, Characterization of Stability and Nasal Delivery Systems for Immunization with Nanoemulsion-Based Vaccines, J. Aerosol Med. Pulm. Drug Deliv. 23 (2010) 77–89. doi:10.1089/jamp.2009.0766.

[180] R.R. Lala, N.G. Awari, Nanoemulsion-based gel formulations of COX-2 inhibitors for enhanced efficacy in inflammatory conditions, Appl. Nanosci. 4 (2014) 143–151. doi:10.1007/s13204-012-0177-6.

[181] S. Khani, F. Keyhanfar, A. Amani, Design and evaluation of oral nanoemulsion drug delivery system of mebudipine, Drug Deliv. 23 (2016) 2035–2043. doi:10.3109/10717544.2015.1088597.

[182] H.S. Mahajan, M.S. Mahajan, P.P. Nerkar, A. Agrawal, Nanoemulsion-based intranasal drug delivery system of saquinavir mesylate for brain targeting, Drug Deliv. 21 (2014) 148–154. doi:10.3109/10717544.2013.838014.

[183] H.O. Ammar, H.A. Salama, M. Ghorab, A.A. Mahmoud, Nanoemulsion as a Potential Ophthalmic Delivery System for Dorzolamide Hydrochloride, AAPS PharmSciTech. 10 (2009) 808–819. doi:10.1208/s12249-009-9268-4.

[184] D.J. McClements, Advances in fabrication of emulsions with enhanced functionality using structural design principles, Curr. Opin. Colloid Interface Sci. 17 (2012) 235–245. doi:10.1016/j.cocis.2012.06.002.

[185] D.J. McClements, J. Rao, Food-Grade Nanoemulsions: Formulation, Fabrication, Properties, Performance, Biological Fate, and Potential Toxicity, Crit. Rev. Food Sci. Nutr. 51 (2011) 285–330. doi:10.1080/10408398.2011.559558.

[186] L. Salvia-Trujillo, R. Soliva-Fortuny, M.A. Rojas-Graü, D.J. McClements, O. Martín-Belloso, Edible Nanoemulsions as Carriers of Active Ingredients: A Review, Annu. Rev. Food Sci. Technol. 8 (2017) 439–466. doi:10.1146/annurev-food-030216-025908.

[187] V.K. Pawar, S.B. Panchal, Y. Singh, J.G. Meher, K. Sharma, P. Singh, H.K. Bora, A. Singh, D. Datta, M.K. Chourasia, Immunotherapeutic vitamin E nanoemulsion synergies the antiproliferative activity of paclitaxel in breast cancer cells via modulating Th1 and Th2 immune response, J. Control. Release. 196 (2014) 295–306. doi:10.1016/j.jconrel.2014.10.010.

[188] B. Ozturk, S. Argin, M. Ozilgen, D.J. McClements, Formation and stabilization of nanoemulsion-based vitamin E delivery systems using natural biopolymers: Whey protein isolate and gum arabic, Food Chem. 188 (2015) 256–263. doi:10.1016/j.foodchem.2015.05.005.

[189] M.E. Helgeson, Colloidal behavior of nanoemulsions: Interactions, structure, and rheology, Curr. Opin. Colloid Interface Sci. 25 (2016) 39–50. doi:10.1016/j.cocis.2016.06.006.

[190] G.L. Hasenhuettl, R.W. Hartel, Food emulsifiers and their applications, Springer, 2008.

[191] T. Zhang, D. Dong, D. Lu, S. Wang, B. Wu, Cremophor EL-based nanoemulsion enhances transcellular permeation of emodin through glucuronidation reduction in UGT1A1-overexpressing MDCKII cells, Int. J. Pharm. 501 (2016) 190–198. doi:10.1016/j.ijpharm.2016.01.067.

[192] A. Azeem, M. Rizwan, F.J. Ahmad, Z. Iqbal, R.K. Khar, M. Aqil, S. Talegaonkar, Nanoemulsion components screening and selection: a technical note., AAPS PharmSciTech. 10 (2009) 69–76. doi:10.1208/s12249-008-9178-x.

[193] V. Klang, C. Valenta, Lecithin-based nanoemulsions, J. Drug Deliv. Sci. Technol. 21 (2011) 55–76. doi:10.1016/S1773-2247(11)50006-1.

[194] C. BRUSEWITZ, A. SCHENDLER, A. FUNKE, T. WAGNER, R. LIPP, Novel poloxamer-based nanoemulsions to enhance the intestinal absorption of active compounds, Int. J. Pharm. 329 (2007) 173–181. doi:10.1016/j.ijpharm.2006.08.022.

[195] S. Uluata, E.A. Decker, D.J. McClements, Optimization of Nanoemulsion Fabrication Using Microfluidization: Role of Surfactant Concentration on Formation and Stability, Food Biophys. 11 (2016) 52–59. doi:10.1007/s11483-015-9416-1.

[196] S.J. Lee, S.J. Choi, Y. Li, E.A. Decker, D.J. McClements, Protein-Stabilized Nanoemulsions and Emulsions: Comparison of Physicochemical Stability, Lipid Oxidation, and Lipase Digestibility, J. Agric. Food Chem. 59 (2011) 415–427. doi:10.1021/jf103511v.

[197] K.J. Scheller, S.J. Williams, A.J. Lawrence, B. Jarrott, E. Djouma, An improved method to prepare an injectable microemulsion of the galanin-receptor 3 selective antagonist, SNAP 37889, using Kolliphor® HS 15, MethodsX. 1 (2014) 212–216. doi:10.1016/j.mex.2014.09.003.

[198] D.J. McClements, Food emulsions : principles, practices, and techniques, CRC Press, 2005.

[199] Y. Singh, J.G. Meher, K. Raval, F.A. Khan, M. Chaurasia, N.K. Jain, M.K. Chourasia, Nanoemulsion: Concepts, development and applications in drug delivery, J. Control. Release. 252 (2017) 28–49. doi:10.1016/j.jconrel.2017.03.008.

[200] J.-U.A.H. Junghanns, R.H. Müller, Nanocrystal technology, drug delivery and clinical applications., Int. J. Nanomedicine. 3 (2008) 295–309. http://www.ncbi.nlm.nih.gov/pubmed/18990939 (accessed July 12, 2017).

[201] T.S.H. Leong, T.J. Wooster, S.E. Kentish, M. Ashokkumar, Minimising oil droplet size using ultrasonic emulsification, Ultrason. Sonochem. 16 (2009) 721–727. doi:10.1016/j.ultsonch.2009.02.008.

[202] † P. Izquierdo, † J. Esquena, ‡ Th. F. Tadros, ‡ C. Dederen, †,§ M. J. Garcia, † and N. Azemar, † C. Solans*, Formation and Stability of Nano-Emulsions Prepared Using the Phase Inversion Temperature Method, (2001). doi:10.1021/LA010808C.

[203] P. Izquierdo, J. Esquena, T.F. Tadros, J.C. Dederen, J. Feng, M.J. Garcia-Celma, N. Azemar, C. Solans, Phase Behavior and Nano-emulsion Formation by the Phase Inversion Temperature Method, Langmuir. 20 (2004) 6594–6598. doi:10.1021/la049566h.

[204] C. Solans, D. Morales, M. Homs, Spontaneous emulsification, Curr. Opin. Colloid Interface Sci. 22 (2016) 88–93. doi:10.1016/j.cocis.2016.03.002.

[205] N. Anton, T.F. Vandamme, The universality of low-energy nano-emulsification, Int. J. Pharm. 377 (2009) 142–147. doi:10.1016/j.ijpharm.2009.05.014.

[206] N. Anton, F. Hallouard, M.F. Attia, T.F. Vandamme, Nano-emulsions for Drug Delivery and Biomedical Imaging, in: Springer, Cham, 2016: pp. 273–300. doi:10.1007/978-3-319-43525-1_11.

[207] A. Gupta, H.B. Eral, T.A. Hatton, P.S. Doyle, Nanoemulsions: formation, properties and applications, Soft Matter. 12 (2016) 2826–2841. doi:10.1039/C5SM02958A.

[208] K. Rahn-Chique, A.M. Puertas, M.S. Romero-Cano, C. Rojas, G. Urbina-Villalba, Nanoemulsion stability: Experimental evaluation of the flocculation rate from turbidity measurements, Adv. Colloid Interface Sci. 178 (2012) 1–20. doi:10.1016/j.cis.2012.05.001.

[209] T. Tadros, P. Izquierdo, J. Esquena, C. Solans, Formation and stability of nano-emulsions, 109 (2004) 303–318. doi:10.1016/j.cis.2003.10.023.

[210] A. Gupta, H.B. Eral, T.A. Hatton, P.S. Doyle, and applications, Soft Matter. 12 (2016) 2826–2841. doi:10.1039/C5SM02958A.

[211] I.M. Lifshitz, V.V. Slyozov, The kinetics of precipitation from supersaturated solid solutions, J. Phys. Chem. Solids. 19 (1961) 35–50. doi:10.1016/0022-3697(61)90054-3.

[212] T. Delmas, H. Piraux, A.-C. Couffin, I. Texier, F. Vinet, P. Poulin, M.E. Cates, J. Bibette, How To Prepare and Stabilize Very Small Nanoemulsions, Langmuir. 27 (2011) 1683–1692. doi:10.1021/la104221q.

[213] † P. Izquierdo, † J. Esquena, ‡ Th. F. Tadros, ‡ C. Dederen, †,§ M. J. Garcia, † and N. Azemar, † C. Solans*, Formation and Stability of Nano-Emulsions Prepared Using the

Phase Inversion Temperature Method, (2001). doi:10.1021/LA010808C.

[214] L. Salvia-trujillo, R. Soliva-fortuny, M.A. Rojas-gra, D.J. Mcclements, O. Mart, Edible Nanoemulsions as Carriers of Active Ingredients : A Review, (2017). doi:10.1146/annurev-food-030216-025908.

[215] M.N. Yukuyama, D.D.M. Ghisleni, T.J.A. Pinto, N.A. Bou-Chacra, Nanoemulsion: Process selection and application in cosmetics - A review, Int. J. Cosmet. Sci. 38 (2016) 13–24. doi:10.1111/ics.12260.

[216] A. Sasikumar, K. Kamalasanan, Nanomedicine for prostate cancer using nanoemulsion: A review, J. Control. Release. 260 (2017) 111–123. doi:10.1016/j.jconrel.2017.06.001.

[217] S. Ganta, M. Talekar, A. Singh, T.P. Coleman, M.M. Amiji, Nanoemulsions in translational research-opportunities and challenges in targeted cancer therapy., AAPS PharmSciTech. 15 (2014) 694–708. doi:10.1208/s12249-014-0088-9.

[218] Y. Ma, D. Liu, D. Wang, Y. Wang, Q. Fu, J.K. Fallon, X. Yang, Z. He, F. Liu, Combinational Delivery of Hydrophobic and Hydrophilic Anticancer Drugs in Single Nanoemulsions To Treat MDR in Cancer, Mol. Pharm. 11 (2014) 2623–2630. doi:10.1021/mp400778r.

[219] S. Ganta, A. Singh, Y. Rawal, J. Cacaccio, N.R. Patel, P. Kulkarni, C.F. Ferris, M.M. Amiji, T.P. Coleman, Formulation development of a novel targeted theranostic nanoemulsion of docetaxel to overcome multidrug resistance in ovarian cancer, Drug Deliv. 23 (2014) 1–13. doi:10.3109/10717544.2014.923068.

[220] H.S. Mahajan, M.S. Mahajan, P.P. Nerkar, A. Agrawal, Nanoemulsion-based intranasal drug delivery system of saquinavir mesylate for brain targeting, Drug Deliv. 21 (2014) 148–154. doi:10.3109/10717544.2013.838014.

[221] E. Ahmad, Y. Feng, J. Qi, W. Fan, Y. Ma, H. He, F. Xia, X. Dong, W. Zhao, Y. Lu, W. Wu, Evidence of nose-to-brain delivery of nanoemulsions: cargoes but not vehicles, Nanoscale. (2017). doi:10.1039/C6NR07581A.

[222] S. Yadav, S.K. Gandham, R. Panicucci, M.M. Amiji, Intranasal brain delivery of cationic nanoemulsion-encapsulated TNFα siRNA in prevention of experimental neuroinflammation, Nanomedicine Nanotechnology, Biol. Med. 12 (2016) 987–1002. doi:10.1016/j.nano.2015.12.374.

[223] A. Kubavat, A. Modi, B. Bajaj, S. Sheikh, S. Prasad, A. Mukhopadhyay, A. Kelkar, B. Swarnkar, M. Vedamurthy, R. Mittal, Efficacy and safety of a nano-emulsion gel formulation of adapalene 0.1% and clindamycin 1% combination in acne vulgaris: A randomized, open label, active-controlled, multicentric, phase IV clinical trial, Indian J. Dermatology, Venereol. Leprol. 78 (2012) 459. doi:10.4103/0378-6323.98077.

[224] L. Liu, C. Bagia, J.M. Janjic, The First Scale-Up Production of Theranostic Nanoemulsions, Biores. Open Access. 4 (2015) 218–228. doi:10.1089/biores.2014.0030.

[225] J. Pannu, A. McCarthy, A. Martin, T. Hamouda, S. Ciotti, A. Fothergill, J. Sutcliffe, NB-002, a novel nanoemulsion with broad antifungal activity against dermatophytes, other filamentous fungi, and Candida albicans., Antimicrob. Agents Chemother. 53 (2009) 3273–9. doi:10.1128/AAC.00218-09.

[226] M.F. Attia, N. Anton, M. Chiper, R. Akasov, H. Anton, N. Messaddeq, S. Fournel, A.S. Klymchenko, Y. Mély, T.F. Vandamme, Biodistribution of X-ray iodinated contrast agent in nano-emulsions is controlled by the chemical nature of the oily core, ACS Nano. 8 (2014) 10537–10550. doi:10.1021/nn503973z.

[227] N.Y. Rapoport, A.M. Kennedy, J.E. Shea, C.L. Scaife, K.-H. Nam, Controlled and targeted tumor chemotherapy by ultrasound-activated nanoemulsions/microbubbles, J. Control. Release. 138 (2009) 268–276. doi:10.1016/j.jconrel.2009.05.026.

[228] X. Song, L. Feng, C. Liang, K. Yang, Z. Liu, Ultrasound Triggered Tumor Oxygenation with Oxygen-Shuttle Nanoperfluorocarbon to Overcome Hypoxia-Associated Resistance in Cancer Therapies, Nano Lett. 16 (2016) 6145–6153. doi:10.1021/acs.nanolett.6b02365.

[229] J.M. Janjic, P. Shao, S. Zhang, X. Yang, S.K. Patel, M. Bai, Perfluorocarbon nanoemulsions with fluorescent, colloidal and magnetic properties, Biomaterials. 35 (2014) 4958–4968. doi:10.1016/j.biomaterials.2014.03.006.

[230] A.A. Kislukhin, H. Xu, S.A. Adams, K.H. Narsinh, R.Y. Tsien, E.T. Ahrens, Paramagnetic fluorinated nanoemulsions for sensitive cellular fluorine-19 magnetic resonance imaging, Nat. Mater. 15 (2015) under review. doi:10.1038/nmat4585.

[231] S.H. Shin, E.-J. Park, C. Min, S. Il Choi, S. Jeon, Y.-H. Kim, D. Kim, Tracking Perfluorocarbon Nanoemulsion Delivery by ^{19}F MRI for Precise High Intensity Focused Ultrasound Tumor Ablation, Theranostics. 7 (2017) 562–572. doi:10.7150/thno.16895.

[232] G.P. Luke, A.S. Hannah, S.Y. Emelianov, Super-Resolution Ultrasound Imaging in Vivo with Transient Laser-Activated Nanodroplets, Nano Lett. 16 (2016) 2556–2559. doi:10.1021/acs.nanolett.6b00108.

[233] A. Gianella, P.A. Jarzyna, V. Mani, S. Ramachandran, C. Calcagno, J. Tang, B. Kann, W.J.R. Dijk, V.L. Thijssen, A.W. Griffioen, G. Storm, Z.A. Fayad, W.J.M. Mulder, Multifunctional Nanoemulsion Platform for Imaging Guided Therapy Evaluated in Experimental Cancer, ACS Nano. 5 (2011) 4422–4433. doi:10.1021/nn103336a.

[234] A.S. Klymchenko, E. Roger, N. Anton, H. Anton, I. Shulov, J. Vermot, Y. Mely, T.F. Vandamme, A. Lamprecht, J.P. Benoit, Q. Luo, G. Zheng, R.J.B. de Jong, C.W. Lowik, Highly lipophilic fluorescent dyes in nano-emulsions: towards bright non-leaking nano-droplets, RSC Adv. 2 (2012) 11876. doi:10.1039/c2ra21544f.

[235] V.N. Kilin, H. Anton, N. Anton, E. Steed, J. Vermot, T.F. Vandamme, Y. Mely, A.S. Klymchenko, Counterion-enhanced cyanine dye loading into lipid nano-droplets for single-particle tracking in zebrafish, Biomaterials. 35 (2014) 4950–4957. doi:10.1016/j.biomaterials.2014.02.053.

[236] S. Wilhelm, A.J. Tavares, Q. Dai, S. Ohta, J. Audet, H.F. Dvorak, W.C.W. Chan, Analysis of nanoparticle delivery to tumours, Nat. Rev. Mater. 1 (2016) 1–12. doi:10.1038/natrevmats.2016.14.

[237] M. Torrice, Does Nanomedicine Have a Delivery Problem?, ACS Cent. Sci. 2 (2016) 434–437. doi:10.1021/acscentsci.6b00190.

[238] T. Lammers, F. Kiessling, M. Ashford, W. Hennink, D. Crommelin, G. Strom, Cancer nanomedicine: is targeting our target?, Nat. Rev. Mater. 1 (2016) 16069.

doi:10.1038/natrevmats.2016.69.

[239] S.E. McNeil, Evaluation of nanomedicines: stick to the basics, Nat. Rev. Mater. 1 (2016) 16073. doi:10.1038/natrevmats.2016.73.

[240] Q. Sun, X. Sun, X. Ma, Z. Zhou, E. Jin, B. Zhang, Y. Shen, E.A. Van Kirk, W.J. Murdoch, J.R. Lott, T.P. Lodge, M. Radosz, Y. Zhao, Integration of nanoassembly functions for an effective delivery cascade for cancer drugs, Adv. Mater. 26 (2014) 7615–7621. doi:10.1002/adma.201401554.

[241] B. Pelaz, C. Alexiou, R.A. Alvarez-Puebla, F. Alves, A.M. Andrews, S. Ashraf, L.P. Balogh, L. Ballerini, A. Bestetti, C. Brendel, S. Bosi, M. Carril, W.C.W. Chan, C. Chen, X. Chen, X. Chen, Z. Cheng, D. Cui, J. Du, C. Dullin, A. Escudero, N. Feliu, M. Gao, M. George, Y. Gogotsi, A. Grünweller, Z. Gu, N.J. Halas, N. Hampp, R.K. Hartmann, M.C. Hersam, P. Hunziker, J. Jian, X. Jiang, P. Jungebluth, P. Kadhiresan, K. Kataoka, A. Khademhosseini, J. Kopeček, N.A. Kotov, H.F. Krug, D.S. Lee, C.-M. Lehr, K.W. Leong, X.-J. Liang, M. Ling Lim, L.M. Liz-Marzán, X. Ma, P. Macchiarini, H. Meng, H. Möhwald, P. Mulvaney, A.E. Nel, S. Nie, P. Nordlander, T. Okano, J. Oliveira, T.H. Park, R.M. Penner, M. Prato, V. Puntes, V.M. Rotello, A. Samarakoon, R.E. Schaak, Y. Shen, S. Sjöqvist, A.G. Skirtach, M.G. Soliman, M.M. Stevens, H.-W. Sung, B.Z. Tang, R. Tietze, B.N. Udugama, J.S. VanEpps, T. Weil, P.S. Weiss, I. Willner, Y. Wu, L. Yang, Z. Yue, Q. Zhang, Q. Zhang, X.-E. Zhang, Y. Zhao, X. Zhou, W.J. Parak, Diverse Applications of Nanomedicine, ACS Nano. 11 (2017) 2313–2381. doi:10.1021/acsnano.6b06040.

[242] K.G. Heinze, A. Koltermann, P. Schwille, Simultaneous two-photon excitation of distinct labels for dual-color fluorescence crosscorrelation analysis, Proc. Natl. Acad. Sci. 97 (2000) 10377–10382. doi:10.1073/pnas.180317197.

[243] S.R. Aragón, R. Pecora, Fluorescence correlation spectroscopy and Brownian rotational diffusion, Biopolymers. 14 (1975) 119–137. doi:10.1002/bip.1975.360140110.

[244] Y. Tian, M.M. Martinez, D. Pappas, Fluorescence correlation spectroscopy: a review of biochemical and microfluidic applications., Appl. Spectrosc. 65 (2011) 115A–124A. doi:10.1366/10-06224.

[245] T. Basch?, W.E. Moerner, M. Orrit, H. Talon, Photon antibunching in the fluorescence of a single dye molecule trapped in a solid, Phys. Rev. Lett. 69 (1992) 1516–1519. doi:10.1103/PhysRevLett.69.1516.

[246] J. Temirov, J.H. Werner, P.M. Goodwin, A.R.M. Bradbury, "Sizing" the oligomers of Azami Green fluorescent protein with FCS and antibunching, in: J. Enderlein, Z.K. Gryczynski, R. Erdmann, F. Koberling, I. Gregor (Eds.), International Society for Optics and Photonics, 2012: p. 82280J. doi:10.1117/12.906843.

[247] J. Ries, P. Schwille, Fluorescence correlation spectroscopy, BioEssays. 34 (2012) 361–368. doi:10.1002/bies.201100111.

[248] J.W. Krieger, A.P. Singh, N. Bag, C.S. Garbe, T.E. Saunders, J. Langowski, T. Wohland, Imaging fluorescence (cross-) correlation spectroscopy in live cells and organisms, Nat. Protoc. 10 (2015) 1948–1974. doi:10.1038/nprot.2015.100.

[249] A.S. Klymchenko, E. Roger, N. Anton, H. Anton, I. Shulov, J. Vermot, Y. Mely, T.F.

Vandamme, Highly lipophilic fluorescent dyes in nano-emulsions: towards bright non-leaking nano-droplets, RSC Adv. (2012) 11876–11886. doi:10.1039/c2ra21544f.

[250] K. Kristensen, J.R. Henriksen, T.L. Andresen, Quantification of leakage from large unilamellar lipid vesicles by fluorescence correlation spectroscopy, Biochim. Biophys. Acta - Biomembr. 1838 (2014) 2994–3002. doi:10.1016/j.bbamem.2014.08.007.

[251] M.F. Khan, M.K. Singh, S. Sen, Measuring Size, Size Distribution, and Polydispersity of Water-in-Oil Microemulsion Droplets using Fluorescence Correlation Spectroscopy: Comparison to Dynamic Light Scattering, J. Phys. Chem. B. 120 (2016) 1008–1020. doi:10.1021/acs.jpcb.5b09920.

[252] K. Kristensen, A. Urquhart, E. Thormann, T. Andresen, Binding of human serum albumin to PEGylated liposomes: insights into binding numbers and dynamics by fluorescence correlation spectroscopy, Nanoscale. (2016). doi:10.1039/C6NR05455B.

[253] Y. Klapper, P. Maffre, L. Shang, K.N. Ekdahl, B. Nilsson, M. Dries, D. Gerthsen, G.U. Nienhaus, S. Hettler, M. Dries, D. Gerthsen, G.U. Nienhaus, Low affinity binding of plasma proteins to lipid-coated quantum dots as observed by in-situ fluorescence correlation spectroscopy, Nanoscale. 7 (2015) 9980–9984. doi:10.1039/C5NR01694K.

[254] J. Xie, K. Nakai, S. Ohno, H.-J. Butt, K. Koynov, S. Yusa, Fluorescence Correlation Spectroscopy Monitors the Hydrophobic Collapse of pH-Responsive Hairy Nanoparticles at the Individual Particle Level, Macromolecules. 48 (2015) 7237–7244. doi:10.1021/acs.macromol.5b01435.

[255] A.Z. Eriksen, J. Brewer, T.L. Andresen, A.J. Urquhart, The diffusion dynamics of PEGylated liposomes in the intact vitreous of the ex vivo porcine eye: A fluorescence correlation spectroscopy and biodistribution study, Int. J. Pharm. 522 (2017) 90–97. doi:10.1016/j.ijpharm.2017.03.003.

[256] T. Forster, Th., Energiewanderung und Fluoreszenz, Naturwissenschaften. 33 (1946) 166–175. doi:10.1007/BF00585226.

[257] http://www.leica-microsystems.com/science-lab/quantitative-fluorescence/, (n.d.).

[258] I. Medintz, N. Hildebrandt, FRET - Förster Resonance Energy Transfer, 2013. doi:10.1002/9783527656028.

[259] H.C. Ishikawa-Ankerhold, R. Ankerhold, G.P.C. Drummen, Advanced Fluorescence Microscopy Techniques?FRAP, FLIP, FLAP, FRET and FLIM, Molecules. 17 (2012) 4047–4132. doi:10.3390/molecules17044047.

[260] http://www.fluortools.com/software/ae/documentation/tools/FRET, (n.d.).

[261] S. Preus, L.M. Wilhelmsson, Advances in Quantitative FRET-Based Methods for Studying Nucleic Acids, ChemBioChem. 13 (2012) 1990–2001. doi:10.1002/cbic.201200400.

[262] B. Valeur, M.N. Berberan-Santos, Molecular Fluorescence: Principles and Applications, 2012. doi:10.1002/9783527650002.

[263] E.S. Butz, M. Ben-Johny, M. Shen, P.S. Yang, L. Sang, M. Biel, D.T. Yue, C. Wahl-Schott, Quantifying macromolecular interactions in living cells using FRET two-hybrid

assays, Nat Protoc. 11 (2016) 2470–2498. doi:10.1038/nprot.2016.128.

[264] E.M. Obeng, E.C. Dullah, M.K. Danquah, C. Budiman, C.M. Ongkudon, FRET spectroscopy—towards effective biomolecular probing, Anal. Methods. 8 (2016) 5323–5337. doi:10.1039/C6AY00950F.

[265] E. a Jares-Erijman, T.M. Jovin, FRET imaging., Nat. Biotechnol. 21 (2003) 1387–1395. doi:10.1038/nbt896.

[266] A. Zeug, A. Woehler, E. Neher, E.G. Ponimaskin, Quantitative intensity-based FRET approaches--a comparative snapshot., Biophys. J. 103 (2012) 1821–7. doi:10.1016/j.bpj.2012.09.031.

[267] T. Skajaa, Y. Zhao, D.J. Van Den Heuvel, H.C. Gerritsen, D.P. Cormode, R. Koole, M.M. Van Schooneveld, J.A. Post, E.A. Fisher, Z.A. Fayad, C. De Mello Donega, A. Meijerink, W.J.M. Mulder, Quantum dot and Cy5.5 labeled nanoparticles to investigate lipoprotein biointeractions via F??rster resonance energy transfer, Nano Lett. 10 (2010) 5131–5138. doi:10.1021/nl1037903.

[268] Y. Zhao, I. van Rooy, S. Hak, F. Fay, J. Tang, C. de L. Davies, M. Skobe, E.A. Fisher, A. Radu, Z.A. Fayad, C. de Mello Donegá, A. Meijerink, W.J.M. Mulder, Near-Infrared Fluorescence Energy Transfer Imaging of Nanoparticle Accumulation and Dissociation Kinetics in Tumor-Bearing Mice, ACS Nano. 7 (2013) 10362–10370. doi:10.1021/nn404782p.

[269] J. Gravier, L. Sancey, J.L. Coll, S. Hirsjärvi, J.P. Benoît, F. Vinet, I. Texier, <title>FRET as a tool for the investigation of the fate of Lipidots contrast agents <emph type="1">in vivo</emph></title>, 7910 (2011) 79100W–79100W–12. doi:10.1117/12.873699.

[270] J. Gravier, L. Sancey, S. Hirsjärvi, E. Rustique, C. Passirani, J.P. Benoît, J.L. Coll, I. Texier, FRET imaging approaches for in vitro and in vivo characterization of synthetic lipid nanoparticles, Mol. Pharm. 11 (2014) 3133–3144. doi:10.1021/mp500329z.

[271] A.L. Lainé, J. Gravier, M. Henry, L. Sancey, J. Béjaud, E. Pancani, M. Wiber, I. Texier, J.L. Coll, J.P. Benoit, C. Passirani, Conventional versus stealth lipid nanoparticles: Formulation and in vivo fate prediction through FRET monitoring, J. Control. Release. 188 (2014) 1–8. doi:10.1016/j.jconrel.2014.05.042.

[272] R. Bouchaala, L. Mercier, B. Andreiuk, Y. M??ly, T. Vandamme, N. Anton, J.G. Goetz, A.S. Klymchenko, Integrity of lipid nanocarriers in bloodstream and tumor quantified by near-infrared ratiometric FRET imaging in living mice, J. Control. Release. 236 (2016) 57–67. doi:10.1016/j.jconrel.2016.06.027.

[273] D. Sobot, S. Mura, S.O. Yesylevskyy, L. Dalbin, F. Cayre, G. Bort, J. Mougin, D. Desmaële, S. Lepetre-Mouelhi, G. Pieters, B. Andreiuk, A.S. Klymchenko, J.-L. Paul, C. Ramseyer, P. Couvreur, Conjugation of squalene to gemcitabine as unique approach exploiting endogenous lipoproteins for drug delivery, Nat. Commun. 8 (2017) 15678. doi:10.1038/ncomms15678.

[274] S.W. Morton, X. Zhao, M.A. Quadir, P.T. Hammond, FRET-enabled biological characterization of polymeric micelles, Biomaterials. 35 (2014) 3489–3496. doi:10.1016/j.biomaterials.2014.01.027.

[275] K.K. Ng, M. Takada, C.C.S. Jin, G. Zheng, Self-sensing porphysomes for fluorescence-

guided photothermal therapy, Bioconjug. Chem. 26 (2015) 345–351. doi:10.1021/bc500595d.

[276] K.J. Chen, Y.L. Chiu, Y.M. Chen, Y.C. Ho, H.W. Sung, Intracellularly monitoring/imaging the release of doxorubicin from pH-responsive nanoparticles using F??rster resonance energy transfer, Biomaterials. 32 (2011) 2586–2592. doi:10.1016/j.biomaterials.2010.11.069.

[277] Y. Zhao, F. Fay, S. Hak, J. Manuel Perez-Aguilar, B.L. Sanchez-Gaytan, B. Goode, R. Duivenvoorden, C. de Lange Davies, A. Bjørkøy, H. Weinstein, Z.A. Fayad, C. Pérez-Medina, W.J.M. Mulder, Augmenting drug-carrier compatibility improves tumour nanotherapy efficacy., Nat. Commun. 7 (2016) 11221. doi:10.1038/ncomms11221.

[278] B.L. Sanchez-Gaytan, F. Fay, S. Hak, A. Alaarg, Z.A. Fayad, C. Pérez-Medina, W.J.M. Mulder, Y. Zhao, Real-Time Monitoring of Nanoparticle Formation by FRET Imaging, Angew. Chemie Int. Ed. (2017). doi:10.1002/anie.201611288.

[279] J.S. Basuki, H.T.T. Duong, A. Macmillan, R.B. Erlich, L. Esser, M.C. Akerfeldt, R.M. Whan, M. Kavallaris, C. Boyer, T.P. Davis, Using fluorescence lifetime imaging microscopy to monitor theranostic nanoparticle uptake and intracellular doxorubicin release, ACS Nano. 7 (2013) 10175–10189. doi:10.1021/nn404407g.

[280] M.L. Viger, W. Sheng, K. Doré, A.H. Alhasan, C.J. Carling, J. Lux, C. De Gracia Lux, M. Grossman, R. Malinow, A. Almutairi, Near-infrared-induced heating of confined water in polymeric particles for efficient payload release, ACS Nano. 8 (2014) 4815–4826. doi:10.1021/nn500702g.

[281] U. Alexiev, P. Volz, A. Boreham, R. Brodwolf, Time-resolved fluorescence microscopy (FLIM) as an analytical tool in skin nanomedicine, Eur. J. Pharm. Biopharm. 116 (2017) 111–124. doi:10.1016/j.ejpb.2017.01.005.

[282] Y. Zhu, C.-S. Choe, S. Ahlberg, M.C. Meinke, U. Alexiev, J. Lademann, M.E. Darvin, Penetration of silver nanoparticles into porcine skin ex vivo using fluorescence lifetime imaging microscopy, Raman microscopy, and surface-enhanced Raman scattering microscopy, J. Biomed. Opt. 20 (2015) 51006-1–8. doi:10.1117/1.JBO.20.5.051006.

[283] N. Alnasif, C. Zoschke, E. Fleige, R. Brodwolf, A. Boreham, E. Rühl, K.-M. Eckl, H.-F. Merk, H.C. Hennies, U. Alexiev, R. Haag, S. Küchler, M. Schäfer-Korting, Penetration of normal, damaged and diseased skin — An in vitro study on dendritic core–multishell nanotransporters, J. Control. Release. 185 (2014) 45–50. doi:10.1016/j.jconrel.2014.04.006.

[284] G.I. Rozenberg, K.B. Monahan, C. Torrice, J.E. Bear, N.E. Sharpless, Metastasis in an orthotopic murine model of melanoma is independent of Ras/raf mutation, Melanoma Res. 20 (2010) 361–371. doi:10.1097/CMR.0B013E328336EE17.

[285] L. Ritsma, E.J.A. Steller, S.I.J. Ellenbroek, O. Kranenburg, I.H.M. Borel Rinkes, J. van Rheenen, Surgical implantation of an abdominal imaging window for intravital microscopy, Nat. Protoc. 8 (2013) 583–594. doi:10.1038/nprot.2013.026.

[286] L. Ritsma, E.J.A. Steller, E. Beerling, C.J.M. Loomans, A. Zomer, C. Gerlach, N. Vrisekoop, D. Seinstra, L. van Gurp, R. Schäfer, D.A. Raats, A. de Graaff, T.N. Schumacher, E.J.P. de Koning, I.H.B. Rinkes, O. Kranenburg, J. van Rheenen, Intravital

Microscopy Through an Abdominal Imaging Window Reveals a Pre-Micrometastasis Stage During Liver Metastasis, Sci. Transl. Med. 4 (2012). http://stm.sciencemag.org/content/4/158/158ra145 (accessed July 21, 2017).

[287] M.A. Miller, S. Gadde, C. Pfirschke, C. Engblom, M.M. Sprachman, R.H. Kohler, K.S. Yang, A.M. Laughney, G. Wojtkiewicz, N. Kamaly, S. Bhonagiri, M.J. Pittet, O.C. Farokhzad, R. Weissleder, Predicting therapeutic nanomedicine efficacy using a companion magnetic resonance imaging nanoparticle, Sci. Transl. Med. 7 (2015). http://stm.sciencemag.org/content/7/314/314ra183 (accessed July 21, 2017).

[288] G.M. Thurber, K.S. Yang, T. Reiner, R.H. Kohler, P. Sorger, T. Mitchison, R. Weissleder, ARTICLE Single-cell and subcellular pharmacokinetic imaging allows insight into drug action in vivo, Nat. Commun. 4 (2013). doi:10.1038/ncomms2506.

[289] D. Soulet, A. Paré, J. Coste, S. Lacroix, W. Alt, Automated Filtering of Intrinsic Movement Artifacts during Two-Photon Intravital Microscopy, PLoS One. 8 (2013) e53942. doi:10.1371/journal.pone.0053942.

[290] S. Lee, C. Vinegoni, M. Sebas, R. Weissleder, Automated motion artifact removal for intravital microscopy, without a priori information., Sci. Rep. 4 VN-re (2014) 4507. doi:10.1038/srep04507.

[291] C.A. Schneider, W.S. Rasband, K.W. Eliceiri, NIH Image to ImageJ: 25 years of image analysis, Nat. Methods. 9 (2012) 671–675. doi:10.1038/nmeth.2089.

[292] R.S. Bradley, M.S. Thorniley, A review of attenuation correction techniques for tissue fluorescence, J. R. Soc. Interface. 3 (2006). http://rsif.royalsocietypublishing.org/content/3/6/1 (accessed July 21, 2017).

[293] M. Choi, S.J.J. Kwok, S.H. Yun, In Vivo Fluorescence Microscopy: Lessons From Observing Cell Behavior in Their Native Environment, Physiology. 30 (2015). http://physiologyonline.physiology.org/content/30/1/40 (accessed July 21, 2017).

[294] M.A. Miller, R. Weissleder, Imaging the pharmacology of nanomaterials by intravital microscopy: Toward understanding their biological behavior, Adv. Drug Deliv. Rev. (2016). doi:10.1016/j.addr.2016.05.023.

[295] W. Jiang, Y. Huang, Y. An, B.Y.S. Kim, Remodeling Tumor Vasculature to Enhance Delivery of Intermediate-Sized Nanoparticles, ACS Nano. 9 (2015) 8689–8696. doi:10.1021/acsnano.5b02028.

[296] H. Cabral, Y. Matsumoto, K. Mizuno, Q. Chen, M. Murakami, M. Kimura, Y. Terada, M.R. Kano, K. Miyazono, M. Uesaka, N. Nishiyama, K. Kataoka, Accumulation of sub-100 nm polymeric micelles in poorly permeable tumours depends on size, Nat. Nanotechnol. 6 (2011) 815–823. doi:10.1038/nnano.2011.166.

[297] M.A. Miller, S. Gadde, C. Pfirschke, C. Engblom, M.M. Sprachman, R.H. Kohler, K.S. Yang, A.M. Laughney, G. Wojtkiewicz, N. Kamaly, S. Bhonagiri, M.J. Pittet, O.C. Farokhzad, R. Weissleder, Predicting therapeutic nanomedicine efficacy using a companion magnetic resonance imaging nanoparticle, Sci. Transl. Med. 7 (2015) 314ra183-314ra183. doi:10.1126/scitranslmed.aac6522.

[298] Y. Matsumoto, J.W. Nichols, K. Toh, T. Nomoto, H. Cabral, Y. Miura, R.J. Christie, N. Yamada, T. Ogura, M.R. Kano, Y. Matsumura, N. Nishiyama, T. Yamasoba, Y.H. Bae,

K. Kataoka, Vascular bursts enhance permeability of tumour blood vessels and improve nanoparticle delivery, Nat Nano. advance on (2016) 1–7. doi:10.1038/nnano.2015.342.

[299] B.R. Smith, P. Kempen, D. Bouley, A. Xu, Z. Liu, N. Melosh, H. Dai, R. Sinclair, S.S. Gambhir, Shape Matters: Intravital Microscopy Reveals Surprising Geometrical Dependence for Nanoparticles in Tumor Models of Extravasation, Nano Lett. 12 (2012) 3369–3377. doi:10.1021/nl204175t.

[300] S. Hak, E. Helgesen, H.H. Hektoen, E.M. Huuse, P.A. Jarzyna, W.J.M. Mulder, O. Haraldseth, C. de L. Davies, The Effect of Nanoparticle Polyethylene Glycol Surface Density on Ligand-Directed Tumor Targeting Studied *in Vivo* by Dual Modality Imaging, ACS Nano. 6 (2012) 5648–5658. doi:10.1021/nn301630n.

[301] A.L.B. Seynhaeve, B.M. Dicheva, S. Hoving, G.A. Koning, T.L.M. Ten Hagen, Intact Doxil is taken up intracellularly and released doxorubicin sequesters in the lysosome: Evaluated by in vitro/in vivo live cell imaging, J. Control. Release. 172 (2013) 330–340. doi:10.1016/j.jconrel.2013.08.034.

[302] W.-S. Lim, P.G. Tardi, N. Dos Santos, X. Xie, M. Fan, B.D. Liboiron, X. Huang, T.O. Harasym, D. Bermudes, L.D. Mayer, Leukemia-selective uptake and cytotoxicity of CPX-351, a synergistic fixed-ratio cytarabine:daunorubicin formulation, in bone marrow xenografts., Leuk. Res. 34 (2010) 1214–23. doi:10.1016/j.leukres.2010.01.015.

[303] M.A. Miller, Y.-R. Zheng, S. Gadde, C. Pfirschke, H. Zope, C. Engblom, R.H. Kohler, Y. Iwamoto, K.S. Yang, B. Askevold, N. Kolishetti, M. Pittet, S.J. Lippard, O.C. Farokhzad, R. Weissleder, Tumour-associated macrophages act as a slow-release reservoir of nano-therapeutic Pt(IV) pro-drug., Nat. Commun. 6 (2015) 8692. doi:10.1038/ncomms9692.

[304] L. Nuhn, S. Gietzen, K. Mohr, K. Fischer, K. Toh, K. Miyata, Y. Matsumoto, K. Kataoka, M. Schmidt, R. Zentel, Aggregation Behavior of Cationic Nanohydrogel Particles in Human Blood Serum, Biomacromolecules. 15 (2014) 1526–1533. doi:10.1021/bm500199h.

[305] S. Bhattacharjee, DLS and zeta potential - What they are and what they are not?, J. Control. Release. 235 (2016) 337–351. doi:10.1016/j.jconrel.2016.06.017.

[306] X. Fan, W. Zheng, D.J. Singh, Light scattering and surface plasmons on small spherical particles, Light Sci. Appl. 3 (2014) e179. doi:10.1038/lsa.2014.60.

[307] D.J. Ross, R. Sigel, Mie scattering by soft core-shell particles and its applications to ellipsometric light scattering, Phys. Rev. E. 85 (2012) 56710. doi:10.1103/PhysRevE.85.056710.

[308] K. Trofymchuk, L. Prodi, A. Reisch, Y. Mély, K. Altenhöner, J. Mattay, A.S. Klymchenko, Exploiting fast exciton diffusion in dye-doped polymer nanoparticles to engineer efficient photoswitching, J. Phys. Chem. Lett. 6 (2015) 2259–2264. doi:10.1021/acs.jpclett.5b00769.

[309] A. Boreham, P. Volz, D. Peters, C.M. Keck, U. Alexiev, Determination of nanostructures and drug distribution in lipid nanoparticles by single molecule microscopy, Eur. J. Pharm. Biopharm. 110 (2017) 31–38. doi:10.1016/j.ejpb.2016.10.020.

[310] M.E. Lobatto, C. Calcagno, A. Millon, M.L. Senders, F. Fay, P.M. Robson, S.

Ramachandran, T. Binderup, M.P.M. Paridaans, S. Sensarn, S. Rogalla, R.E. Gordon, L. Cardoso, G. Storm, J.M. Metselaar, C.H. Contag, E.S.G. Stroes, Z.A. Fayad, W.J.M. Mulder, Atherosclerotic plaque targeting mechanism of long-circulating nanoparticles established by multimodal imaging, ACS Nano. 9 (2015) 1837–1847. doi:10.1021/nn506750r.

[311] Y. Gimenez, B. Busser, F. Trichard, A. Kulesza, J.M. Laurent, V. Zaun, F. Lux, J.M. Benoit, G. Panczer, P. Dugourd, O. Tillement, F. Pelascini, L. Sancey, V. Motto-Ros, 3D Imaging of Nanoparticle Distribution in Biological Tissue by Laser-Induced Breakdown Spectroscopy., Sci. Rep. 6 (2016) 29936. doi:10.1038/srep29936.

[312] S. Sindhwani, A.M. Syed, S. Wilhelm, W.C.W. Chan, Exploring Passive Clearing for 3D Optical Imaging of Nanoparticles in Intact Tissues, Bioconjug. Chem. 28 (2017) 253–259. doi:10.1021/acs.bioconjchem.6b00500.

[313] S. Sindhwani, A.M. Syed, S. Wilhelm, D.R. Glancy, Y.Y. Chen, M. Dobosz, W.C.W. Chan, Three-Dimensional Optical Mapping of Nanoparticle Distribution in Intact Tissues, ACS Nano. 10 (2016) 5468–5478. doi:10.1021/acsnano.6b01879.

[314] D.-E. Lee, H. Koo, I.-C. Sun, J.H. Ryu, K. Kim, I.C. Kwon, M.G. Bawendi, J. V. Frangioni, S.P. Park, W.K. Moon, T. Hyeon, S.M. Larson, U. Wiesner, M.S. Bradbury, S.S. Gambhir, C.H. Ahn, Multifunctional nanoparticles for multimodal imaging and theragnosis, Chem. Soc. Rev. 41 (2012) 2656–2672. doi:10.1039/C2CS15261D.

[315] R. Bouchaala, N. Anton, H. Anton, T. Vandamme, J. Vermot, D. Smail, Y. Mély, A.S. Klymchenko, Light-triggered release from dye-loaded fluorescent lipid nanocarriers in vitro and in vivo, Colloids Surfaces B Biointerfaces. 156 (2017) 414–421. doi:10.1016/j.colsurfb.2017.05.035.

[316] Jinqiang Jiang, and Xia Tong, Y. Zhao*, A New Design for Light-Breakable Polymer Micelles, (2005). doi:10.1021/JA0521019.

[317] E.R. Gillies, J.M.J. Fréchet, S.D. Fowler, Y. Sakurai, T. Seto, K. Kataoka, J.R. Geffner, A new approach towards acid sensitive copolymer micelles for drug delivery, Chem. Commun. 103 (2003) 1640–1641. doi:10.1039/B304251K.

[318] F. Ai, C.A. Ferreira, F. Chen, W. Cai, Engineering of radiolabeled iron oxide nanoparticles for dual-modality imaging, Wiley Interdiscip. Rev. Nanomedicine Nanobiotechnology. 8 (2016) 619–630. doi:10.1002/wnan.1386.

List of publications

1) <u>Redouane Bouchaala</u>, Luc Mercier, Bohdan Andreiuk, Yves Mély, Thierry Vandamme, Nicolas Anton, Jacky G. Goetz, Andrey S. Klymchenko. Integrity of lipid nanocarriers in bloodstream and tumor quantified by near-infrared ratiometric FRET imaging in living mice *Journal of Controlled Release. 2016, 236, 57-67*

2) <u>Redouane Bouchaala</u>, Nicolas Anton, Halina Anton, Thierry Vandamme, Yves Mély, Djabi Smail, Andrey S. Klymchenko. Light-triggered release of dyes from fluorescent lipid nanocarriers *in vitro* and *in vivo*. *Journal of Colloids and Surfaces B: Biointerfaces 156 (2017) 414–421*

3) <u>Redouane Bouchaala</u>, Ludovic Richert, Nicolas Anton, Thierry Vandamme, Yves Mély, Andrey S Klymchenko. Fluorescence correlation spectroscopy as a method to quantify the release of NR668 dyes from lipid nanocarriers in biological media *(in preparation)*

4) Mohamed F. Attia, Nicolas Anton, <u>Redouane Bouchaala</u>, Pascal Didier, Youri Arntz Nadia Messaddeq, Andrey S. Klymchenko, Yves Mély and Thierry F. Vandamme. Functionalization of nano-emulsions with an amino-silica shell at the oil-water interface. *RSC Advances. 2015, 5, 74353-74361.*

List of Conferences

1. <u>Redouane Bouchaala</u>, Luc Mercier, Bohdan Andreiuk, Yves Mély, Thierry Vandamme, Nicolas Anton, Jacky G. Goetz, Andrey S. Klymchenko *MAF 2015 conference, Würzburg, Germany, 2015.* (Poster presentation).

2. <u>Redouane Bouchaala</u>, Nicolas Anton, Halina Anton, Thierry Vandamme, Yves Mély, Djabi Smail, Andrey S. Klymchenko. *Journées du campus d'Illkirch (JCI), Strasbourg, France April 13-14, 2015.* (Poster presentation).

3. <u>Redouane Bouchaala</u>, Luc Mercier, Bohdan Andreiuk, Yves Mély, Thierry Vandamme, Nicolas Anton, Jacky G. Goetz, Andrey S. Klymchenko. *FRET 2 - Göttingen, Germany, 2016.* (Poster presentation).

4. <u>Redouane Bouchaala</u>, Luc Mercier, Bohdan Andreiuk, Yves Mély, Thierry Vandamme, Nicolas Anton, Jacky G. Goetz, Andrey S. Klymchenko. *Journées du campus d'Illkirch (JCI), Strasbourg, France April 21-22, 2016.* (Oral presentation).

5. <u>Redouane Bouchaala</u>, Ludovic Richert, Nicolas Anton, Thierry Vandamme, Djabi Smail, Yves Mély, Andrey S Klymchenko. *Clinical Nanomedicine and Targeted Medicine, Basel, 2017.* (Poster presentation).

6. <u>Redouane Bouchaala</u>, Luc Mercier, Bohdan Andreiuk, Yves Mély, Thierry Vandamme, Nicolas Anton, Jacky G. Goetz, Andrey S. Klymchenko. *International conference on photochemistry Strasbourg, France.2017.* (Poster presentation),

7. <u>Redouane Bouchaala</u>, Ludovic Richert, Nicolas Anton, Thierry Vandamme, Djabi Smail, Yves Mély, Andrey S Klymchenko. *MAF 2017 conference, Brugge, Belgium, 2017.* (Poster presentation).

Résumé en français

De nos jours, les nanovecteurs et nanoparticules constituent un domaine attractif pour les chercheurs et l'industrie pharmaceutique, en raison de leur éventuelle application en tant que système de délivrance de médicaments pour des applications biomédicales.

Ils ont la capacité d'améliorer la pharmacocinétique, la solubilité et le profil de toxicité de certains médicaments, et potentiellement augmenter leur index thérapeutique. Cependant, les résultats décevants des essais cliniques récents ont contraint certains à remettre en question le potentiel des nanovecteurs en tant que moyen de délivrance de médicaments et créer un débat sur ce problème-là.

La mauvaise délivrance peut être le résultat de l'instabilité des nanovecteurs, leurs conceptions, la pharmacocinétique et la biodisponibilité, ou simplement en raison de la variabilité biologique intrinsèque. La complexité des nanovecteurs nécessite une évaluation quantitative in vitro et in vivo approfondie de leur comportement, en mettant l'accent sur l'encapsulation, la stabilité, les interactions sanguines et les propriétés de libération de molécules.

Le but de mon projet de doctorat est le développement de techniques basées sur la fluorescence pour la caractérisation de l'intégrité des nanovecteurs lipidiques et la libération de molécules actives in vitro et in vivo. En utilisant des fluoprophores spécialement conçus comme modèles de médicaments, les points suivants ont été abordés :

➢ L'intégrité des nanovecteurs lipidiques et la libération de molécules suivie par la technique FRET (transfert d'énergie résonnant de type Förster) in vitro et in vivo.

➢ L'intégrité des nanovecteurs lipidiques et la libération de molécules suivie par la technique FCS (fluorescence spectroscopie de corrélation).

➢ L'encapsulation de nanovecteurs organiques et la libération de molécules caractérisée par la technique du blanchiment chimique.

➢ La libération contrôlée déclenchée par la lumière de molécules actives à partir des nanovecteurs lipidiques in vitro et in vivo.

Adopter et développer ces techniques pourrait aider à surmonter les défis et les difficultés à obtenir une caractérisation rapide et quantitative de la stabilité nanovecteurs et de leur libération des molécules directement dans les milieux biologiques et les organismes vivants.

Dans cette thèse nous avons utilisé principalement des nanovecteurs lipidiques qui apparaissent comme des candidats prometteurs pour l'administration de médicaments et le ciblage du cancer, en raison de leur faible toxicité, leur biodégradabilité et capacité à encapsuler des molécules actives ou agents de contraste. Cependant, en raison de la mauvaise compréhension de leur comportement et intégrité in vivo, leur translation du laboratoire aux applications biomédicales est limitée.

Dans une première partie (Part II-1) en utilisant le FRET entre deux fluorochromes infrarouges spécialement conçus, l'intégrité des nanovecteurs lipidiques dans le sang et la tumeur cible a été évaluée et quantifiée par imagerie ratiométrique dans le proche infrarouge chez les souris vivantes.

Nous avons émis comme hypothèse que la technique FRET (Transfert d'énergie résonante de type Förster) peut être exploité pour l'étude en temps réel de la stabilité des nanovecteurs in vivo, en raison de l'extrême sensibilité de FRET à la distance donneur-accepteur. Par conséquent ; l'encapsulation d'un ensemble de donneur-accepteur à l'intérieur des nanovecteurs devrait garantir une haute efficacité FRET lorsque la nanoparticule est intacte. Ensuite, la perte des signaux FRET indiquerait la désintégration des nanovecteurs associée avec la libération de ses composants dans le milieu (Figure 1).
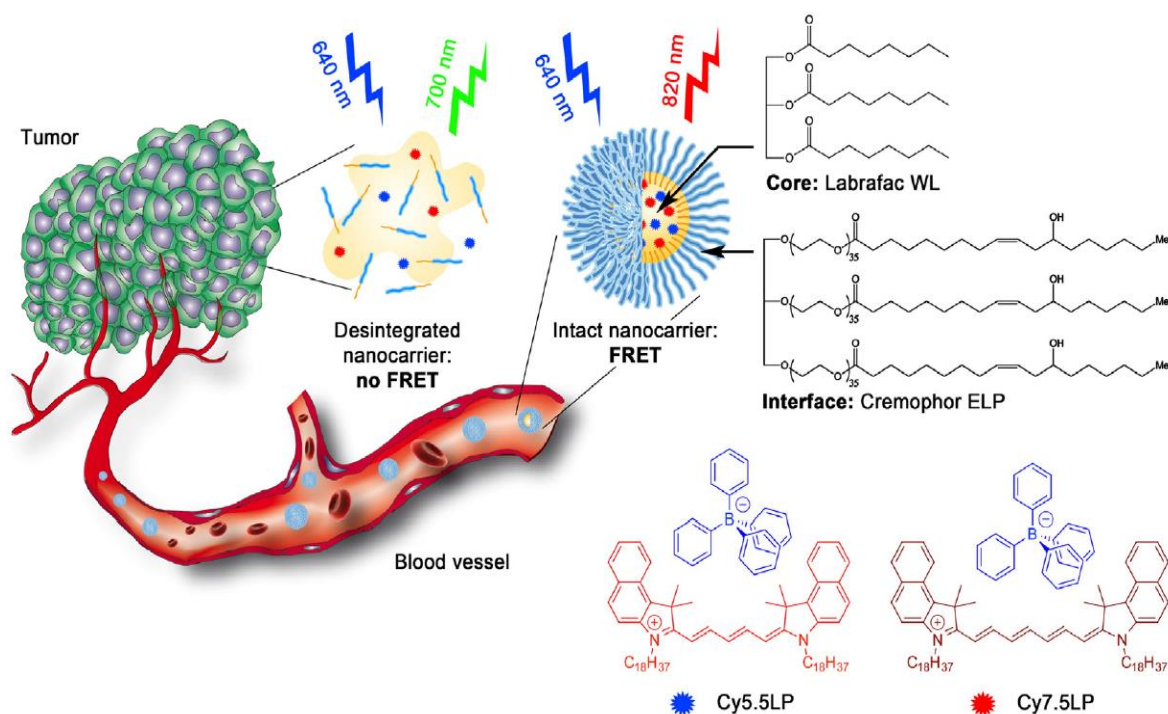
Figure 1. Concept des nanovecteurs FRET qui peuvent rendre compte de leur intégrité en modifiant leur couleur d'émission. Les structures chimiques de l'huile LabrafacWL (triglycéride à chaîne moyenne) et Cremophor ELP (tensioactif PEGylé) ainsi que les cyanines lipophiles 5.5 et 7.5 (Cy5.5LP et Cy7.5LP) avec leurs contre-ions volumineux hydrophobes sont présentés.

En utilisant notre approche récemment développée du conter-ion hydrophobe (TPB), nous avons encapsulé à l'intérieur des nanovecteurs lipidiques de 100 nm de taille deux colorants cyanines NIR lipophiles : Cy 5.5 / TPB en tant que donneur FRET et Cy 7.5 / TPB en tant qu'accepteur.

Ensuite, notre concept basé sur le FRET pour quantifié l'intégrité des nanovecteurs a été validé in vitro par spectrophotométrie pour vérifier la réponse de nos nanovecteurs FRET à leur désintégration. De la même manière, nous avons évalué la stabilité de ces nanovecteurs FRET en les incubant dans du sérum (100%), un modèle de milieu biologique in vivo. Les résultats ont montré une bonne stabilité de nos nanovecteurs, ce qui les rend appropriés pour l'imagerie PIR (proche infrarouge) de l'animal entier par injection intraveineuse. Puis, ces nanovecteurs ont été injectés rétro-orbitalement chez des souris saines et porteuses de tumeurs. En utilisant l'imagerie PIR des animaux entiers en deux couleurs, nous avons pu quantifier le contenu des nanovecteurs et leur intégrité directement dans la circulation sanguine, le foie et les tumeurs xénogreffes de souris vivantes.

Cette méthodologie a révélé que les nanovecteurs sont restés stables dans la circulation sanguine pendant au moins 6h. Ils se sont rapidement accumulés dans la tumeur sous forme presque intacte (77% après 2h) grâce à l'effet de perméabilité et de rétention (EPR), puis se sont désintégrés avec une demi-vie de 4,4h (figure 2). En conclusion, nous avons développé une approche FRET qui permet la visualisation directe et la quantification de l'intégrité des nanovecteurs in vivo.
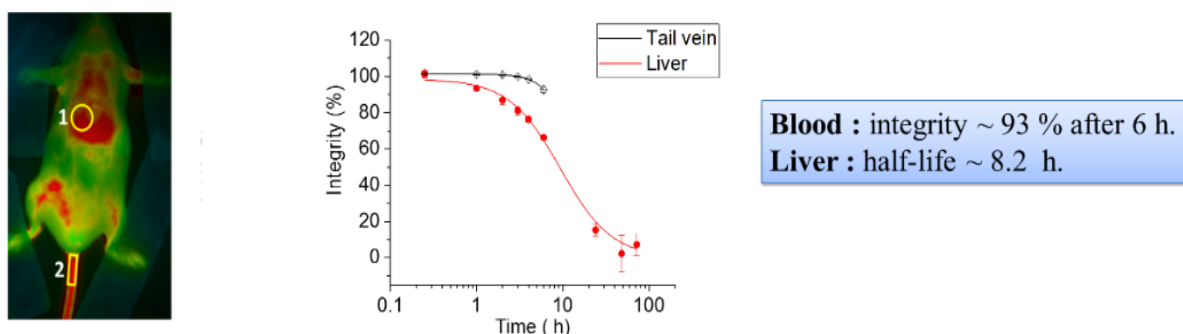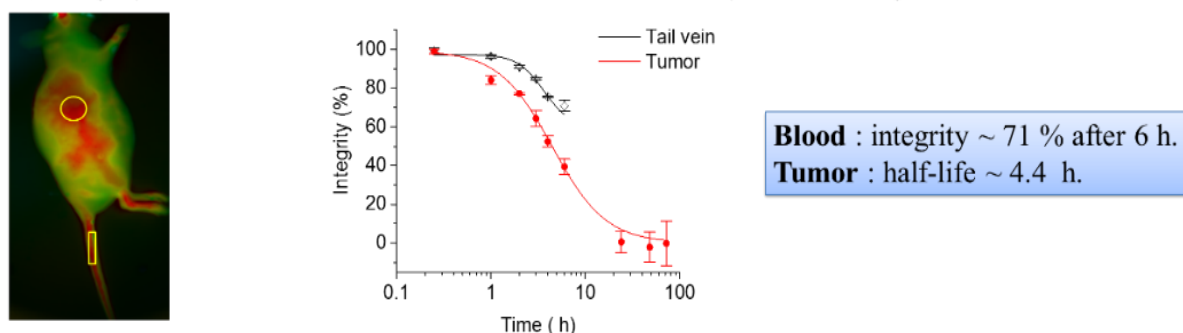

Figure 2. Analyse quantitative de l'intégrité des nanovecteurs lipidiques chez : A) les souris saines et B) les souris portant une tumeur. L'intégrité a été estimée en fonction de l'étalonnage de notre système d'imagerie in vivo.

Dans la deuxième partie de cette thèse (Part II-2), nous avons étudiés les phénomènes de libération de molécules à partir des nanovecteurs. Ces phénomènes sont un défi important qui doit être abordé, avec des techniques et des méthodes de caractérisation quantitative, capables de fonctionner directement in situ dans des milieux biologiques complexes. Comme le montre le premier projet, le FRET est une approche puissante pour étudier l'intégrité et la libération des marchandises. Ici, nous avons cherché une méthode alternative qui n'exige pas un double marquage des nanovécteurs. Pour cela, on a développé un test rapide et simple basé sur la FCS (Fluorescence spectroscopie de corrélation) pour la quantification in situ de la libération du

contenu des différents nanovecteurs lipidiques, encapsulant comme un modèle de molécules, le dérivé hydrophobe du Nil Rouge NR668.

Dans la configuration FCS, la libération de fluorochrome devrait affecter la luminosité des nanovecteurs lipidiques et la quantité d'espèces émissives en solution. Cependant, dans ce cas, la fluorescence du fluorochrome libéré ainsi que l'auto-fluorescence du milieu peuvent altérer les mesures de FCS.

A partir de cette problématique, nous avons introduit la molécule fluorescente, calcéine, dans le milieu extérieur, afin de nous fournir une fluorescence de fond qui pourrait modéliser l'émission du fluorochrome libéré et / ou de l'auto-fluorescence du milieu. Deux séries d'expériences ont été réalisées, dans le premier on a gardé la concentration de NR668 constante à l'intérieur des nanovécteurs lipidiques, mais on a augmenté la concentration de calcéine dans le milieu extérieur, pour imiter la libération de fluorochrome libre associée à l'apparence des espèces émissives dans le milieu. Dans la deuxième série, la concentration du NR668 dans les nanovecteurs lipidiques a été augmenté tout en maintenant constante la concentration de calcéine. Cela imiterait les changements dans la teneur en fluorochrome dans les nanovecteurs lipidiques en raison de la fuite de fluorochrome. Ensuite, les paramètres de FCS suivants ont été étudiés : (i) la luminosité B et (ii) le nombre d'espèces émissives N et (iii) l'écart-type SD de la fluctuation du signal.

Les résultats suggèrent que parmi les paramètres de FCS, le nombre d'espèces fluorescentes N (généralement utilisées pour ce type d'expérience) et la luminosité par particules B ne sont pas des paramètres appropriés pour la quantification de libération car ils sont affectés par les molécules présentes dans le milieu de manière non linéaire. Le seul paramètre, qui semble utile pour la quantification de la libération, est l'écart-type SD. Il est indépendant des petites molécules individuelles libres en solution et dépend linéairement de la teneur en fluorochrome à l'intérieur des nanovecteurs lipidiques. Cependant, la valeur SD n'est pas un paramètre absolu et dépend fortement des réglages instrumentaux, ainsi que de la concentration des nanovecteurs. Par conséquent, nous avons introduit un paramètre normalisé SD / SD0, où SD_0 représente l'écart-type de la fluctuation du signal pour les nanovécteurs à 1% NR668 sans fuite. Ce nouveau paramètre est indépendant de la concentration des nanovecteurs et de la puissance du laser.

La dépendance obtenue de SD / SD_0 a ensuite été utilisée en fonction de la concentration de fluorochrome NR668 à l'intérieur des nanovecteurs, en tant que courbe d'étalonnage après utilisation de l'ajustement linéaire (Figure 3).
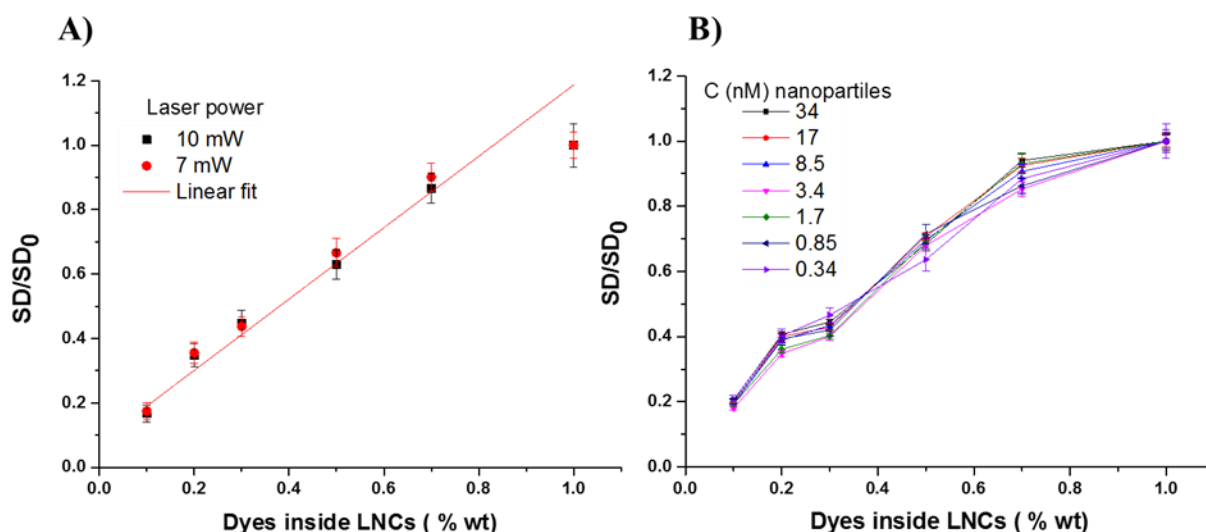

Figure 3. Normalisation de SD / SD_0 et étalonnage. (A) le paramètre SD / SD_0 en fonction de NR668 à l'intérieur des nanovecteurs (LNC), avec changement de puissance laser. Courbe d'étalonnage du paramètre SD / SD_0 vs NR668 à l'intérieur des (B), le paramètre SD / SD0 en fonction de NR668 à l'intérieur des nanovecteurs (LNC), avec variation des concentrations de LNC. Les barres d'erreur représentent l'erreur-type de la moyenne (n = 3).

Finalement, on a réalisé une expérience de libération en incubant 1% des nanovecteurs NR668 à 20, 37 et 60 ° C dans trois milieux différents : milliQ eau, eau en présence des nanovecteurs vierges ou avec 10% de FBS. Les résultats montrent que les nanovecteurs (LNC) sont très stables dans l'eau, alors que dans le milieu FBS, ils libèrent leur contenu d'une manière dépendante de la température. A 37 ° C, la libération est relativement lente atteignant 50% seulement après 6 heures d'incubation.

Cette nouvelle méthode de quantification est simple, car elle ne nécessite que la détection de l'écart-type de la fluctuation du signal, sans aucune analyse de la courbe d'autocorrélation. Elle peut être appliquée pour la quantification de la libération in situ à partir de différents nanovecteurs.

Troisièmement (Part II-3), en utilisant le blanchiment du Nil Rouge par le dithionite de sodium, nous avons établi une approche originale pour étudier l'état physique des nanovecteurs et le niveau d'encapsulation des fluorochromes. Les questions qui ont émané cette partie-là sont les suivantes :

- Capacité des nanovecteurs à encapsuler des molécules hydrophobes avec différents niveaux d'hydrophobicité ?

- Efficacité du piégeage et de la répartition des molécules dans les nanovecteurs.

- Effet de la nature des nanovecteurs, de la matrice, de la taille et de la méthode de préparation sur la répartition des molécules et l'encapsulation.

- La diffusion des molécules actives à l'intérieur des nanovecteurs.

Répondre à ces questions-là pourrait nous renseigner sur la stabilité de ces nanovecteurs en milieu biologique, leur taux de libération et leur profil, ainsi que sur la présence des phénomènes de libération soudaine. De plus, la compréhension de la nature physique du noyau des nanovecteurs (solide ou liquide ?) est importante pour prédire la cinétique de libération des molécules encapsulées.

Nous avons essayé de répondre à ces questions en utilisant différents nanovecteurs lipidiques et polymériques. Deux fluorochromes ont été utilisés comme modèle de médicaments : le Nil Rouge et sa version plus hydrophobe NR668. Dans la recherche biomédicale, le Nil Rouge a été utilisé et discuté comme modèle de médicament hydrophobe pour évaluer la solubilisation et l'encapsulation à l'intérieur des nanoparticules. Le Nil Rouge est hautement émissif et présente des propriétés solvatochromiques. Il contient un fragment de quinoïde, qui est une cible potentielle de réduction par le dithionite de sodium $Na_2S_2O_4$.

Sur la base de la réaction de blanchiment du Nil Rouge par le dithionite de sodium $Na_2S_2O_4$, nous avons développé une technique qui peut nous renseigner sur l'état physique des nanovecteurs et le niveau d'encapsulation du fluorochrome (leur accessibilité). Cette technique est basée sur le blanchiment du fluorochrome Nile Rouge (NR) et de son analogue hydrophobe (NR668) par le dithionite de sodium, lequel blanchiment entraîne une inhibition de la fluorescence (Figure 4).

- ★ NR/NR668
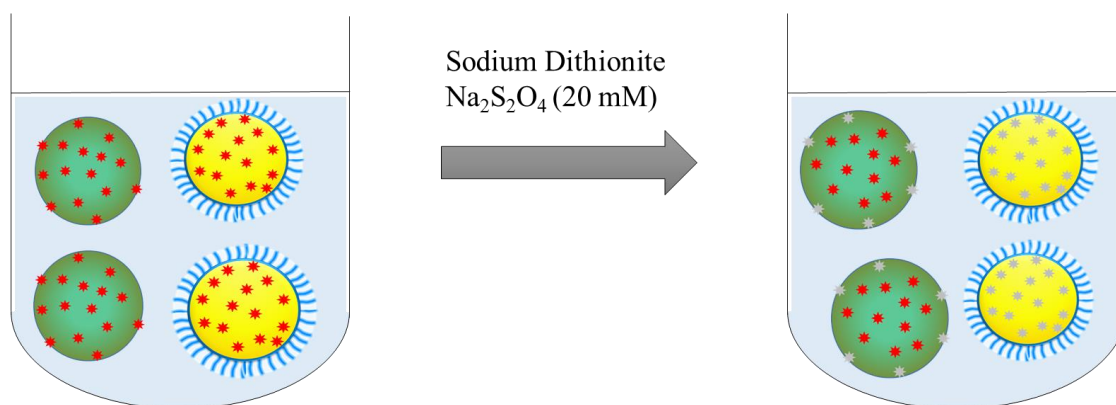- Lipid nanoparticles
- Polymeric nanoparticles

Figure 4. Concept de l'expérience de réduction par le dithionite de sodium Na2S2O4 avec l'encapsulation des nanovecteurs lipidiques et polymériques NR et NR 668.

Cinq nanovecteurs lipidiques et polymères différents ont été formulés avec des fluorochromes NR et NR 668.

La taille des nanovecteurs obtenus ont été mesurée par DLS. Une taille similaire a été obtenue avec NR ou NR668 pour chaque type de nanovecteurs. Pour les systèmes lipidiques, une taille de ~ 31 nm a été noté pour les nanoémulsions (LBF NCs) et les nanoparticules lipidiques solides (Sup C NCs). Le PLGA et le PMMA-MA NC_S présentaient une taille de 32 et 42 nm, respectivement, lorsqu'ils étaient formés à pH 7,4. Pour le PLGA à pH 3,4 et le PMMA-MA à pH 6,4, les nanovecteurs étaient beaucoup plus gros (170-180 nm). Dans les méthodes de nanoprécipitation, le pH est un facteur important pour la taille des nanovecteurs polymériques car il contrôle la charge des groupes carboxylates libres et donc la charge de surface des particules. Lors de la formation avec la méthode d'évaporation du solvant, la taille des nanovecteurs PLGA (PLGA SE) était de 245-260 nm. Pour ces séries de nanovecteurs, les spectres d'émission ont été mesurés, pour avoir les caractéristiques spectroscopiques nécessaires.

Ensuite, nous avons mesuré l'évolution de l'intensité de fluorescence des nanovecteurs en présence de l'agent réducteur sodium dithionite Na2S2O4. Ainsi, les fluorochromes NR668 et NR devraient être blanchis après la réaction avec le dithionite et perdre leur fluorescence. Etant donné que le dithionite de sodium est un di-anion hautement polaire et ne peut pas pénétrer

dans le noyau hydrophobe des nanoparticules, il peut blanchir le fluorochrome exclusivement du côté externe (Figure 5).
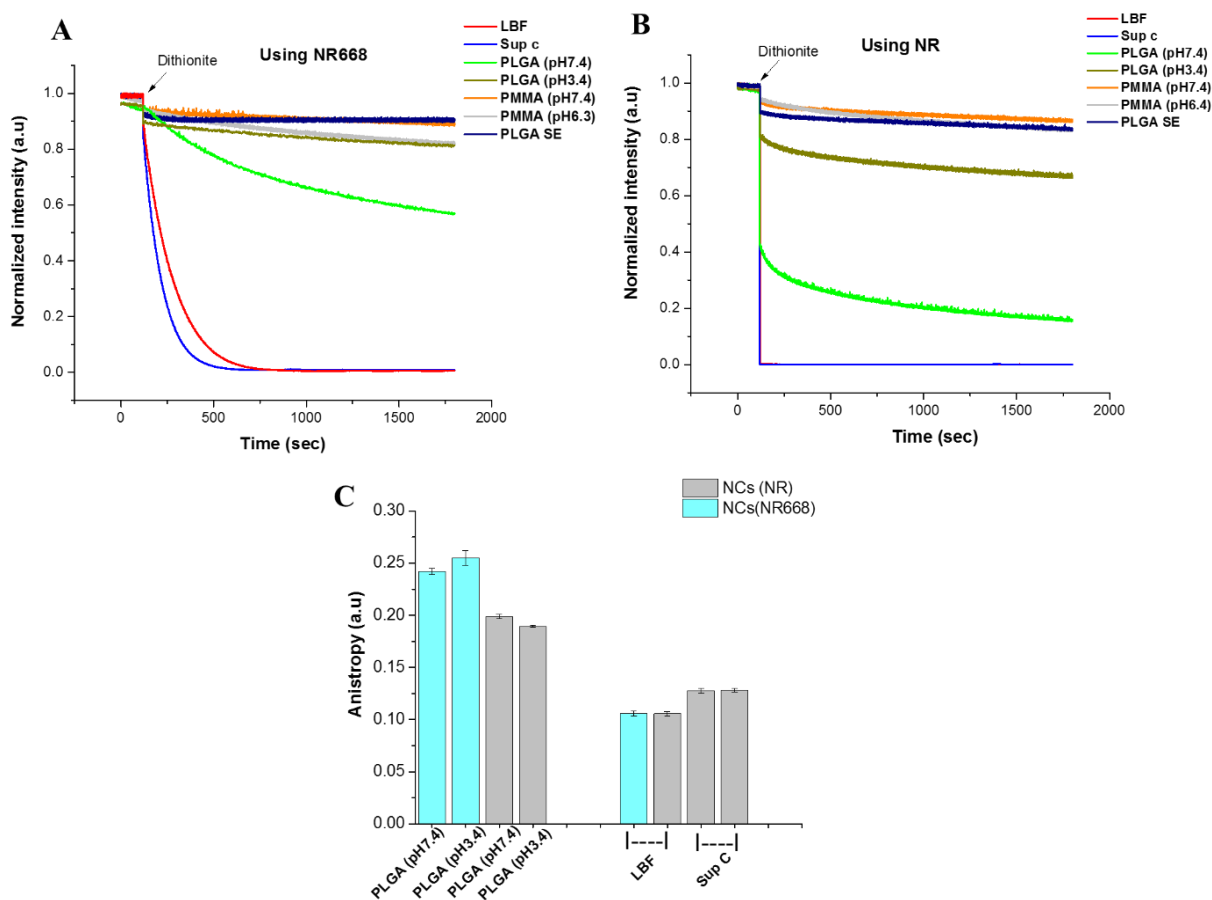

Figure 5. Diminution de la cinétique d'intensité de fluorescence normalisée des nanovecteurs lipidiques et polymériques en présence de dithionite de sodium. (A) nanovecteurs encapsulant NR668. (B) des nanovecteurs encapsulant NR. (C) Anisotropie de fluorescence des nanovecteurs PLGA, LBF et Sup C.

La cinétique de décroissance de la fluorescence dépend fortement du type des nanovecteurs et du fluorochrome encapsulé. Il est clair que pour les nanovecteurs lipidiques, la décroissance de fluorescence est beaucoup plus rapide que pour les nanovecteurs polymères. De plus, dans les nanovecteurs lipidiques, la fluorescence chute presque à zéro, ce qui indique un blanchiment efficace de presque tous les fluorochromes encapsulés. Dans le cas des LBF NC, c'est clairement en raison de la diffusion des fluorochromes à l'intérieur du noyau lipidique, de sorte que chaque colorant pourrait atteindre la surface des NC suivie par le blanchiment. Pour les nanovecteurs à base de Sup C on peut dire que sous forme de petites nanoparticules et en présence d'une grande quantité de tensioactif, Sup C est à l'état liquide à température ambiante.

Dans les nanovecteurs polymériques, la décroissance de la fluorescence était beaucoup plus lente et incomplète par rapport aux lipidiques, ce qui indique que les fluorochromes sont bien mieux encapsulés dans les polymères et ne peuvent pas diffuser librement dans le noyau. Aussi on peut noter que les nanovecteurs à base de PLGA de grande diamètre ont une meilleure encapsulation et une meilleure protection pour les fluorochromes hydrophobes NR668, comparé aux mêmes nanovecteurs de petit taille. Cela peut s'expliquer par un plus petit rapport surface / volume dans les nanovecteurs plus importants, ce qui limiterait l'exposition du NR668 à la surface.

Ensuite, dans le cas de nanovecteurs PMMA-MA des deux tailles, seulement 6% du signal NR668 a été perdu en présence de dithionite. Cela signifie que la matrice PMMA-MA permet une meilleure encapsulation et protection de NR668 par rapport à la matrice PLGA. Cette conclusion est importante pour l'encapsulation des médicaments avec des nanovecteurs polymériques, afin d'éviter le problème de la libération d'éclatement se produisant avec certains nanovecteurs. En outre, lorsque les PLGA NC sont préparés avec la méthode d'évaporation du solvant (PLGA SE), ils présentent une accessibilité beaucoup plus faible des fluorochromes pour le dithionite par rapport aux NC préparés par nanoprécipitation. Nous prévoyons que lors de l'utilisation de la méthode d'évaporation du solvant, les fluorochromes sont mieux encapsulés par rapport à la nanoprécipitation. En effet, la nanoprécipitation est un processus cinétique très rapide, où l'encapsulation des colorants est probablement médiocre par rapport à la technique d'évaporation du solvant. Une plus grande taille de nanovecteurs (260 nm) préparée par évaporation du solvant pourrait être le deuxième facteur favorisant une meilleure encapsulation des fluorochromes. Il convient de noter que notre méthode pourrait clairement distinguer le noyau liquide des nanovecteurs lipidiques du noyau solide de nanovecteurs à base polymère, parce que la différence dans la cinétique de blanchiment dithionite était drastique.

En conclusion de cette partie, la technique de blanchiment au dithionite nous a permis de déterminer les paramètres qui influencent l'encapsulation du contenu des nanovecteurs (taille, méthode de préparation, composition, etc.). De plus, cette technique permet d'étudier la diffusion des molécules actives au sein des nanovécteurs, leur accessibilité à la surface et, par conséquent, les phénomènes de libération. Il est important de noter que nous pouvons distinguer clairement les noyaux contenant du noyau liquide de ceux contenant du noyau solide, en raison des différences spectaculaires dans la cinétique de blanchiment. De plus, nous avons trouvé que le PMMA-MA est bien meilleur que le PLGA pour l'encapsulation de molécules lipophiles (en particulier avec une lipophilie moyenne) grâce à un protocole de nanoprécipitation.

En dernière partie (Part II-4), nous avons montré que les nanovecteurs lipidiques encapsulant des fluorochromes apparaissent comme un outil prospectif pour la libération contrôlée par la lumière de molécules actives in vitro et in vivo. Nous avons décrit comment utiliser la lumière visible pour induire la libération des fluorochromes encapsulés dans des nanovecteurs lipidiques (nanoémulsions), similaires à ceux étudiés dans les parties précédentes. Cette étude a été réalisée avec des nanovecteurs de 32 nm de diamètre synthétisés par auto-émulsification et incorporant NR688, l'analogue hydrophobe du Nil Rouge (Figure 6).
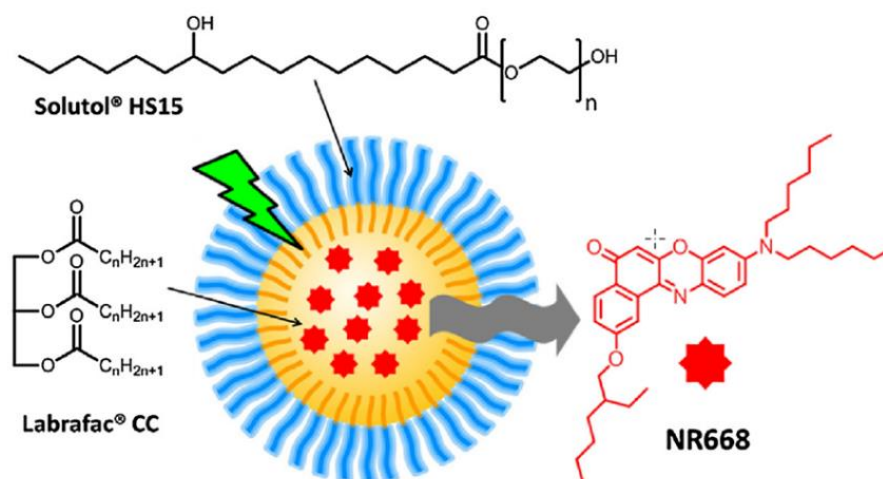

Figure 6. Concept : nanovecteurs lipidiques et l'effet de la lumière sur le dérivé du Nil Rouge encapsulé NR668.

Ces nanovecteurs ne pénètrent pas dans les cellules après plusieurs heures d'incubation à 37 °C. Cependant, après une illumination au microscope pendant 30 secondes à la longueur d'onde d'absorption de NR668 (535 nm), une accumulation rapide du fluorochrome dans les cellules a été montrée. Ce phénomène a été observé à 1 et 5% de concentration du et caractérisé par une différence entre l'intensité de fluorescence intracellulaire et extracellulaire. Ces résultats mettent en évidence le rôle des nanovecteurs, qui encapsulent NR668 empêchant sa fuite à l'intérieur des cellules, mais assurant sa libération après l'illumination.

Le même phénomène a été observé in vivo sur des poissons-zèbre, où des sondes fluorescentes ont été libérées dans les cellules endothéliales et les tissus après l'illumination des nanovecteurs circulant dans le sang. En utilisant la spectroscopie de corrélation de fluorescence, nous avons pu prouver qu'en éclairant les nanovecteurs avec une longueur d'onde et une puissance définies, une libération contrôlée du contenu est obtenue (Figure 7). Puisque ce processus est inhibé par la présence de sulfite de sodium, un agent appauvrissant en oxygène, on peut conclure que le

mécanisme de la libération déclenchée par la lumière dépend de l'oxygène, c'est-à-dire qu'il implique des processus de photo-oxydation. Néanmoins, nous ne pouvons pas exclure la possibilité d'un effet photo-thermique, qui pourrait également induire la libération du colorant.
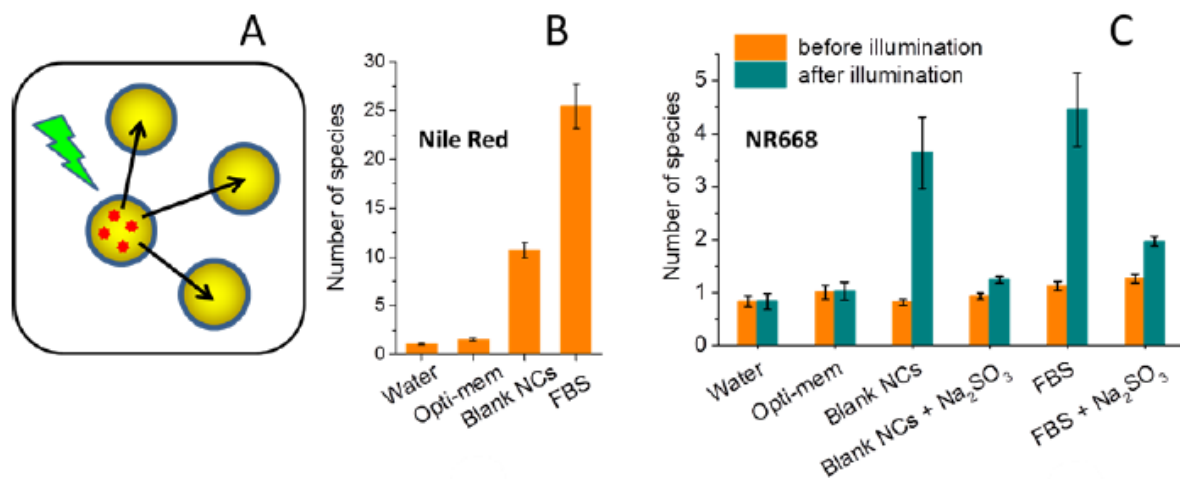

Figure 2. Étude de spectroscopie de corrélation de fluorescence (FCS) de la libération de fluorochrome induite par la lumière dans des milieux biologiques modèles. (A) Photo-libération en présence des nanoémulsions vierges. (B) Contrôle positif avec Nil Rouge, montrant une augmentation du nombre d'espèces émissives en raison de la libération spontanée de fluorochrome dans les nanoémulsions vierges environnantes. (C). Suivi du nombre de variations d'espèces fluorescentes par FCS pour les nano-gouttelettes chargées de NR668 dans différents milieux avant et après illumination.

Enfin, pour élucider si c'est les nanovécteurs entiers qui sont délivrés ou seulement leur contenu, les cellules ont été incubées avec un mélange de nanovecteurs encapsulant séparément NR668 et F888, des fluochromes hautement hydrophobes de différentes couleurs. Dans cette situation, les nanovécteurs chargés à la fois NR668 et F888 devraient être détectés à l'intérieur des cellules si tous les nanovécteurs entrent après l'éclairement. Cependant, il a été révélé que seul le signal NR668 a été observé à l'intérieur des cellules après illumination, ce qui suggère que l'illumination laser induit la libération des fluorochromes NR668 des nanovecteurs dans les cellules, mais ne pouvait pas vraiment induire l'internalisation des nanovecteurs toutes entiers.

En outre, nous avons montré que l'illumination de NR668 peut provoquer la libération dans les cellules d'un autre fluorochrome fortement hydrophobe (F888) co-encapsulé dans les mêmes nanovecteurs lipidiques. Sur la base de ces résultats, les nanovecteurs lipidiques chargés de fluorochrome apparaissent comme un outil prospectif pour des applications biomédicales permettant la libération de molécules actives contrôlées par illumination.

Les résultats dans le cadre de cette thèse suggèrent que les nanovecteurs lipidiques à base de nanoémulsion ont un grand potentiel en tant que vecteur de délivrance de médicaments. Une grande variété de molécules thérapeutiques pourrait être encapsulée et délivrée par l'effet EPR. De plus, ils présentent une très bonne stabilité et biodistribution in vivo. Les nanoémulsions peuvent être une plate-forme pour la libération contrôlée de molécules actives, avec une variété de stimulus. De plus, des modifications de surface des nanovecteurs lipidiques peuvent être envisagées pour des applications de ciblage. Cependant, pour le moment, il reste un défi avant que les surfactants à la surface des gouttelettes de nanoémulsion soient assez mobiles et puissent facilement se détacher de la surface dans les milieux biologiques. Enfin, les techniques de fluorescence développées ont fourni des outils appropriés pour surmonter les défis et les difficultés d'obtenir une caractérisation quantitative rapide de nanovecteurs telle que la stabilité et la libération de la cargaison directement en milieu biologique. De plus, ces nouvelles méthodes peuvent être appliquées à divers nanovecteurs organiques et inorganiques et pourraient devenir des références standards pour l'évaluation des nanovecteurs.

Bouchaala Redouane

Nanoparticules organiques fluorescentes à base de lipides : intégrité et relargage de principes actifs in vitro et in vivo

Résumé

Pour une application optimale des nanovecteurs comme système de délivrance de médicaments, il est nécessaire de caractériser pleinement leur intégrité, et leurs propriétés d'encapsulation et de libération de leur contenue. Mon projet de doctorat consiste à développer des méthodes basées sur la fluorescence pour caractériser l'intégrité de ces nanovecteurs lipidiques et la libération des molécules actives in vitro et in vivo. Premièrement, en utilisant le FRET entre deux fluorochromes infrarouges spécialement conçus, l'intégrité des nanovecteurs lipidiques dans le sang et la tumeur cible a été évaluée et quantifiée par imagerie ratiométrique dans le proche infrarouge chez les souris vivantes. Deuxièmement, nous avons développé un test rapide et simple basé sur la FCS pour la quantification in situ de la libération du contenu des différents nanovecteurs. Troisièmement, en utilisant le blanchiment du Nil Rouge par le dithionite de sodium, nous avons établi une approche originale pour étudier l'état physique des nanovecteurs et le niveau d'encapsulation des fluorochromes. En conclusion, nous avons montré que les nanovecteurs lipidiques encapsulant des fluorochromes apparaissent comme un outil prospectif pour la libération contrôlée par la lumière de molécules actives in vitro et in vivo.

Mots-clés : nanoparticules, nano-véhicules lipidiques, fluorescence, FRET, relargage, intégrité.

Résumé en anglais

For effective application of nanocarriers as drug delivery system, it is necessary to fully characterize their integrity, encapsulation, and release properties. The aim of my PhD project is to develop fluorescence-based methods for characterizing integrity of lipid nanocarriers and the release of active molecules in vitr o and in vivo. First, using FRET between specially designed near-infrared dyes the integrity of lipid nanocarriers in bloodstream and tumor was assessed and quantified by near-infrared ratiometric imaging in living mice. Second, we have developed fast and simple FCS-based assay for in situ quantification of release from different NCs. Third, using Nile Red bleaching by sodium dithionite, we established an original approach to study the physical state of the nanocarriers and the level of dye encapsulation. Finally, we showed that dye-loaded lipid nanocarriers appear as a prospective tool for light-controlled release of active molecules in vitro and in vivo.

Keywords: nanoparticles, lipid nanocarriers, fluorescence, FRET, release, integrity.